NUREG/CR-5679
SAND 98-2701

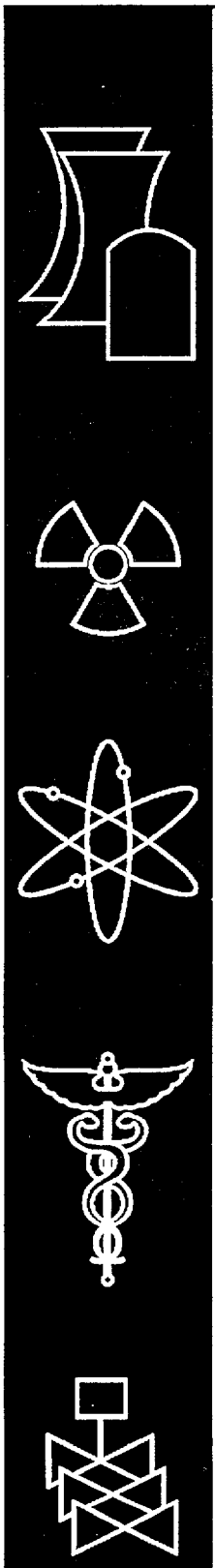

Design, Instrumentation, and Testing of a Steel Containment Vessel Model

Sandia National Laboratories

U.S. Nuclear Regulatory Commission
Office of Nuclear Regulatory Research
Washington, DC 20555-0001

AVAILABILITY NOTICE

Availability of Reference Materials Cited in NRC Publications

NRC publications in the NUREG series, NRC regulations, and *Title 10, Energy,* of the *Code of Federal Regulations,* may be purchased from one of the following sources:

1. The Superintendent of Documents
   U.S. Government Printing Office
   P.O. Box 37082
   Washington, DC 20402–9328
   <http://www.access.gpo.gov/su_docs>
   202–512–1800
2. The National Technical Information Service
   Springfield, VA 22161–0002
   <http://www.ntis.gov>
   1–800–553–6847 or locally 703–605–6000

The NUREG series comprises (1) brochures (NUREG/BR-XXXX), (2) proceedings of conferences (NUREG/CP-XXXX), (3) reports resulting from international agreements (NUREG/IA-XXXX), (4) technical and administrative reports and books [(NUREG-XXXX) or (NUREG/CR-XXXX)], and (5) compilations of legal decisions and orders of the Commission and Atomic and Safety Licensing Boards and of Office Directors' decisions under Section 2.206 of NRC's regulations (NUREG-XXXX).

A single copy of each NRC draft report for comment is available free, to the extent of supply, upon written request as follows:

Address: Office of the Chief Information Officer
Reproduction and Distribution
Services Section
U.S. Nuclear Regulatory Commission
Washington, DC 20555–0001
E–mail: <DISTRIBUTION@nrc.gov>
Facsimile: 301–415–2289

A portion of NRC regulatory and technical information is available at NRC's World Wide Web site:

<http://www.nrc.gov>

After January 1, 2000, the public may electronically access NUREG-series publications and other NRC records in NRC's Agencywide Document Access and Management System (ADAMS), through the Public Electronic Reading Room (PERR), link <http://www.nrc.gov/NRC/ADAMS/index.html>.

Publicly released documents include, to name a few, NUREG-series reports; *Federal Register* notices; applicant, licensee, and vendor documents and correspondence; NRC correspondence and internal memoranda; bulletins and information notices; inspection and investigation reports; licensee event reports; and Commission papers and their attachments.

Documents available from public and special technical libraries include all open literature items, such as books, journal articles, and transactions, *Federal Register* notices, Federal and State legislation, and congressional reports. Such documents as theses, dissertations, foreign reports and translations, and non-NRC conference proceedings may be purchased from their sponsoring organization.

Copies of industry codes and standards used in a substantive manner in the NRC regulatory process are maintained at the NRC Library, Two White Flint North, 11545 Rockville Pike, Rockville, MD 20852–2738. These standards are available in the library for reference use by the public. Codes and standards are usually copyrighted and may be purchased from the originating organization or, if they are American National Standards, from—

American National Standards Institute
11 West 42nd Street
New York, NY 10036–8002
<http://www.ansi.org>
212–642–4900

NUREG/CR-5679
SAND 98-2701

Design, Instrumentation, and Testing of a Steel Containment Vessel Model

Manuscript Completed: February 1999
Date Published: February 2000

Prepared by
V. K. Luk, M. F. Hessheimer, G. S. Rightley,
L. Dwight Lambert, E. W. Klamerus

Sandia National Laboratories
Albuquerque, NM 87185-0744

Prepared for

Systems Safety Department
Nuclear Power Engineering Corporation
Tokyo, 105 Japan
Under Funds-in Agreement No. DE-F104-91AL73734

T. Hashimoto, NUPEC Project Manager

Division of Engineering Technology
Office of Nuclear Regulatory Research
U.S. Nuclear Regulatory Commission
Washington, DC 20555-0001
Under Containment Integrity Under Extreme Loads JCN A1401

J. F. Costello, NRC Project Manager

NUREG/CR-5679 has been reproduced from the best available copy.

Abstract

The Nuclear Power Engineering Corporation (NUPEC) of Japan and the US Nuclear Regulatory Commission (NRC), Office of Nuclear Regulatory Research, are co-sponsoring and jointly funding a Cooperative Containment Research Program at Sandia National Laboratories. As a part of this program, a steel containment vessel model was tested to failure in the high pressure test on December 11–12, 1996. The model, which is representative of a steel containment for an improved Japanese Mark II Boiling Water Reactor Plant, has a geometric scale of 1:10 and a thickness scale of 1:4. The objectives of the steel containment vessel model test were to obtain measurement data of the structural response of the model up to its failure in order to validate analytical modeling, to find the pressure capacity of the model, and to observe the failure mechanisms.

The steel containment vessel model was surrounded by a contact structure, which provided a simplified representation of some features of actual concrete shield buildings in reactor plants. The model underwent radial expansion under internal pressurization, and the gap between the two structures closed in local areas where contact occurred. This special feature was designed to provide measurement data on load re-distribution on contact between the two structures to validate the contact algorithms in finite element codes.

The model and the contact structure were instrumented with strain gages, displacement transducers, contact detection devices, pressure transducers, and thermocouples. More than 97% of the installed instruments survived the high pressure test.

After 16.5 hours of continuous operation with monotonic increases in pressure, the high pressure test was terminated when a leakage was detected and the pressurization system at its maximum flow capacity could not maintain the pressure inside the model. The maximum pressure achieved during the high pressure test was 4.66 MPa (676 psig) or approximately 5.97 times the scaled design pressure. Posttest model inspection revealed that the leakage was caused by a large tear, approximately 190-mm-long, along a weld seam at the outside edge of the equipment hatch reinforcement plate. A small meridional tear, roughly 85-mm-long, was also discovered in a vertical weld inside a semi-circular weld relief opening at the middle stiffening ring above the equipment hatch.

The posttest metallurgical evaluation provided critical information on the deformation pattern and the failure mode and mechanisms of the two tears and on the strain concentrations in a few locally necked areas. All material deformation and tear observed in the samples, which were made from the sections removed from the model, were ductile in nature. There was no evidence of material flaws, defects, or brittle behavior in the base metal or welds. The tears that occurred resulted from exceeding the local plastic ductility of the alloy.

Contents

Appendices

Figures

Tables

Executive Summary

A cooperative containment research program, co-sponsored and jointly funded by the Nuclear Power Engineering Corporation (NUPEC) of Japan and the Office of Nuclear Regulatory Research at the Nuclear Regulatory Commission (NRC), was established at Sandia National Laboratories (SNL) in 1991 to continue the research effort on containment integrity. This program consists of conducting static, pneumatic overpressurization tests at ambient temperature on two scale models of actual containment buildings for nuclear power plants in Japan. The two models are the mixed-scale steel containment vessel (SCV) and the 1:4-scale prestressed concrete containment vessel (PCCV) models. The high pressure tests provide test data to validate the analytical methodology to predict the structural behavior of nuclear containment buildings under pressure loading beyond the design basis accident.

This report provides a detailed account of all activities in the SCV model test project. The SCV model is representative of a steel containment for an improved Japanese Mark II Boiling Water Reactor Plant. The model has a geometric scale of 1:10 and a thickness scale of 1:4. The objective of the SCV model test is to obtain measurement data of the structural response of the model up to its failure in order to validate analytical modeling, to find the pressure capacity of the model, and to observe the failure mechanisms.

The SCV model was surrounded by a contact structure (CS), which provided a simplified representation of some features of actual concrete shield buildings in reactor plants. The gap between the two structures would shrink and eventually close in local areas where contact occurred when the model underwent radial expansion under internal pressurization. This special arrangement was designed to provide measurement data on load re-distribution on contact between the two structures to validate the contact algorithms in finite element codes.

The high pressure test on the SCV model was conducted December 11–12, 1996 at SNL. After 16.5 hours of continuous operation with monotonic increases in pressure, the test was terminated when a leakage was detected and the pressurization system at its maximum flow capacity could not maintain the pressure inside the model. The maximum pressure achieved during the test was 4.66 MPa (676 psig) or approximately 5.97 times the scaled design pressure. Posttest model inspection revealed that the leakage was caused by a large tear, approximately 190-mm-long, along a weld seam at the outside edge of the equipment hatch reinforcement plate. A small meridional tear, roughly 85-mm-long, was also discovered in a vertical weld inside a semi-circular weld relief opening at the middle stiffening ring above the equipment hatch.

The model and the contact structure were instrumented with strain gages, displacement transducers, contact detection devices, pressure transducers, and thermocouples. More than 97% of the installed instruments survived the high pressure test. All data from the high pressure test were properly corrected, and the complete set of corrected test data is included in this report. The equipment hatch area was heavily instrumented with strain gages to record its deformation response. Some gages located close to the large tear recorded high strain concentrations and provided the qualitative information used to infer the strain history at the large tear. No gages had been placed near the small tear that was not predicted in the pretest analysis. The global free-field model responses were provided by the gages in the upper conical shell section. The test data registered by these gages, with a maximum strain reading of about 2%, suggested that the model behaved in an almost axisymmetric manner.

Detailed posttest metallurgical evaluation was performed to obtain definitive information about the tear initiation site and the failure mode and mechanisms. The evaluation was performed on samples that were machined from the sections removed from the model. Evaluation results provided critical information about the deformation pattern and the failure mode and mechanisms of the two tears and on the strain concentrations in a few locally necked areas. The large tear at the equipment hatch experienced strong local necking deformations that occurred in the weld heat affected region of the SPV490 alloy plate. Hardness measurements and metallographic analysis indicate that heat from the welding process resulted in localized microstructural alteration and reduced hardness and strength of the SPV490 alloy plate. The small tear also occurred within the weld heat affected region of the SGV480 alloy plate.

All material deformation and the two tears observed in the samples were ductile in nature. There was no evidence of material flaws, defects, or brittle behavior in the base metal or welds. The tears that occurred resulted from exceeding the local plastic ductility of the alloy.

Acknowledgments

The Steel Containment Vessel (SCV) project consumed eight years of hard work and concerted effort from many people to bring it to its successful completion. The Project Team deeply appreciates their support and cooperation.

The Project Team acknowledges guidance, support, and encouragement from Drs. Hideo Ogasawara and Kenji Takumi, current and former Director and General Manager, respectively, Systems Safety Department, Nuclear Power Engineering Corporation (NUPEC) of Tokyo, Japan. The Project Team is also indebted to Dr. James F. Costello, Senior Structural Engineer, Structural and Geological Engineering Branch, Division of Engineering Technology, Nuclear Regulatory Commission, for his continuous guidance and encouragement.

Special thanks are extended to the engineers at Hitachi Works, Japan, for the design and fabrication of the SCV model and to the staff at Chicago Bridge and Iron Services, Inc. for designing, fabricating, and installing the contact structure.

The Peer Review Panel members made a significant contribution to the program's success by their periodic program reviews and valuable suggestions.

Acronyms

ASME	American Society of Mechanical Engineers
BWR	boiling water reactor
CPOT	cable potentiometer
CS	contact structure
DAS	data acquisition system
DET	Division of Engineering Technology
DOE	Department of Energy
DoR	Data of Record
GPIB	general purpose interface bus
HAZ	heat affected zone
JIS	Japan Industry Standard
LOCA	loss-of-coolant accident
LVDT	linear variable differential transformer
MITI	Ministry of International Trade and Industry
MST	Mountain Standard Time
NRC	Nuclear Regulatory Commission
NSS	nuclear steam supply
NUPEC	Nuclear Power Engineering Corporation
PC	personal computer
PCCV	prestressed concrete containment vessel
PLC	programmable logic controller
PWR	pressurized water reactor
RES	Office of Nuclear Regulatory Research
RTD	resistance temperature detector
SCV	steel containment vessel

SEM	scanning electron microscope
SNL	Sandia National Laboratories
UTS	ultimate tensile strength
V&V	validation and verification

1. Introduction

The Nuclear Power Engineering Corporation (NUPEC) of Japan and the US Nuclear Regulatory Commission (NRC), Office of Nuclear Regulatory Research have co-sponsored and jointly funded a cooperative containment research program at Sandia National Laboratories (SNL). NUPEC was founded in 1976 as the Nuclear Power Engineering Center under the initiative of academia and private corporations. Supported by the Agency for Natural Resources and Environment of the Ministry of International Trade and Industry, NUPEC is mandated to advance the performance and public acceptance of commercial nuclear power plants through engineering tests, safety analyses, information acquisition and analyses, and public relations activities. Within NUPEC, the Systems Safety Department is conducting research for the integrity of reactor containment vessels during severe accidents. Containment integrity tests include experiments and analyses of debris cooling phenomena, hydrogen combustion behavior, fission products transport behavior, and containment structural behavior. In addition, this department at NUPEC coordinates the cooperative containment program with the NRC and manages program activities with SNL and other subcontractors.

The Office of Nuclear Regulatory Research (RES) at US NRC plans, recommends, and implements programs of nuclear regulatory research, standards development, and resolution of safety issues for nuclear power plants and other facilities regulated by the NRC. Within RES, the Division of Engineering Technology (DET) plans, develops, and directs comprehensive research programs and standards development for nuclear and materials safety. In the nuclear safety area, there are programs in the design, qualification, construction, maintenance, inspection, and testing of current and advanced nuclear power plants. For materials safety, program activities include material characteristics, aging, and seismic and engineering aspects of these facilities and materials. Within DET, the Structural and Geological Engineering Branch has the lead for determining structural adequacy of structures and systems and for the coordinating and interfacing activities associated with the ASME Code Section III. This branch coordinates the cooperative containment program with NUPEC and manages SNL activities.

Sandia National Laboratories is a multi-program national security laboratory, operated by Sandia Corporation, a subsidiary of Lockheed Martin Company, for the US Department of Energy. Sandia's Nuclear Energy Technology Center has provided engineering and scientific support in the areas of reactor safety and safeguards to the NRC and the DOE for more than 20 years. A significant area of support has included analytical and experimental efforts to address issues related to severe accidents and containment integrity.

This cooperative containment program builds on the combined expertise of these organizations and continues to advance the understanding of the response of nuclear containment structures to pressure loading beyond the design basis accident and the ability to predict, analytically, the structural behavior. This is accomplished by conducting static, pneumatic overpressurization tests at ambient temperature of scale models of actual containment vessels for nuclear power plants in Japan. NUPEC and the NRC formulated the overall scope of the program and NUPEC, under the contract by Ministry of International Trade and Industry, Japan, is responsible for design and construction of the models. Sandia is funded by NUPEC to develop and operate a facility for conducting these tests, review the model designs and provide design support, instrument the models and collect data during the pressure tests, and report the results of the test. The NRC is funding Sandia to perform pre- and posttest analyses of the models and to conduct the pressure tests. All funding is directed to Sandia through agreements with the Department of Energy's Work-for-Others Office in the Science and Technology Transfer Division.

Tests of two containment models have currently been authorized under this program. The first test of a mixed-scale model of an Improved Mark-II type steel containment vessel (SCV) for a Boiling Water Reactor (BWR) was conducted in December 1996. This report describes the preparations leading up to the SCV test, the conduct of the pressure test, and presents the results. The results of the pre- and posttest analyses performed by Sandia are reported separately (Porter et al., 1996; Ludwigsen et al., 1998). Preparations are currently (1998) in progress for the second test of a 1:4-scale model of a prestressed concrete containment vessel (PCCV), and the results will be documented in a separate series of NUREG contractor reports.

1.1 Background

Containment vessels in nuclear power plants comprise, with the penetrations and other pressure boundary components, the final barrier between the environment and the nuclear steam supply system. The functions of the containment are to:

1. contain any radioactive material that may be released from the primary system (reactor vessel, steam generators, piping) in the event of an accident;

2. act as a supporting structure for operational equipment.

For US containments, the design loads and their combinations as well as the response limits are specified in the American Society of Mechanical Engineers (ASME) Boiler and Pressure Vessel Code. Initially, severe accidents were not part of the design basis due to their perceived low probability of occurrence, and pressure relief valves were not required. In Japan, MITI Directive controls the design of containment, and the design standard of containment is specified in the MITI Notification No. 501 and in JEAG4601. Containment buildings have been an integral part of commercial nuclear power plants in Japan and the United States since the first units were constructed in the 1960s.

With the accident at Three Mile Island in the United States in 1979, attention turned to the capacity of containment systems beyond their design basis. Sandia conducted a preliminary study (Blejwas, 1982), commissioned by the NRC, to identify some experiments that had been conducted to investigate this issue but concluded that the scope of the tests and the data did not provide sufficient insight into the problem. As a result, a program, including scale model tests coupled with detailed structural analysis, was formulated by the NRC to investigate the integrity of containment systems beyond their design basis. The primary objective of the NRC program was, and continues to be, the validation of analytical methods used to predict the performance of light water reactor containment systems when subjected to loads beyond those specified in the design codes. While some insights could be gained into structural response and failure mechanisms of actual containments, it was also recognized that the determination of the capacity of actual containments could not be determined solely from tests of simplified scale models. The results of this program, as summarized by Parks et al., (1991) concluded that there was significant reserve capacity in the containment vessels to resist loads above the design basis and that although the analytical efforts were encouraging, uncertainties remained about structural response and failure mechanisms.

Remaining uncertainties regarding the response of containment structures led to discussions among NUPEC, the NRC, and SNL that culminated in a 1991 agreement to start the NUPEC/NRC Cooperative Containment Program. In parallel with this cooperative program, there are independent efforts sponsored and conducted by both NRC and NUPEC. These efforts include investigating the response of penetrations (Parks et al., 1991; Lambert and Parks, 1994), the effects of aging on containment structure capacity (Cherry, 1996), and the seismic capacity of containment structures (Nakamura et al., 1997; James et al., 1997).

1.2 Scope of the Steel Containment Vessel Test

Nuclear power plants in Japan and the United States generally utilize one of two types of light water reactor systems, boiling water reactors (BWR) and pressurized water reactors (PWR). The containment vessels for the boiling water reactors in Japan are typically free-standing welded steel shells surrounded by a reinforced concrete reactor shield wall. Typical of this type of containment is the improved Mark II containment vessel. A sectional view of the prototype containment is shown in Figure 1.1. The improved Mark II is based on the original General Electric Mark II containment; however, it features a containment volume approximately 30% greater than that of the standard Mark II for improvement of maintainability of the containment vessel. There are no examples of improved Mark II containment vessels in the United States. However, the unique geometry of the improved Mark II containment, fabrication details and procedures, and aspects of interaction with the concrete shield building are relevant to the severe accident studies of BWR Mark I containments in the United States. As a result, NUPEC and the NRC agreed on a scale model of an improved Mark II BWR containment for the first test subject in the Cooperative Containment Program.

1.2.1 Model Features and Scale

Consistent with the objectives of the sponsoring organizations, the features and scale of the SCV

model were chosen so that the response of the model would mimic the global behavior of the prototype and local details, particularly those around penetrations, would be represented. Because both NUPEC and SNL (under NRC sponsorship) were continuing component tests of both full-size and scaled penetrations, it was decided that the penetrations represented in the SCV model, the drywell head and the equipment hatch, would be non-functional, i.e., they were welded shut and the flanges would be represented by continuous structural elements (Takumi, 1992). Some non-functional structural elements of the SCV model are shown in Figure 1.2. It is not very difficult to analyze the wetwell portion because of its configuration and the presence of a wide gap between the containment vessel and the shield wall in the wetwell, and therefore the decision was made to model only the upper portion of the model. Hence the concrete basemat and the wall-basemat junction were omitted from the scale model. Furthermore, the effects of internal structures and components were judged to be negligible on the structural response of the containment and were not included in the model. The model was truncated in the cylindrical portion, above the normal height of the suppression pool. A stiff ring girder and heavy spherical closure head were attached to the model at this elevation to complete the pressure boundary. All model penetrations needed solely for test purposes (e.g., instrumentation and pressurization ports, personnel access) were made through this bottom head. A comparison of a prototype containment and the SCV model is shown in Figure 1.3.

Finally the scale of the model was chosen so that the features and fabrication details of the prototype could be reproduced with relative ease, while allowing the model to be fabricated in Japan and shipped to the test site at SNL via conventional surface transport. Considering these criteria, it was decided that an overall geometric scale of 1:10, resulting in a model roughly 3 m in diameter and almost 6 m tall, would allow an adequate representation of the details of interest while keeping the model small enough for transport. Due to the thickness dependence of the material properties, it was also decided that the scale for the vessel wall thickness would be 1:4, to utilize materials with mechanical characteristics similar to the prototype. This "mixed scale" also reduced the fabrication and handling difficulties that would have occurred with a very thin vessel wall.

Although this mixed scale would perturb the prototypical vessel pressures by a factor of 2.5 (10/4), membrane and bending strains in the vessel are linearly related to pressure; therefore the response of the model should still resemble that of the prototype. While this mixed scale would affect the buckling response of the torispherical drywell head, the prototype was designed to preclude buckling at the design pressures.

Finally it was recognized that under severe accident conditions of temperature and pressure, the improved Mark II containment might make contact with the surrounding concrete shield building and respond differently than a free-standing model would. It was decided to include a contact structure around the SCV model that would interact with it in a manner similar, although not identical, to the prototypical shield building.

Details of the design and fabrication of the SCV model and the contact structure are described in Chapters 2 and 3.

1.2.2 Loading

By definition, the scope of this program was limited to addressing the capacity of containment vessels to loads beyond the design basis, the so-called severe accident loads. Design accident loads for light water reactor containment vessels are typically based on the loss-of-coolant accident (LOCA) and are defined by a "bounding" pressure and temperature transients. The term "severe accidents" is used to describe an array of conditions that could result in loads, in excess of the design basis loads, on the containment. The definition of severe accident loads, which is not as rigorous as the design basis loads definition, results from a consideration of various postulated failure scenarios of the primary nuclear system, up to and including a complete core meltdown and breach of the reactor pressure vessel. The resulting pressure and thermal loading characteristics depend on the unique features of the nuclear steam supply (NSS) system and the containment structure in addition to the postulated accident.

For this test program, it was necessary to decide whether both thermal and pressure loads would be applied to the model, either separately or simultaneously, what the pressurization medium should be, and whether the transient characteristics of these loads should be considered. Programmatically, the decision to perform a **static**, **pneumatic** overpressurization test at **ambient** temperature was dictated by risk and cost considerations and previous experience.

The effects of severe accident temperature loads on the structural response of the containment building are primarily limited to (1) the effects of elevated temperatures on the mechanical properties of the materials and (2) the mechanical loads resulting from differential or constrained thermal expansion. The effects of temperature on the material properties can be determined from standard material tests methods. These test results could be incorporated into the evaluation of the prototypical containment vessels without adding this complexity and cost (in terms of generating the thermal environment and protecting the instrumentation) to the SCV model test. Regarding the stresses imposed by differential thermal expansion, there are only a few locations in a steel and/or concrete containment building where these effects are significant, notably at the junction of the containment wall and the basemat or, in the case of the SCV model, at the gap between the containment vessel and the shield building. Again the added complexity and cost of simulating the thermal environments to reproduce these local effects was judged not to be justified for the SCV model because the model penetrations were non-functional. Both NUPEC and SNL (under NRC sponsorship) have separately conducted tests of full-size and scale models of penetrations under combined severe accident pressure and temperature conditions to address these local effects. Therefore, the decision was made to conduct the SCV model test at **ambient** temperature.

The containment volume during a severe accident consists of a combination of air, steam, and other by-products of the accident, including hydrogen and particulates (aerosols). Because the primary program interest is in the structural response of the containment to pressure loads and not measuring leak rates (see Subsection 1.2.3), there is no need to reproduce the containment environment. Hence, the choice of a pressurization medium becomes somewhat arbitrary and is dictated by safety and operational considerations. Hydrostatic testing is preferable from a safety viewpoint; however, it raises operational problems and requires protection of sensitive electronics and wiring from the water under high pressure. **Pneumatic** testing, while more dangerous, does not present any risks that cannot be managed cost effectively and does not require any unusual measures to protect the instrumentation. Nitrogen gas was chosen as the pressurization medium for the SCV model tests primarily for operational considerations. Fairly large quantities could be delivered at the test site in liquid form with a limited amount of fixed equipment. Nitrogen gas also has the advantage of being dry for instrumentation considerations, and it allows more accurate estimates of leakage rate if a small leak should develop prior to termination of the test.

The design and operation of the pressurization system are described in Chapter 6.

The test plan and conduct of the pressure tests are summarized in Chapter 7.

1.2.3 Response

The SCV model instrumentation suite was designed to measure the global behavior in free-field locations of the model and the local structural response of the model near discontinuities. Global response measurements included both displacements referenced to a global or fixed reference and surface strain measurements at a regular pattern of azimuths and elevations to characterize the overall shape of the model. Local response measurements consisted of surface strain measurements concentrated near structural discontinuities. In areas where membrane behavior was expected to dominate the response, only one surface of the model, typically the interior, was instrumented. Where significant bending could occur, both surfaces were instrumented. Both hoop and meridional strains were measured.

Because the representative penetrations were not functional in the model and it was not expected that the model would exhibit any significant leakage prior to gross structural failure (i.e., material separation resulting in uncontrolled venting) rigorous leak rate measurements were not performed during the high pressure test. Therefore, pressure measurement requirements were limited to characterizing the mechanical response as a function of pressure and to control the pressurization rate. While there was no attempt to simulate severe accident temperature conditions, a limited set of thermal measurements was taken to maintain the ambient temperature at near steady-state conditions and to correct strain measurements for any temperature variations that might occur.

In addition to these quantitative response measurements, the response of the SCV model was also monitored qualitatively using still and video (normal speed) photography and acoustic monitoring.

The design and implementation of the model instrumentation suite are described in Chapter 4.

Performance requirements and features of the data acquisition system are summarized in Chapter 5. A summary and discussion of the high pressure test results are provided in Chapter 8. The results of the posttest inspections and metallurgical evaluations are summarized in Chapters 9. The corrected test data, including a description of the corrections applied to the raw data, are included in the appendices along with a summary of the acoustic emission data recorded during the test.

One important aspect of the SCV model response in the high pressure test is the concept of **failure**. There were no explicit failure criteria defined for the SCV model in advance of the pressure test. In the United States, the functional failure for the prototypical containment is defined in the regulations as containment leak rates exceeding 1–1.5% of the containment volume per day (Lobner et al., 1990), considering maximum offsite dose rates due to fission product release to the environment. In Japan, the functional failure is defined in design specification made by the utility company and not in the regulations. This concept of functional failure is not meaningful for a test of the structural capacity of a containment vessel model, especially when most of the operational leak paths have been eliminated from the model (Horschel et al., 1993). In the case of the SCV model test, the pressurization system was designed to allow the model to be pressurized to levels significantly above those expected to cause local strains in the model to exceed the ultimate strain limits of the materials. The test would be terminated when the model and the pressurization system were incapable of maintaining or increasing the model pressure or when the safe operational limit of the pressurization system was exceeded. In this report, the term **failure refers to the operational inability to maintain pressure in the model**, not functional failure of the containment system in terms of leak or dose rates.

1.3 Project Organization

As noted in the Introduction, NUPEC and the NRC are the sponsoring organizations for this cooperative containment research program. Programmatic authorization to pursue this area of research is provided to these organizations by the ministerial or executive offices of their respective national governments as dictated by statute. Technical guidance was provided by panels of expert advisers from academia and industry in each country. In Japan, the Structural Advisory Committee met regularly with NUPEC personnel to review the program plans and status, while in the United States, a special Peer Review Panel provided the same support to NRC and SNL personnel.

Within the cooperative framework agreed on by NUPEC and the NRC, NUPEC designed and supplied the SCV model (fabricated at Hitachi Works, Ltd., a major BWR vendor in Japan) to SNL for instrumentation and testing. NUPEC also funded SNL to provide programmatic and design support to plan and prepare the test site, instrument the model, and design and assemble the data acquisition system. In addition, NUPEC also provided funding for the design (by SNL) and the fabrication (by Chicago Bridge and Iron Services, Inc.) of the contact structure. NRC funded Sandia to perform pre- and posttest analyses of the model and to conduct the test.

Regular Technical Working Group meetings were held in both Japan and the United States, involving program personnel from NUPEC, (including its contractors), the NRC, and Sandia. The purpose of these meetings was to plan and coordinate program activities and resolve technical issues. Separate meetings were held to discuss administrative issues related to cost and schedule.

Both NUPEC and NRC funded SNL to coordinate a Round Robin Analysis effort. This activity consisted of inviting other nuclear safety research organizations from government, industry and academia in the United States, Japan and other countries to perform independent analyses to predict and evaluate the response of the SCV model. SNL acted as the focal point for this effort in terms of disseminating and consolidating the work of the participating organizations. Six independent organizations in addition to NUPEC and SNL participated in this effort, performing pre- and posttest analyses and meeting before and after the SCV model test to discuss and compare analysis results. The efforts of these Round Robin participants are documented in separate NUREG Contractor Reports (Luk and Klamerus, 1996; 1998).

1.4 Project Schedule

The SCV model test project commenced in June 1991. The model designed by NUPEC was fabricated at the Hitachi Works in Japan in 1994 and delivered to the Containment Technology Test Facility-West at Sandia National Laboratories, Albuquerque, New Mexico on March 8, 1995. Figure

1.4 illustrates the layout of the test site. The SCV model was housed inside the fragment barrier (Building 9949). A safety zone consisting of a circular area with radius of 304.8 m (1000 ft) was maintained and monitored throughout the high pressure test. The command center in Building 9950, situated about 600 m away from the SCV model, served as headquarters for conducting the high pressure test.

The installation of the model into the fragment barrier through its roof is illustrated in Figure 1.5. Figure 1.6 shows the model, with exterior instrumentation, inside the fragment barrier. After completing the as-built measurements of the SCV model, the contact structure (CS) was designed, fabricated, and installed over the SCV model on December 5, 1995. Prior to installation of the CS, all instrumentation of the exterior of the model was installed, and the instrumentation on the inside of the model was completed by September 1996. A pretest analysis meeting for the Round Robin participants was held in Albuquerque on October 1–2, 1996 to review the predictions by each participant and inspect the model prior to the pressure tests.

A leak and instrumentation test of 0.2 P_d was conducted October 3, 1996 followed by a low pressure test to 1.5 P_d on November 7, 1996. The high pressure test of the SCV model began at 10:00 a.m. Mountain Standard Time on December 12, 1996 and was completed at 2:30 a.m. the following morning. Six months after the test, the CS was removed to allow visual inspection of the exterior surface of the model. Sections of the model were then removed for the detailed metallurgical evaluation. The corrected test data were sent to the sponsors and Round Robin participants, and a posttest Round Robin meeting was held in Albuquerque May 20–21, 1998 to discuss the test results and compare the posttest analyses. This final test report was completed for publication and distribution in December 1998.

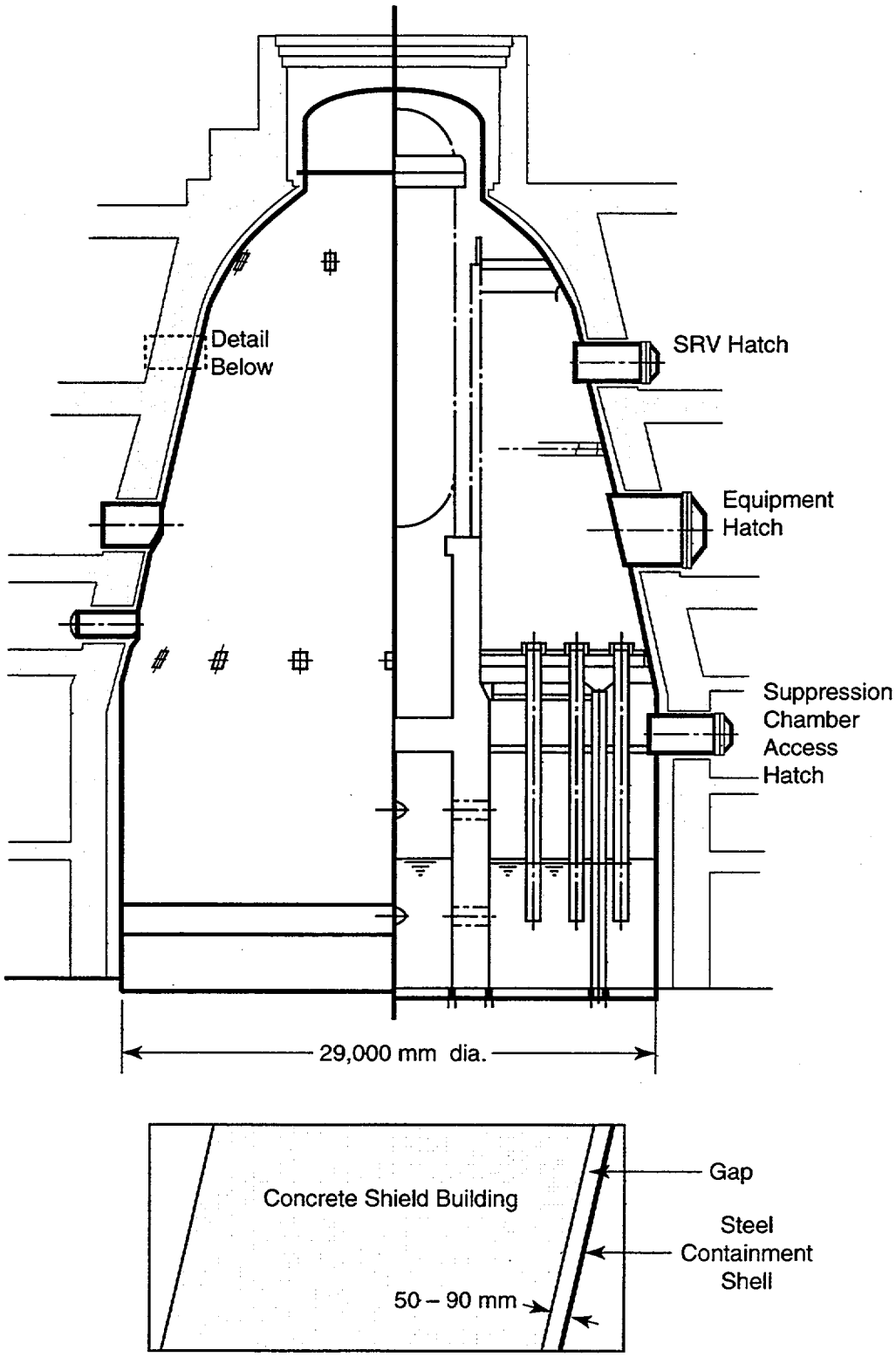

Figure 1.1 Elevation of an improved Mark II boiling water reactor containment building.

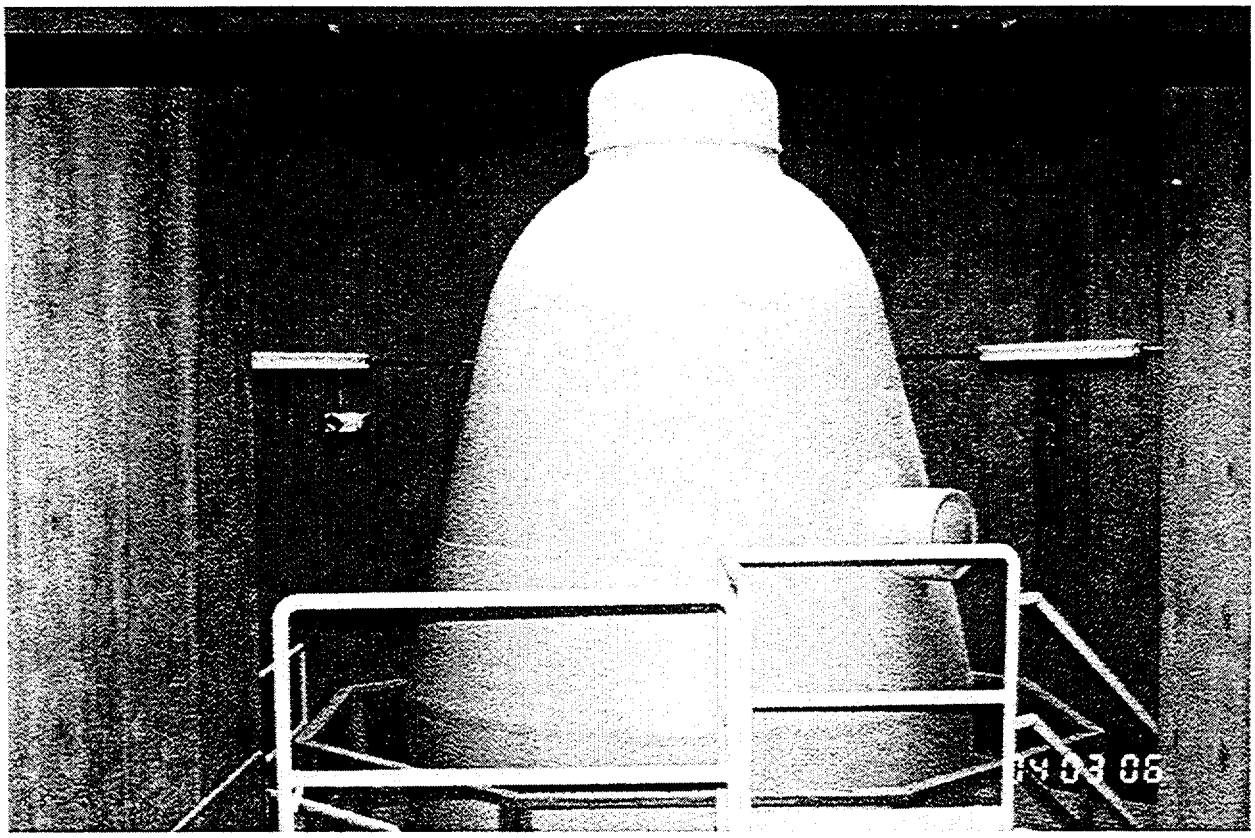

Figure 1.2 SCV model showing that the equipment hatch and the top head flange were welded shut.

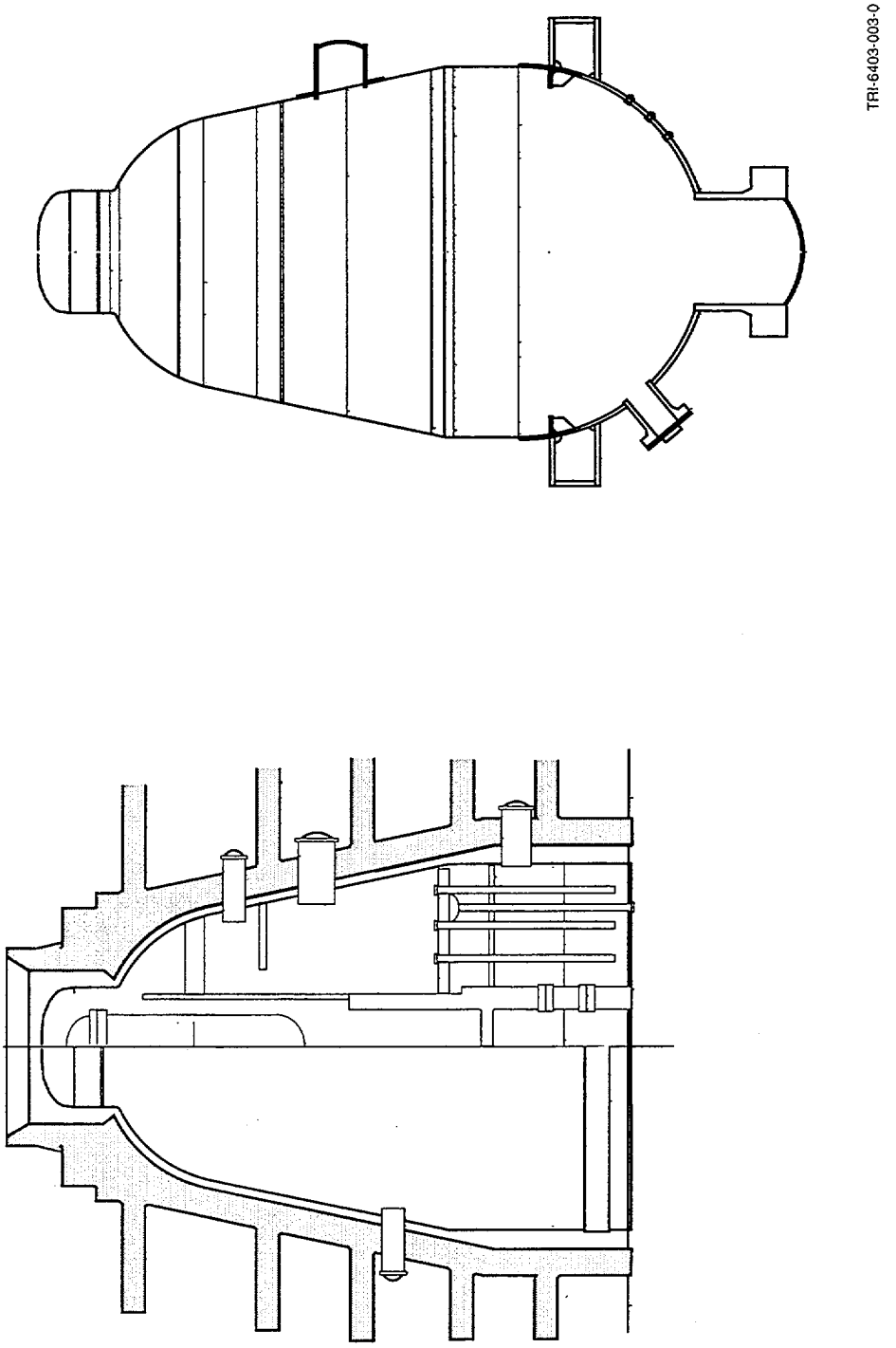

Figure 1.3 Comparison of prototype containment and SCV model.

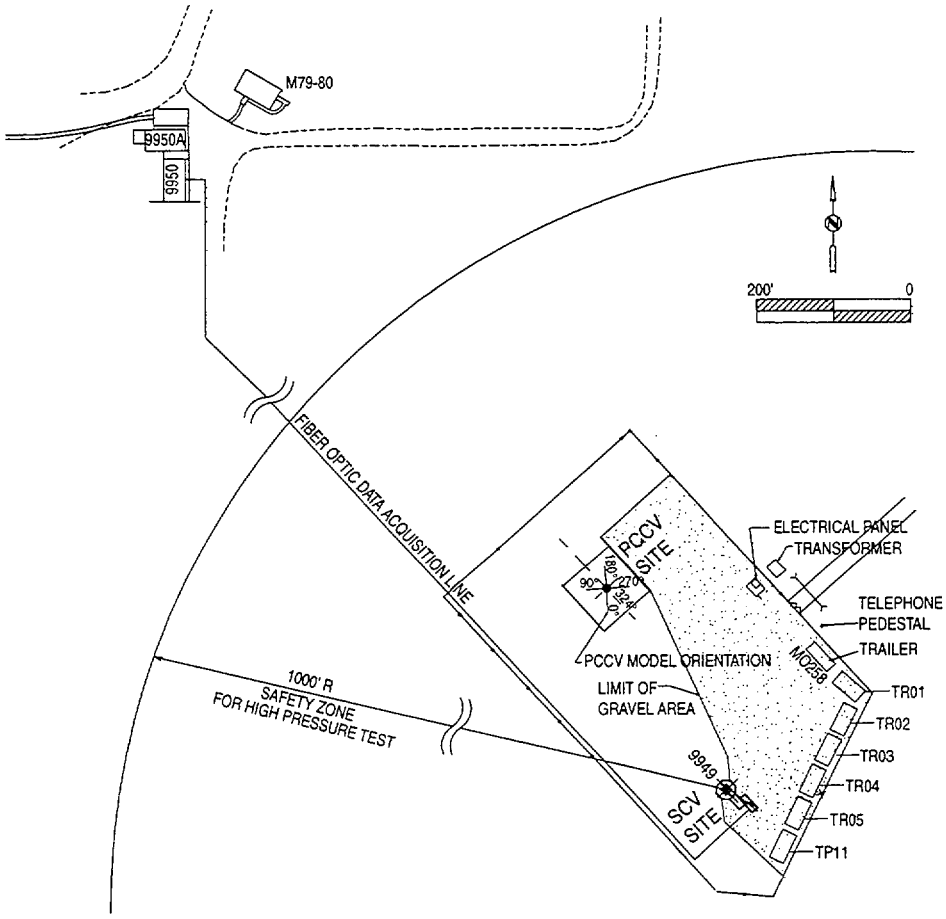

Figure 1.4 Layout of the test site.

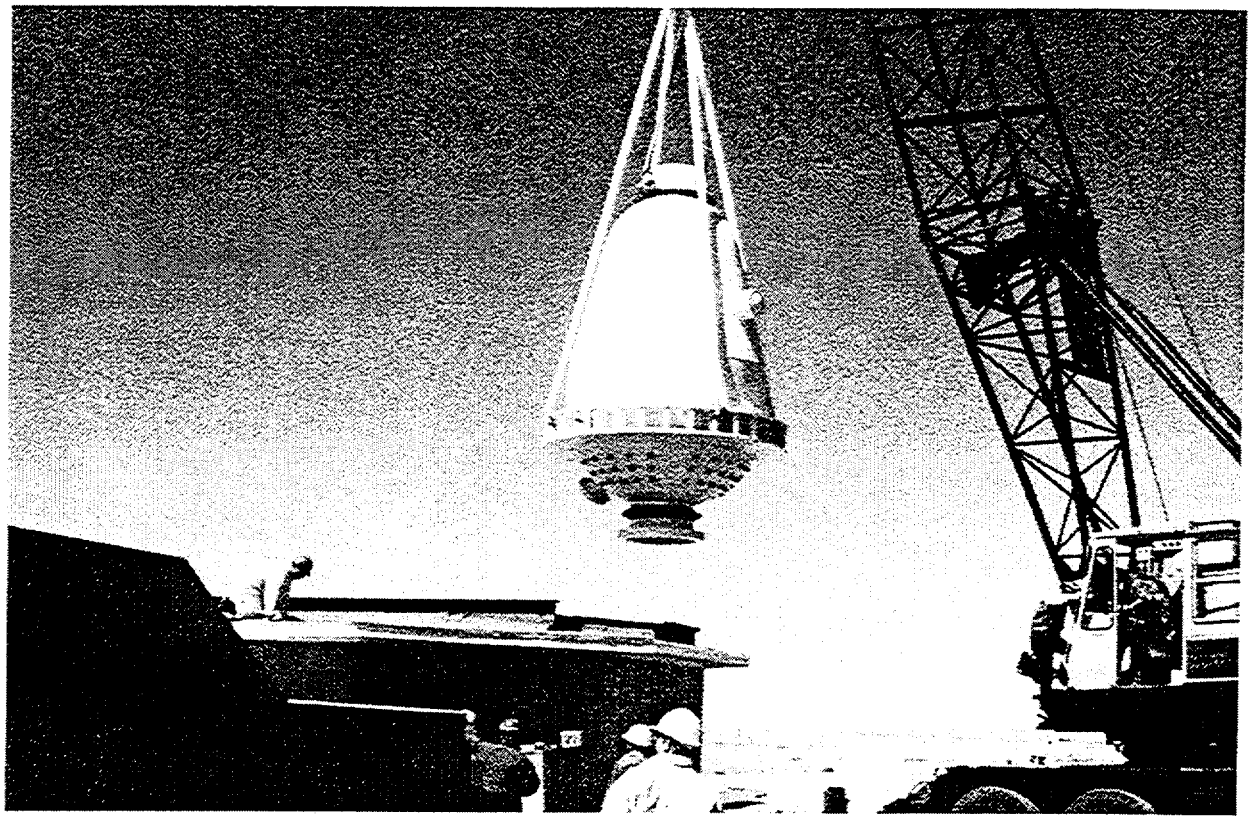

Figure 1.5 SCV model installation into the fragment barrier through its roof.

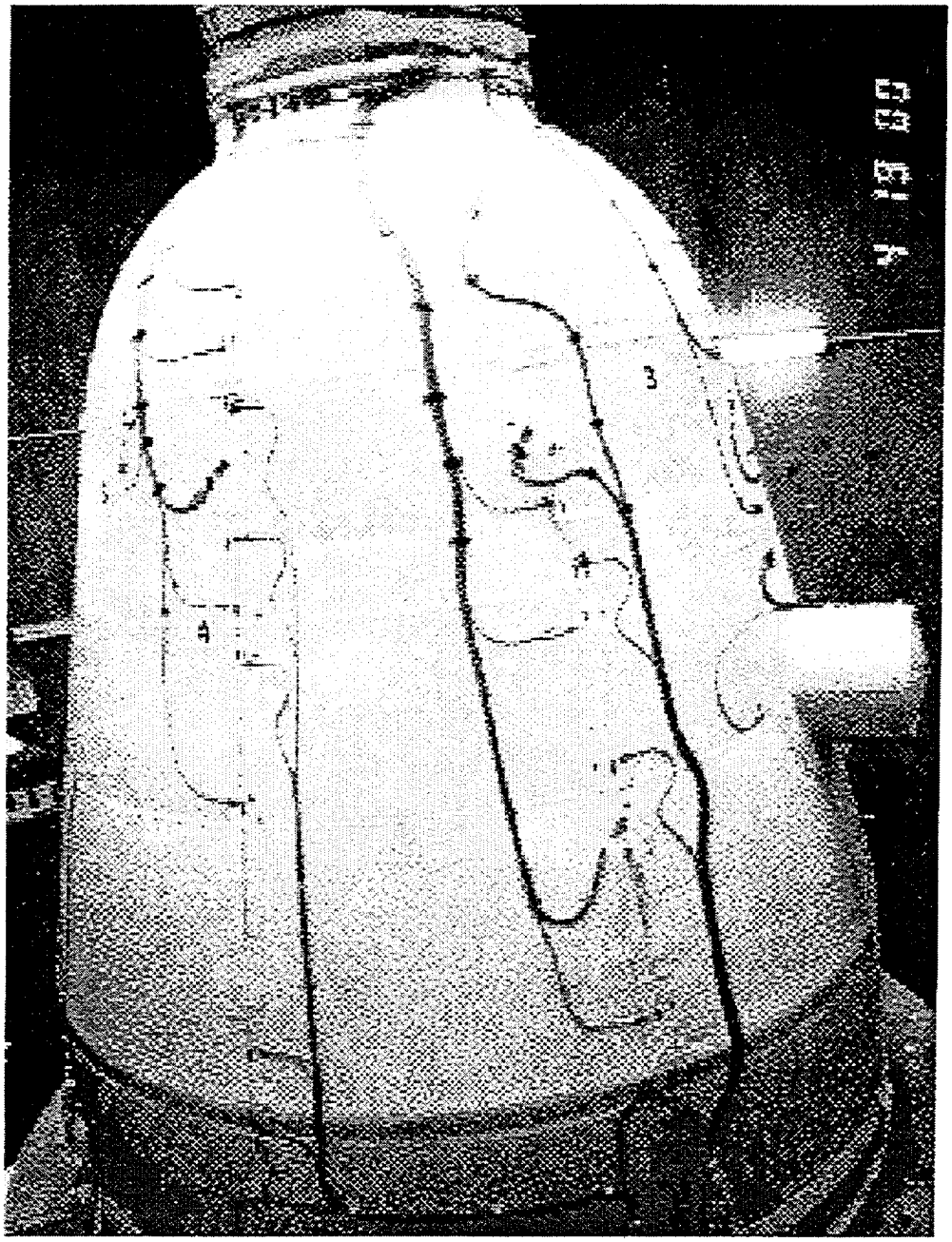

Figure 1.6 SCV model with exterior instrumentation.

2. Design and Fabrication of the SCV Model

2.1 Model Description

The steel containment vessel (SCV) model is scaled 1:4 in shell thickness and 1:10 in overall geometry from a prototype Improved Mark-II Boiling Water Reactor (BWR) containment structure. A concrete shield building surrounds the actual containment. The model, weighing 15,800 kg, is 2.9 m in its largest diameter and 5.9 m tall, with an enclosed volume of about 21 m^3.

The essential features of the SCV model are illustrated in Figure 2.1. The SCV model is partitioned into various sections by means of a top head flange and three stiffeners. From the top of the model, the model is composed of a top head, a knuckle region, a spherical shell section, a conical shell section, a cylindrical shell section, and a thickened bottom head. The SCV model includes some details of the actual containment such as the equipment hatch penetration and reinforcement plate, the drywell head, and the SGV480/SPV490 material transition location. All other hatches, airlocks, and inward penetrations are omitted from the SCV model. In addition, the lower wetwell and the wall-basemat junction were not included in the model. Instead, a thick bottom head was selected to complete the pressure boundary. All internal structures that do not affect the structural responses of the model under pressurization are omitted from the model. All thickness variations in the model occur on its outer surface and the inner surface of the model is smooth. The design drawings of the SCV model are in Appendix A.

The SCV model in Figure 2.1 is shown surrounded by a contact structure (CS) whose design and fabrication is described in detail in Chapter 3. Appendix B contains the design drawings for the CS.

The design pressure of the prototype containment is 0.31 MPa. The design pressure, P_d, for the model is calculated as:

$$\frac{10(\text{geometric scale})}{4(\text{thickness scale})} \times 0.31 MPa = 0.78\ MPa\,(113 psig)$$

Figure 2.2 shows the SCV model seated inside a shipping cradle prior to its placement in the fragment barrier.

2.2 Model Fabrication

The SCV model was fabricated at Hitachi Works, Ltd., Japan. Sections of the model were cold rolled and welded along meridional joints to form ring segments. Stiffeners were attached by horizontal welds to the interior of ring segments. The middle section of the model was completed by joining together all ring segments with horizontal welds, followed by the welding of the equipment hatch reinforcement plate. The top and bottom heads were formed separately as single-unit sections. The three sections were eventually welded together to form the model. The design drawings of the model are included in Appendix A. All weld procedures performed on the SCV model were based on the Japan Industry Standard (JIS). The welded portions of the SCV model were the same as those of the actual containment. The JIS numbers for the two steel alloys in the SCV models are:

SGV480 steel: JIS G 3118 (weld material: JIS Z 3212 d 5016)

SPV490 steel: JIS G 3115 (weld material: JIS Z 3212 d 5816)

There was no post-weld heat treatment used for any weld procedures. Welding the equipment hatch unit caused a sizable amount of local radial inward depression. This local out-of-roundness was revealed through the as-built measurements of the model.

The integrity of all weld joints was examined by dye penetrant tests. A leak-proof pneumatic test at 1.125 P_d was conducted on the fabricated SCV model by NUPEC at Hitachi Works.

2.3 Material Properties

The portion of the SCV model above the ring support girder consists of two materials: SGV480 steel and SPV490 steel. According to JIS specification, the SGV 480 steel is prescribed to carbon steel plates for pressure vessels for intermediate and moderate temperature service in JIS G 3118. SPV 490 steel is prescribed to steelplates for pressure vessels for immediate temperature service in JIS G 3115. The nominal properties for these two materials are:

SGV480 steel:

- minimum yield strength: 265 MPa
- tensile strength: 480 to 590 MPa
- minimum elongation: 17%

SPV490 steel:

- minimum yield strength: 490 MPa
- tensile strength: 610 to 735 MPa
- minimum elongation:
  - 18% for 9 mm thickness
  - 25% for 17.5 mm thickness

Uniaxial tensile tests were also conducted on specimens of the virgin SGV480 steel and SPV490

steel plates. The specimens were taken from the actual material lots used to construct the model. Tensile tests were performed on material taken from 12 locations on the model, with different shell thickness. The data on measured material properties are provided in Appendix C.

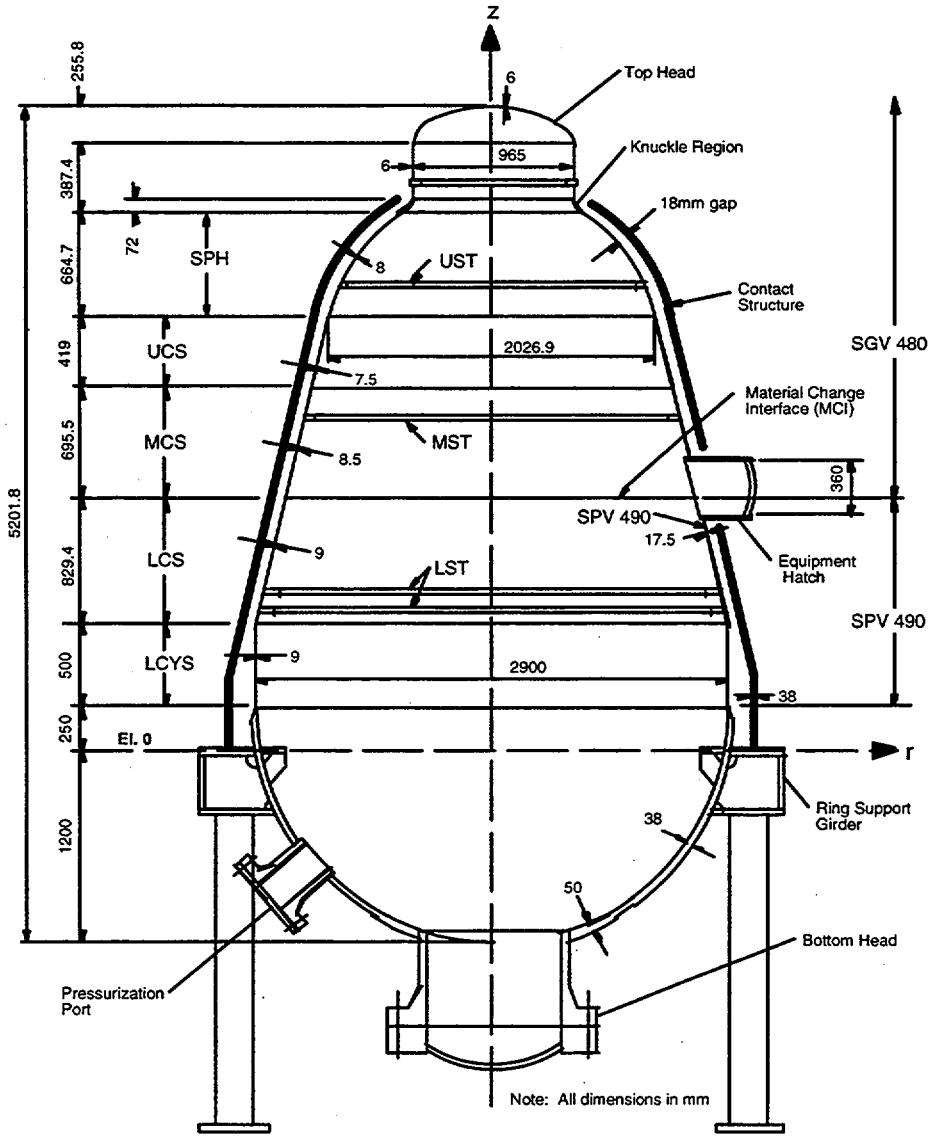

Nomenclature:

Location Designation	Description
THD	top head
KNU	knuckle
SPH	spherical shell
UST	upper stiffener
UCS	upper conical shell
MST	middle stiffener
MCS	middle conical shell
MCI	material change interface
LCS	lower conical shell
LST	lower stiffeners
LCYS	lower cylindrical shell

Figure 2.1 Elevation view of the SCV/CS assembly.

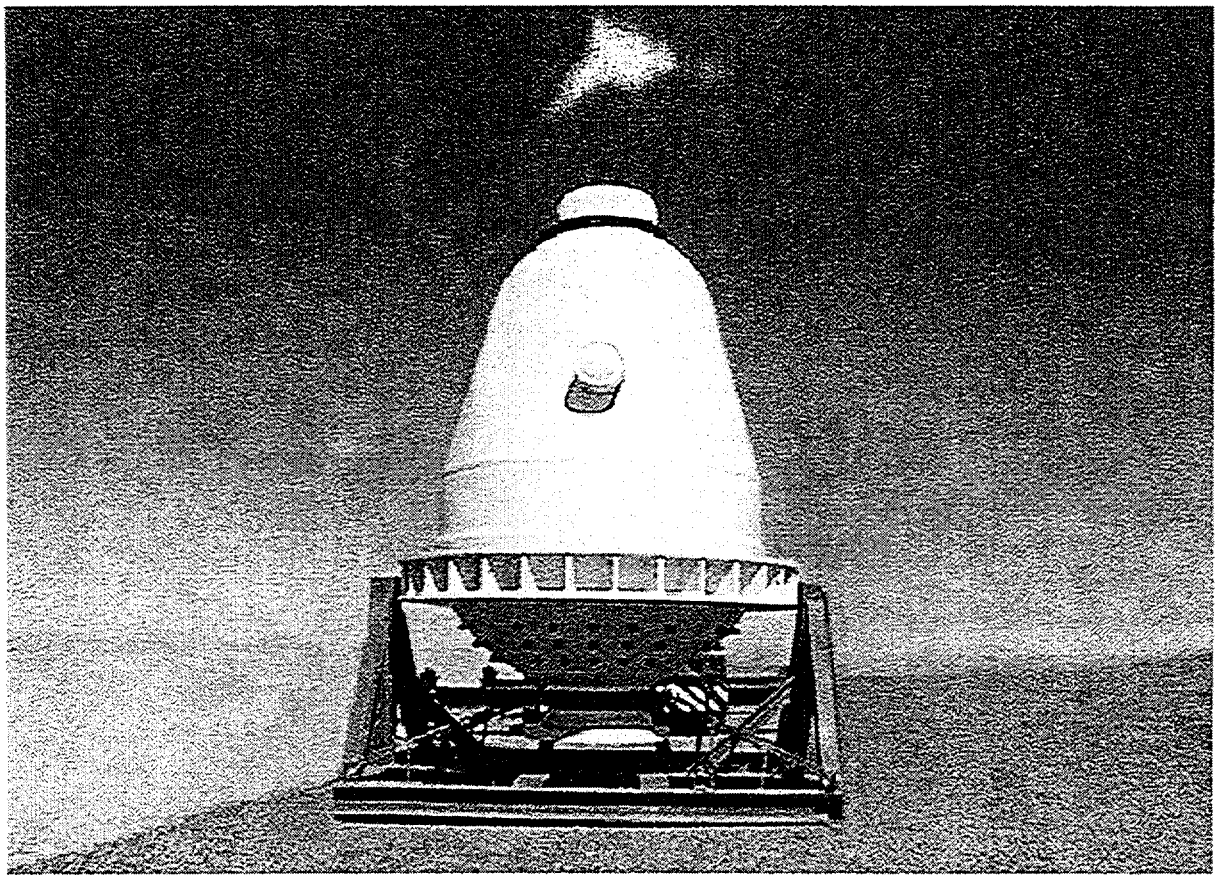

Figure 2.2 SCV model.

3. Design and Fabrication of Contact Structure

3.1 Background

In the prototypical plant, the reinforced concrete shield building surrounds the steel containment vessel (SCV). The shield wall is not a uniform axisymmetric shell, but a complex arrangement of floor slabs and walls that define functional areas. In some areas, concentric wall panels are located adjacent to the containment vessel, while other areas are open. Wherever the shield wall approaches the containment vessel, a gap of 90 mm is maintained between the structures to allow for thermal expansion of the containment vessel under normal operating conditions. Under severe accident conditions, the containment vessel could expand and make contact with the concrete shield wall due to temperature or pressure loading or a combination of both. It was concluded that the response of a free-standing SCV model might differ significantly from the prototypical containment vessel partially confined by the shield wall. In addition, one of the test objectives was the validation of codes used to analyze prototypical plants, and modeling of contact between the containment vessel and shield building poses a significant challenge for numerical simulations.

As a result, it was decided to place a surrogate structure representing the concrete shield wall over the SCV model to allow an investigation of the contact mechanism and provide a more realistic simulation of the containment vessel responses. Various options for the surrogate structure were considered with regard to the difficulties and the associated expenses of the fabrication and installation processes. The final choice was a concentric, axisymmetric steel shell called a contact structure (CS).

3.2 Design of Contact Structure

The CS is a bell-shaped structure (Figure 2.1) constructed of SA-516-70 steel with a nominal thickness of 38 mm. This material has a nominal yield strength of 258 MPa and a nominal ultimate strength of 476 MPa. The CS was designed to remain elastic due to contact up to 10 P_d. The bottom of the CS was welded to the top surface of the ring support girder after it was placed over the model, and its top was open at the elevation of the knuckle region. The CS did not touch the exterior surface of the model at any point prior to the pressure test.

The pressurization test on the SCV model was initially planned to be executed in two phases: the SCV model as a stand-alone structure in Phase I and surrounded by an unstiffened surrogate structure in Phase II. The test plan was later revised to conduct the pressurization test in a single phase with the CS as the surrogate structure. The gap dimension of 18 mm was chosen so that it was adequate to meet the original Phase I test objective and, at the same time, sufficiently small for the contact between the SCV model and the CS to take place prior to the termination of the high pressure test. The fabrication tolerances of the SCV model and the CS were also taken into consideration in deciding the final gap dimension.

Prior to designing the CS, the SCV model was measured at 20 elevations along each of eight azimuths at 45° intervals. Reduction of these measurements (Appendix B) showed that the axis of the SCV model is close to the theoretical axis with the maximum deviation less than 7.4 mm. The exterior radius of the SCV model at each measurement elevation, except location # 6 which has a deviation of 7.4 mm, is within the specified tolerance of ± 6 mm.

There were 70 holes, 12.7 mm in diameter, drilled in the CS in four arrays, 90° apart. These holes were used to measure the gap between the CS and the SCV model for aligning the CS during its installation, and later to install the contact detection devices to monitor the gap closure during the high pressure test. In addition, four 50.8-mm depressions were counterbored into the inside of the CS to allow for continuation of strain measurements of the SCV model after it had contacted the CS during pressure testing. The lead wires of strain gages placed between the two structures would most likely be squeezed when local contact occurred. Appendix B contains the design drawings for the CS.

3.3 Fabrication and Installation of Contact Structure

The CS was fabricated at Chicago Bridge & Iron Services, Inc. The spherical, conical, and cylindrical sections of the CS, constructed of SA-516-70 steel plates with a minimum thickness of 38 mm, were hot-formed to shape in a hydraulic press. These sections were welded together by pre-qualified weld procedures. After stress relief, the CS was mounted on a

vertical boring mill for final machining of the inside diameter. The mill was programmed to cut the inside diameter to the precise shape described on the design drawings in Appendix B. The specified tolerance on the CS radius of –0 mm and +4 mm at any elevation was well within the accuracy of the mill.

As shown in CS Design Drawing No. 2 in Appendix B, there is a cutoff plate in the conical section, situated underneath the opening for the equipment hatch barrel of the SCV model. This cutoff plate served to facilitate the installation of the CS over the SCV model. After the CS was placed over the SCV model, the cutoff plate was field-welded onto the CS. This weld process generated excessive local heating to the conical section and caused an extensive amount of radially inward depression, with a maximum inward movement of 6 mm at one of the measurement openings in the cutoff plate. (Incidentally, this locally depressed area on the CS was situated very close to the similar depressed area of the equipment hatch on the SCV model.) Therefore, the final gap measurements still fell within the reasonable range of more than 13.36 mm (see drawings in Appendix B).

After the CS was installed over the SCV model, the gap dimension between the CS and the SCV model was measured at each of the 70 measurement locations. By design, the gap dimensions at the lowest three measurement locations (in the lower cylindrical shell section of the SCV model) are much larger than the design dimension of 18 mm (see Appendix B). The majority of measured gap dimensions everywhere else lie between 18 mm and 22 mm. A minimum gap dimension of 13.36 mm was recorded at a measurement location below the equipment hatch.

4. Instrumentation of the SCV Model

This section provides a consolidated account of the instrumentation system on the steel containment vessel (SCV) model. It includes a detailed description of the types and the location of instruments installed on the SCV model and the contact structure (CS). The entire instrumentation effort is documented in detail in the SCV Instrumentation Plan[1].

The selection of the types and the locations of instruments was partially guided by the predicted response of the SCV model in the pretest analysis effort (Porter et al., 1996).

4.1 Instrumentation Objectives

A suite of instruments was installed on the SCV model and the CS to monitor the response of the model during the high pressure test as well as to gather data to satisfy the following program objectives:

1. To measure the strain distribution, both membrane and bending components, on the interior and exterior surfaces of the model;

2. To measure the displacements of the model, relative to the CS and to the bottom head of the model;

3. To measure the gap sizes between the SCV model and the CS;

4. To provide information on the spread of contact between the SCV model and the CS; and

5. To relate all data to the internal pressure loads on the model.

4.2 Instrument Types

This section discusses the types of data that were gathered on the SCV model and the CS during the high pressure test. The decision on instrument types is based, in part, on the previous containment experiences at Sandia National Laboratories (SNL) and the pretest analysis predictions as well as the program objectives of the experiment. The cost and the relative complexity of instrument installation and data acquisition were also considered in the decision process.

4.2.1 Strain Measurements

One of the methods to evaluate the structural behavior of the SCV model in the high pressure test is through the measurement of local strains over the model surface. These measurements were made using standard electrical-resistance strain gages, which were installed in selected locations and a variety of orientations, to record local model responses as a function of the pressure loads. The decision on the location and orientation of the gages was based on pretest analysis predictions of the model response and engineering judgment.

The selection and placement of strain gages were designed to provide information on both global and local responses of the model. The global response includes deformation in the free field, which is far away from any structural or geometrical discontinuities, and axisymmetric behavior. In this project, there were many strain gages installed on the model to measure local responses to capture the maximum membrane and bending strain components and the steep strain gradients.

All strain gages, except those around the equipment hatch, recorded strains in either hoop (circumferential) or meridional (axial) direction. Around the equipment hatch, gages were aligned in a radial manner (with respect to the hatch geometry) to provide data on the complicated deformation pattern. There were strain gages installed on both the interior and the exterior surfaces of the model. A few matching pairs of interior and exterior gages were placed to provide strain histories to calculate local bending moments. All exterior gages and their lead wires might be damaged at locations where local contact occurred between the SCV model and the CS. There were four counterbored holes drilled in the CS to allow continuous monitoring of four strain gages after contact.

Multi-element strip gages were installed in areas where large strain gradients were predicted by the pretest analysis. These areas included the top head near the knuckle and around the equipment hatch. Figure 4.1 shows a typical strip gage configuration. The strip gages, which were 10 elements long but

[1] Rightley, M.J. and Lambert, L.D., "SCV Instrumentation Plan," Project Report No. R-SN-S-001, Rev. B, Sandia National Laboratories, Albuquerque, NM, September 1996.

with only five of them wired, had a cross axis compensation gage installed immediately adjacent to them to allow for posttest correction of the inherent cross axis sensitivity errors. There were 17 strip gages installed on the exterior surface and 13 on the interior surface of the SCV model. Bending moments were obtained through the use of single element gages mounted to the exterior surface opposite one of the strip elements. One of the dilemmas of placing strip gages is that these must be mounted on a smooth surface, but were targeted to measure large strain gradients that usually occurred around discontinuities with rough surfaces such as weld seams. Therefore, the strip gages could provide only limited information for their intended purposes.

Another type of multi-element strain gages installed on the SCV model was the three-element strain rosette gages, designed to measure biaxial strains. The rosette gages, shown in Figure 4.2 in the 0°, 45°, 90° configuration, were intended to provide membrane strain data to determine the principal strains and orientation of the principal axes. These gages were installed in areas where bending moments were considered very small, such as the free field midway between the stiffener rings.

Single-element strain gages were used to determine local strains both on the interior and exterior surfaces of the model in areas where the strain gradient was predicted to be small or, as stated previously, to provide complementary data for evaluating bending moments opposite the strip gages. Orientation of the single-element strain gages, in either hoop or meridional direction, was based on the pretest analysis predictions.

4.2.2 Pressure Measurements

Accurate measurements of the internal nitrogen gas pressure in the SCV model at all times during the high pressure test were essential for two reasons. First, the readings from the pressure transducers guided the pressurization sequence of the test conduct. Second, the history of the pressure data was a key component for the integrity of the entire set of the test data.

Two high-accuracy pressure transducers used to measure the pressure history of the high pressure test were mounted on one of the four support legs at the bottom side of the ring support girder. The transducers were connected to the inside of the model with a 6.35-mm-diameter stainless steel line through one of the instrumentation feedthroughs (see Figure 2.2). Posttest evaluation indicated that the two transducers recorded almost identical pressure data.

4.2.3 Displacement Measurements

Displacement data were instrumental in providing integrated information on the global deformation behavior of the SCV model. A host of displacement measuring devices was used to collect this set of data.

The most commonly used displacement measuring device in this test project was the variable-resistance linear displacement transducer (also known as resistance potentiometers or rheostats). Capable of producing displacement data over the expected ranges of tens of millimeters, these transducers operated through the use of a spring-loaded wire cable mounted to a known reference location. The other end of the cable was attached to the desired measurement location on the model. The baseline zero displacement of the cable was recorded prior to the high pressure test. The length changes in the cable (either extension or retraction) caused by the motion of the attachment point were sensed as changes in the resistance of the potentiometers. The data were then correlated to the linear distance change between the anchor point and the attachment point.

A central support column, rigidly anchored inside the model along its axis with attachment to the ring support girder, provided the reference frame for all interior horizontal and vertical cable potentiometers. The interior horizontal cable potentiometers were oriented radially to measure the local radial displacements. One vertical and two horizontal cable potentiometers were also installed at the base of the central support column to monitor its movements. In addition, exterior horizontal cable potentiometers were installed on the SCV model and anchored on the inside walls of the fragment barrier to provide additional displacement data.

The motion of the central support column was also monitored to allow for the determination of absolute displacement data. Two inclinometers were installed at the top of the central support column to measure its tilt along orthogonal axes. The posttest evaluation of the tilt data indicated that the rotation of the central support column was negligible, so the displacement data were not adjusted for this.

Ten linear variable differential transformers (LVDTs), installed through the openings placed in the

CS, were used to monitor the gap closure between the model and the CS. The LVDTs operated by monitoring the change in length of a probe that was integral to the housing of the transducer. An AC input signal and signal conditioning electronics were required to modulate the AC output to a DC voltage suitable for the data acquisition systems. These devices were chosen for the gap width measurements because the probe tip, which contacted the measurement surface, was free to slide along the surface in case in-plane motion occurred.

4.2.4 Temperature Measurements

Temperature data of the SCV surfaces were recorded to provide compensation to the strain gage data that were sensitive to temperature changes between the environment in which the gage was calibrated and the one in which it was used. All measured strain data were compensated for this temperature difference. Thermocouples were installed on both the interior and the exterior surfaces of the SCV model to record the temperature data. Because the temperature sensitivity of the strain gages is very small in the range of temperatures to which the model was exposed during the high pressure test, only a few of these transducers were installed.

4.2.5 Video Coverage

Internal video coverage of the SCV model was performed to observe the large-scale deformation and the potential failure of the model at a few selected locations. High pressure compatible video cameras were used to gather these data.

Three cameras were used to monitor the interior of the SCV model, two on the top head (with different angles and fields of view) and one focused on the equipment hatch. In addition, seven standard video cameras were used to record the exterior of the model, three on the top head, three on the equipment hatch and one for an overall view.

4.2.6 Contact Detection

Pin-type standard industry microswitches (low voltage) were inserted through the openings in the CS shell to monitor the gap closure between the SCV model and the CS. They were set to actuate within one millimeter of the inner wall of the CS providing an on/off signal to the data acquisition system.

There was a total of 56 contact detectors installed on the CS in meridionally aligned rows arranged every 90°. (The LVDTs mentioned in Section 4.2.3 replaced the contact detectors at 10 locations with azimuth angles of 0° and 270°.)

4.2.7 Summary of Instrumentation

Table 4.1 lists the types and the number of instruments installed on the SCV model for the high pressure test.

Table 4.1 Instruments Installed on SCV Model for High Pressure Test

Instruments	Number Used
Strain Gages	single elements (meridional direction): 121 single elements (hoop direction): 34 strips (5 elements): 30 rosettes: 98
Pressure Transducers	2
Displacement Transducers	CPOTs : 66 (55 horizontal, 11 vertical) LVDTs: 10 Inclinometers: 2
Thermocouples	type K: 11 type T: 9
Contact Detectors	56

4.3 Data Integrity Verification

Two types of instrument checking activities were performed to ensure the data integrity for the high pressure test: (1) instrument continuity checks and (2) instrument functionality checks. These checks were done at regular intervals beginning with receipt of the instruments themselves through the readiness demonstration of the integrated instrumentation/data acquisition system. The results of these checks, documented on standardized forms, are part of the formal test record to ensure the data quality and data storage viability.

Functionality verification was based on two methods of instrument integrity evaluation. These methods are described below.

4.3.1 Instrument Continuity Checks

Basic continuity checks were performed on a regular basis for each instrument. These checks indicated whether the active element of any particular instrument was still intact after the instrument had been transported, handled, installed, and wired. In addition, because the measured resistance of the sensor was recorded, any anomalous changes to the electrical character of the device became apparent if changes in the measured resistivity were observed. The record of these checks also acts as a quality assurance document to maximize the percentage of successfully installed instruments on the model.

4.3.2 Instrument Functionality Checks

Instrument functionality checks were performed by actually monitoring the output signal of a particular instrument and verifying that signal for a known input stimulus. This process required a low level of stimulation of the sensor and an estimate of its response magnitude.

Full functionality checks were performed in the later stages of the installation and electrical connection of the instrumentation to verify the integrity of all wiring junctions that were made in the instrument's signal path. These checks were especially helpful to ensure that the multi-pin pressure feedthrough connectors had been wired properly according to the wiring diagrams for the data acquisition system. In addition, in the event that open circuits were observed during the initial operation of the entire system, identification of the problem's location was greatly simplified by using functionality check results.

4.4 Summary

Appendix D lists the instrumentation, including information on the installed location and the sensor designation. Appendix D also includes a set of three instrumentation drawings that provide the location and orientation of the instruments. Locations of the interior and the exterior gages are illustrated in the first two drawings. The third drawing shows the gage locations surrounding the equipment hatch. Appendix D documents are sufficient to identify the location of each instrument and its associated data acquisition system (DAS).

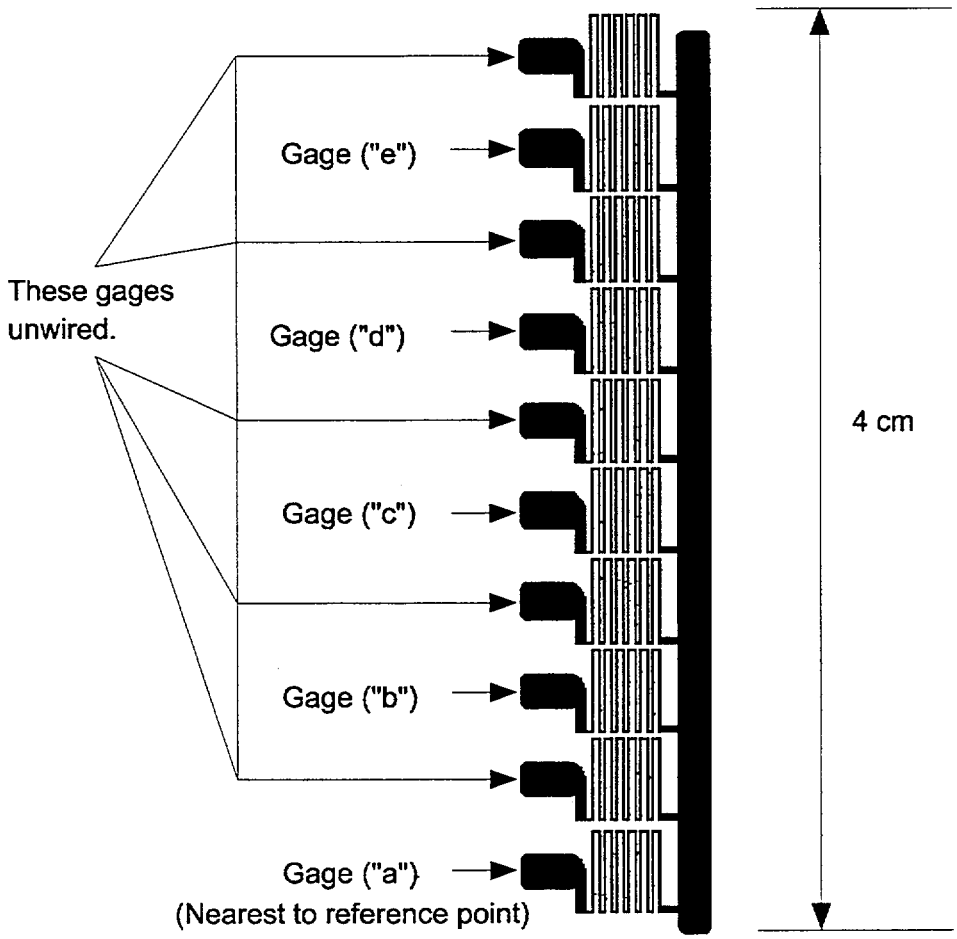

Figure 4.1 Strip strain gage nomenclature.

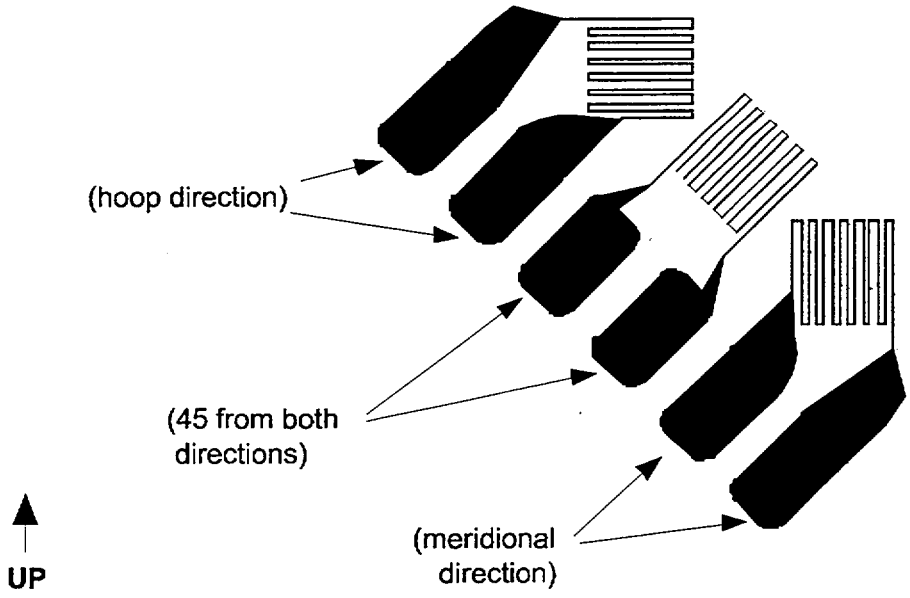

Figure 4.2 Configuration and nomenclature of rosette strain gage.

5. Pressurization System

The SCV Pressurization System is a computer-controlled gas pressurization system designed to establish and maintain the prescribed pressure and temperature in the steel containment vessel (SCV) model during the high pressure test[2]. The SCV Pressurization System consisted of the following components:

- high pressure source
- valve gallery
- heaters
- control system

The high pressure source consisted of a truck with liquid nitrogen that was gasified at the truck and regulated to a prescribed pressure and temperature. The source pressure was specified to be approximately 17.25 MPa (2500 psi), and temperature was maintained at about ambient temperature inside the fragment barrier (~15°C). The nitrogen truck was located near the command post (Building 9950 in Fig. 1.4). The pressurized nitrogen gas was then piped above ground onto the Containment Technology Test Facility site and into the valve gallery located adjacent to the fragment barrier (see Fig. 1.4).

The valve gallery consisted of several valves, a flowmeter, and several sensors and was used to control the flow of nitrogen gas. The valve gallery skid contained the hookup for the pressure source, a pneumatic isolation valve, two pressure relief valves, two automatic fill valves, an automatic bleed valve, a manual bleed valve, two pressure sensors, two temperature sensors and an output line. The nitrogen gas was then piped through the fragment barrier wall and into the SCV model. The flow of nitrogen gas through the valve gallery could be maintained between 100 and 1500 scfm up to the maximum allowable (from a site safety aspect) pressure inside the SCV model of 12.4 MPa (1800 psi).

The high pressure test was conducted in day and night time in December when the atmospheric temperature might be less than 10°C. The nitrogen gas inside the piping might be cooled flowing from the source to its entry into the SCV model. Therefore, in addition to the gas temperature being controlled at the source, the gas could also be heated in the piping prior to entering the SCV model. The piping system consisted of an outlet from the valve gallery into a rigid piping, through the fragment barrier, to a heater source, which contained four 5 kW immersion-type heaters, before entering the SCV model. These heaters were installed to provide additional heating to the nitrogen gas, if needed, to maintain its temperature within an ambient range (~15°C). In addition, a backup heater was placed inside the SCV model to heat up the gas should its temperature inside the model drop below the ambient temperature.

The control system consisted of a personal computer (PC) that communicated with a programmable logic controller (PLC). The PC and the Pressurization System operator were located in the command post, and the PLC was installed on the valve gallery skid adjacent to the fragment barrier. The PLC read the necessary data: the flowmeter, temperature at valve gallery and inside SCV model, and pressure in and out of valve gallery and inside SCV model. This set of data was then sent to the PC. Based on the data received and requirements input by the operator, the PC sent the information back to the PLC that controlled all the automatic valves on the valve gallery, and the heaters inside the fragment barrier and the SCV model. Schematics of the entire pressurization system are shown in Figures 5.1 and 5.2.

[2] Klamerus, E.W., "SCV Pressurization System Data Package," Project Document No. R-SN-I-006, Rev. A, Sandia National Laboratories, Albuquerque, NM, September 1996.

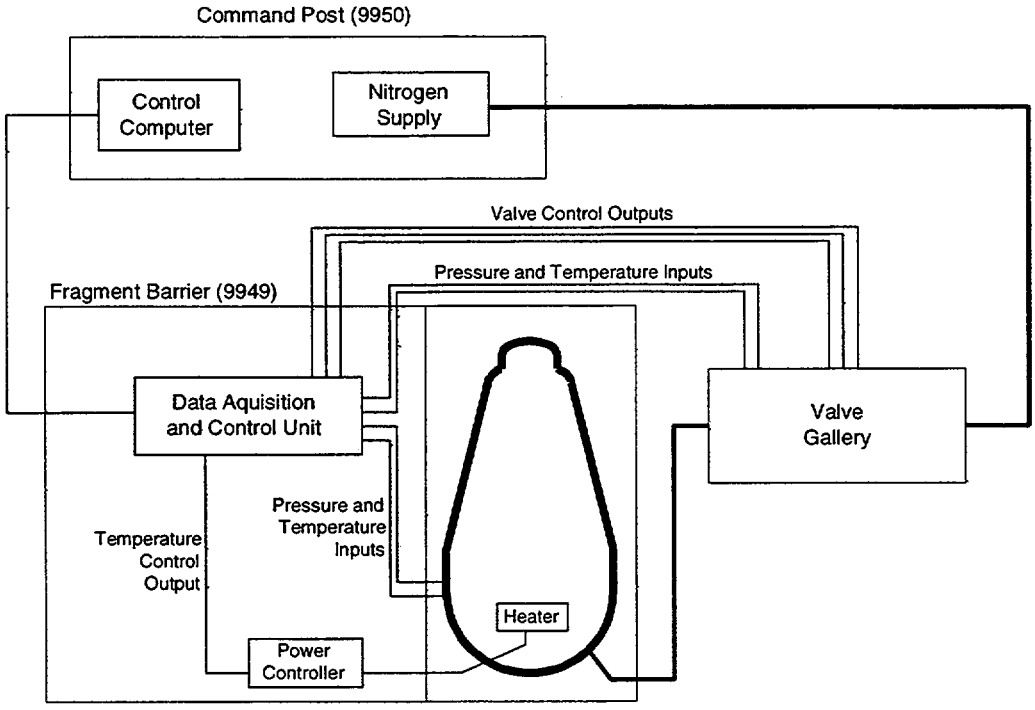

Figure 5.1 Control system schematic for SCV pressurization system.

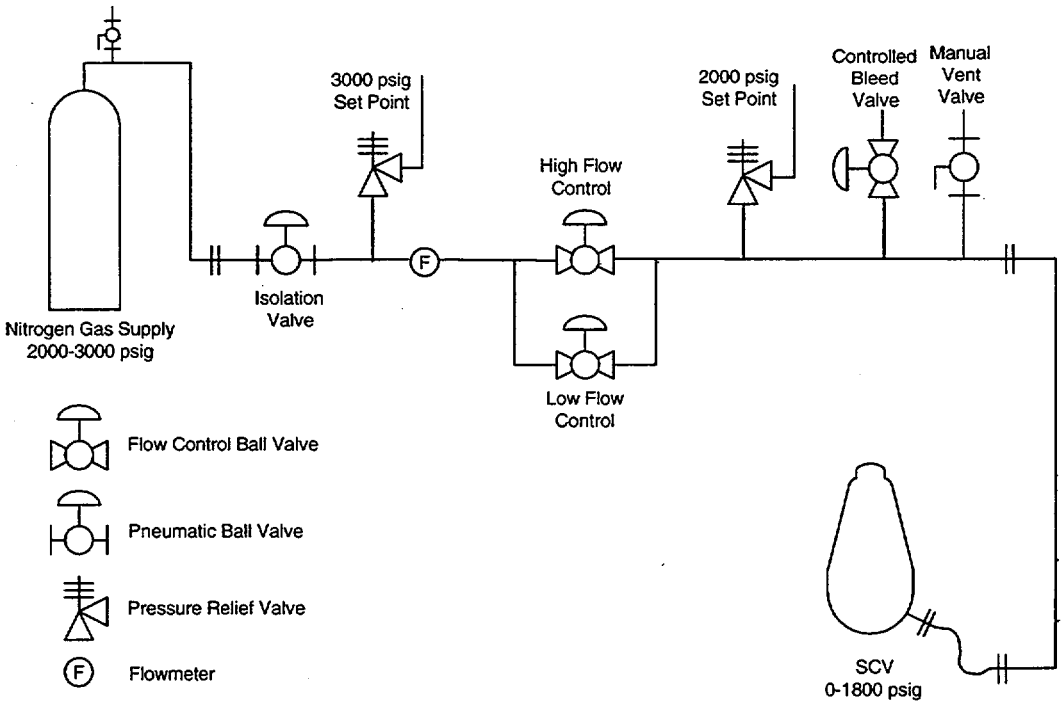

Figure 5.2 Piping and valve schematic for SCV pressurization system.

6. Data Acquisition System

This chapter describes the steel containment vessel (SCV) data acquisition system (DAS), its software and hardware assembly, and specific requirements for its performance. The validation and verification tests on the DAS were performed to demonstrate its compliance with the requirements. A detailed description of the DAS is available in the SCV DAS User's Manual[3].

6.1 DAS Scope

6.1.1 DAS Objectives

The DAS played an important role in the high pressure test. It served to provide data on the model response to guide the conduct of the test and to assemble and store data systematically throughout the test. The DAS was required to fulfill the following tasks to ensure its proper functioning:

1. Be fully functional, approved, and verified at the time of model testing.

2. Provide a real-time display of sensor output in engineering units to monitor operations.

3. Be capable of scanning sensor data during pressure testing within two minutes, performing stability checks, and storing dynamic and Data of Record (DoR) data.

6.1.2 DAS Requirements

The primary requirements of the data acquisition and display system for the high pressure test were:

1. To record the output of the instrumentation in a minimal noise environment with high confidence of accuracy;

2. To store the raw data in a protected file on redundant media during the acquisition;

3. To allow for control of all pertinent data acquisition parameters during the test;

4. To display data on the monitor, upon request during the test, from any instrument or group of instruments; and

5. To provide posttest copies of the data files, in either PC or Macintosh format on a convenient storage medium.

6.2 Description of the SCV Data Acquisition System

6.2.1 Hardware Description

The SCV/DAS hardware configuration is shown in Figure 6.1. There were approximately 800 instruments installed on the model. Each of these instruments was connected to a terminal board by lead wires. From the terminal board the signal from the instrument was carried to a specific channel on a specific card located in a mainframe. The channel location defined the general purpose interface bus (GPIB) address for the gage, allowing for correct acquisition, tracking, and recording of the data from the gage. There were several mainframes located in the alcove of the fragment barrier. From the mainframes, a fiber optic cable carried the signals from all the instruments to the data acquisition computer located in the command post. The data acquisition computer stored the data on redundant media and also made the data available to the display computer, which allowed the response of instruments to be tracked on a real-time basis. The stored data were protected and used for posttest data analysis.

6.2.2 Software Description

The software that was used to control the data acquisition system and to display the acquired data during the test was developed through the use of National Instrument's Labview™ software package. The basic building block of Labview™ is called the virtual instrument (VI). A VI is similar to a sub-program or a module of code. The data acquisition program was made up of multiples of VIs each representing a code module with a specific purpose.

The SCV/DAS software was separated into three major parts: the primary program group used to gather and store the data during the test, a secondary program group used to display the data during the test, and a utility group of programs to be used both

[3] Rightley, G.S., "SCV Data Acquisition Systems User's Manual," Project Report No. R-SI-S-019, Rev. 0, Sandia National Laboratories, NM, April 1998.

before and after the test. These utility routines were designed to accomplish the following tasks:

1. formation of the configuration file and channel set-up,

2. DAS system diagnostics and self-testing,

3. channel and instrument integrity evaluations,

4. noise evaluations, and

5. posttest data presentation and storage.

6.2.2.1 Software Structure

The data acquisition software (the primary group) required input information in the form of configuration files and was responsible for data scanning, immediate redundant data storage, and fault limit detection and announcement.

The data display software (the secondary group) used as input the data that had been gathered by the data acquisition software. The display software accessed not the stored data files on the acquisition computer but rather global variables that were shared by the acquisition and display computers. This software was responsible for displaying the test data on demand in the form requested by the user. Several different display modes were developed, including a stability review, strain and displacement distributions, and a primary graphical user interface.

The primary responsibilities of the utility group were to provide the necessary information on input channel configuration to the data acquisition and display softwares.

6.2.3 Data Acquisition Performance Requirements

The DAS was required to read accurately all the data channels and to perform specific operations based on the readings. The following set of terms was used to describe the pertinent qualities of the data acquisition system:

1. sampling time - the amount of time needed by the DAS to record *one* channel of data in a *typical* data scan. This quantity included the time needed by the computer to perform data processing and multiplexer switching operations, but did not include the time to display the data afterwards or to scan channels on another mainframe.

2. scan time - the total amount of time required for the DAS computer to scan all the configured channels, excluding any data display or "write-to-disk" commands.

3. mainframe scan time - the total amount of time required for the DAS computer to scan all the configured channels on a particular mainframe.

4. cycle time - the amount of time required for the DAS software to perform a complete scan and to store the data on specified storage devices.

5. load penalty - defined as the time penalty incurred in the DAS performance caused by the input/output processing requirements.

6. data of record - all data collected during the scan in which the entire test system had been declared "static" during one pressure step. These data were the final test data because the test is designed for static recording. All other data used to evaluate the stability of the test system were not considered "Data of Record" but were recorded and protected in the same manner.

Based on this terminology, the following set of DAS performance requirements was developed:

1. data acquisition with a sampling frequency of greater than 100 Hz,

2. maximum scan time of less than 90 seconds for the entire set of configured channels,

3. maximum cycle time of 180 seconds, and

4. maximum load penalty of 6.

6.2.4 Data Storage Requirements

To ensure that uncorrupted data were properly stored during the test, it was required that the test data be immediately stored on two storage devices. One of these devices was required to be a removable medium (such as a Bernoulli disk). The second device was the data acquisition computer's hard drive. Additionally, the data were stored in the shared global variables for use by the display computer.

6.3 Software Validation and Verification Testing

A carefully planned series of tests was run on the DAS software package to ensure that the collected data were error free and properly protected after being read by the DAS. This effort, called validation and verification (V&V), was structured to allow minor changes to the software to be made in the course of package development. The entire software package was tested in its final form, and the results of the V&V testing were documented before the DAS software package was used to collect test data.

6.4 Input/Output File Structure

Details of the file structure for the SCV/DAS software package are provided in Appendix E.

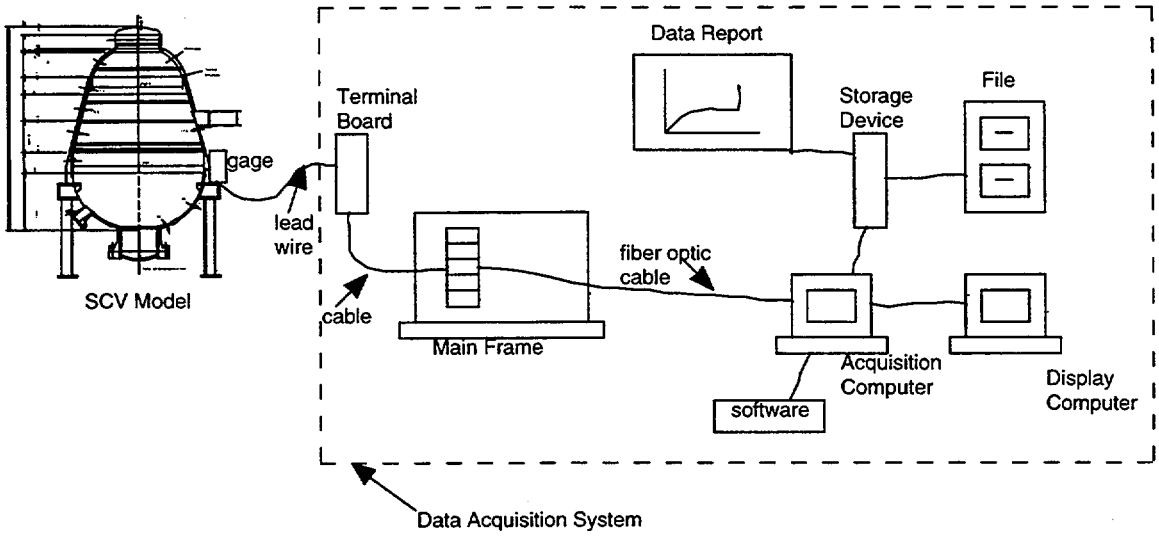

Fig. 6.1 SCV/DAS hardware configuration.

7. SCV Pressure Tests

The Steel Containment Vessel Model Test Plan[4] and the ES&H Operating Procedure[5] describe the tasks performed to prepare the steel containment vessel (SCV) model for the three pressure tests. These tests were conducted in the following order:

1. leak and instrumentation test (0.2 P_d) (October 3, 1996),
2. low pressure test (1.5 P_d) (November 7, 1996), and
3. high pressure test (model failure) (December 11–12, 1996).

Each test was conducted in accordance with the test sequence described in the SCV test plan. There was a pretest briefing preceding each test to ensure that all required pretest checklists for all test operations were completed. A posttest briefing was held immediately after each test to collect all relevant documents generated during the test and the completed posttest checklists verifying safe shutdown of the tests.

The conduct of the three pressure tests is summarized in this chapter. Data from the high pressure test are described in Chapter 8.

7.1 Leak and Instrumentation Test

The leak and instrumentation test was the first pressure test on the instrumented SCV model. It was conducted October 3, 1996 to verify that the model was leak proof and to check the functionality of the installed instruments, the pressurization system, and the data acquisition system. The maximum pressure for this test was set at 0.2 P_d or 0.172 MPa.

7.1.1 Test Sequence

This test consisted of three load cycles as shown in Figure 7.1. The first load cycle was a 0.1 P_d test consisting of two pressure increments of 0.05 P_d or 0.04 MPa. The dwell time for each of the two pressure stages was 30 minutes or longer for performing all system functionality checks. Depressurization followed this cycle and was done in one step. The second load cycle was a 0.2 P_d test with two pressure increments of 0.1 P_d or 0.08 MPa. There were two pressure stages with a dwell time of two minutes each. Depressurization followed and was done in one step. The same procedure was repeated in the third load cycle except that this time the pressure rise of 0.2 P_d was done in one step. The purpose of the second and the third load cycles was to check the performance of the pressurization system subjected to different pressure increments.

The actual pressurization sequence for the test was recorded independently by the pressure control system and the two pressure transducers installed inside the SCV model. Figure 7.2 shows the pressure profile recorded by the pressure control system for the three stages of the pressurization sequence. The readings of pressure profile on the two pressure transducers are plotted in Figure 7.3. These transducers produced almost identical pressure readings.

The temperature of nitrogen gas inside the SCV model was monitored by two resistance temperature detectors, one just below the apex of the top head and the other at the gas inlet in the bottom hemisphere. The temperature variations are shown in Figure 7.2. The temperature recorded by the upper thermocouple was consistently higher than that recorded by the lower one. The reason for this temperature variation is that the four elements of the robust heater provided excessive heating to the incoming gas and the hotter gas had a tendency to rise upward. Action was taken after the test to modify the software controlling the functioning of the heater to moderate and limit the heat supply to the incoming gas.

7.1.2 Pressurization System

During the first load cycle, a leak was detected at the purge valve installed on the SCV model. This valve was tightened and the leak stopped. A leak was also found at the manual vent valve on the valve gallery. The seal inside this valve was replaced after the test. In addition, an identical valve was installed in series on top of the existing valve. This valve was monitored closely during the low pressure test.

---

[4] V.K. Luk, "Steel Containment Vessel Model Test Plan," Project Report No. R-SN-S-003, Rev. B, Sandia National Laboratories, Albuquerque, NM, December 1996.

[5] V.K. Luk, "ES&H Operating Procedure – Testing of the Steel Containment Vessel (SCV) Model," Project Report No. R-SI-S-005, Rev. B, Sandia National Laboratories, Albuquerque, NM, December 1996.

7.1.3 Instruments

The posttest evaluation was performed on the test data recorded by all strain gages, displacement transducers, and the linear variable differential transformer (LVDT) displacement transducer. The plotted data on most instruments appeared reasonably appropriate as responses to pressure loading, suggesting that the instruments functioned properly.

The data for the instruments installed at the 43 standard output locations for the Round Robin pretest predictions were also evaluated. These data did not show any unexpected behavior.

A few questionable plots were identified, leading to an extensive re-inspection of wiring and installation of the instruments for these plots. The sources of the impaired instruments were found, and the problem was then fixed.

7.1.4 Summary

The leak and instrumentation test provided the first chance to examine the performance of the SCV model under pressure loading and to exercise the pressurization and data acquisition systems. All test objectives were accomplished. All problems that were detected from the data of this test were repaired after their root causes were discovered.

7.2 Low Pressure Test

The low pressure test was conducted November 7, 1996. The objectives of this test were:

1. To detect any leakage on the pressurization system and the subassemblies of the SCV model, including bottom head flange, pressure flange and feedthroughs at pressures up to 0.5 P_d;

2. To perform functionality checks on installed instruments and associated wiring, data acquisition system and display computer at pressures up to 1.5 P_d; and

3. To execute this test as a dress rehearsal for the high pressure test.

7.2.1 Test Sequence

The low pressure test was performed according to the planned pressurization sequence in Figure 7.4. The pressurization sequence was slightly modified to accommodate leak tests to be performed at pressure levels of 0.14 MPa, 0.28 MPa, and 0.39 MPa. The pressure level of 0.39 MPa was maintained for 60 minutes to allow test personnel to secure the test site and evacuate from it. The actual pressurization sequence for the test was recorded independently by the pressure control system and the two pressure transducers installed inside the SCV model. Figure 7.5 shows the pressure profile recorded by the pressure control system. The readings of the pressure profile on the two pressure transducers are shown in Figure 7.6.

The temperature of nitrogen gas inside the SCV model was monitored by two resistance temperature detectors, and the temperature profiles are shown in Figure 7.5. The temperature recorded by the upper thermocouple was consistently higher than that shown by the lower one. Even though the heat supply from the heaters was moderated, it was still difficult to obtain closer temperature readings from the two thermocouples. To reduce the temperature effect on the variations of responses of instruments, the temperature inside the SCV model, recorded by these two thermocouples, would not be allowed to exceed 38°C (100°F) at any time during the high pressure test.

7.2.2 Pressurization System

No leakage was detected on the pressurization system during each of the three pressure levels when the leak test was performed. The manual vent valve on the valve gallery, which was repaired after a leak was found during the leak and instrumentation test, functioned well during this test.

7.2.3 Instruments

The posttest evaluation was performed on the test data recorded by all strain gages, displacement transducers, and LVDTs. The plotted data on most instruments appeared normal in response to the pressure loading, thus indicating that the instruments functioned properly.

7.2.4 Summary

The low pressure test was conducted November 7, 1996, and all test objectives were accomplished. After careful posttest evaluation of data plots for all instruments, it was found that all installed instruments functioned properly except the two exterior weldable strain gages installed on the lower cylindrical shell section.

7.3 High Pressure Test

The high pressure test was allowed to proceed only after the functionality checks of all operating systems were satisfactorily completed because this test was set up for a monotonic pressure rise and the cycle of unloading and reloading was not desirable. The pretest briefing, held December 10, 1996, was attended by all high pressure test personnel. At the briefing, the functions and responsibilities of every member of the test team were reiterated, and all pretest checklists, excluding a few which needed to be completed on the test day, were signed off. The high pressure test was conducted December 11–12, 1996. All corrected test data are part of this report (Appendix F). High pressure test data files are provided in Appendix G of this document.

7.3.1 Test Conduct

The high pressure test started at 10 a.m. December 11, 1996 after the pretest preparations had been accomplished. The test proceeded in accordance with a planned pressurization sequence that was divided into three stages:

- First stage (0 - ≈4.6 P_d)

  During this stage, the SCV model would expand as a stand-alone structure. The model behaved essentially in the elastic domain throughout this stage.

- Second stage (≈4.6 P_d)

  This pressure condition was held constant for 30 minutes to demonstrate the accomplishment of the original Phase I test objective, which was intended to make sure that the model behaved as a stand-alone structure and that no contact between the model and the contact structure occurred during this stage.

- Third stage (≈4.6 P_d - model failure)

  The model behaved in the plastic domain throughout this stage. As the pressure continued to increase, so did the time required to arrive at a state of steady structural response. Accordingly, the incremental pressure rise for each step was reduced, and the dwell time during each step was lengthened.

A detailed breakdown of the planned test sequence up to 5.52 MPa (800 psig) is shown in Figure 7.7.

7.3.1.1 First Stage (0 - 4.6 P_d)

The recorded test sequence in the first stage is shown in detail in Figure 7.8. In each dwell time of at least six minutes, data were collected in every two-minute interval, during which critical data were compared using the following criterion:

$$\frac{Q_t - Q_{t-\Delta t}}{Q_{t-\Delta t}} \leq 0.02$$

where Q_t and $Q_{t-\Delta t}$ are the data at the current and the previous time interval, respectively. The critical data set for the stability criterion included all strain gages and displacement transducers except strain gages on the exterior of the contact structure, and gages (cable potentiometers [CPOTs], inclinometers) which monitor motion of the central column. The decision to proceed to the next pressure increment was dependent on the number of critical gages passing the stability criterion. Typically, the percentage of critical gages satisfying the stability criterion should exceed 95% before proceeding with the next increment; however, in some instances, the decision was made to proceed even though a lower percentage of gages passed. All pressure rise steps were set to take three minutes to reach an equilibrium condition, except a few starting steps that took more time.

The first stage was completed at an internal pressure of 4.2 P_d when the average displacement of four displacement transducers (0°, 90°, 180°, and 270°) at a given elevation reached 9 mm.

The temperatures inside the model, recorded by the resistance temperature detectors (RTDs), were not allowed to exceed 38°C (100°F) at any time during the test. After each pressure step, when either steady-state temperature reached 32°C (90°F), the heaters were turned off for subsequent steps until the steady-state temperature dropped to 16°C (60°F).

7.3.1.2 Second Stage (4.6 P_d)

The pressure condition of 4.2 P_d was held at a constant level for 30 minutes in the second stage (see Figure 7.9).

7.3.1.3 Third Stage (4.6 P_d - model failure)

The model behaved in the plastic domain throughout this stage. Figure 7.10 shows the recorded test sequence in this stage. The pressure rise time was kept at a minimum of three minutes for each pressure step.

The maximum pressure increment was maintained at 0.1 P_d for each pressure step.

The dwell time increased with pressure because the SCV model took a longer time to achieve its equilibrium state in the plastic domain. Data were collected in two-minute intervals, during which critical data were compared using the same criterion described before. The next pressure increment was followed only after this criterion had been satisfied. The maximum strain was monitored very closely every where on the SCV model to identify potential failure locations. The increase of strain or displacement as a function of pressure at critical locations was also monitored at all times during the high pressure test to provide an indicator of an imminent model failure.

In addition to the instruments such as strain gages and displacement transducers, an acoustic emission device consisting of 24 sensors was installed on the SCV model. This device continuously monitored the SCV model and provided additional information to indicate potential locations of model failure. The device and its results generated from the test are discussed in detail in Appendix H.

7.3.2 Termination of Test

At about 2:30 a.m. on December 12, 1996, after approximately 16.5 hours of continuous and monotonic pressurization of the SCV model, rapid venting of the model was observed, and the pressurization system, operating at capacity (1300 scfm), was unable to maintain pressure in the model. A decision was then made to terminate the test. The maximum internal pressure achieved during the test was 4.66 MPa (676 psig) or roughly six times the design pressure. Predetermined procedures were followed to depressurize the model, to store all test data securely, and to complete all posttest checklists.

A few hours after the test was terminated, safety procedures were followed to enter the fragment barrier, to unlock the bottom flange, and to gain access to the interior of the SCV model. It was found that a tear approximately 190 mm long, developed along the weld seam at the outside edge of equipment hatch reinforcement plate. This tear might cause the model leakage leading to the termination of the high pressure test.

7.3.3 Summary

The high pressure test of the SCV model was conducted December 11–12, 1996. The test was terminated when a tear developed at a pressure of 4.66 MPa (676 psig) or approximately six times the design pressure. The evaluation of the data recorded by all instruments and the posttest inspection of the SCV model are discussed in detail in Chapter 8.

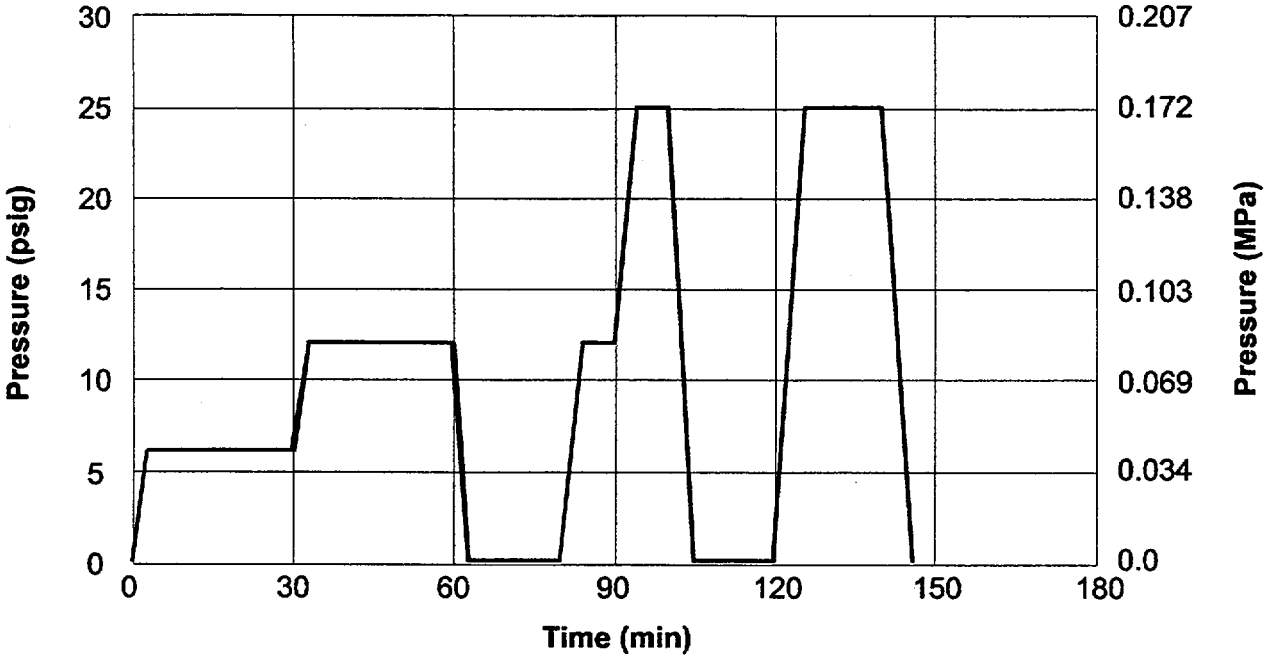

Figure 7.1 Planned pressurization sequence for the leak and instrumentation test.

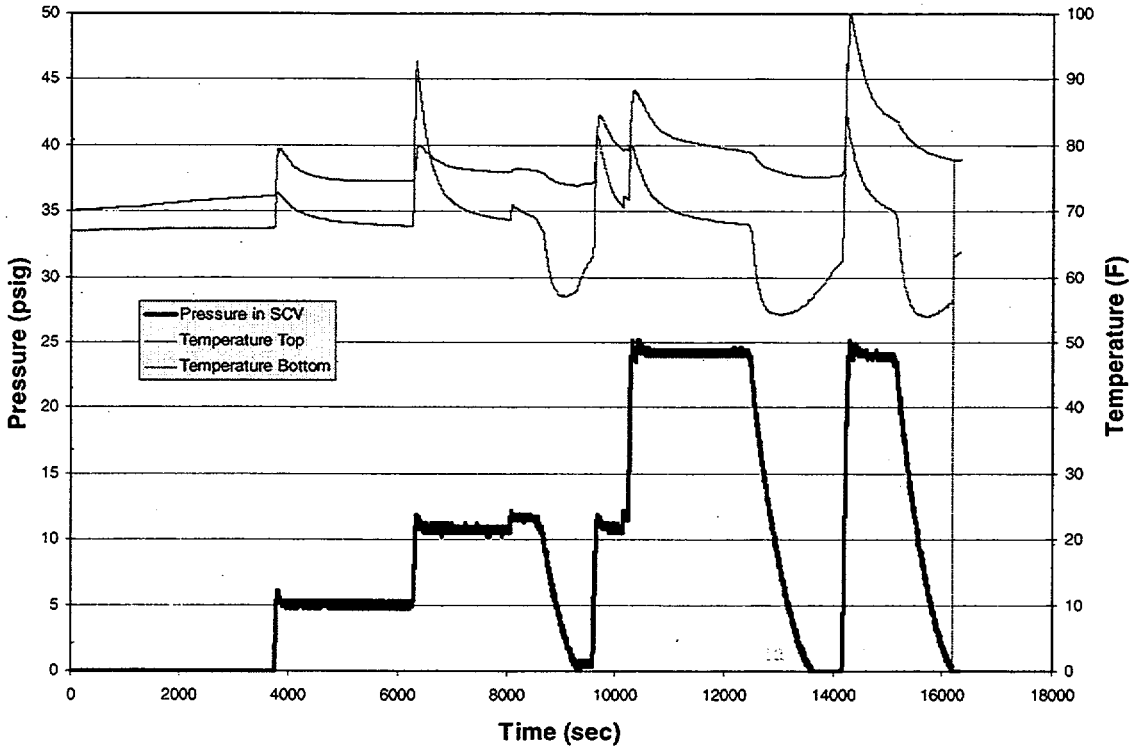

Figure 7.2 Profiles of recorded pressure by pressure control system and temperature by RTDs for the leak and instrumentation test.

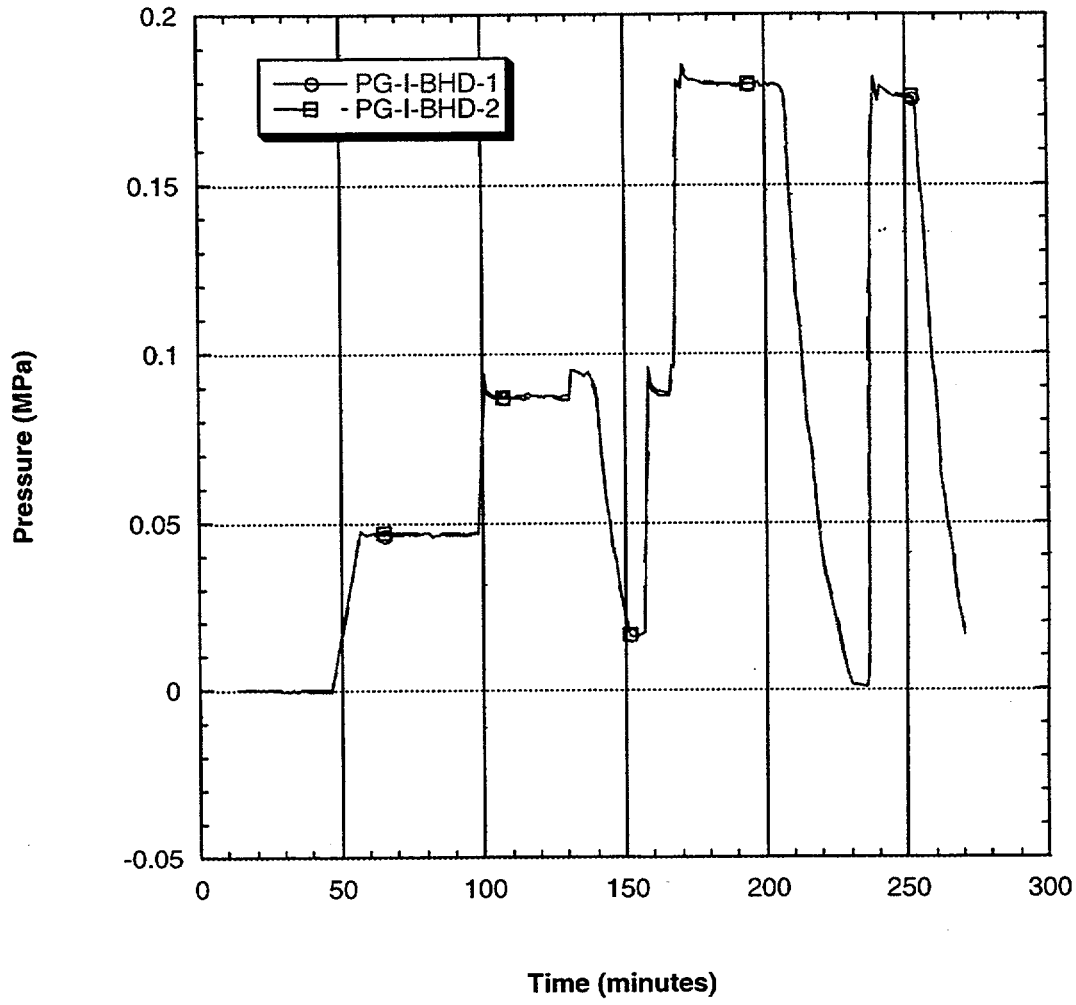

Figure 7.3 Pressure profile recorded by the two DAS pressure transducers measuring pressure inside the SCV model for the leak and instrumentation test.

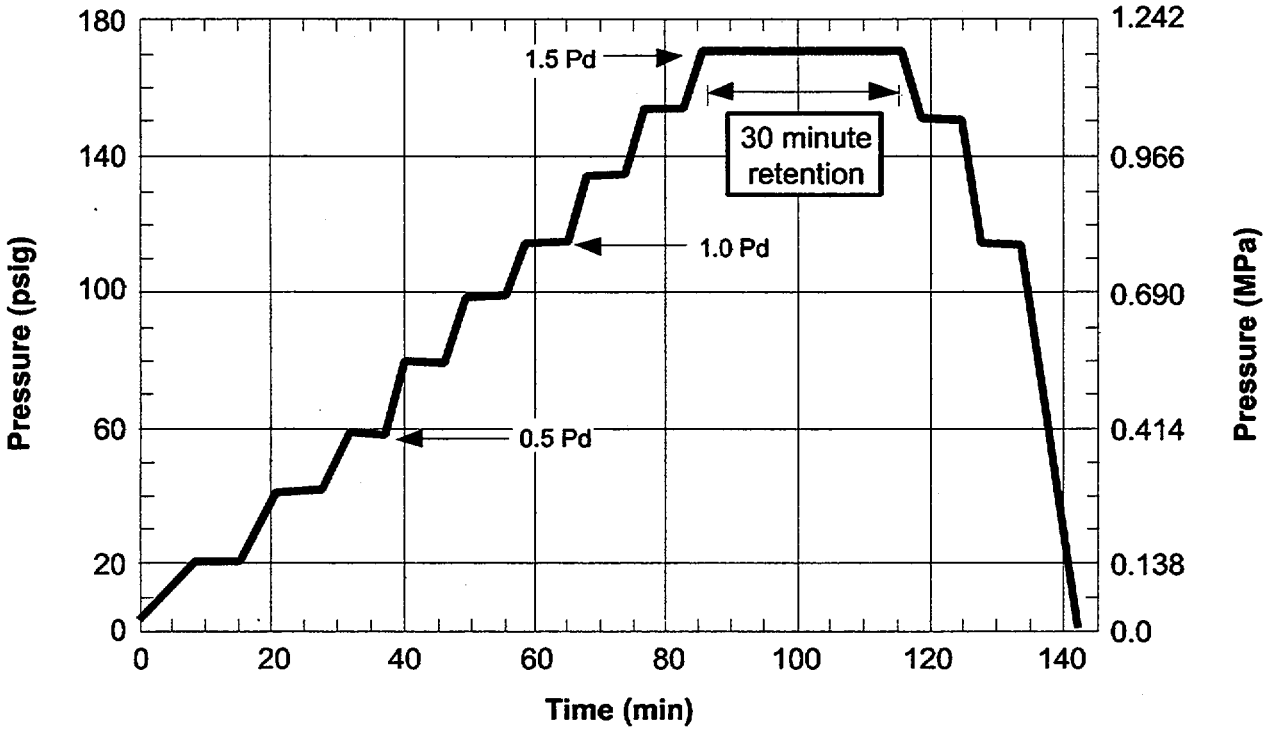

Figure 7.4 The planned pressurization sequence for the low pressure test.

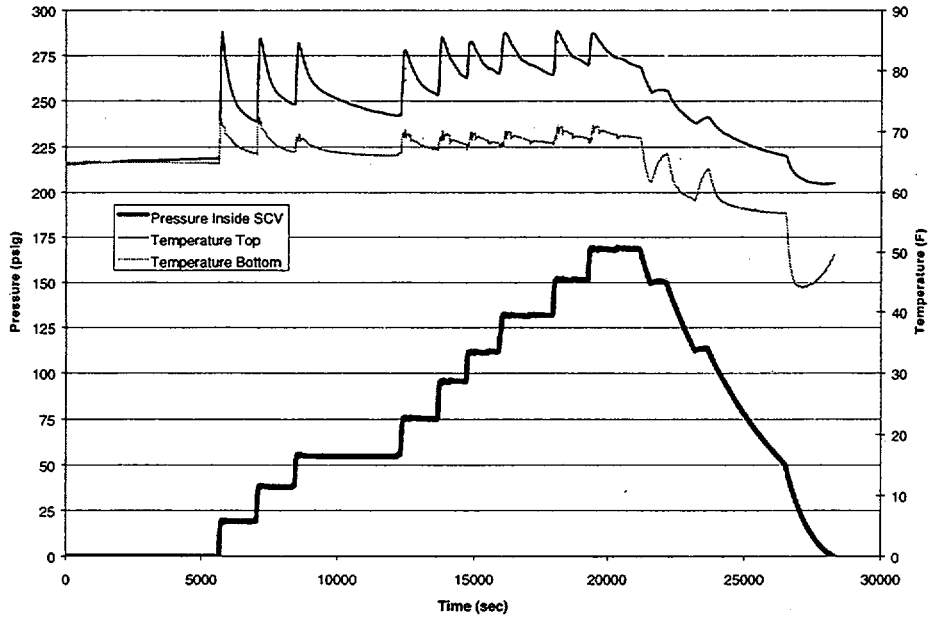

Figure 7.5 Profiles of recorded pressure by pressure control system and temperature by RTDs for the low pressure test.

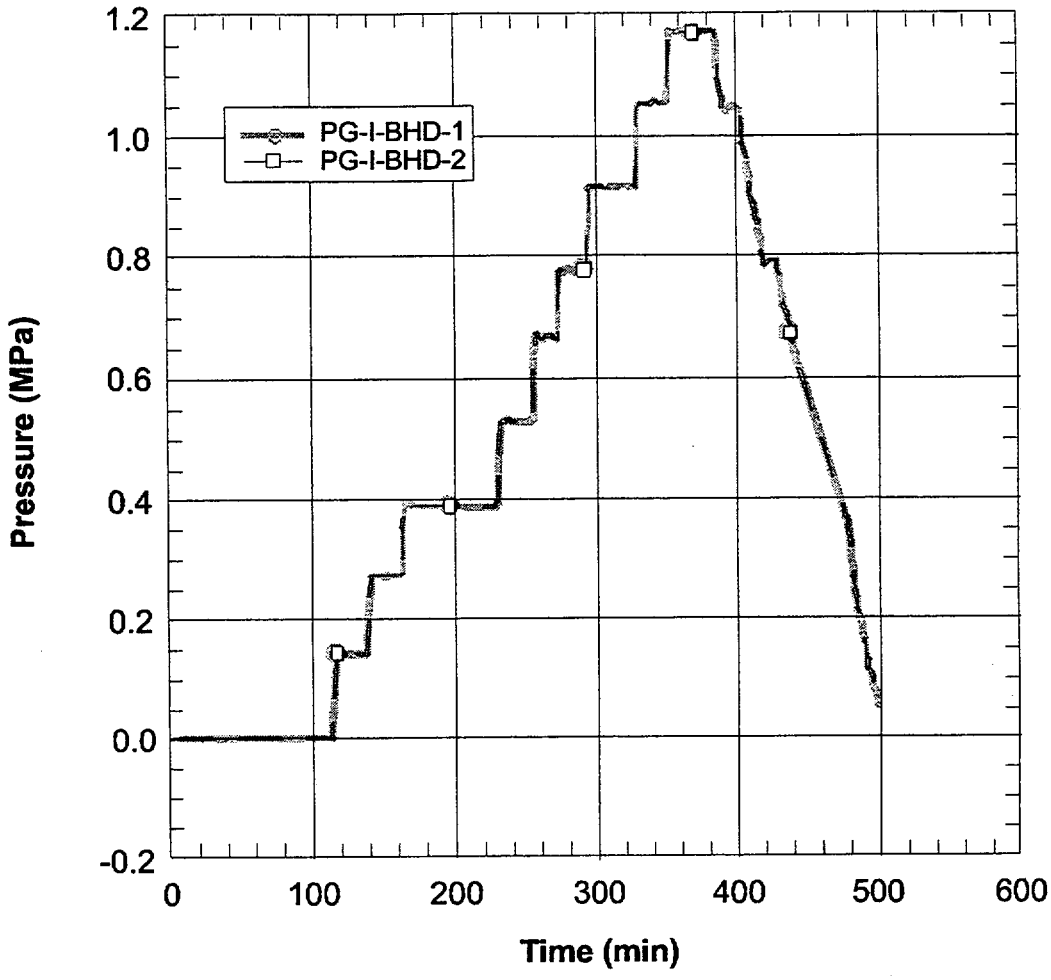

Figure 7.6 Pressure profile recorded by the two pressure transducers for the low pressure test.

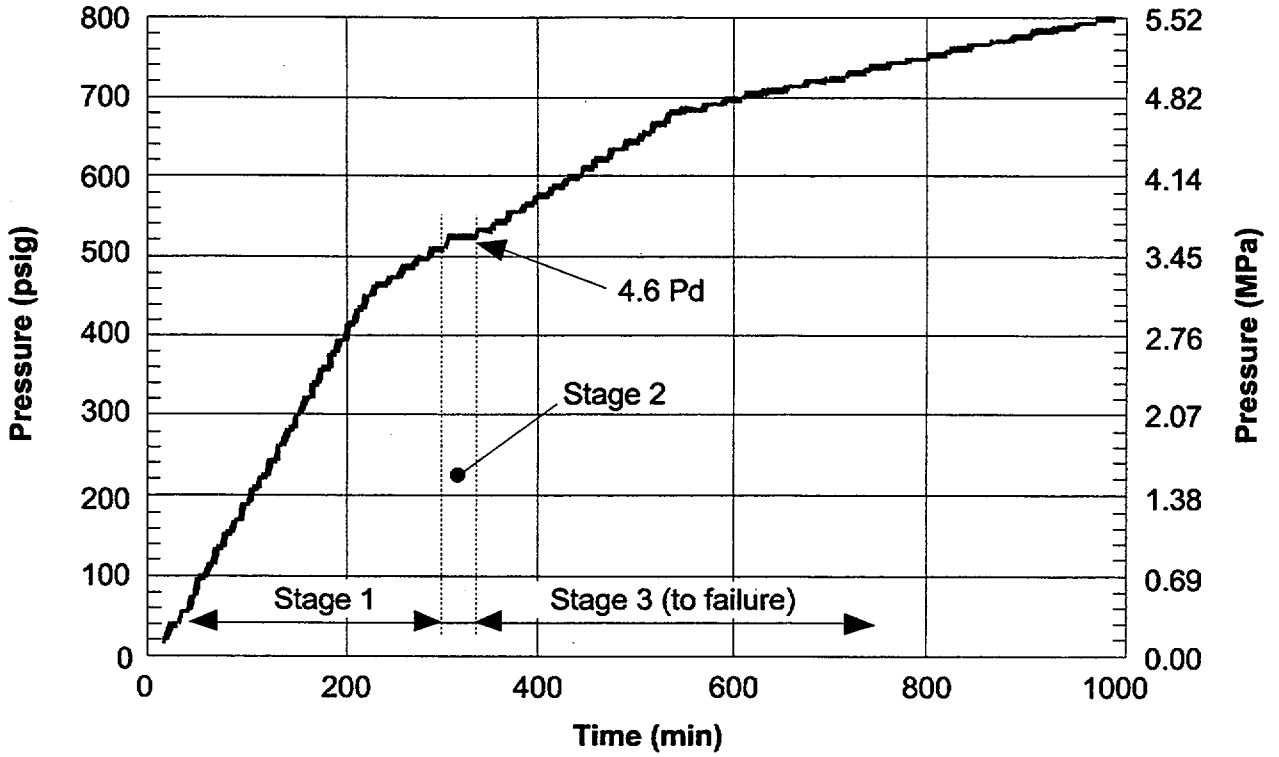

Figure 7.7 Detailed breakdown of the planned test sequence for the high pressure test.

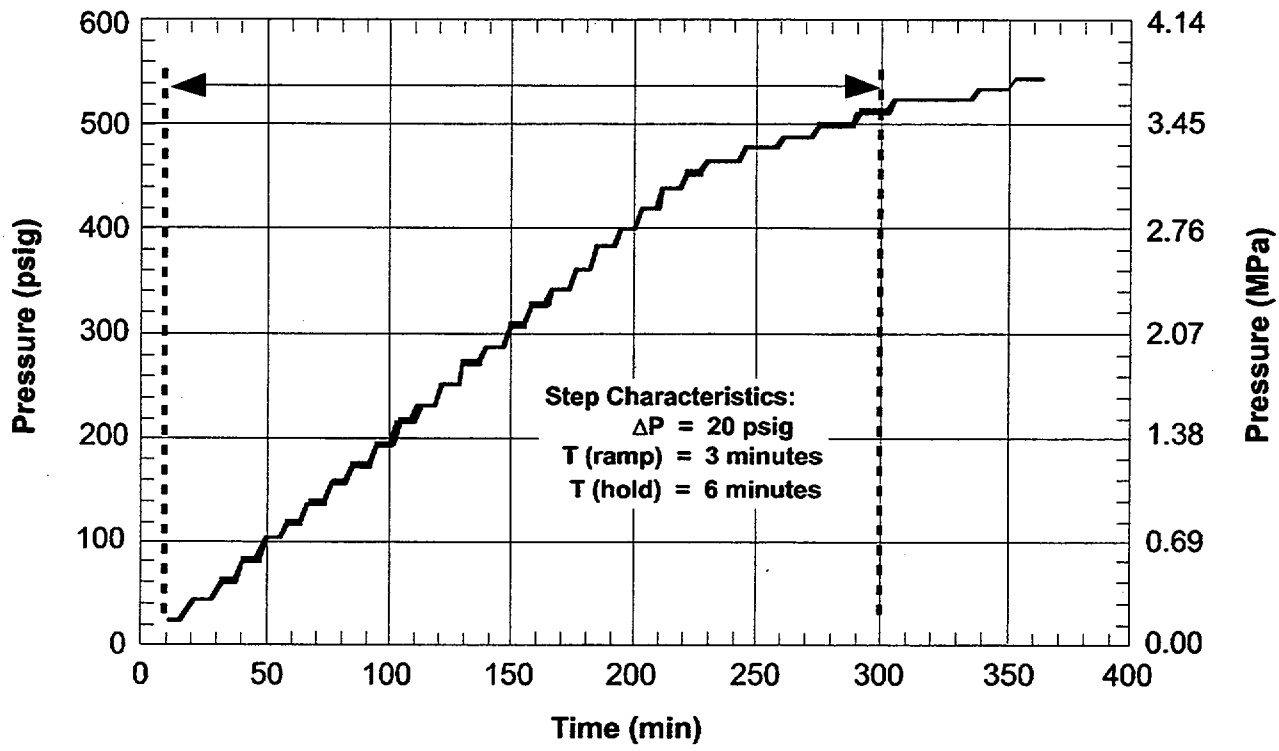

Figure 7.8 Recorded pressurization sequence for the first stage of the high pressure test.

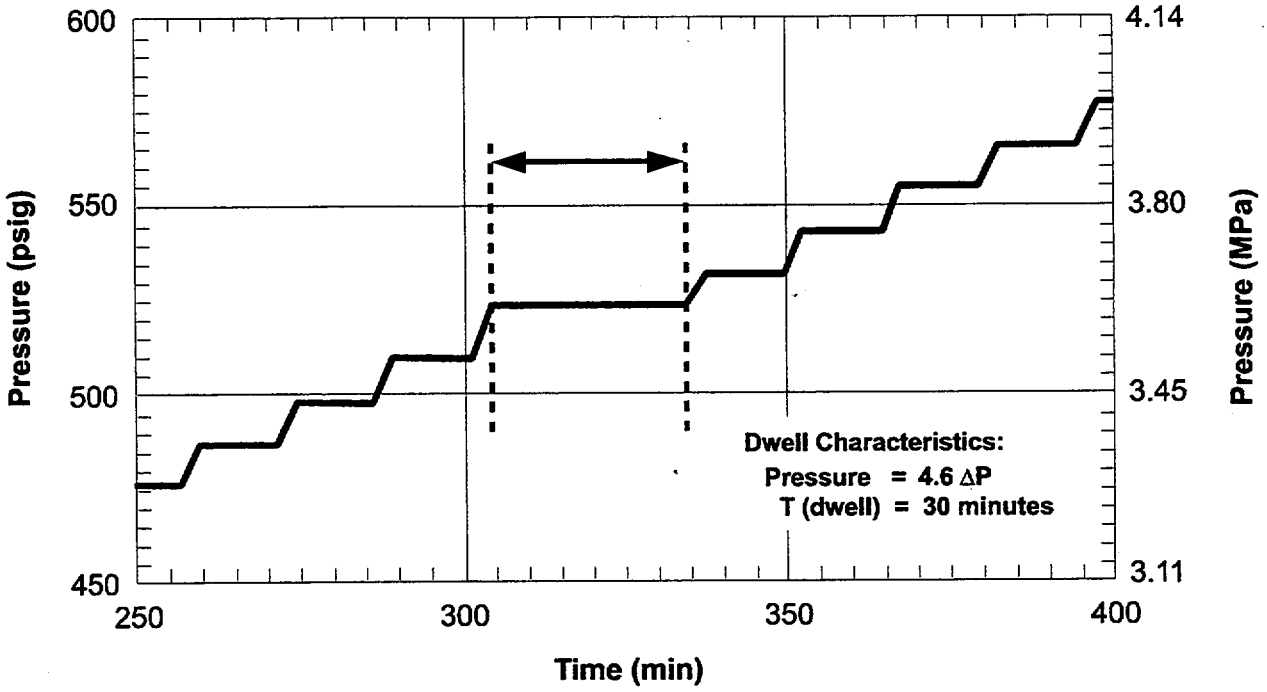

Figure 7.9 Recorded pressurization sequence for the second stage of the high pressure test.

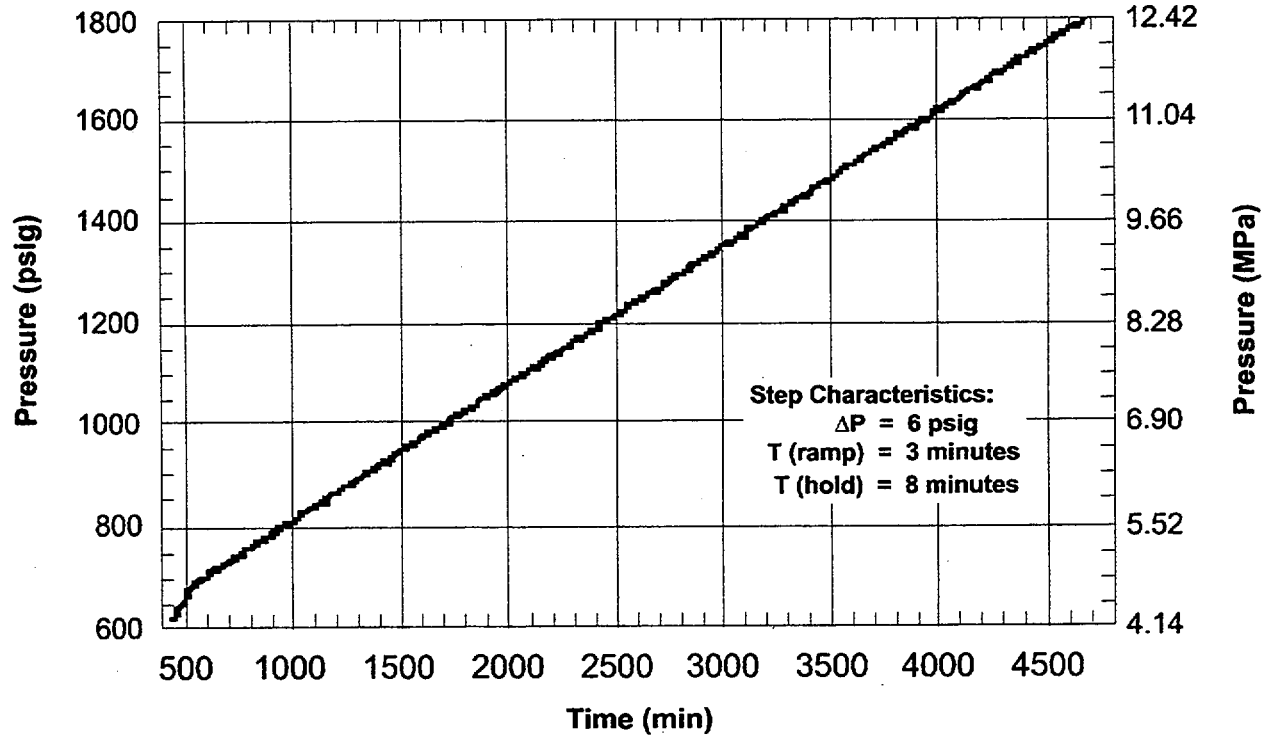

Figure 7.10 Recorded pressurization sequence for the third stage of the high pressure test.

8. High Pressure Test Data

8.1 Introduction

The high pressure test was terminated at a pressure of 4.66 MPa (676 psig) or 5.97 times the scaled design pressure. This test produced two tears in the steel containment vessel (SCV) model: a large tear along the outside edge of a weld seam at the equipment hatch reinforcement plate, and a small tear inside a semi-circular weld relief opening at the middle stiffening ring. There was a large array of strain gages installed around the equipment hatch to provide information on the local model deformation behavior around the large tear, but no gages were installed near the small tear to provide a record of local deformation leading to its occurrence (Matsumoto et al., 1997; Luk et al., 1998).

Attention in Section 8.2 is focused on the local high strain concentrations and steep strain gradients around the large tear. The free-field responses and the displacement profiles of the model were examined to provide an overall perspective of the global model behavior. A detailed discussion of these evaluations is presented in Section 8.3.

More than 97% of the instruments survived the high pressure test. Many of the failed gages, consisting primarily of gages on the exterior of the model, were damaged when the model made contact with the contact structure (CS). The raw strain data were corrected to compensate for temperature variations and cross-axis strains, and the displacement data were corrected to account for any movement of the center support column to which the displacement transducers were anchored. The data correction process is detailed in Appendix F. The complete data record is included in Appendix G.

8.2 Local Model Response Adjacent to Equipment Hatch

An extensive array of single element, strip, and rosette strain gages was installed around the equipment hatch to obtain a relatively accurate map of the local strain pattern. The network of interior strain gages and the location of the large tear are shown in Figure 8.1. The same mapping of gages and the large tear is graphically presented in Figure 8.2, highlighting a few critical strain gages around the equipment hatch viewed from the inside of the model. A strip gage (STG-I-EQH-16) installed adjacent to the upper end of the large tear registered a maximum strain of 4.2%, and the two rosette gages (RSG-I-EQH-12 and -8) above it recorded maximum strains of 3.7% and 2.8%, respectively. The rosette gage (RSG-I-EQH-22) slightly below the lower end of the tear recorded a maximum strain of 1.3%. However, the highest strain reading, 8.7%, was recorded by a strip gage (STG-I-EQH-37) situated at 3 o'clock, just above the material change interface. Posttest inspection discovered a local thinned area directly below this gage, indicating excessive local deformation might occur there. Figure 8.3 shows the strain data recorded by these gages around the equipment hatch.

Although the pretest analysis results predicted failure in the vicinity of the equipment hatch at pressure levels very close to the actual failure pressure, a detailed comparison of the calculated and measured strains highlights some areas of discrepancy. First, posttest observations indicate that the highest strains occurred in the higher strength SPV490 shell, below the material change interface, rather than in the weaker SGV480 shell as predicted by the analyses. Second, the near-field strains around the equipment hatch were almost double those predicted by the analysis. Finally, it was a local shell area, detected in the pretest inspection, whose thickness was about 20% smaller than its neighbors, that was the focus of concern in the pretest analysis. However, this local thinning appeared to have little effect on the response in the vicinity of the equipment hatch.

A small meridional tear, approximately 55 mm long, was found in a vertical weld (at an azimuth angle of 201°) inside a semi-circular weld relief opening at the middle stiffening ring above the equipment hatch (Figure 8.4). It appeared that this small tear, which might have occurred first, did not grow, and the pressurization system was able to compensate for any leakage through this tear. This tear had a counterpart at a similar, diametrically opposed detail. While no tear developed at the opposing location, necking in the weld was observed. The pretest analysis did not predict any high strain concentrations in the vicinity of the small tear, and therefore no strain gages were installed there to record the strain history. In the posttest analysis effort, a three-dimensional finite element model, reflecting the structural details surrounding the small tear, was generated to investigate the local strain distribution (Ludwigsen et al., 1998).

8.3 Global Model Response

The global model response was monitored using the strain gages at free-field locations and an array of interior displacement transducers that measured the strains and the displacements, respectively, at several elevations along four cardinal azimuths (0°, 90°, 180°, and 270°).

The maximum free-field hoop strains ranging from 1.7 to 2.0% were measured by four exterior gages at 4.5 MPa (560 psig) at the upper conical shell section at an elevation of 2536 mm above the ring support girder (Figure 8.5). The strain recording by two exterior gages, RSG-O-UCS-9a and -13a was interrupted when the gages were damaged by the contact between the model and the CS. Hoop strains calculated from the displacement measurements ($\Delta r/r$) were consistent with the strain gage measurements at these locations. The narrow range of strain variations suggests that the model, excluding the area around the equipment hatch, behaved in an axisymmetric manner as expected.

The hoop strains at the four cardinal azimuths in other regions of the SCV model are plotted in Figure 8.6 for the knuckle region, Figure 8.7 for the spherical shell section, Figure 8.8 for the lower conical shell section, and Figure 8.9 for the lower cylindrical shell section. The plots of the hoop strains in these figures demonstrate that the SCV model deformed in an approximately axisymmetric fashion in these regions. Figure 8.10 shows the variation of hoop strains at the top head region. The four rosette strain gages that measured these strain data were placed at various radial distances from the model apex. In particular, the gage at 180° was very close to the edge of the torospherical head. This gage might be subjected to a dissimilar combination of loading due to its location, resulting in a different set of hoop strains from the other three.

The spatial variation of displacements at the four cardinal azimuths at 4.5 MPa is shown in Figure 8.11. The displacement profiles were completed by interpolating the data recorded by the transducers at various elevations. It should be noted that the displacement pattern is fairly axisymmetric with the exception of 90°, the azimuth where the equipment hatch is located. The displacements at this azimuth location in the lower conical shell section, below the material change interface, were much larger than those at the free-field azimuths (0°, 180°, and 270°). This is of particular interest in light of the fact that this area was actually compressed inward during fabrication of the model and this was also the area where the large tear occurred.

The spatial variation of displacements as a function of pressure at a representative free-field azimuth (270°) is shown in Figure 8.12. This figure indicates a disproportional increase in radial displacement of the model between 3 and 4 MPa, suggesting that global yielding of the model might occur somewhere in this pressure interval. Observable slow-down in radial growth of the model occurred beyond 4 MPa when the model made local contact with the CS.

Additional radial displacement plots at the middle and upper conical shell sections as a function of pressure are shown in Figures 8.13 and 8.14, respectively. The manner in which the plots in these two figures and Figure 8.5 started to curve upward at about 2.5 MPa suggests that the onset of global yielding of the model might have occurred as early as 2.5 MPa. Additionally, it can be inferred from these figures that generalized contact between the model and the CS began at pressures between 4.0 and 4.5 MPa.

8.4 Leak Behavior

The time histories of the pressure transducer, the flowmeter, and the two thermocouples during the last twenty minutes of the high pressure test are shown in Figure 8.15. These time histories may be useful in evaluating the leak behavior of the SCV model during the propagation of the large tear. The leak rate can be approximated directly from the flow rate data when the pressure reading remains steady. For the duration with unsteady pressure, the leak rate can be estimated from the information in this figure.

8.5 Summary and Discussions

More than 97% of instruments survived the high pressure test. All test Data of Record were corrected for posttest evaluation. An extensive network of strain gages was installed around the equipment hatch area to record the local deformation behavior. Recorded data provide a fairly accurate mapping of the local response in proximity to the large tear.

The global free-field response of the model can be characterized by the hoop strains. The narrow range of variation of these strains at a given elevation suggested that the model, excluding the equipment hatch area, might behave in an axisymmetric manner in the high pressure test. Displacement data indicated that

the equipment hatch area overcame an out-of roundness from a local inward compression caused by the welding of the equipment hatch onto the model and that it underwent additional expansion, exhibiting larger radial displacements than those at the other azimuth locations of the shell section.

The high pressure test data were evaluated and compared with the pretest analysis predictions (Ludwigsen et al., 1998).

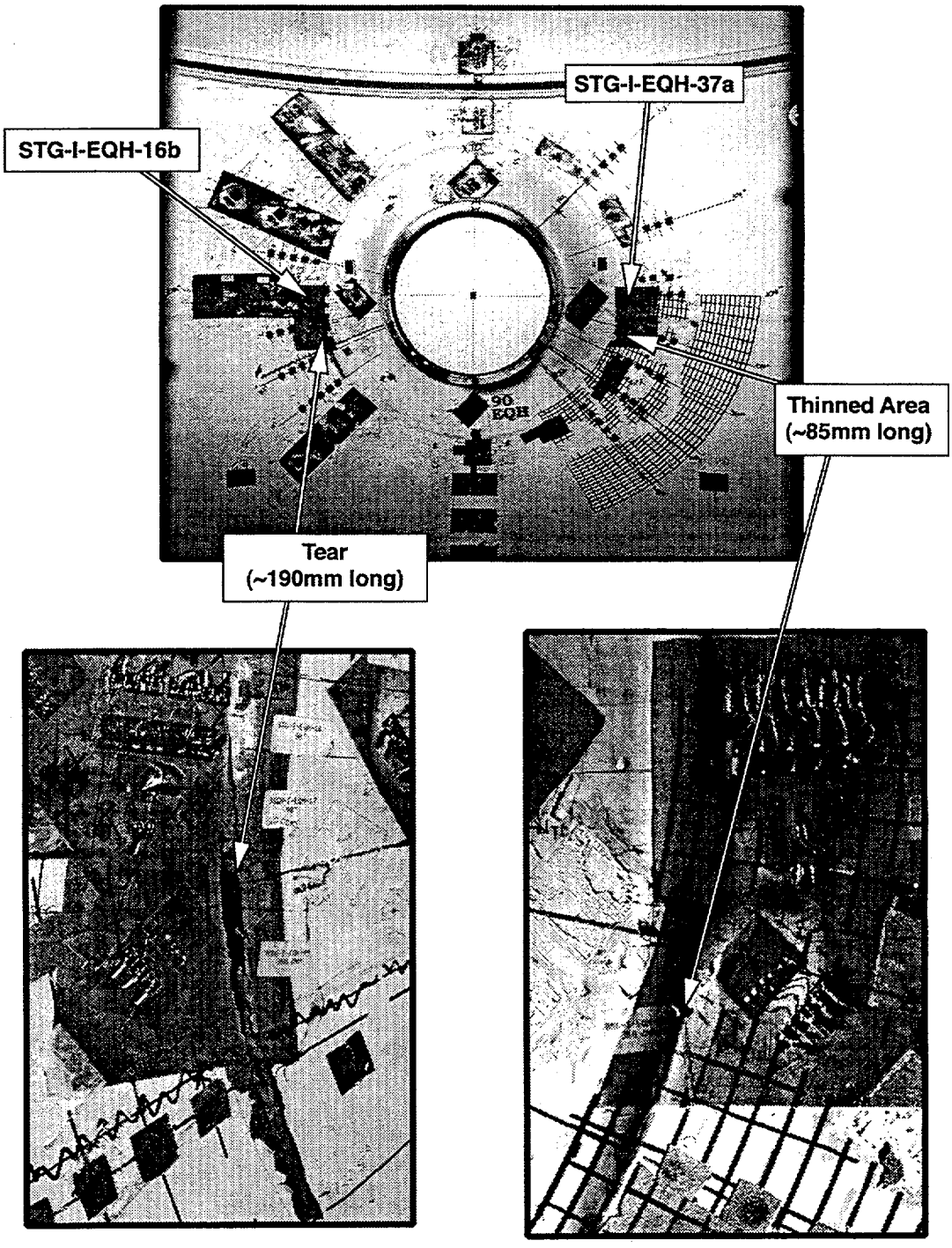

Figure 8.1 Posttest interior view of the equipment hatch.

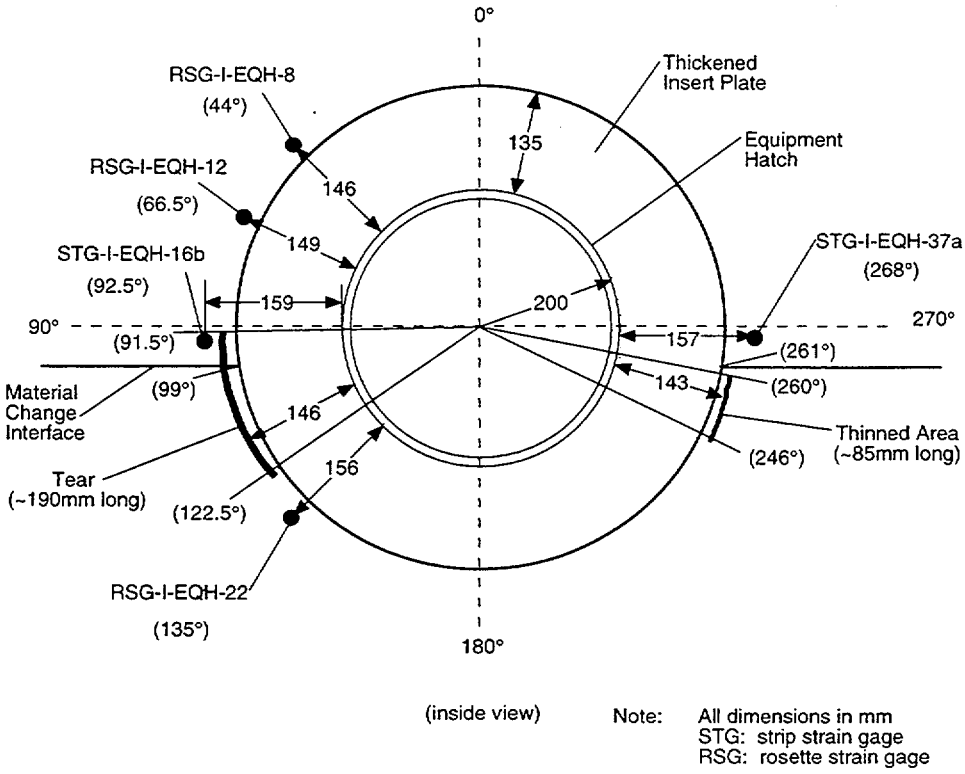

Figure 8.2 Interior elevation of equipment hatch.

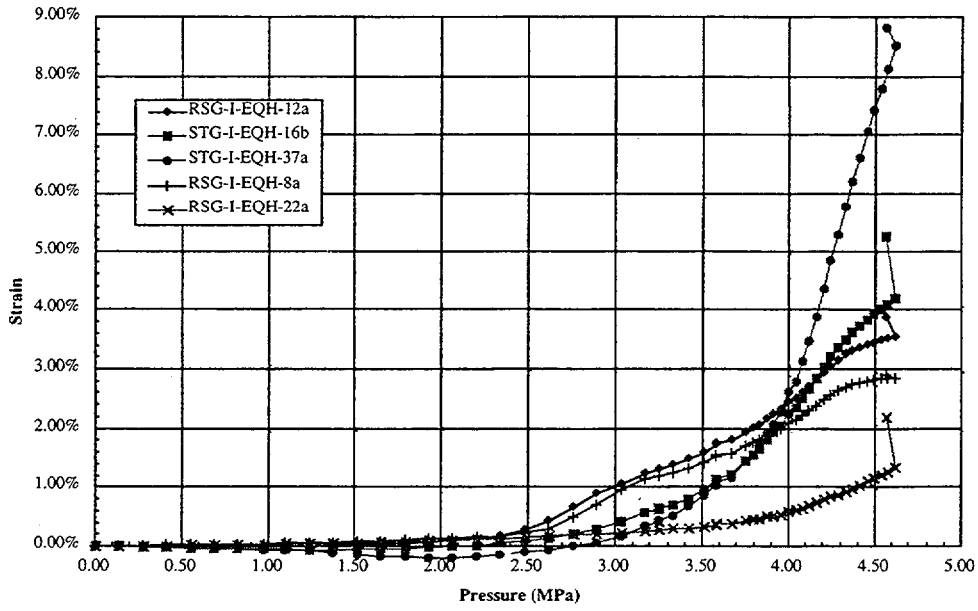

Figure 8.3 Strain history of a few critical gages around equipment hatch.

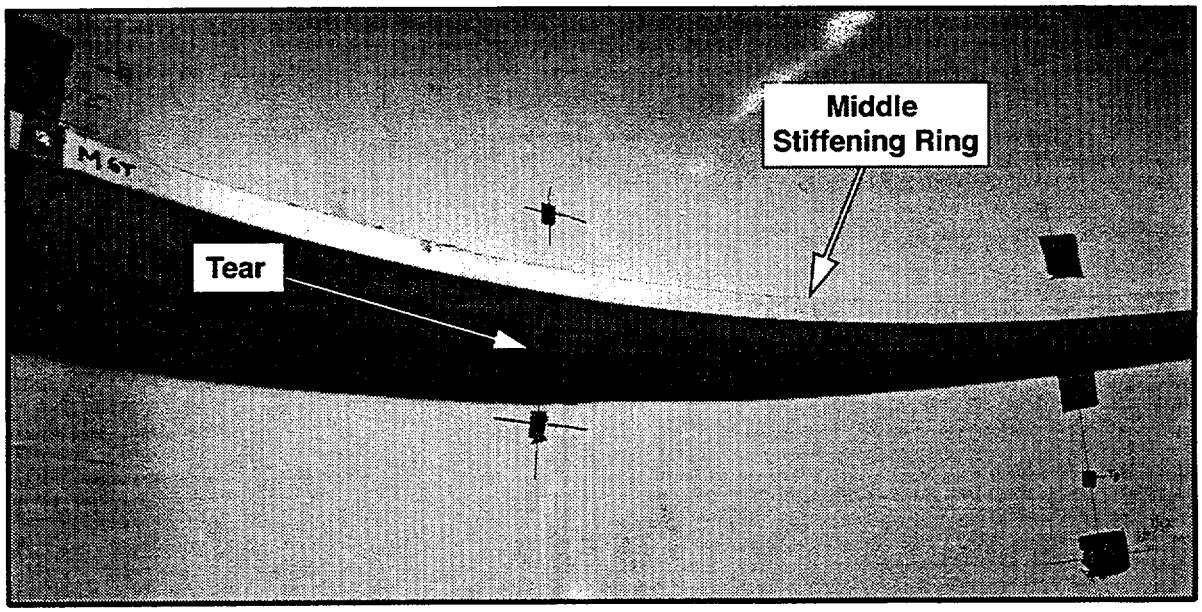

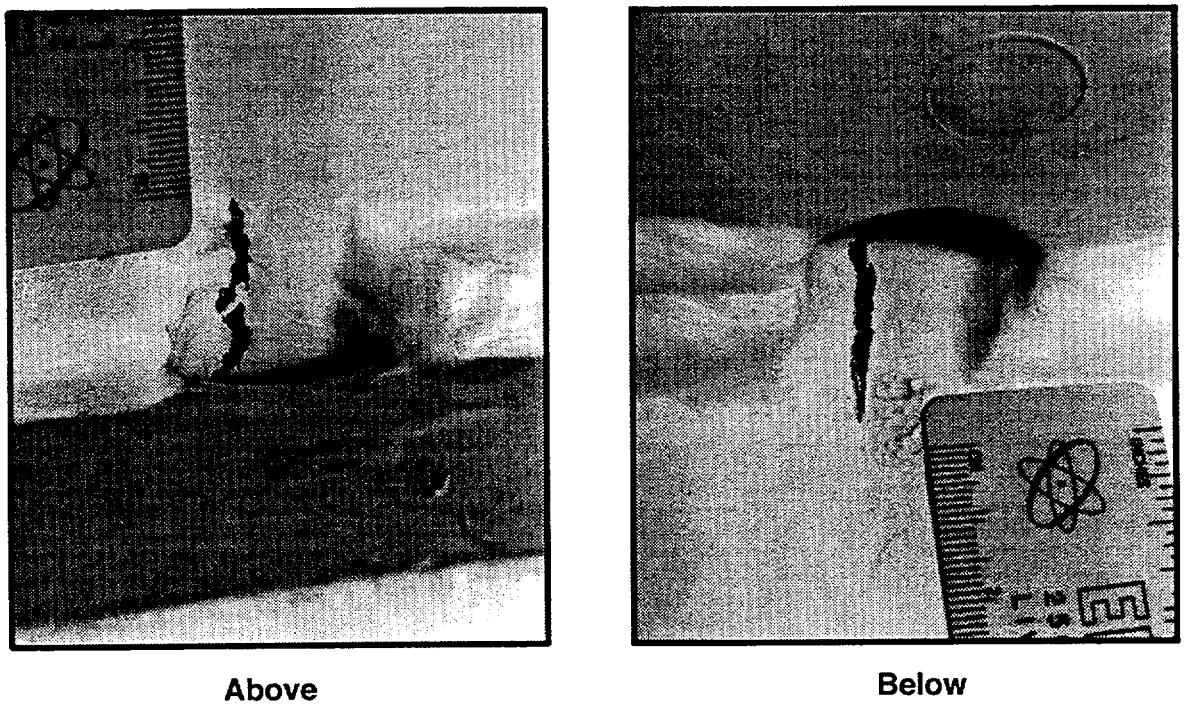

Figure 8.4 Posttest interior view of the small tear at the middle stiffening ring.

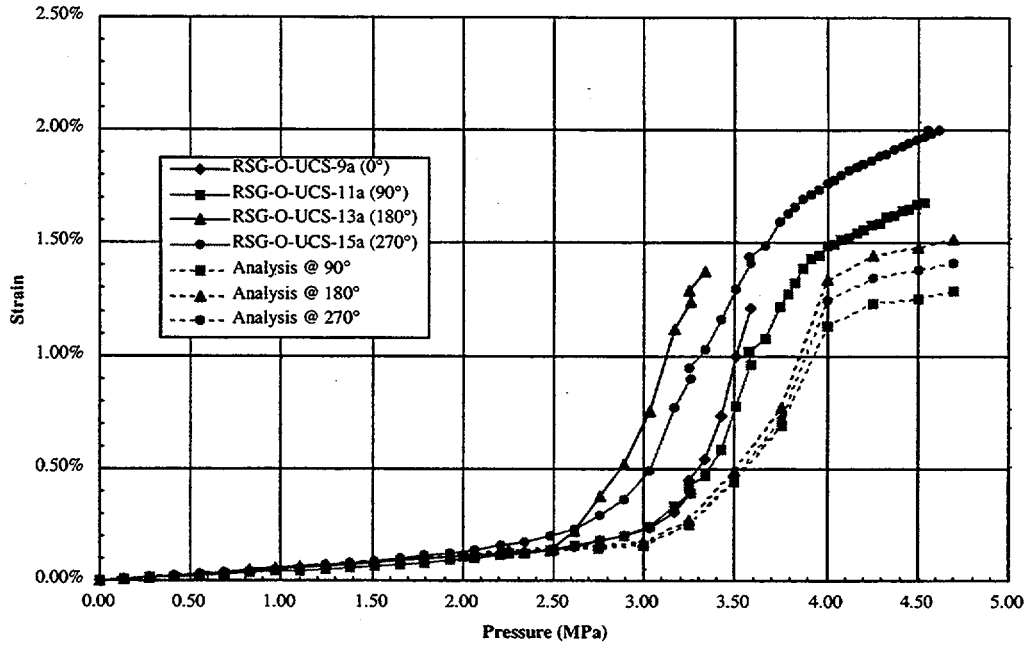

Figure 8.5 Free-field hoop strain at upper conical shell section, elev. 2536 mm.

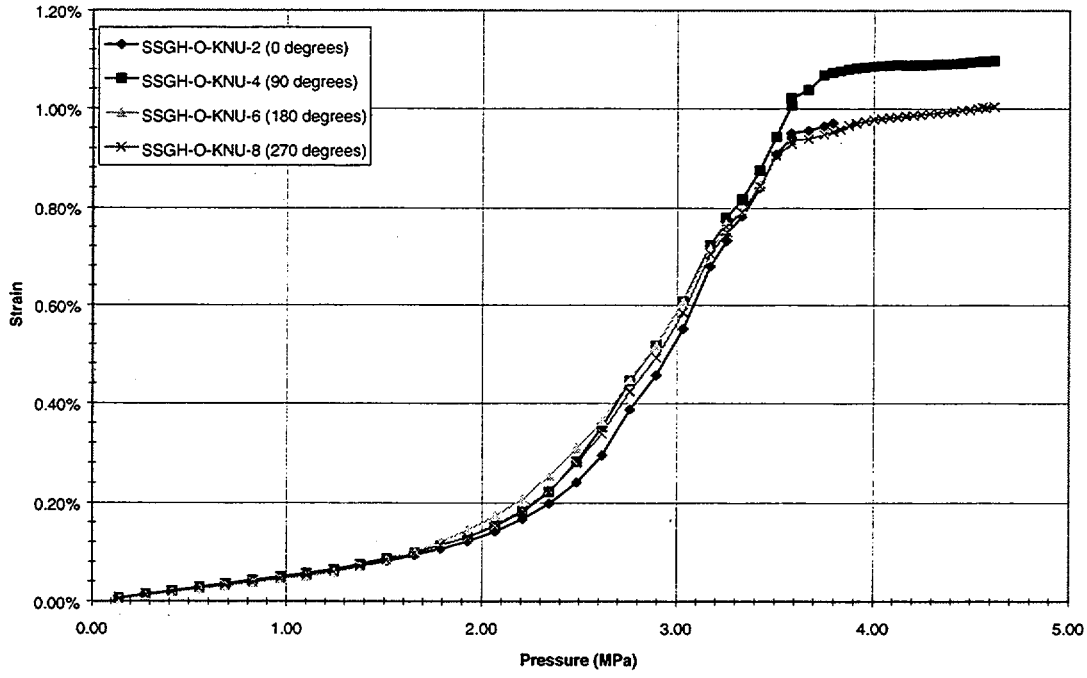

Figure 8.6 Hoop strain at knuckle region, elev. 3319 mm.

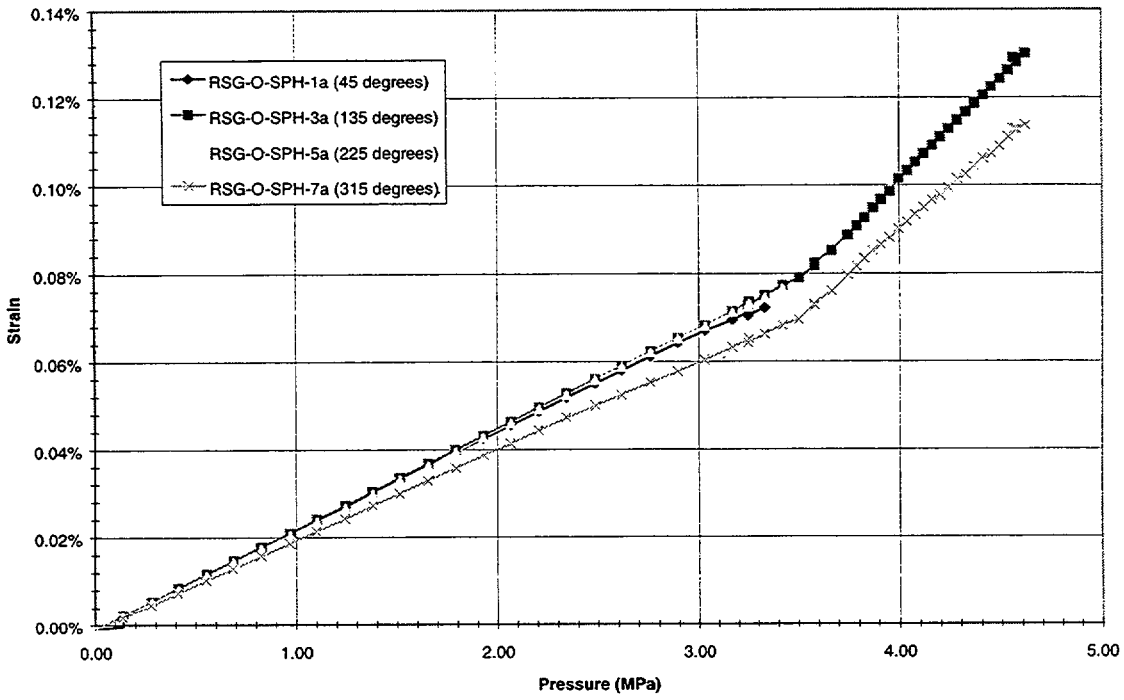

Figure 8.7 Hoop strain at spherical shell section, elev. 3132 mm.

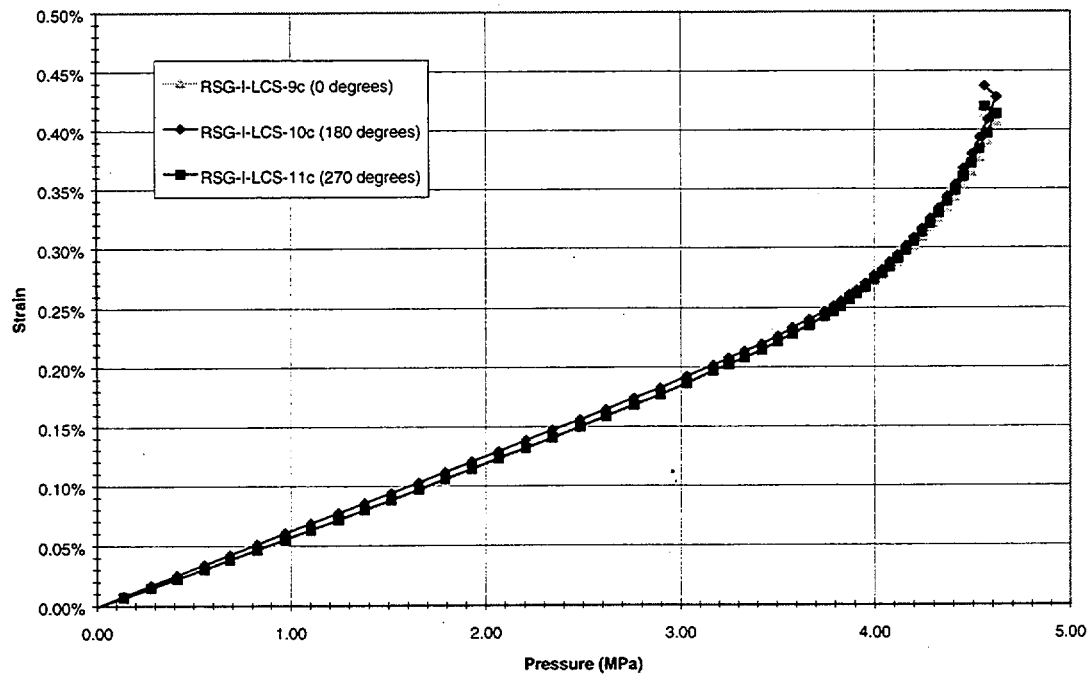

Figure 8.8 Hoop strain at lower conical shell section, elev. 1254 mm.

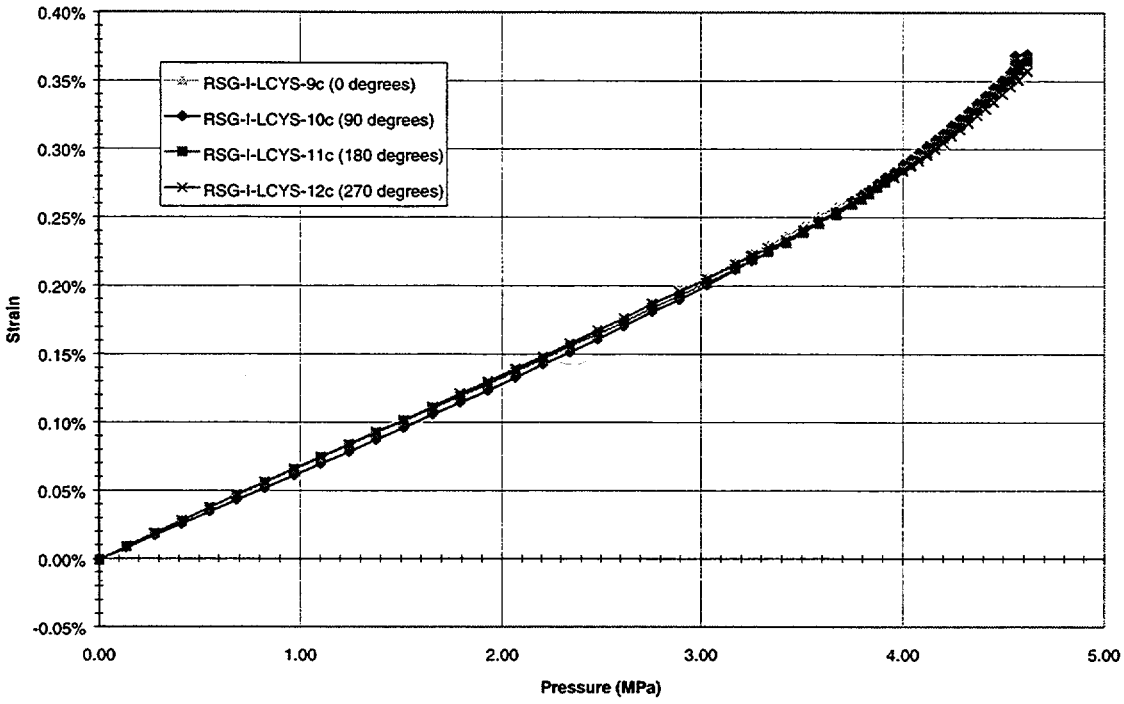

Figure 8.9 Hoop strain at lower cylindrical shell section, elev. 500 mm.

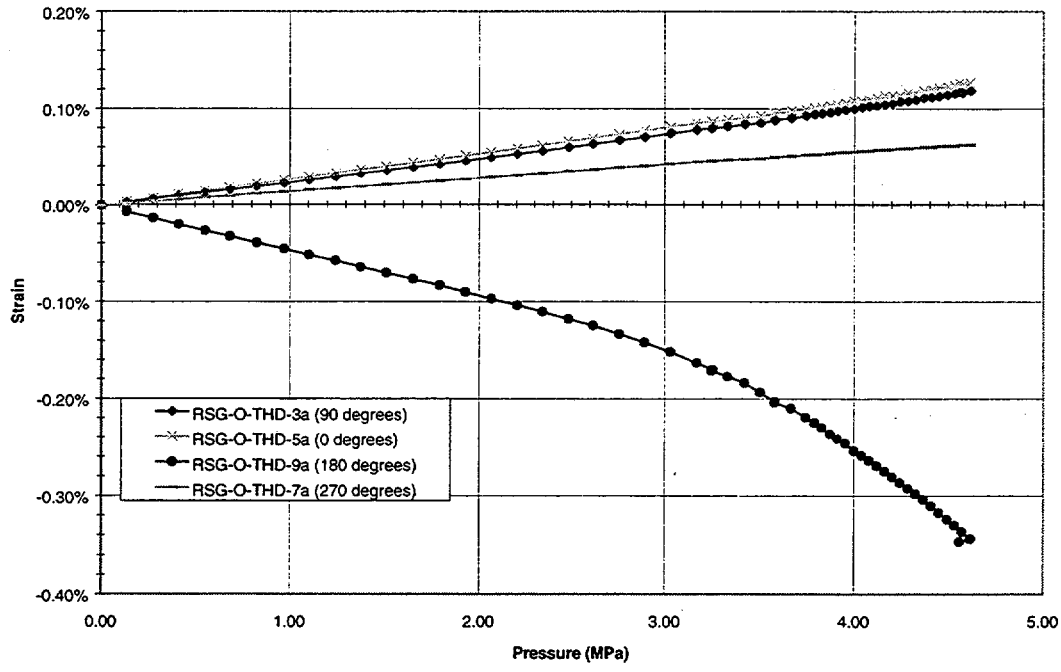

Figure 8.10 Hoop strain at top head region.

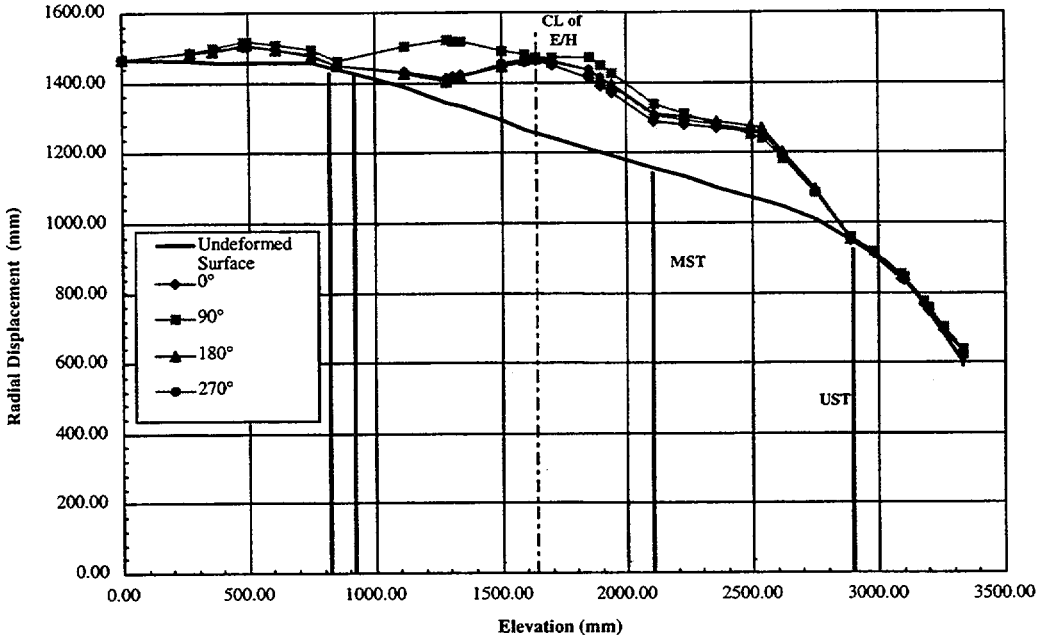

Figure 8.11 Radial displacement contours (10×) at 4.5 MPa.

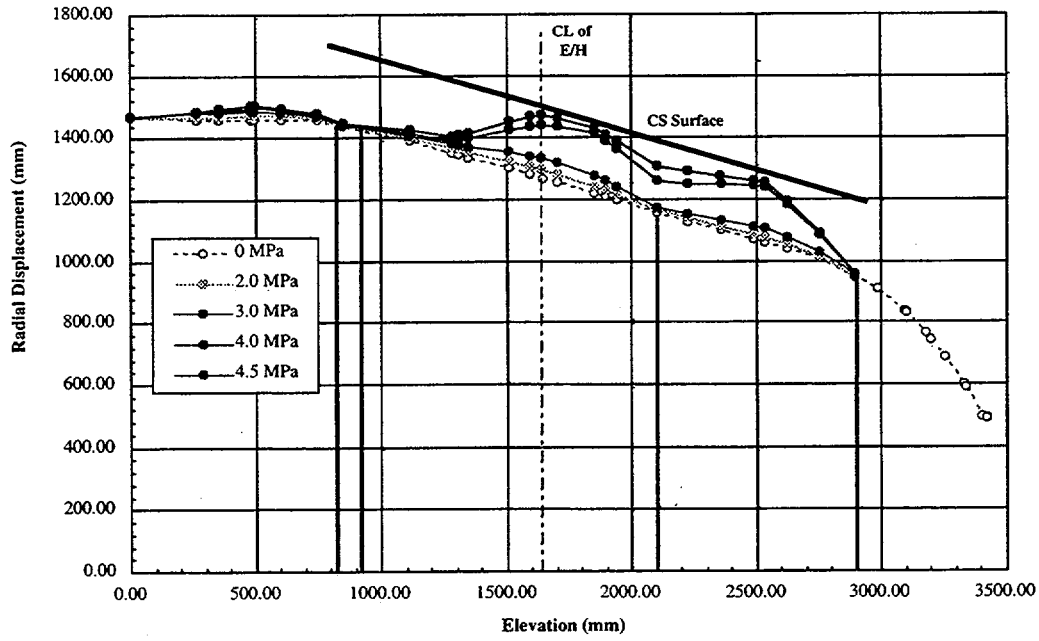

Figure 8.12 Radial displacement contours (10×) at azimuth location of 270°.

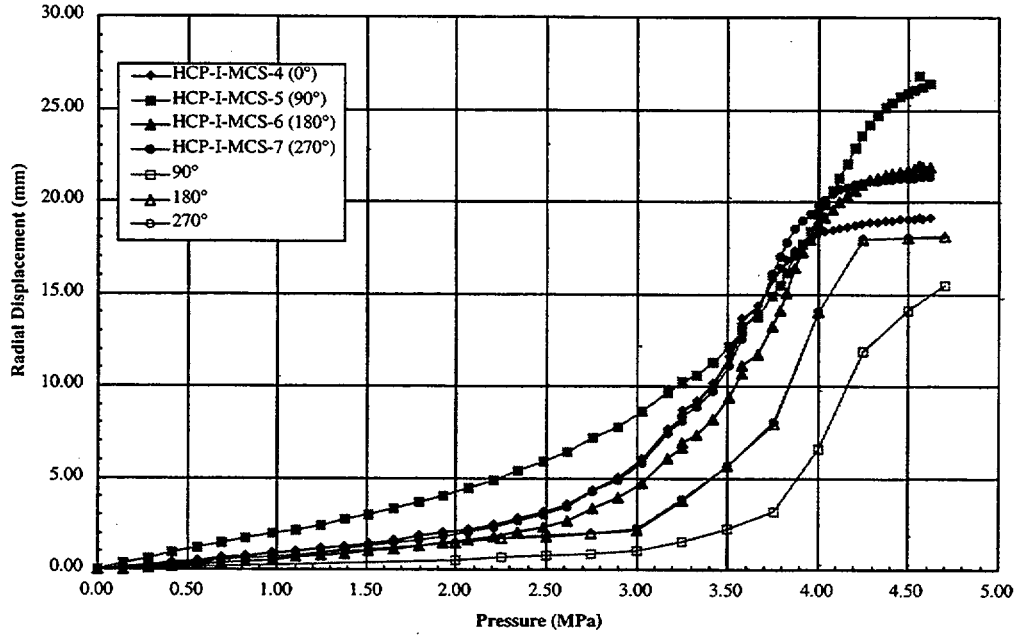

Figure 8.13 Radial displacements at middle conical shell section, elev. 1850 mm.

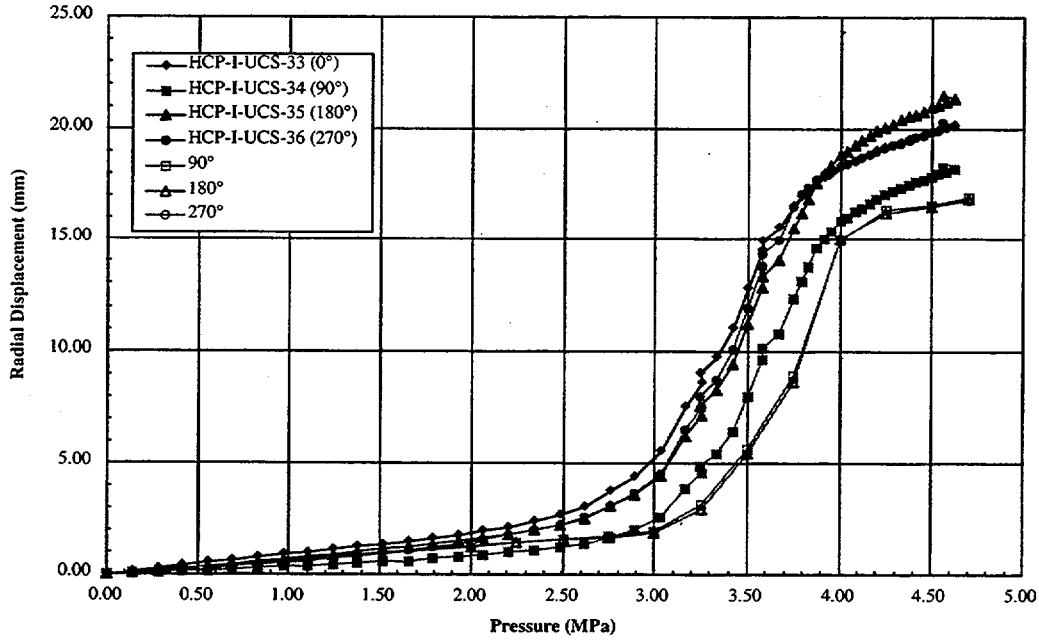

Figure 8.14 Radial displacements at upper conical shell section, elev. 2536 mm.

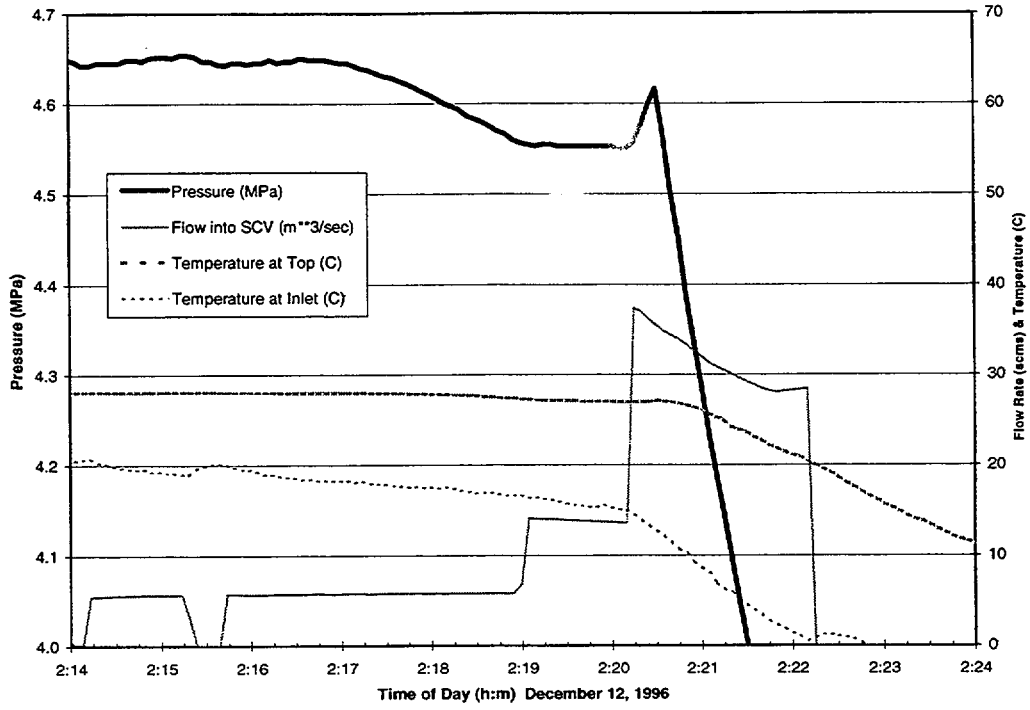

Figure 8.15 Time histories of pressure transducer, flowmeter, and thermocouples in the last twenty minutes of the high pressure test.

THIS PAGE INTENTIONALLY LEFT BLANK.

9. Posttest Metallurgical Evaluation Results

9.1 Introduction

A visual and metallurgical analysis of the steel containment vessel (SCV) model was performed after the high pressure test that caused damage at several locations on the model. The purpose of this analysis is to determine the extent that the condition and properties (such as microstructure, strength, ductility, or flaws) of the two steels, SGV480 and SPV490, and structural assembly features contributed to the observed damage at each location. This analysis attempted to assess, in particular, whether the damage was premature due to any existing conditions in the steel shells. The findings from the metallurgical evaluation should be evaluated in conjunction with the results of the posttest model analysis in order to complete a comprehensive failure analysis of the model. The details of the metallurgical evaluation results are reported by Van Den Avyle and Eckelmeyer (1998).

9.2 Description of Damage and Sample Locations

Three types of localized damage regions were visually observed on the model. These are discussed in detail in the following sections of this chapter. The damage locations and the approximate sizes of sections cut from the model are shown in Figure 9.1.

1. At the equipment hatch, a tear formed at the 74° azimuth at the junction of the hatch reinforcement plate and the 9-mm-thick SPV490 steel plate at the lower conical shell section. Symmetrically on the other side of the hatch at the 106° location, a localized neck formed at the similar position (Figure 9.2).

2. Damage occurred at two locations 180° apart, associated with the middle stiffening ring. A tear formed in the model wall next to a weld relief opening in the stiffening ring (Figure 9.3) at position 201°, and a local neck formed at the similar location at 21°.

3. Local necks formed within the vertical weld lines at the 160° and 340° positions in the lower conical shell section (Figure 9.4). These necks and other areas of local deformation were visible on the exterior surface of the model where the paint coating cracked.

9.2.1 Tear and Deformation at the Equipment Hatch

The tear at the 74° position near the equipment hatch was approximately 190 mm long, with an additional several centimeters of localized necking extending from either end of the tear (Figure 9.5). The local deformation is evident from the cracked paint. An interior view of the same tear is shown in Figure 9.6. Three samples were cut from the area of the tear for metallurgical analysis. These samples included SCV-74-1 and SCV-74-3, which came from the untorn locally deformed regions on either end of the tear, and were mounted and sectioned to examine the deformation and local microstructures. Sample SCV-74-2 spanned the tear, and its fracture surfaces were analyzed by scanning electron microscopy to determine the failure mode.

The structurally equivalent location near the equipment hatch at 106° showed similar localized necking deformation, however here the strain was not large enough to result in tearing (Figure 9.7). The total length of the local deformation was approximately 85 mm. Two samples were cut from the necked region, SCV-106-1 and SCV-106-2. Figure 9.8 shows an interior view of the local area around the equipment hatch where the deformation appears as offsets in ink grid markings in the necked location.

In both of these locations, the high strain concentration followed the weld seam between the thick (17.5–mm-thick SPV490) equipment hatch reinforcement plate and the thinner (9-mm-thick SPV490) model shell. In Figure 9.5, the horizontal measurement tape was placed at the material change interface along the line of the horizontal weld seam between the middle conical shell section (8.5-mm-thick SGV480 steel) and the lower conical shell section (9-mm-thick SPV490 steel). Most of the deformation and tearing occurred along the weld seam between the reinforcement plate and the lower conical shell section; however, the localized strain also was detected across the horizontal weld seam into the SGV480 steel shell in the middle conical shell section. Sample SCV-74-3 (Figure 9.5) contained material from both alloys (the reinforcement plate and the middle conical shell section).

9.2.2 Tearing and Deformation at Openings in the Middle Stiffening Ring

The middle stiffening ring (19 mm thick, 55 mm wide) was welded circumferentially edge-on around the middle conical shell section (8.5-mm-thick SGV480 steel). At locations 21° and 201°, 180° apart, there are weld relief openings cut out of the stiffener ring next to the model wall to accommodate the vertical welds joining the steel plates forming the middle conical shell section. These openings are approximately semi-circular and 32 mm wide. A tear formed in the model wall at the weld relief opening in the stiffening ring at location 201°, and a local neck formed in the similar site at location 21°. The tear/local necks are vertically oriented within the vertical weld seam. Figure 9.9 shows an exterior view of the torn area at location 201° and the sample SCV-201 that was cut out transverse to the tear direction. A similar sample was taken at location 21° (SCV-21).

9.2.3 Localized Deformation at Vertical Welds in Lower Conical Shell Section

Local necks formed within the vertical weld seams at the locations 160° and 340° that connect the two steel shells forming the lower conical shell section (Figure 9.4). These shells are made of 9-mm-thick SPV490 steel. A close-up exterior view of this local deformation is shown in Figure 9.10. A sample, SCV-340 was cut out for metallurgical analysis (Figure 9.11).

9.3 Microstructures and Properties of Steel Alloys

The compositions, strength, and ductility values for several thicknesses of the two steel alloys, SGV480 and SPV490, used to construct the SCV model are reported in Table 9.1. Analysis of polished cross-sections of the samples taken from the model showed that the two alloy steels were substantially different.

To characterize the relative strength levels of welds and alloy base metal at regions of the SCV model where damage occurred, indentation hardness measurements were taken on the specimens for metallurgical analysis. The Rockwell B scale was used for all hardness measurements, which were calibrated to standard test blocks and were taken in the thickness dimension of the steel plates. Specimen surfaces were ground and polished. The hardness values were correlated to the ultimate tensile strength using published tables for carbon steel (*ASM Metals Handbook*, 1967). Base metal hardness measurements were typically taken at the edge of the specimen, as far as possible from any weld within the specimen. It should be noted that the base metal hardness would normally refer to metal plate that did not experience plastic deformation or any weld heating. However, the base metal location might have experienced some heating from the weld process in some cases, and was likely influenced by the overall plastic strain in the SCV model wall in all cases.

9.3.1 SGV480 Alloy

This material was found in sample SCV-21 and the thinner half of sample SCV-74-3. This alloy was specified to have a minimum yield strength of 265 MPa, 480 to 590 MPa ultimate tensile strength, and a minimum elongation of 15–17%, depending on thickness. The data shown in Table 9.1 indicate the material met these specifications

Table 9.1 Compositions and Properties of SCV Steel Alloys

Alloy	Thickness (mm)	Composition (%)	Yield Strength (MPa)	Tensile Strength (MPa)	Elongation (%)
SGV480	7.5	0.18 C, 0.23 Si, 1.16 Mn, 0.007 P, 0.001 S	403	556	26
SGV480	8	Same as above	389	532	26
SGV480	8.5	Same as above	411	560	24
SPV490	9	0.10 C, 0.24 Si, 1.29 Mn, 0.002 P, 0.001 S, 0.48 Ni, 0.03 Cr, 0.17 Mo, 0.04 V	710	727	27
SPV490	38	Same as above	566	650	45

This alloy's base metal microstructure was found to consist of a heavily banded ferrite and pearlite. This is typical of a hot-rolled carbon steel. Its Rockwell B hardness number was found to be 89.2, suggesting an ultimate tensile strength of ~610 MPa (*ASM Metals Handbook*, 1967). The average hardness measurements are given in Table 9.2; a complete listing of all hardness values is given in Appendix I. This is ~10% higher than the reported ultimate tensile strength (UTS) of 560 MPa, indicating that this material experienced net section yielding and a small amount of plastic strain hardening during the high pressure test. No undeformed plate was available for hardness measurement, since the SCV model experienced plastic deformation.

When welded, the reaustenitized heat affected zone (HAZ) transformed mostly to a ferrite and pearlite microstructure similar to, but somewhat finer than the base metal. A limited number of hardness measurements indicated that the heat affected zone was slightly harder than the base metal, 92.8 Rockwell B, due to the finer microstructure. Based on the observed microstructures, it is unlikely that the properties of this material would change significantly with variations in section thickness.

9.3.2 SPV490 Alloy

This material was found in the thicker half of Sample SCV-74-3, as well as in both halves of samples SCV-74-1, SCV-106-1, SCV-106-2, and SCV-340. This alloy was specified to have 490 MPa minimum yield strength, 610 to 740 UTS, and 18–25% elongation. The measured yield and ultimate tensile strengths, reported in Table 9.1, are 710 and 727 MPa, respectively, for the 9-mm plate material. Strengths are substantially lower for the 38-mm plate material (566 and 650 MPa).

Base metal hardness measurements from a reference plate of SPV490 steel plate, which is not a part of the model, showed an average Rockwell B value of 98.8 ±0.07 (Table 9.2). This number compares well with an overall average base metal hardness of 97.4 Rockwell B from the cut samples, correlating to an UTS of ~733 Mpa, which is consistent with the reported UTS of 727 MPa.

The SPV490 alloy was found to have a much different microstructure, one typical of low-carbon martensite or bainite. This most likely was the result of cooling from the hot rolling (or austenitizing) temperature (*ASM Metals Handbook*, 1990). When welded, a much different microstructure was developed in the SPV490 reaustenitized HAZs. These HAZs were found to have significantly lower hardness, 90.7 Rockwell B in areas that had not been substantially deformed (Table 9.2). The measurements of undeformed HAZs were taken on the 17.5-mm-thick plate side of the welds, where the increased thickness did not allow plastic deformation. This suggests a HAZ ultimate tensile strength of ~625 MPa, which is 100 MPa lower than that of the base metal, and near the lower design specification limit for UTS. More detailed hardness measurements indicated that the lowest HAZ hardness occurred near both sides of the boundary of the reaustenitized HAZ and the adjacent partially austenitized material, where the alloy was completely tempered, but not austenitized. These areas of lowest hardness are the logical result from the heating of the welding process of the model.

The band of reduced hardness is quite narrow, at least in the thick sections; it is approximately 2–3 mm wide in the thick (17.5 mm) sections of SPV490 specimens. Beyond that the hardness seemed roughly equivalent to that of the bulk base metal. The available samples did not permit measurement of the width of the decreased hardness band in the thin SPV490 specimens, where extensive plastic deformation and necking occurred.

The metallurgy of this steel, particularly the controlled cooling required to obtain the desired mechanical properties, makes it highly likely that properties would vary with section thickness. This apparently is responsible for the lower strengths reported in Table 9.1 for thicker sections of this material.

9.3.3 Weld Metal

Metallographic examination revealed that all of the welds were made in multiple passes. Frequently the initial passes were made on the inside of the model and the later passes on the outside. The hardness of the fusion zones (Table 9.2) was found to an average Rockwell B hardness of 95.6, with the final fusion regions being slightly harder (~97), and the altered earlier passes being slightly softer (~94). No significant weld defects were observed in any of the samples.

Table 9.2 Hardness Values for SCV Samples

Listed in order are: Rockwell B Hardness Averages, Standard Deviations, and Numbers of Measurements.

Sample	Material	Base Metal[a]	HAZ	Fusion Zone
SCV-74-1	SPV490	98.1 ±1.03 10	91.5 ±1.06 5	95.1 ±1.05 5
SCV-74-3	SPV490	94.2 ±0.39 5	90.9 ±1.80 5	92.1[b] ±0.96 5
SCV-74-3	SGV480	89.2 ±0.15 5	92.2[c] ±1.49 5	Same as above
SCV-106-1	SPV490	97.4 ±1.12 20	92.1 ±1.69 5	97.1 ±1.11 15
SCV-106-2	SPV490	97.0 ±1.34 15	88.6 ±1.04 5	95.0 ±2.58 10
SCV-340	SPV490	98.0 ±0.84 20	96.7[c] ±1.83 10	97.6 ±0.55 15
SCV-21	SGV480	88.8 ±1.26 5	92.8 ±0.56 4	95.5 ±0.92 6
SGV480 Avg[d]		89.0	92.8	95.5
SPV490 Avg[d]		97.4	90.7	96.2
SPV490 Reference Plate		98.8 ±0.07 10		

[a] "Base Metal" measurements, except for the SPV490 reference plate, were taken at the far edges of sectioned samples; these samples experienced some plastic deformation, and the sample edges might have been heated during welding of the structure.

[b] Fusion zone between SGV480 and SPV490; not included in averages.

[c] HAZ deformed during pressurization of vessel; it is likely that hardness of material prior to deformation was lower; not included in averages.

[d] Weighted averages; more hardness measurements were made in some samples than others. See Appendix H.

9.4 Metallographic Analysis of Damaged Regions

9.4.1 Samples from Damaged Region around Equipment Hatch

The SCV model test was terminated when an ~190-mm-long tear developed in the model wall adjacent to the equipment hatch at the 74° location. Macro-examination of the fracture surfaces indicated that this tear initiated in the 9-mm-thick SPV490 shell near where it was welded to the thicker reinforcement plate of the same material. The tear extended parallel to the weld from this initiation site in both directions, one half remaining in the 9-mm-thick SPV490 shell, and the other half crossing into the 8.5-mm-thick SGV480 shell. The corresponding area on the opposite side of the equipment hatch at 106° location exhibited substantial necking, but no tearing.

Table 9.3 Thickness Reduction Measured in Necked Regions of Each Sample

Sample	Material	% Thickness Reduction	Necking and Tear Location
SCV-74-2	SPV490	44.6[a]	HAZ
SCV-74-1	SPV490	38.4[b]	HAZ
SCV-74-3	SGV480	41.5[b]	HAZ
SCV-106-1	SPV490	15.0	HAZ
SCV-106-2	SPV490	31.1	HAZ
SCV-21	SGV480	12.8	HAZ
SCV-201	SGV480	37.8	HAZ
SCV-340	SPV490	11.9 (side 1) 4.2 (side 2)	HAZ

[a] near tear initiation site
[b] just ahead of tear

Seven samples were examined from the deformed and torn regions near the equipment hatch: three from the tear initiation region (SCV-74-2 A, B, and C), one from each end of the tear (SCV-74-1 and SCV-74-3), and two from the necked region on the opposite side of the equipment hatch (SCV-106-1 and SCV-106-2). Each sample consisted of a thin section of the model shell (8.5-mm-thick SGV480 in sample SCV-74-3, or 9-mm-thick SPV490 in all of the other samples) welded to a section of the thicker (17.5 mm) reinforcement plate of SPV490 which surrounds the equipment hatch. The thickness reductions measured in each of these areas are shown in Table 9.3. It is apparent that both materials underwent substantial plastic deformation prior to tearing.

Metallographic examination of all of these samples revealed weld fusion zones, adjacent weld heat affected zones, and base metal microstructures. These are shown in Figures 9.12 through 9.15. In all cases necking was found to have concentrated in the weld heat affected zone. Eventual failure occurred by a ~45° shear in the heavily deformed regions. No other flaws or provocative microstructural features were found to be associated with these failures.

Figure 9.12(a) shows the torn SPV490 HAZ near the lower end of the tear at the 74° location (Sample SCV-74-1). This weld connects 9-mm-thick SPV490 shell on the left to the 17.5-mm-thick SPV490 reinforcement plate around the equipment hatch. The weld fusion zone, with at least five weld passes, is shown in Figure 9.12(b); the thicker plate is on the right. The necking and subsequent tearing are concentrated approximately 10 mm away from the fusion zone in the lower hardness region of the HAZ. Taken near the other (upper) end of the tear, Sample SCV-74-3 shows a similar view of the necked region in SGV480 shell in the HAZ of the weld to the equipment hatch reinforcement plate (Figure 9.13). The samples taken from the necked region on the other side (106°) of the equipment hatch have the same appearance (Figures 9.14 and 9.15).

The figures of the SPV490 alloy plate, combined with hardness data discussed in Section 10.3.2, provide information to estimate the extent of thermal softening of this material away from the welds. The HAZ is comprised of two regions: (1) a dark etching reaustenitized part of the HAZ below the weld fusion zone, etched dark in Figures 9.11 through 9.15, and (2) a lightly etched band of reduced hardness next to the reaustenitized dark HAZ (measured to extend an additional 2–3 mm into the thick sections of SPV490). The reaustenitized HAZ depth ranges from 4–6 mm for both the thin and thick sides of the welds. This indicates that the depths of thermal penetration were similar for the two thicknesses. Because the band of reduced hardness in the metal adjacent to the reaustenitized portion (dark region) HAZ is approximately 2–3mm wide in the thick sections of SPV490, it is reasonable to conclude that the reduced hardness band in the thinner plate would also be on the order of 2–3 mm.

Metallographic examination of samples near the tear initiation site (SCV-74-2 A, B, and C) revealed evidence of substantial local plastic shear deformation below the tear surface near the inner and outer plate surfaces (Figure 9.16), but less local shear deformation in the interior of the model wall (Figure 9.17). This suggests that failure initiated internally within the material, rather than at surface defects.

The tear surface on Sample SCV-74-2 was examined in the scanning electron microscope (SEM) to determine tearing crack growth mode and to check for flaws or initiation sites. The entire surface of the sample was comprised of ductile shear voids, characteristic of ductile shear overload failure. No surface or subsurface flaws were noted. On these tear surfaces with ductile shear void, it was not possible to locate individual tear initiation points. The detected tear morphology is consistent with ductile overload tearing failure, by shear, after the neck formed.

9.4.2 Samples from Damaged Region in Middle Stiffening Ring

Sample SCV-21 at the 21° location, in the middle conical shell section, consisted of two sections of 8.5-mm-thick SGV480 shell vertically welded together and then welded to a perpendicular stiffening ring of the same material. This ring was designed with an approximately 32-mm-wide weld relief opening adjacent to the inner model surface; the openings were over the vertical welds. Deformation of the stiffening ring during the high pressure test caused localized plastic deformation of the model wall at the opening and produced a vertical necked region within the vertical weld.

Sample SCV-21 consisted mostly of weld metal and HAZ (Figure 9.18). The sample is aligned along the direction of the stiffening ring, and the opening in the ring is captured in cross-section. The wall plate is at the bottom of the section, with the neck evident at the bottom of the opening (the model vertical direction is perpendicular to the micrograph). The necked region is primarily composed of weld HAZ. The hardness of the wall was found to be consistent with that of the SGV480 wall material in sample SCV-74-3. The measured reduction-in-area in the wall adjacent to the cut-out of the stiffening ring is shown in Table 9.3.

The tear surface of the tear in Sample SCV-201 was viewed in the SEM to determine the failure mode. The SEM results indicated that the tear formed primarily in shear as a ductile overload failure. No flaws were noted that would have contributed to premature failure. The measured reduction-in-area in the wall adjacent to the cutout of the stiffening ring at 201° is shown in Table 9.3.

9.4.3 Samples from Deformed Vertical Weld Area in Lower Conical Shell Section

Sample SCV-340 consisted of two sections of 9-mm-thick SPV490 plates welded vertically to one another. The microstructures and hardnesses of the fusion zone, HAZs, and base metal were similar to those described previously (Figure 9.19). Deformation was concentrated in the HAZs adjacent to each side of the weld, because of the low hardness in these regions. The reductions-in-area measured for each side of the weld are shown in Table 9.3.

9.5 Conclusions

1. Strong local necking deformation occurred at two locations around the equipment hatch; at one, the 74° location, a large, stable shear tear formed which caused a leak in the SCV model. These deformations occurred preferentially in the weld heat affected region of the SPV490 alloy plate.

2. Hardness measurements and metallographic analysis indicate that heat from the welding process resulted in localized microstructural alteration and reduced hardness and strength of the SPV490 alloy plate. The region of reduced hardness adjacent to the weld included the reaustenitized (dark etching) weld HAZ, 4–6 mm wide, and a narrow zone of reduced hardness HAZ, approximately 2–3 mm wide. The weld fusion zone was not significantly softer than the SPV490 base metal.

3. A second tear formed in the model wall, at a weld relief hole in the stiffening ring, at the 201° location where a vertical weld joined plates of SGV480 steel. A similar region at 21° location formed a localized neck. These deformations also occurred within the weld heat affected region.

4. The microstructure and hardening mechanisms present in the SPV490 alloy make it sensitive to thermal history from the forming or welding process. The SGV480 alloy is less sensitive because of its simpler microstructure and chemistry.

5. All material deformation and tear observed in the samples were ductile in nature. There was no evidence of material flaws, defects, or brittle behavior in the base metal or welds. The tears that occurred resulted from exceeding the local plastic ductility of the alloy.

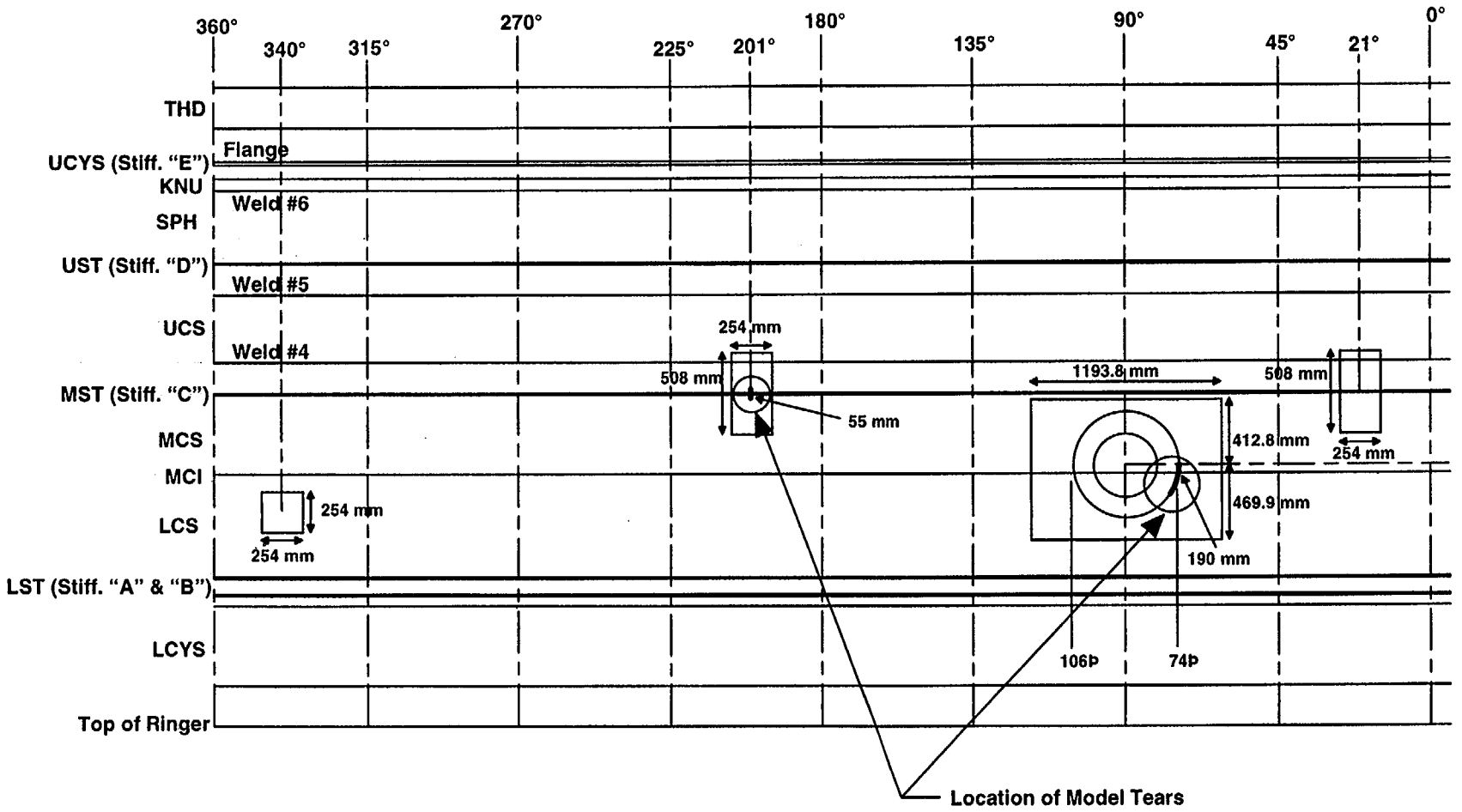

Figure 9.1 Elevation view of SCV model identifying sectioned sample locations.

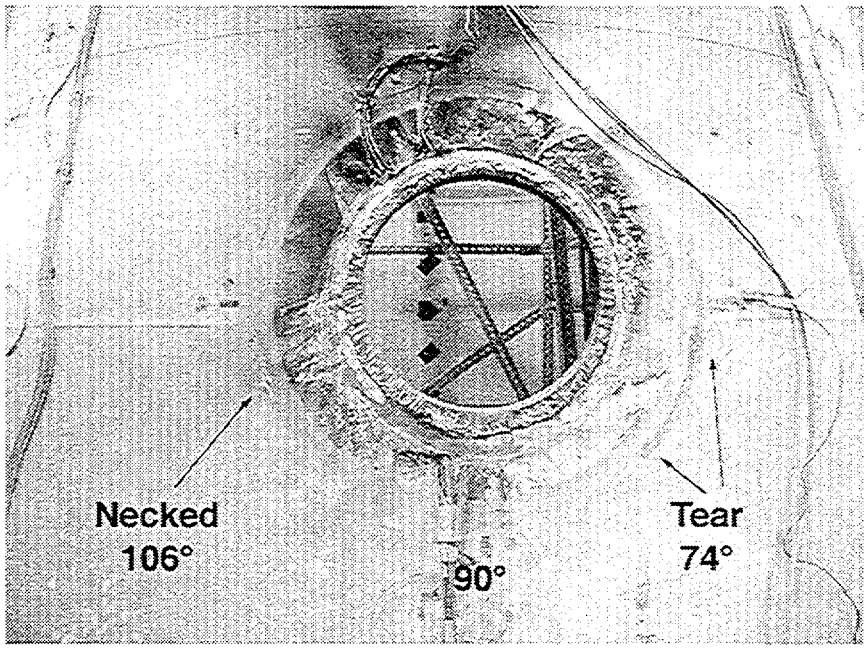

Figure 9.2 Exterior view of the equipment hatch (after removal of barrel) showing torn and necked areas.

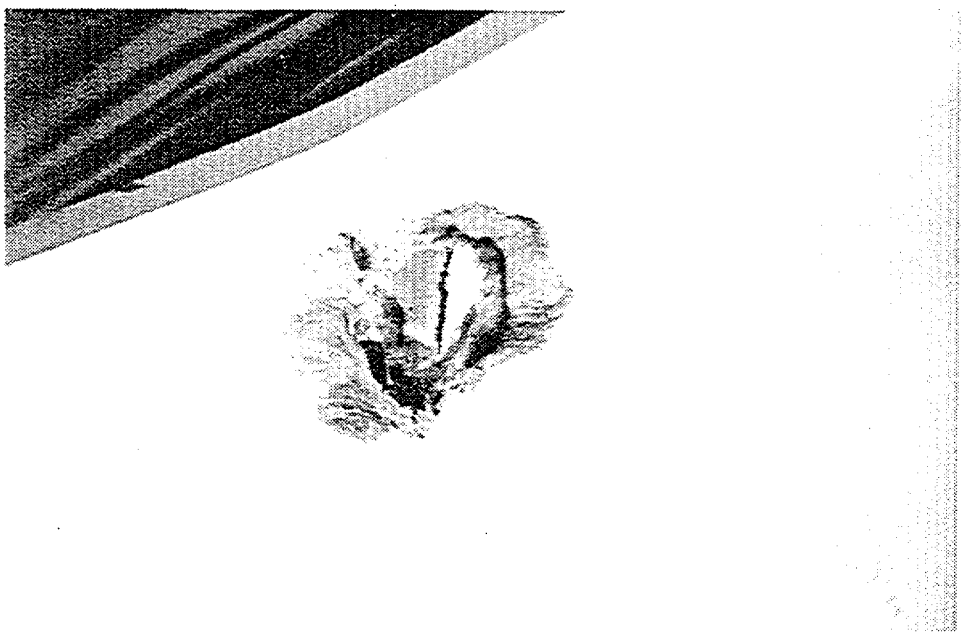

Figure 9.3 Interior view of the tear next to a vertical weld seam inside a weld relief opening in the middle stiffening ring.

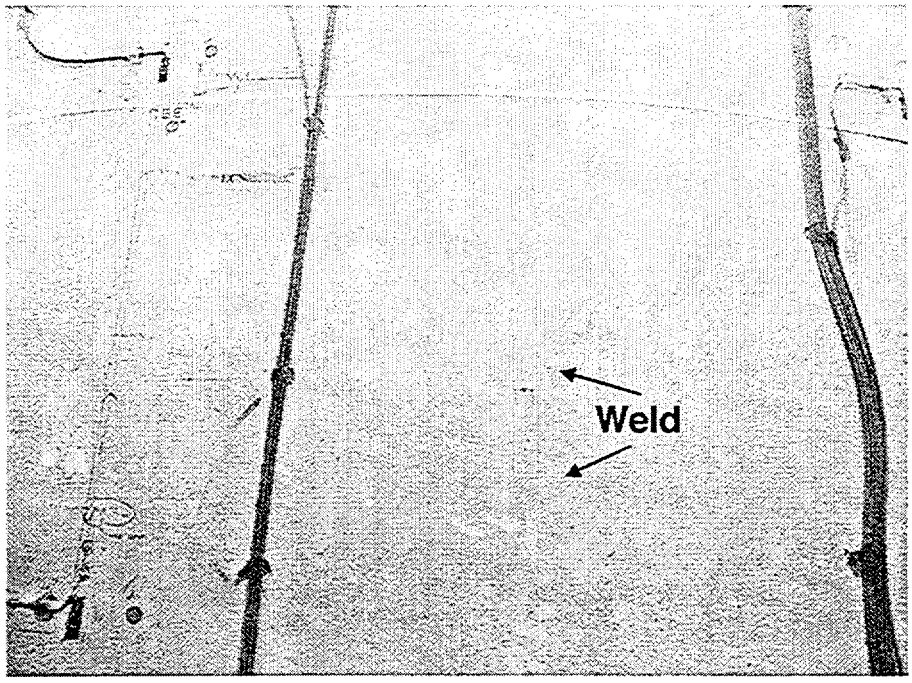

Figure 9.4 Exterior view of stretched paint coating along vertical weld seam in lower conical shell section.

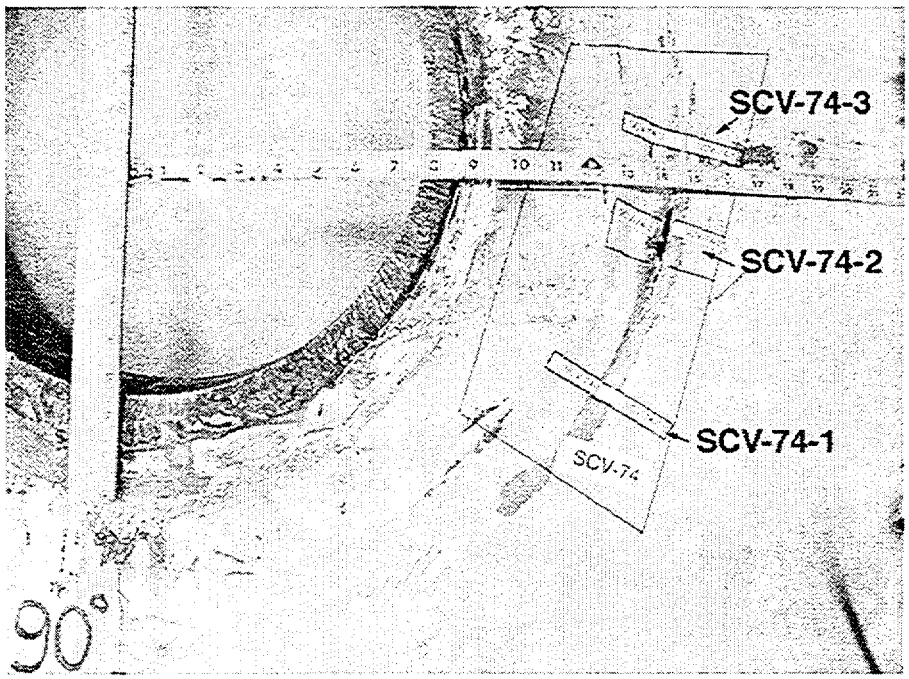

Figure 9.5 Exterior view of equipment hatch showing the tear at 74° and sectioned sample locations.

Figure 9.6 Interior view of tear at location 74° near the equipment hatch.

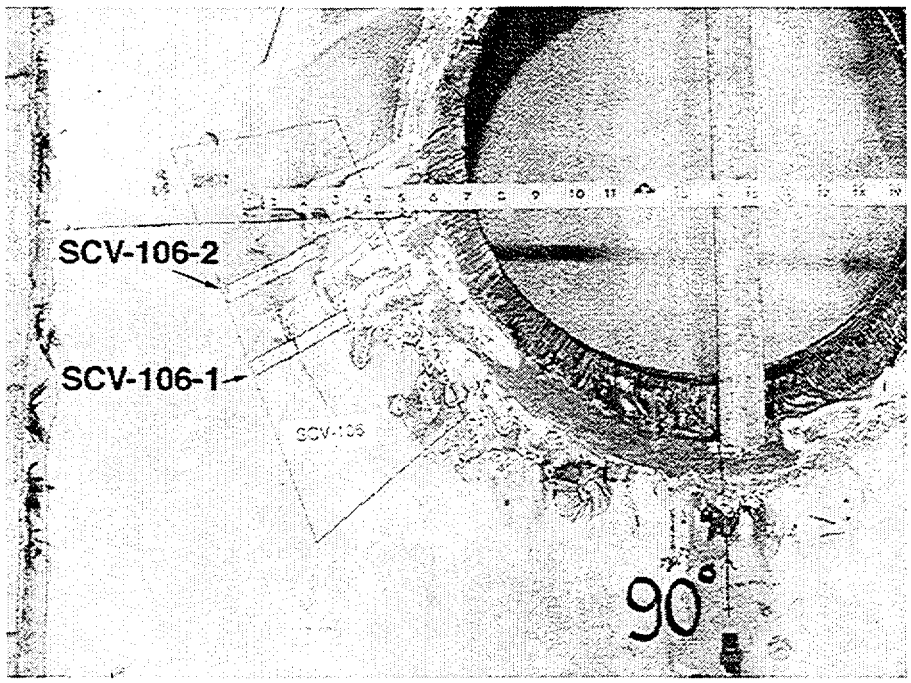

Figure 9.7 Exterior view of a local area around equipment hatch showing the necked region at location 106° and samples for metallurgical analysis.

Figure 9.8 Interior view of a local area around equipment hatch showing the necked region at location 106°.

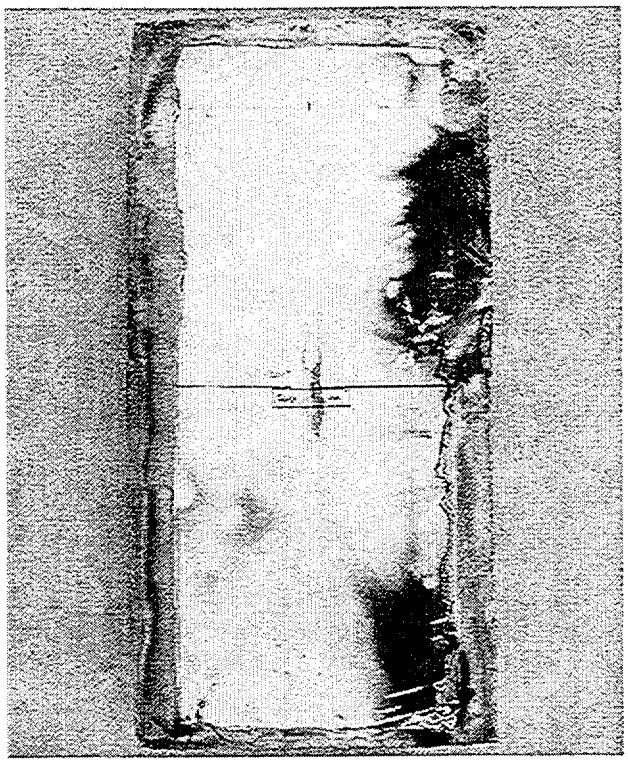

Figure 9.9 Exterior view of the tear at location 201° in middle stiffening ring.

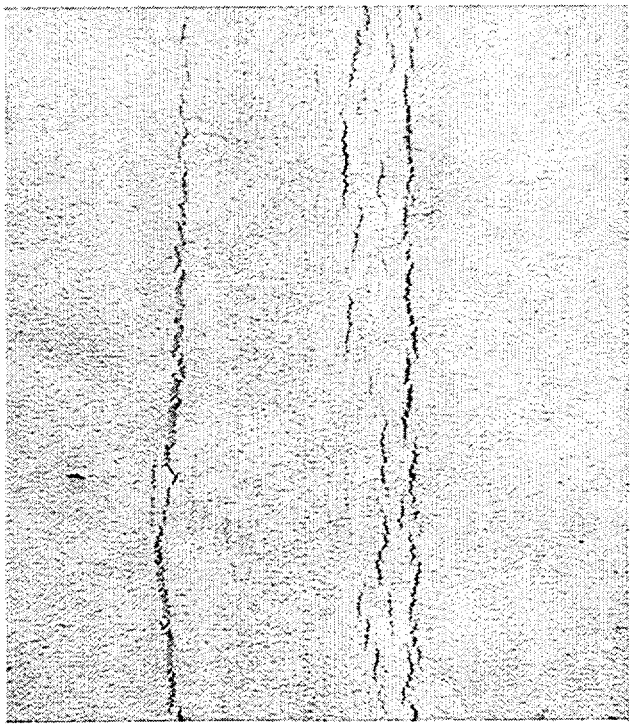

Figure 9.10 Close-up of exterior view of local deformation as paint cracks at the vertical weld seam at location 340° in lower conical shell section.

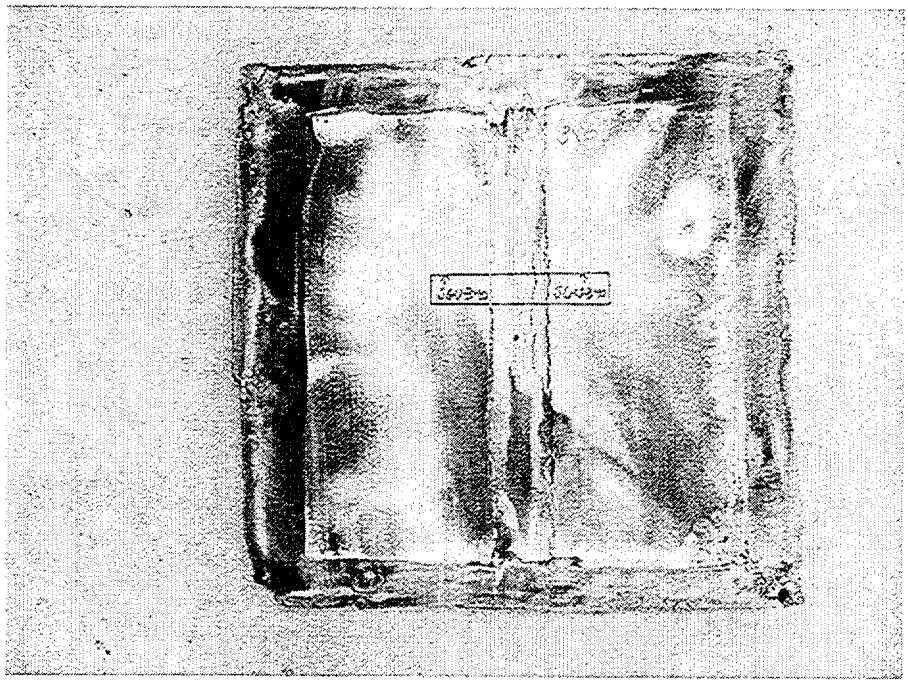

Figure 9.11 Sample SCV-340 taken from vertical weld seam at location 340° in lower conical shell section.

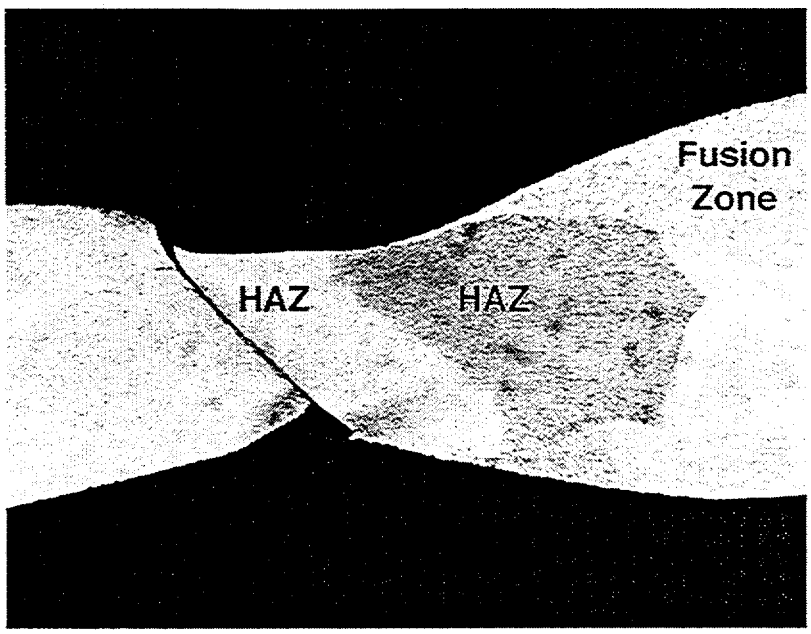

(a)

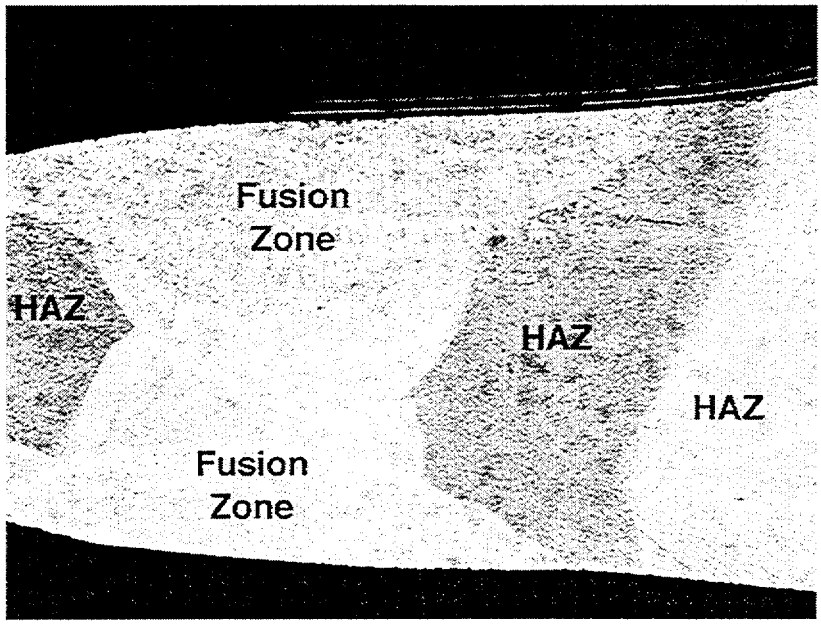

(b)

Figure 9.12 Sample SCV-74-1 near bottom of tear adjacent to equipment hatch: (a) shear tear in lower hardness weld HAZ in 9 mm SPV490 wall material, with weld fusion zone on right; (b) view to right of (a) showing fusion zone and weld HAZ into 17.5 mm SPV490 reinforcement plate. Reaustenitized HAZ areas are dark regions on either side of fusion zone.

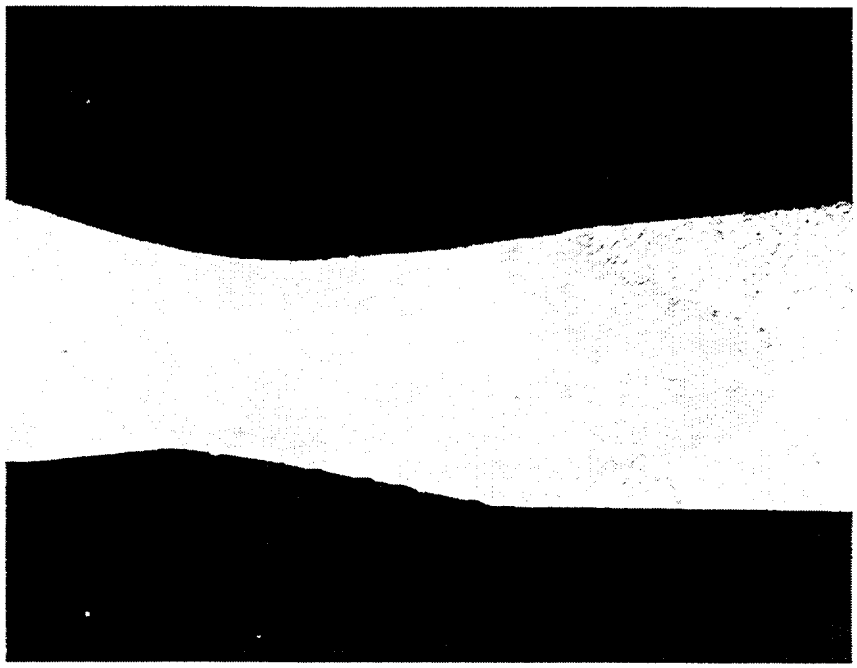

(a)

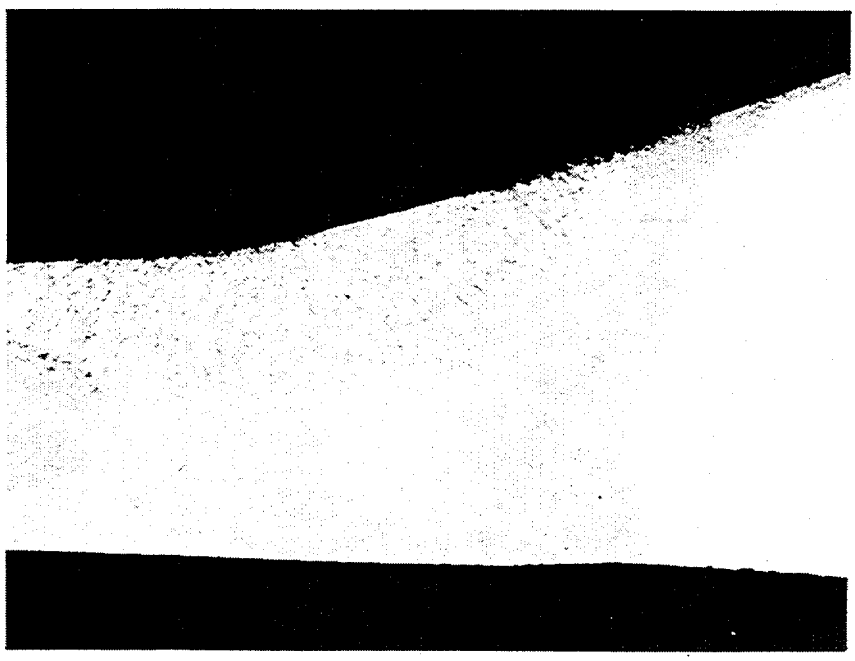

(b)

Figure 9.13 Sample SCV-74-3 near top of tear adjacent to equipment hatch: (a) deformed and necked region in weld HAZ of 8.5 mm SGV480 wall material with weld fusion zone on right; (b) view to right of (a) showing fusion zone and weld HAZ into 17.5-mm-SPV490 reinforcement plate.

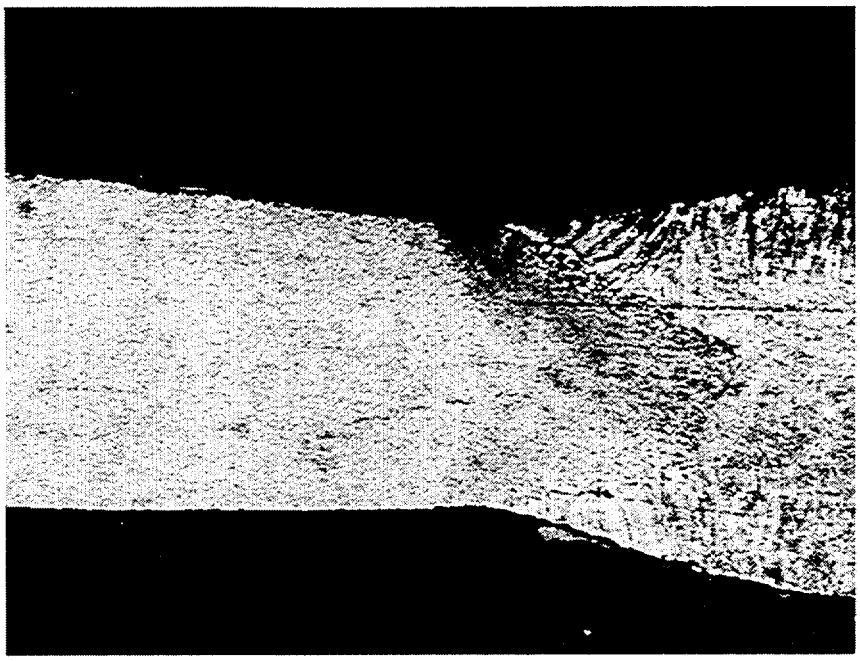

(a)

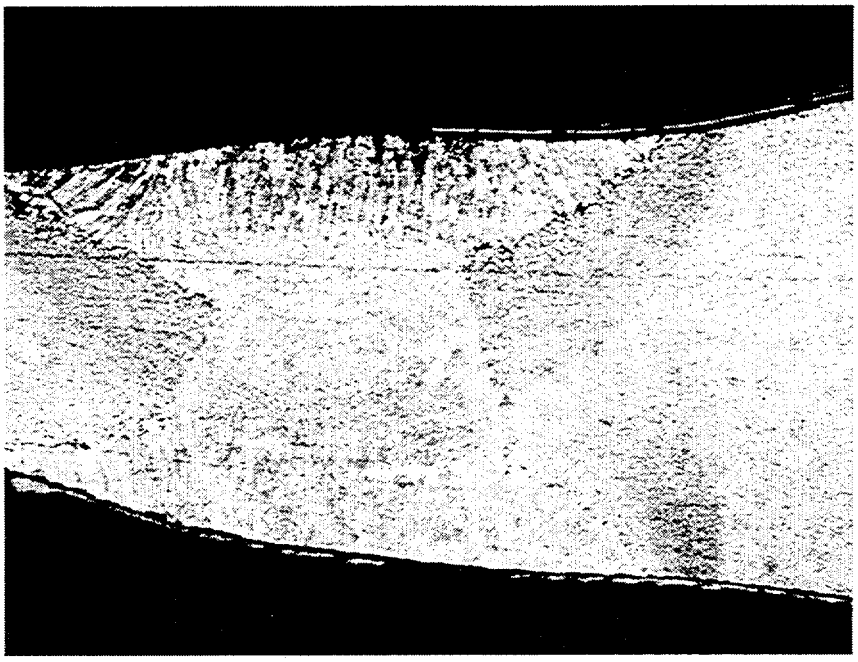

(b)

Figure 9.14 Microstructure of necked region (sample SCV-106-1) at 106° location near equipment hatch: (a) thinning deformation in weld HAZ in SPV490 alloy plate with weld fusion zone at right side; (b) view to right of (a) showing weld fusion zone and HAZ of 17.5-mm-SPV490 reinforcement plate.

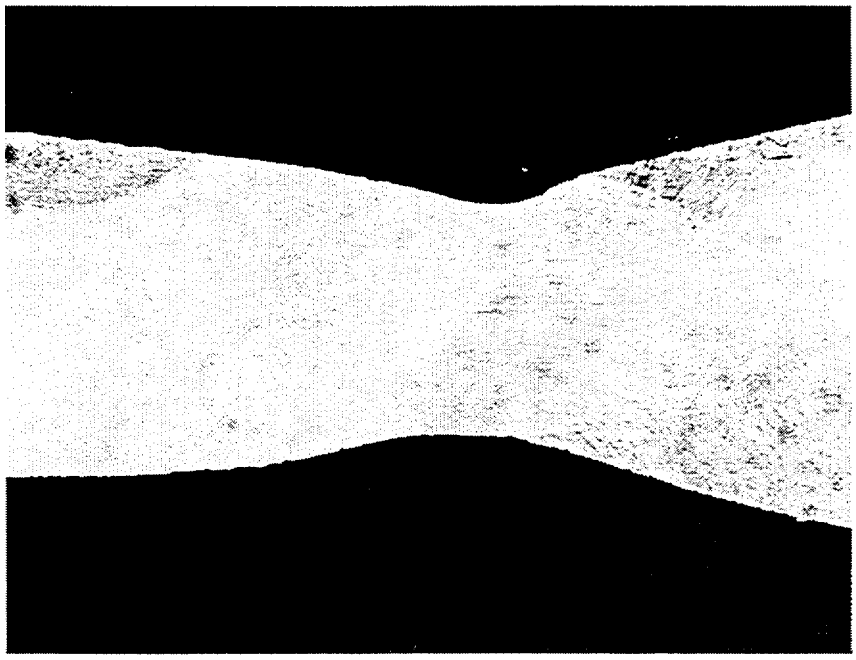

(a)

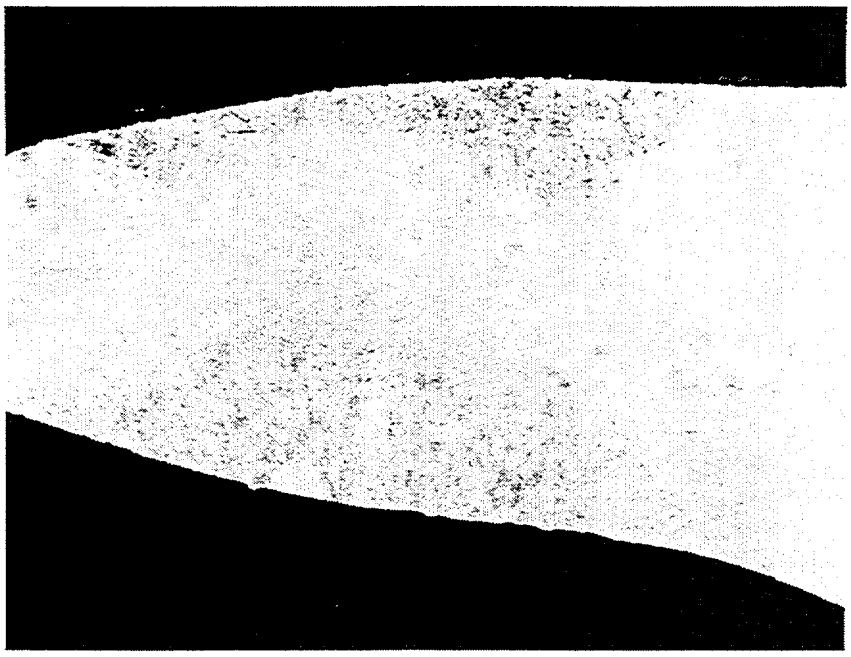

(b)

Figure 9.15 Microstructure of necked region (sample SCV-106-2) at 106° location near equipment hatch: (a) thinning deformation at base metal and weld HAZ in SPV490 alloy plate with weld fusion zone at right side; (b) view to right of (a) showing weld fusion zone and HAZ of 17.5-mm-SPV490 reinforcement plate.

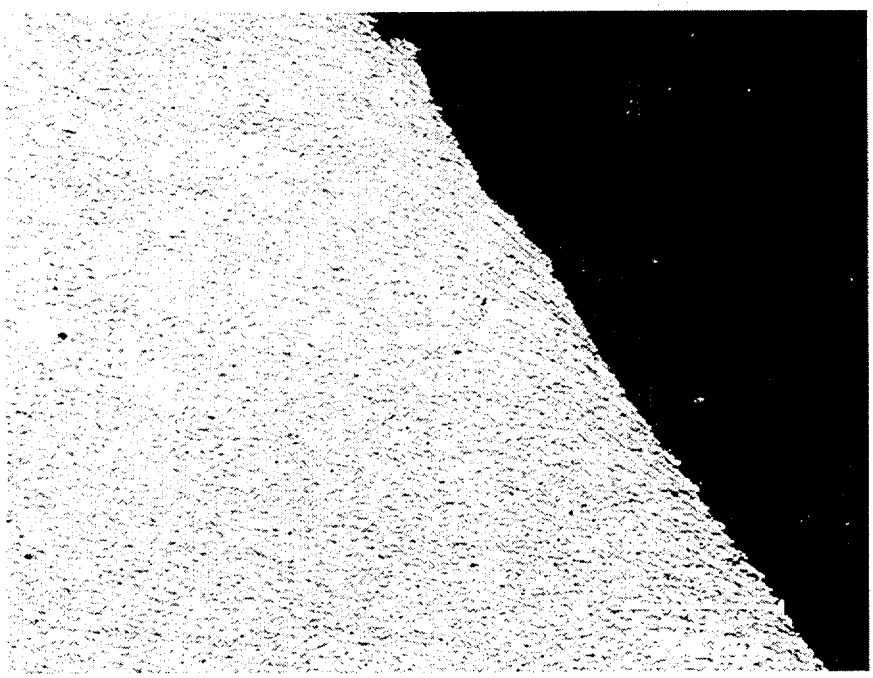

Figure 9.16 Local shearing associated in Sample SCV-74-2 with tearing near inner and outer surfaces near tear initiation site, and typical of the entire tear away from the initiation site, 100×.

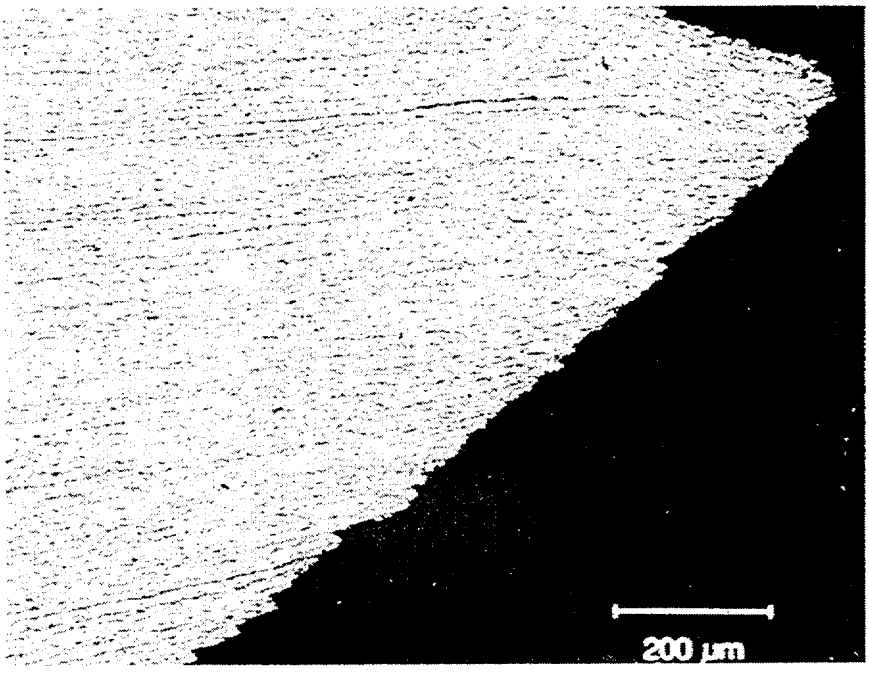

Figure 9.17 Relative absence of local shearing below the tear surface in the interior of Sample SCV-74-2 denotes the actual tear initiation site, 100×.

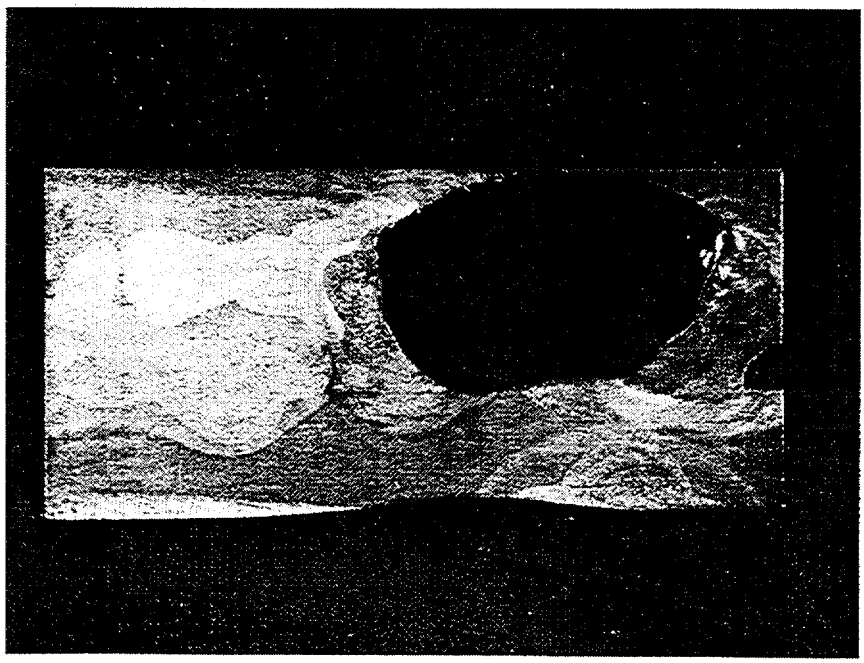

Figure 9.18 Microstructure of Sample SCV-21. The neck in the vessel wall was located at the left side of the bottom of the hole in this view.

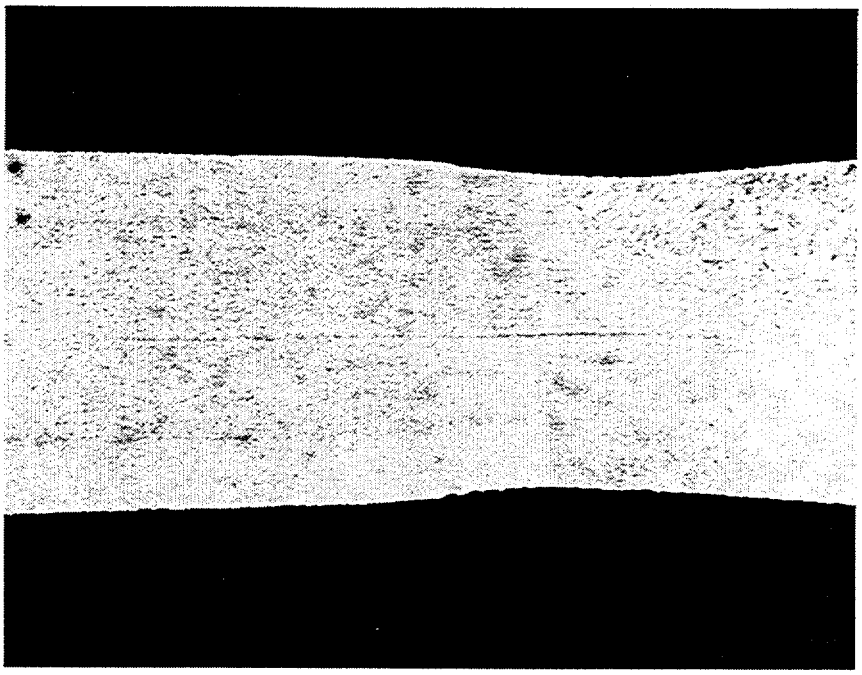

(a)

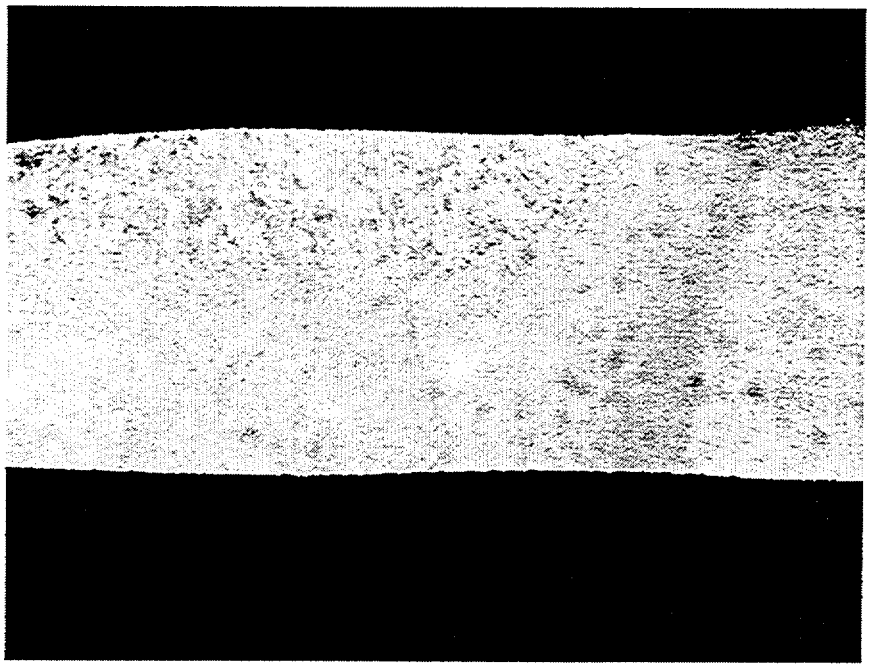

(b)

Figure 9.19 Cross-sectional microstructure of vertical weld at 340° location between plates of 9 mm SPV490 steel, Sample SCV-340: (a) plate material at left, necked HAZ at center, and weld fusion zone at right; (b) weld area to right of (a) showing, left to right, weld fusion zone, slightly necked HAZ, and 9 mm plate.

THIS PAGE INTENTIONALLY LEFT BLANK.

10. Summary and Conclusion

After about five years of preparation spent designing and fabricating the steel containment vessel (SCV) and the contact structure (CS), instrumenting the model, and developing the data acquisition and pressurization systems, the high pressure test on the model was conducted December 11–12, 1996 at Sandia National Laboratories. The high pressure test was terminated, after 16.5 hours of monotonic pressure loading, when the pressurization system with its maximum flow capacity could not maintain the pressure inside the model. The maximum achieved in the test was 4.66 MPa (676 psig) or 5.97 times the scaled design pressure.

Posttest inspection revealed that the leakage was caused by a large tear, approximately 190-mm-long, at a weld seam at the outside edge of the equipment hatch reinforcement plate. A small meridional tear, about 55-mm-long, was also discovered in a vertical weld inside a semi-circular weld relief opening at the middle stiffening ring above the equipment hatch. It is speculated that the small tear developed at a lower pressure than the large tear. Posttest analysis of the acoustic emission data partially supports this speculation. However, the propagation of the small tear was self-arrested, and the pressurization system was able to compensate for the leakage caused by it.

A unique feature of this project is the presence of the CS over the model. The CS, representing some functions of a surrounding shield building, provided an almost rigid structure with which the model made contact after the gap between the two structures was closed.

There was a large variety of instruments installed on the model and the CS, including rosette, strip and single element strain gages, displacement transducers, LVDTs, contact detection devices, pressure transducers, and thermocouples. More than 97% of these instruments survived the high pressure test. An extensive array of strain gages was installed around the equipment to capture it deformation response. Some gages, whose positions were very close to the large tear, recorded high strain concentrations and provided qualitative information used to infer the strain history at the large tear. Detailed posttest metallurgical evaluation was carried out to obtain definitive information on the tear initiation site and the failure mode and mechanisms. No gages were place near the small tear that was not predicted in the pretest analysis. All corrected test data are part of this report (Appendix F).

The posttest metallurgical evaluation produced critical information on the deformation pattern and the failure mode and mechanisms of the two tears and on the strain concentration in a few locally necked areas. Samples made from the sections removed from the model underwent different evaluation processes. Major metallurgical findings are summarized below:

- The large tear at the equipment hatch experienced strong local necking deformations that occurred in the weld heat affected region of the SPV490 alloy plate. Hardness measurements and metallographic analysis indicate that heat from the welding process of the model resulted in localized microstructural alteration and reduced hardness and strength of the SPV490 alloy plate.

- The small tear also occurred within the weld heat affected region of the SGV480 alloy plates.

- All material deformation and tear observed in the samples were ductile in nature. There was no evidence of material flaws, defects, or brittle behavior in the base metal or welds. The tears that occurred resulted from exceeding the local plastic ductility of the alloy.

11. References

Arai, S., T. Matsumoto, M. Goto, Y. Naruse, T. Mieda, and H. Yamanaha, "Pressurization Test on the Equipment Hatch Model," *Proceedings of the 14th International Conference on Structural Mechanics in Reactor Technology*, Vol. 5, pp. 9–16, Lyon, France, August 17–22, 1997.

ASM Metals Handbook, Desk Edition. 1998. 2nd ed., Materials Park, Ohio: ASM International, pp. 72–73, Table 8.

ASM Metals Handbook. 10th ed., pp. 389–423. 1990. "High Strength Structural and High Strength Low Alloy Steels," section "Acicular ferrite/low-carbon bainite steels," pp. 404–405.

Blejwas, T.E., A.W. Dennis, R.L. Woodfin, and W.A. Von Riesemann. *Background Study and Preliminary Plans for a Program on the Safety Margins of Containments.* NUREG/CR-2549, SAND82-0324. Albuquerque, NM: Sandia National Laboratories. May 1982.

Cherry, J. "Analysis of Containment Structures with Corrosion Damage," *Proceedings of the 24th Water Reactor Safety Information Meeting*, Vol. 1, pp. 333–352, Bethesda, Maryland, October 21–23, 1996.

Horschel, D.S., J.S. Ludwigsen, M.B. Parks, L.D. Lambert, R.A. Dameron, and Y.R. Rashid. *Insights into the Behavior of Nuclear Power Plant Containments during Severe Accidents.* SAND90-0119. Albuquerque, NM: Sandia National Laboratories, June 1993.

James, R.J., Y.R. Rashid, J. Cherry, N.C. Chokshi, S. Nakamura. "Analytical Prediction of the Seismic Response of a Prestressed Concrete Containment Vessel," *Proceedings of the 14th International Conference in Structural Mechanics in Reactor Technology*, Vol. 7, pp. 151–160, Lyon, France, August 17–22, 1997.

Lambert, L.D. and M.B. Parks. *Experimental Results from Containment Piping Bellows subjected to Severe Accident Conditions.* NUREG/CR-6154, SAND94-1711, Vol. 1. Albuquerque, NM: Sandia National Laboratories. September 1994.

Lobner, P., C. Donahoe, and C. Vavallin, *Overview and Comparison of U.S. Commercial Nuclear Power Plants.* NUREG/CR-5640, SAIC-89/1541. San Diego, CA: Science Application International Corporation, September 1990.

Ludwigsen, J.S., V.K. Luk, and M.F. Hessheimer. *Posttest Analysis of the Steel Containment Vessel Model.* NUREG/CR-6649, SAND99-2954. Albuquerque, NM: Sandia National Laboratories. December 1999.

Luk, V.K. and E.W. Klamerus. *Round Robin Pretest Analyses of a Steel Containment Vessel Model and Contact Structure Assembly Subject to Static Internal Pressurization.* NUREG/CR-6517, SAND96-2899. Albuquerque, NM: Sandia National Laboratories. November 1996.

Luk, V.K. and E.W. Klamerus. *Round Robin Posttest Analyses of a Steel Containment Vessel Model.* NUREG/CR-5678, SAND98-2700. Albuquerque, NM: Sandia National Laboratories. December 1998.

Luk, V.K., J.S. Ludwigsen, M.F. Hessheimer, T. Matsumoto, K. Komine, and J.F. Costello. "Results of Steel Containment Vessel Model Test," *Proceedings of 1998 ASME/JSME Joint Pressure Vessels and Piping Conference*, San Diego, California, July 26–30, 1998.

Matsumoto, T., K. Komine, S. Arai, V. K. Luk, M. F. Hessheimer, and J. F. Costello, "Preliminary Results of Steel containment Vessel Model," *Proceedings of the 14th International Conference in Structural Mechanics on Reactor Technology*, Vol. 5, pp. 81–87, Lyon, France, August 17–22, 1997.

Nakamura, S., Y. Sasaki, K. Horibe, M. Nakajima, K. Hoshino, T. Takahashi, T. Hagesawa, T. Kei, T. Meida, K. Takigushi, and H. Akiyama. "Plan of the Seismic Proving Test for Reinforced Concrete Containment Vessel: Test Plan and Test Model Design," *Proceedings of the 14th International Conference in Structural Mechanics on Reactor Technology*, Vol. 11, pp. 83–90, Lyon, France, August 17–22, 1997.

Parks, M.B., H.P. Walther, and L.D. Lambert. "Experiments to Determine the Leakage Behavior of Pressure-Unseating Equipment Hatches," *Proceedings of the 11th International Conference on Structural Mechanics in Reactor Technology*, Tokyo, Japan, August 1991.

Porter, V.L., P.A. Carter, and S.W. Key. *Pretest Analysis of the Steel Containment Vessel Model.* NUREG/CR-6516, SAND96-2877. Albuquerque, NM: Sandia National Laboratories. November 1996.

Takumi, K., A. Nonaka, K. Umeki, Y. Yoshida, O. Oyamada, H. Furakawa, K. Saito, J.F. Costello, W.A. von Riesemann, M.B. Parkes, and R.A. Watson, "Plan on Test to Failure of a Steel Containment Vessel Model," Proceedings of the 5th Workshop on Containment Integrity, NUPEC/CP-0120, SAND91-0173, Washington, DC, May 12–14, 1992.

Van Den Avyle, J.A. and K.H. Eckelmeyer. *Posttest Metallurgical Evaluation Results for SCV High Pressure Test.* SAND98-2702. Albuquerque, NM: Sandia National Laboratories. 1998.

Appendix A

Design Drawings of the Steel Containment Vessel (SCV) Model

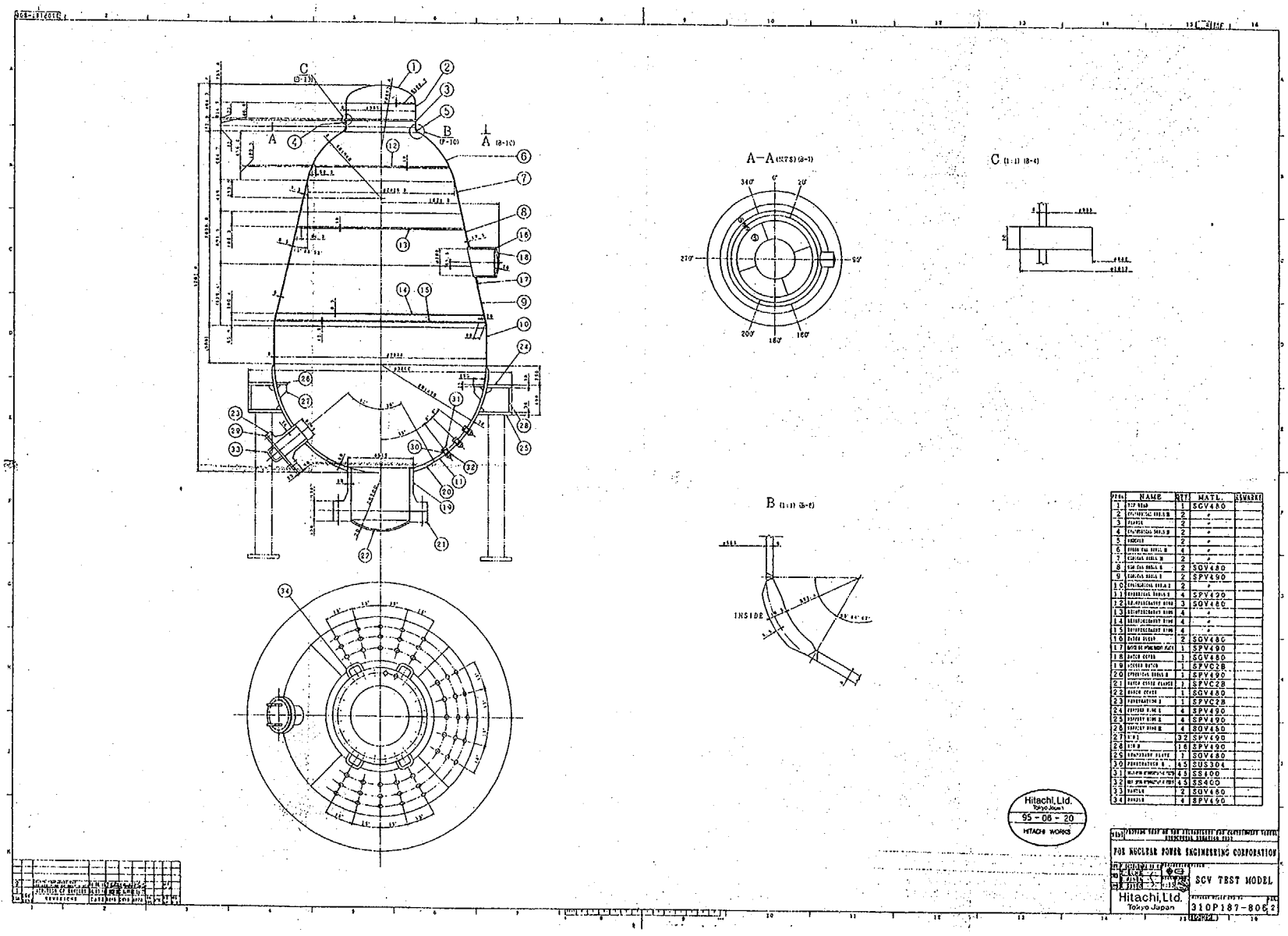

Figure A.1 Steel containment vessel (SCV) model – dimensional layout.

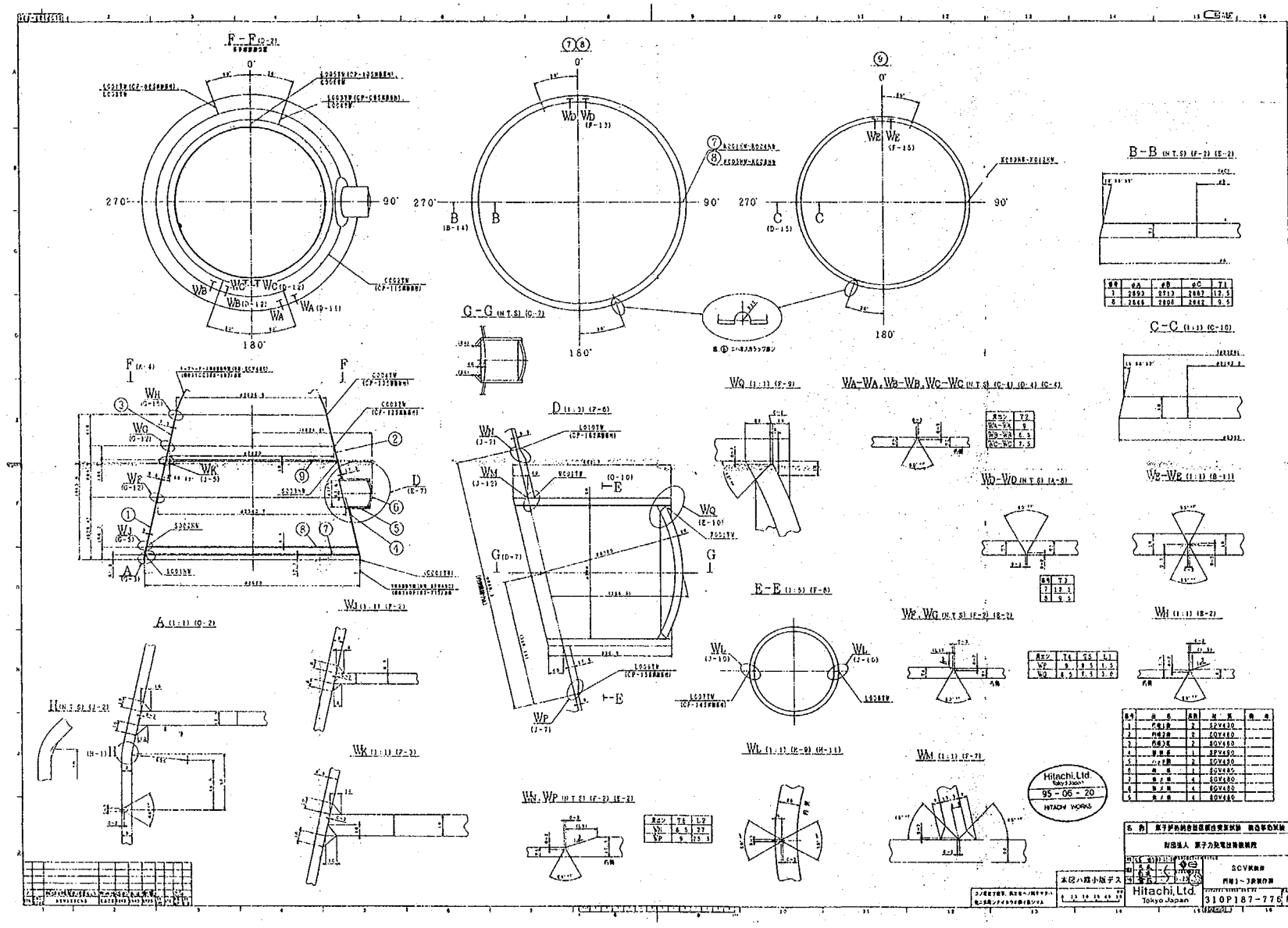

Figure A.2 Steel containment vessel (SCV) model -- middle section.

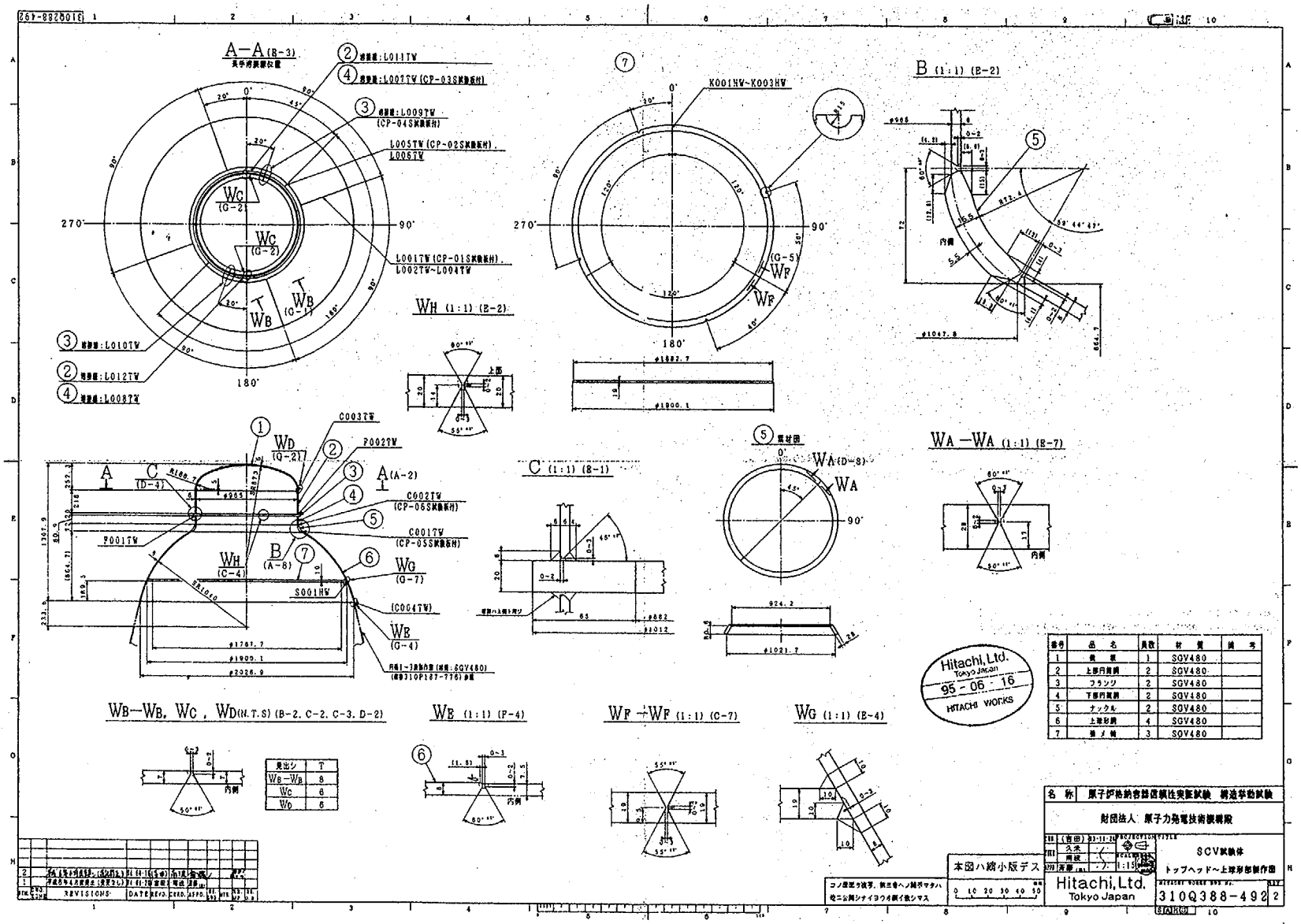

Figure A.3 Steel containment vessel (SCV) model – upper section.

Appendix B

Design Drawings of the Contact Structure (CS)

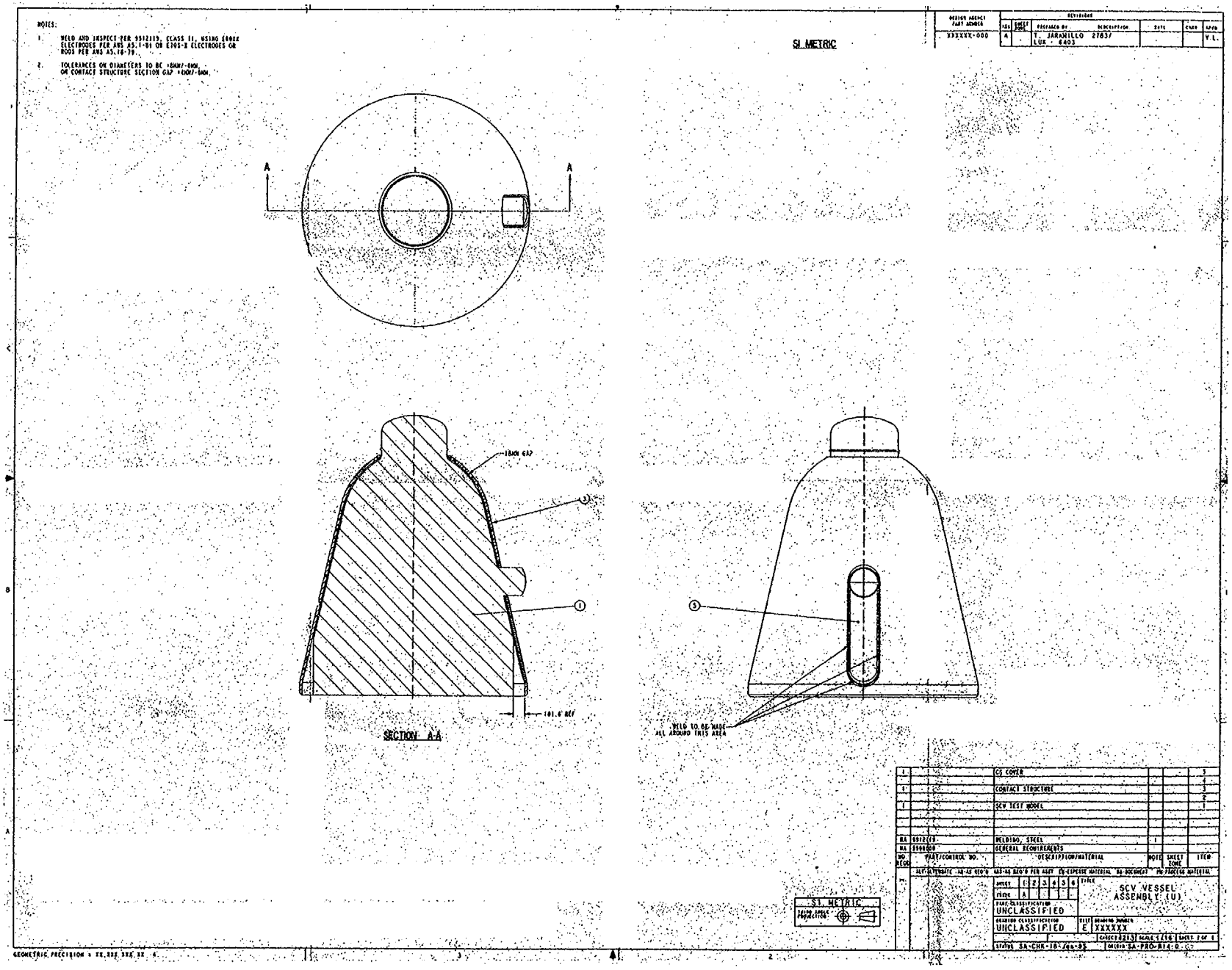

Figure B.1 Contact structure (CS) assembly.

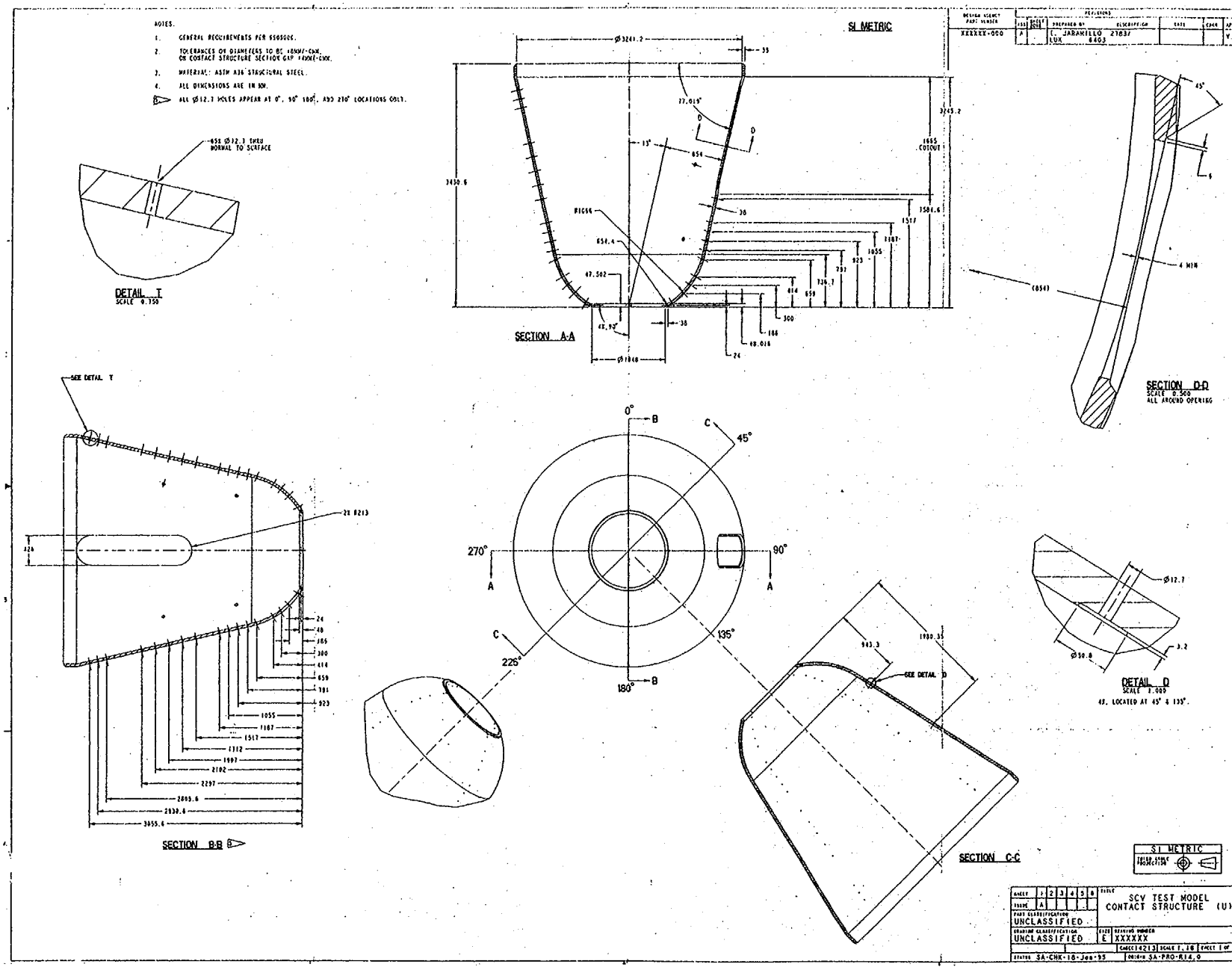

Figure B.2 Contact structure (CS) details.

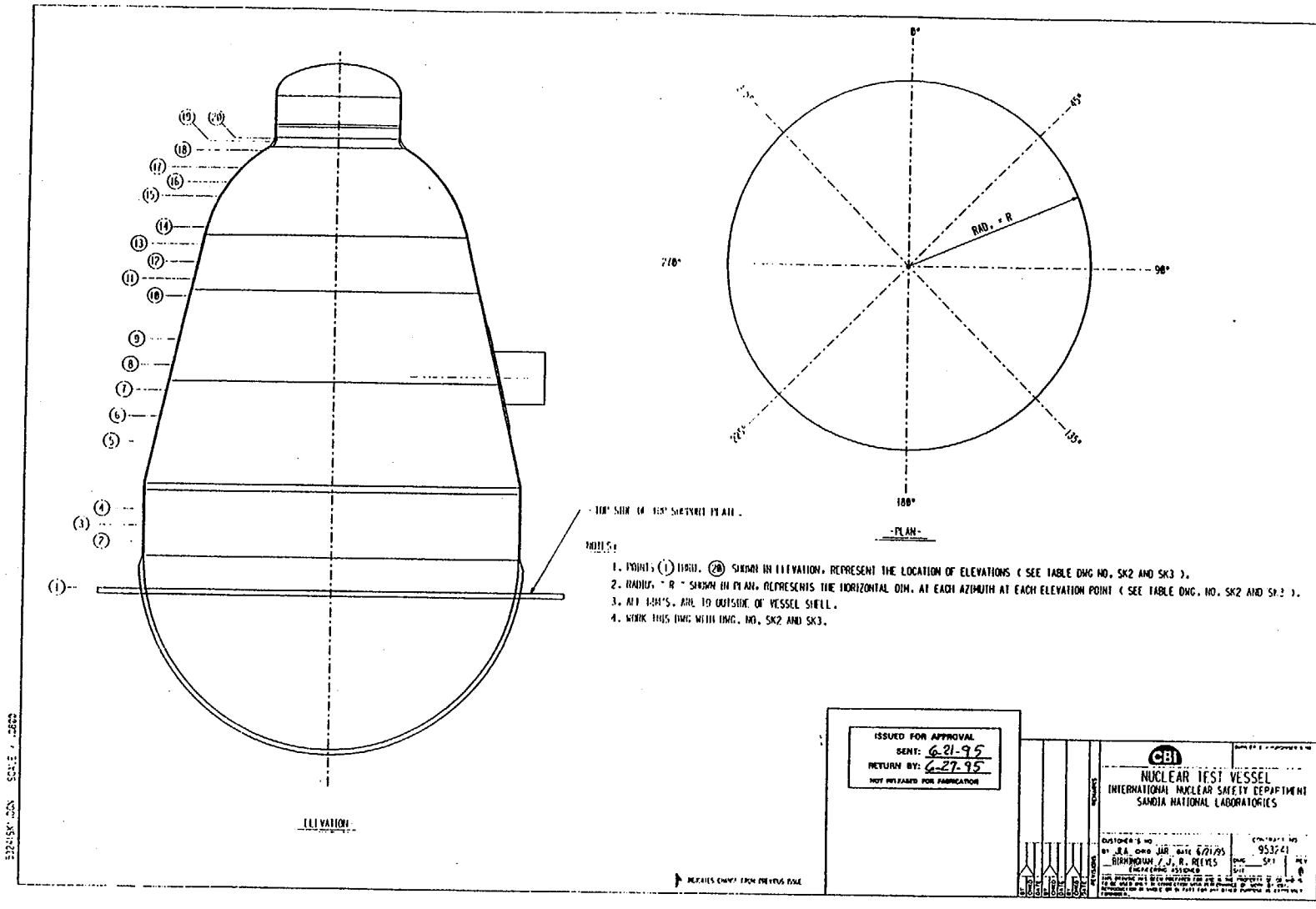

Figure B.3 Measurement locations on the as-built steel containment vessel (SCV) model.

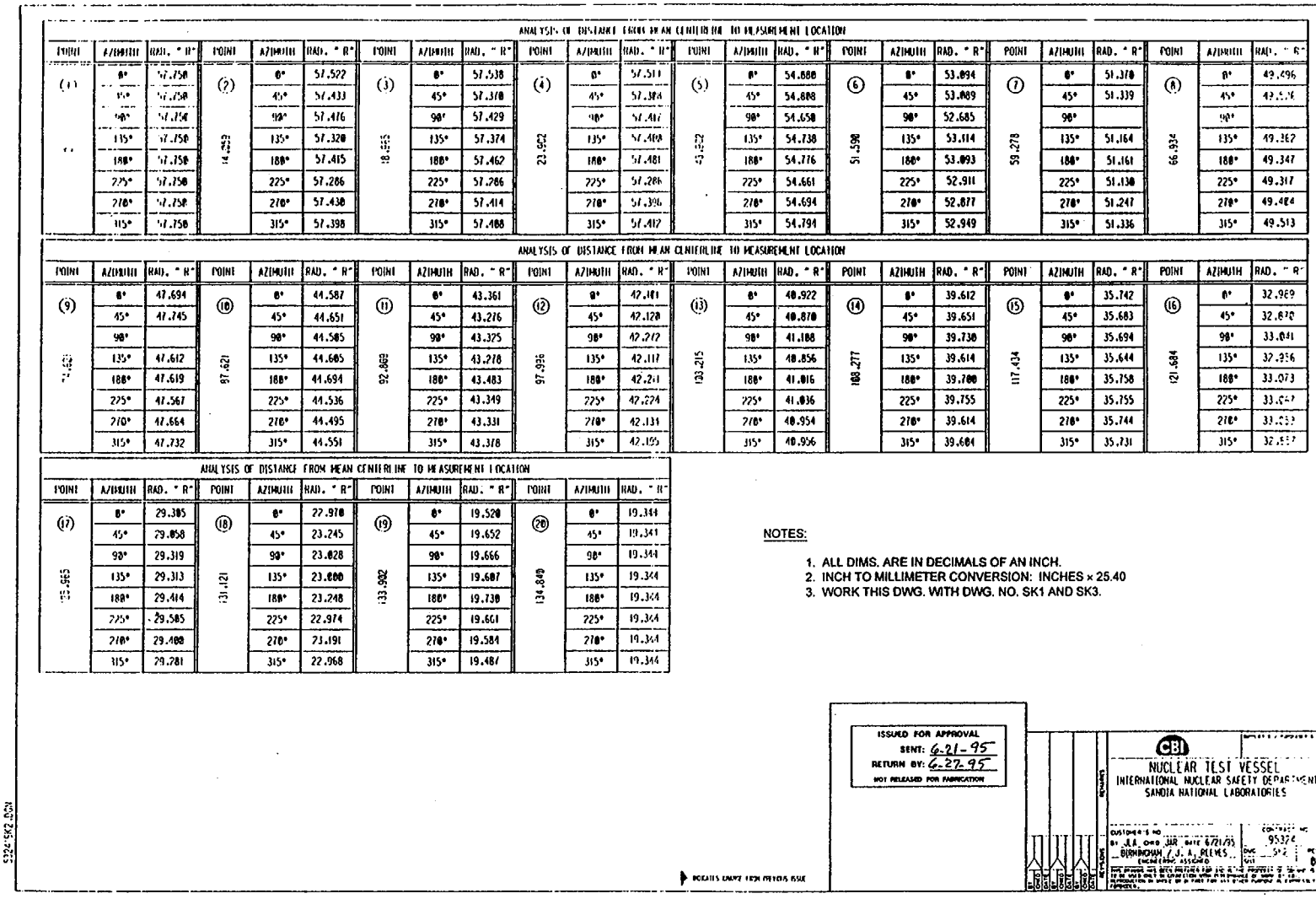

ANALYSIS OF DISTANCE FROM MEAN CENTERLINE TO MEASUREMENT LOCATION

POINT	AZIMUTH	RAD. " R"	POINT	AZIMUTH	RAD. " R"	POINT	AZIMUTH	RAD. " R"	POINT	AZIMUTH	RAD. " R"	POINT	AZIMUTH	RAD. " R"	POINT	AZIMUTH	RAD. " R"	POINT	AZIMUTH	RAD. " R"	POINT	AZIMUTH	RAD. " R"
(1)	0°	57.758	(2)	0°	57.522	(3)	0°	57.538	(4)	0°	57.511	(5)	0°	54.888	(6)	0°	53.894	(7)	0°	51.378	(8)	0°	49.496
	45°	57.758		45°	57.433		45°	57.378		45°	57.384		45°	54.808		45°	53.089		45°	51.339		45°	49.536
	90°	57.758		90°	57.476		90°	57.429		90°	57.417		90°	54.658		90°	52.685		90°			90°	
	135°	57.758		135°	57.320		135°	57.374		135°	57.408		135°	54.738		135°	53.114		135°	51.164		135°	49.362
	180°	57.758		180°	57.415		180°	57.462		180°	57.481		180°	54.776		180°	53.093		180°	51.161		180°	49.347
	225°	57.758		225°	57.286		225°	57.286		225°	57.286		225°	54.661		225°	52.911		225°	51.130		225°	49.317
	270°	57.758		270°	57.438		270°	57.414		270°	57.396		270°	54.694		270°	52.877		270°	51.247		270°	49.484
	315°	57.758		315°	57.398		315°	57.488		315°	57.417		315°	54.794		315°	52.949		315°	51.336		315°	49.513
		14.453						18.555			23.952			43.522			51.598			59.278			66.934

ANALYSIS OF DISTANCE FROM MEAN CENTERLINE TO MEASUREMENT LOCATION

POINT	AZIMUTH	RAD. " R"	POINT	AZIMUTH	RAD. " R"	POINT	AZIMUTH	RAD. " R"	POINT	AZIMUTH	RAD. " R"	POINT	AZIMUTH	RAD. " R"	POINT	AZIMUTH	RAD. " R"	POINT	AZIMUTH	RAD. " R"	POINT	AZIMUTH	RAD. " R"
(9)	0°	47.694	(10)	0°	44.587	(11)	0°	43.361	(12)	0°	42.181	(13)	0°	40.922	(14)	0°	39.612	(15)	0°	35.742	(16)	0°	32.969
	45°	47.745		45°	44.651		45°	43.276		45°	42.128		45°	40.870		45°	39.651		45°	35.683		45°	32.870
	90°			90°	44.585		90°	43.325		90°	42.272		90°	41.188		90°	39.738		90°	35.694		90°	33.041
	135°	47.612		135°	44.605		135°	43.278		135°	42.117		135°	40.856		135°	39.614		135°	35.644		135°	32.956
	180°	47.619		180°	44.694		180°	43.483		180°	42.241		180°	41.016		180°	39.700		180°	35.758		180°	33.073
	225°	47.567		225°	44.536		225°	43.349		225°	42.224		225°	41.036		225°	39.755		225°	35.755		225°	33.047
	270°	47.664		270°	44.495		270°	43.331		270°	42.131		270°	40.954		270°	39.614		270°	35.744		270°	33.059
	315°	47.732		315°	44.551		315°	43.378		315°	42.195		315°	40.956		315°	39.684		315°	35.731		315°	32.557
					87.621			92.869			97.956			103.215			108.277			117.434			121.684

ANALYSIS OF DISTANCE FROM MEAN CENTERLINE TO MEASUREMENT LOCATION

POINT	AZIMUTH	RAD. " R"	POINT	AZIMUTH	RAD. " R"	POINT	AZIMUTH	RAD. " R"	POINT	AZIMUTH	RAD. " R"
(17)	0°	29.385	(18)	0°	27.978	(19)	0°	19.520	(20)	0°	19.344
	45°	29.058		45°	23.245		45°	19.652		45°	19.341
	90°	29.319		90°	23.028		90°	19.666		90°	19.344
	135°	29.313		135°	23.000		135°	19.607		135°	19.344
	180°	29.414		180°	23.248		180°	19.738		180°	19.344
	225°	29.585		225°	22.974		225°	19.661		225°	19.344
	270°	29.488		270°	23.191		270°	19.584		270°	19.344
	315°	29.281		315°	22.968		315°	19.487		315°	19.344
		125.965			131.421			133.982			134.849

NOTES:

1. ALL DIMS. ARE IN DECIMALS OF AN INCH.
2. INCH TO MILLIMETER CONVERSION: INCHES × 25.40
3. WORK THIS DWG. WITH DWG. NO. SK1 AND SK3.

ISSUED FOR APPROVAL
SENT: 6-21-95
RETURN BY: 6-27-95
NOT RELEASED FOR FABRICATION

CBI
NUCLEAR TEST VESSEL
INTERNATIONAL NUCLEAR SAFETY DEPARTMENT
SANDIA NATIONAL LABORATORIES

DRAWN BY J.R. CHECKED JHR DATE 6/21/95
BIRMINGHAM / J. A. REEVES
ENGINEERING ASSOCIATES

CONTRACT NO. 95374
DWG. SK2
REV. 0

5324-SK2.DGN

Figure B.4 Measurement data on the as-built steel containment vessel (SCV) model.

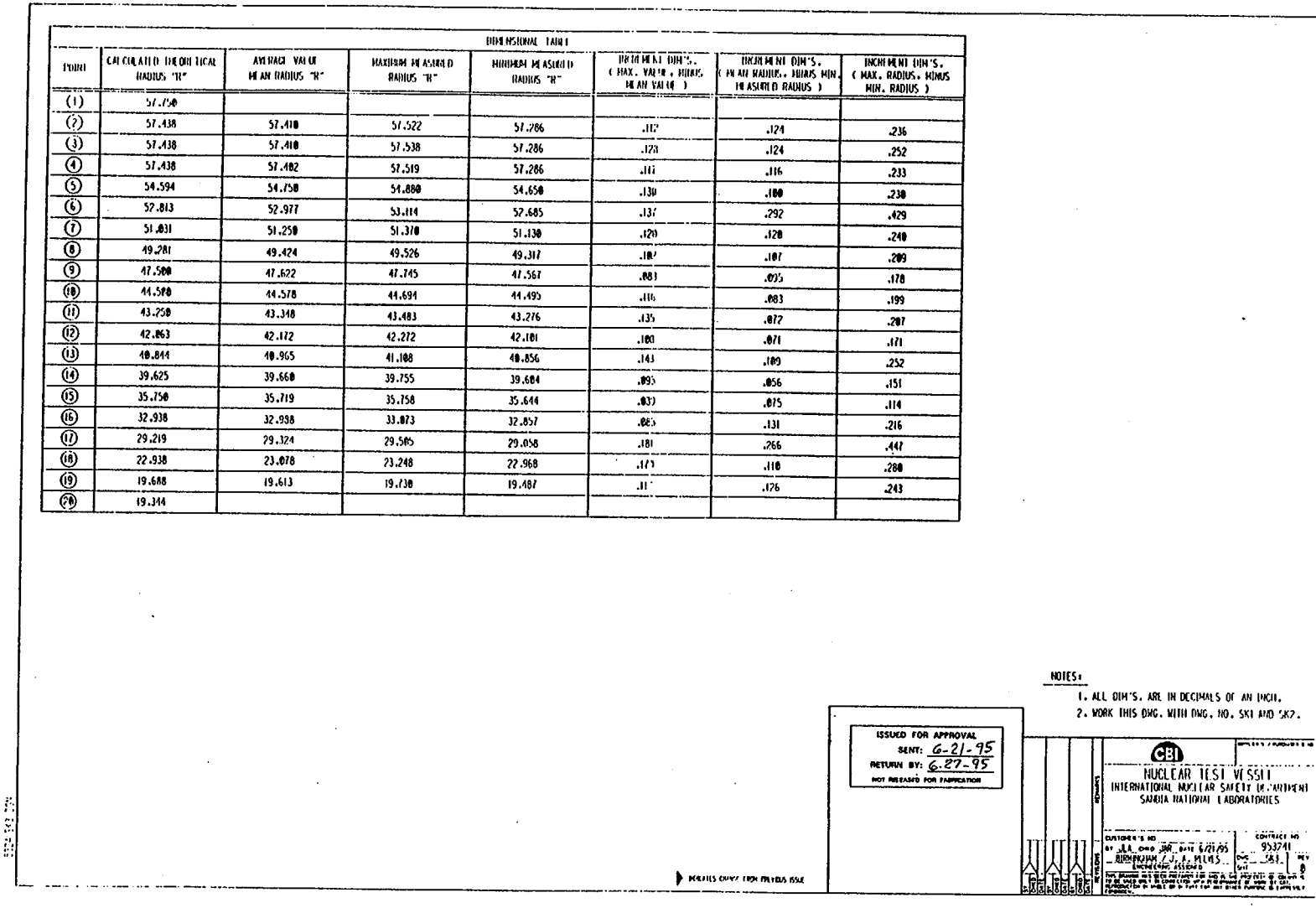

DIMENSIONAL TABLE

POINT	CALCULATED THEORETICAL RADIUS "R"	AVERAGE VALUE MEAN RADIUS "R"	MAXIMUM MEASURED RADIUS "R"	MINIMUM MEASURED RADIUS "R"	INCREMENT DIM'S. (MAX. VALUE , MINUS MEAN VALUE)	INCREMENT DIM'S. (MEAN RADIUS , MINUS MINIMUM MEASURED RADIUS)	INCREMENT DIM'S. (MAX. RADIUS, MINUS MIN. RADIUS)
(1)	57.750						
(2)	57.438	57.410	57.522	57.286	.112	.124	.236
(3)	57.438	57.410	57.538	57.286	.128	.124	.252
(4)	57.438	57.402	57.519	57.286	.117	.116	.233
(5)	54.594	54.758	54.880	54.650	.130	.108	.230
(6)	52.813	52.977	53.114	52.685	.137	.292	.429
(7)	51.031	51.250	51.370	51.130	.120	.120	.240
(8)	49.281	49.424	49.526	49.317	.102	.107	.209
(9)	47.500	47.622	47.745	47.567	.083	.055	.178
(10)	44.598	44.578	44.694	44.495	.116	.083	.199
(11)	43.250	43.348	43.483	43.276	.135	.072	.207
(12)	42.863	42.172	42.272	42.101	.100	.071	.171
(13)	40.844	40.965	41.108	40.856	.143	.109	.252
(14)	39.625	39.660	39.755	39.604	.095	.056	.151
(15)	35.750	35.719	35.758	35.644	.039	.075	.114
(16)	32.938	32.938	33.073	32.857	.085	.131	.216
(17)	29.219	29.324	29.505	29.058	.181	.266	.447
(18)	22.938	23.078	23.248	22.968	.171	.110	.280
(19)	19.688	19.613	19.730	19.487	.117	.126	.243
(20)	19.344						

NOTES:
1. ALL DIM'S. ARE IN DECIMALS OF AN INCH.
2. WORK THIS DWG. WITH DWG. NO. SK1 AND SK2.

ISSUED FOR APPROVAL
SENT: 6-21-95
RETURN BY: 6-27-95
NOT RELEASED FOR FABRICATION

CBI
NUCLEAR TEST VESSEL
INTERNATIONAL NUCLEAR SAFETY PROGRAM
SANDIA NATIONAL LABORATORIES

CONTRACT NO 953741
DWG SK1

Figure B.5 Reduction of measurement data on the as-built steel containment vessel (SCV) model.

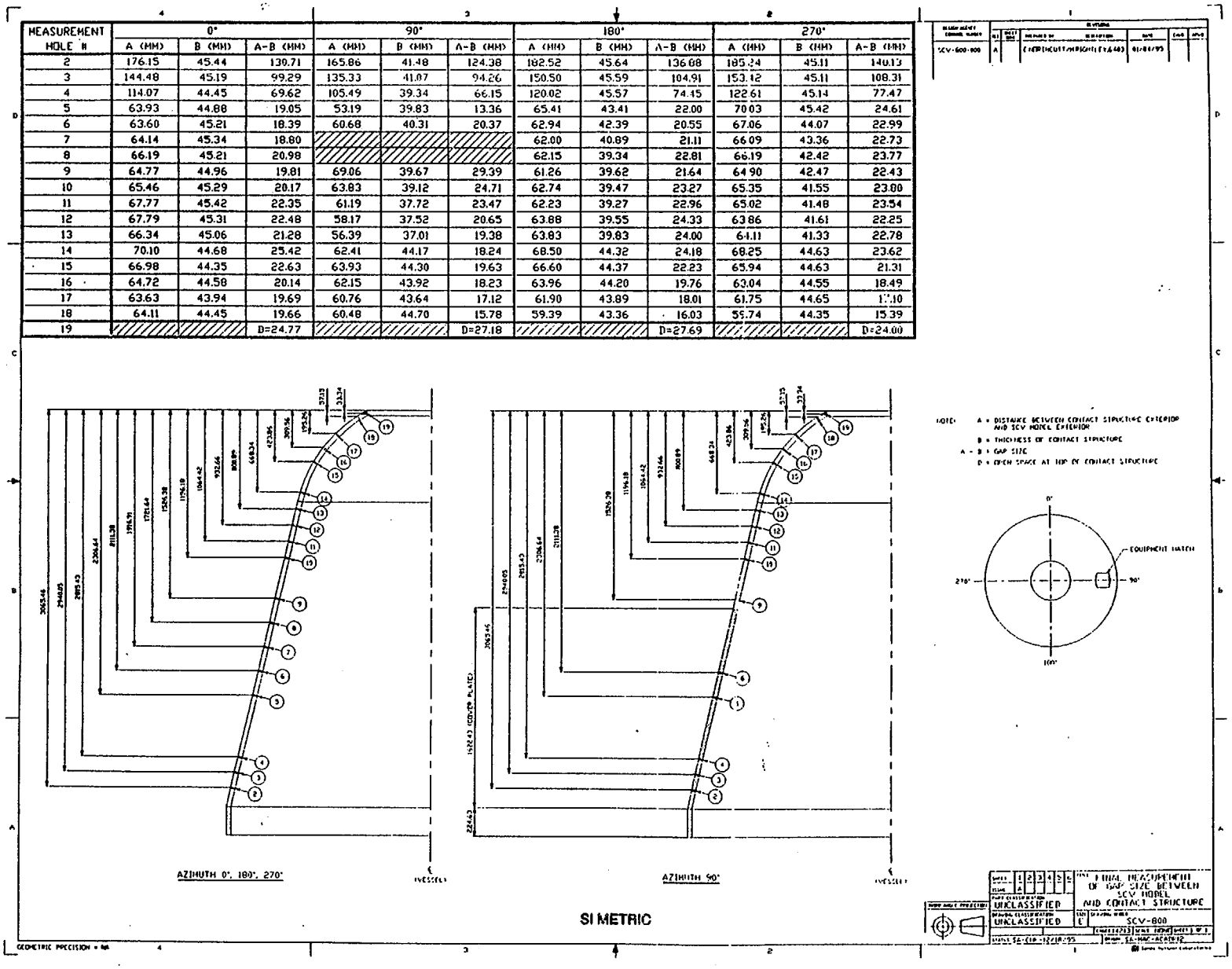

MEASUREMENT HOLE #	0°			90°			180°			270°		
	A (MM)	B (MM)	A-B (MM)	A (MM)	B (MM)	A-B (MM)	A (MM)	B (MM)	A-B (MM)	A (MM)	B (MM)	A-B (MM)
2	176.15	45.44	130.71	165.86	41.48	124.38	182.52	45.64	136.88	185.24	45.11	140.13
3	144.48	45.19	99.29	135.33	41.07	94.26	150.50	45.59	104.91	153.12	45.11	108.31
4	114.07	44.45	69.62	105.49	39.34	66.15	120.02	45.57	74.45	122.61	45.14	77.47
5	63.93	44.88	19.05	53.19	39.83	13.36	65.41	43.41	22.00	70.03	45.42	24.61
6	63.60	45.21	18.39	60.68	40.31	20.37	62.94	42.39	20.55	67.06	44.07	22.99
7	64.14	45.34	18.80				62.00	40.89	21.11	66.09	43.36	22.73
8	66.19	45.21	20.98				62.15	39.34	22.81	66.19	42.42	23.77
9	64.77	44.96	19.81	69.06	39.67	29.39	61.26	39.62	21.64	64.90	42.47	22.43
10	65.46	45.29	20.17	63.83	39.12	24.71	62.74	39.47	23.27	65.35	41.55	23.80
11	67.77	45.42	22.35	61.19	37.72	23.47	62.23	39.27	22.96	65.02	41.48	23.54
12	67.79	45.31	22.48	58.17	37.52	20.65	63.88	39.55	24.33	63.86	41.61	22.25
13	66.34	45.06	21.28	56.39	37.01	19.38	63.83	39.83	24.00	64.11	41.33	22.78
14	70.10	44.68	25.42	62.41	44.17	18.24	68.50	44.32	24.18	68.25	44.63	23.62
15	66.98	44.35	22.63	63.93	44.30	19.63	66.60	44.37	22.23	65.94	44.63	21.31
16	64.72	44.58	20.14	62.15	43.92	18.23	63.96	44.20	19.76	63.04	44.55	18.49
17	63.63	43.94	19.69	60.76	43.64	17.12	61.90	43.89	18.01	61.75	44.65	17.10
18	64.11	44.45	19.66	60.48	44.70	15.78	59.39	43.36	16.03	59.74	44.35	15.39
19			D=24.77			D=27.18			D=27.69			D=24.00

Figure B.6 Final measurement of gap size between steel containment vessel (SCV) model and contact structure (CS).

Appendix C

Uniaxial Tensile Test Data of SGV480 and SPV490 Steels

Table 1. Dimensions of Test Specimens

D (mm)	L (mm)	R (mm)	P (mm)
~14	50	15	60
~10	35	12	50
~6	21	10	35
~4	14	6	24
~3	11	4	20

L: Gage Length

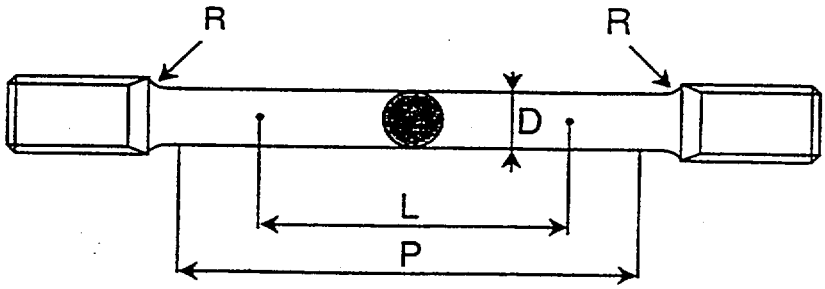

TRI-5403-012-0

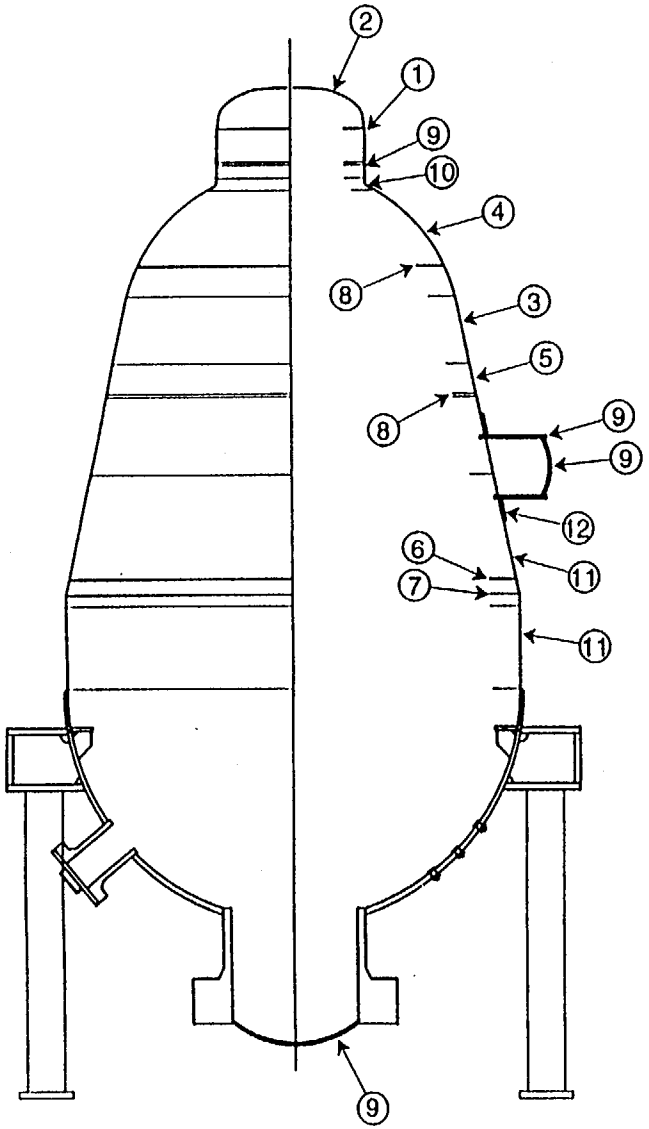

TRI-6403-013-0

Table 2. Outline of SCV Material Tests

Location	Material	Thickness (mm)	Table Number	Direction	Specimen Number
1 Top Head Shell	SGV480	6	4	Roll Rectangular	R1, R2 T1, T2
2 Top Head	SGV480	6	5	Roll Rectangular	R3, R4 T3, T4
3 Conical Shell 3	SGV480	7.5	6	Roll Rectangular	R5, R6 T5, T6
4 Spherical Shell	SGV480	8	7	Roll Rectangular	R7, R8 T7, T8
5 Conical Shell 2	SGV480	8.5	8	Roll Rectangular	R9, R10 T9, T10
6 Reinforcement Ring	SGV480	9.5	9	Roll Rectangular	R11, R12 T11, T12
7 Reinforcement Ring	SGV480	12.5	10	Roll Rectangular	R13, R14 T13, T14
8 Reinforcement Ring	SGV480	19	11	Roll Rectangular	R15, R6 T15, T6
9 Flange, Hatch Cover Hatch SLeeve	SGV480	20	12	Roll Rectangular	R17, R18 T17, T18
10 Knuckle	SGV480	28	13	Roll Rectangular	R19, R20 T19, T20
11 Cylindrical Shell Conical Shell	SPV490	9	14	Roll Rectangular	R21, R22 T21, T22
12 Hatch Reinforcement Plate	SPV490	17.5	15	Roll Rectangular	R23, R24 T23, T24

Table 3. Failure Results of Tensile Test

Location	Specimen #	Gage Length L (mm)	Elongation Lf (mm)	Elongation (%)	Initial Diameter D (mm)	Final Diameter Df (mm)	Reduction of Area (%)
1	R1	11.0	15.18	38.0	3.01	1.34	80.2
	R2	11.0	15.23	38.5	3.01	1.47	76.1
	T1	11.0	15.49	40.8	3.01	1.33	80.5
	T2	11.0	15.34	39.5	3.01	1.33	80.5
2	R3	11.0	15.17	37.9	3.01	1.50	75.2
	R4	11.0	15.20	38.2	3.02	1.51	75.0
	T3	11.0	14.78	34.4	3.00	1.52	74.3
	T4	11.0	15.03	36.6	3.00	1.54	73.6
3	R5	11.0	15.22	38.4	3.00	1.36	79.4
	R6	11.0	15.33	39.4	3.01	1.36	79.6
	T5	11.0	15.39	39.9	2.99	1.41	77.8
	T6	11.0	15.24	38.5	2.99	1.36	79.3
4	R7	14.0	19.61	40.1	4.02	1.92	77.2
	R8	14.0	19.02	35.9	4.02	1.99	75.5
	T7	14.0	19.20	37.1	4.01	2.02	74.6
	T8	14.0	19.38	38.4	4.02	2.07	73.5
5	R9	14.0	19.48	39.1	4.01	1.94	76.6
	R10	14.0	19.99	42.8	4.03	1.94	76.8
	T9	14.0	19.27	37.6	4.03	2.10	72.8
	T10	14.0	19.08	36.3	4.00	2.08	73.0
6	R11	14.0	19.64	40.3	4.02	1.80	80.0
	R12	14.0	19.73	40.9	4.00	1.82	79.3
	T11	14.0	19.40	38.6	4.01	2.08	73.1
	T12	14.0	19.22	37.3	4.02	1.99	75.5
7	R13	21.0	28.53	35.9	6.01	2.90	76.7
	R14	21.0	28.64	36.4	6.01	2.91	76.6
	T13	21.0	28.79	37.1	6.02	3.01	75.0
	T14	21.0	28.72	36.8	6.00	2.98	75.3
8	R15	35.0	49.33	40.9	10.00	5.16	73.4
	R16	35.0	48.83	39.5	10.01	5.09	74.1
	T15	35.0	49.00	40.0	10.01	5.15	73.5
	T16	35.0	49.37	41.1	10.00	5.12	73.8
9	R17	35.0	49.43	41.2	10.01	5.07	74.3
	R18	35.0	48.82	39.5	10.00	5.11	73.9
	T17	35.0	48.21	37.7	10.02	5.38	71.2
	T18	35.0	49.16	40.5	10.03	5.34	71.7
10	R19	50.0	69.26	38.5	14.01	7.38	72.3
	R20	50.0	70.22	40.4	14.01	7.28	73.0
	T19	50.0	68.78	37.6	14.00	7.54	71.0
	T20	50.0	68.76	37.5	14.01	7.57	70.8
11	R21	14.0	18.17	29.8	4.02	1.63	83.6
	R22	14.0	18.21	30.1	4.02	1.67	82.7
	T21	14.0	18.04	28.9	4.02	1.52	85.7
	T22	14.0	17.90	27.9	4.01	1.64	83.3
12	R23	35.0	45.50	30.0	10.01	4.36	81.0
	R24	35.0	45.48	29.9	10.01	4.42	80.5
	T23	35.0	45.64	30.4	10.01	4.48	80.0
	T24	35.0	45.71	30.6	10.01	4.42	80.5

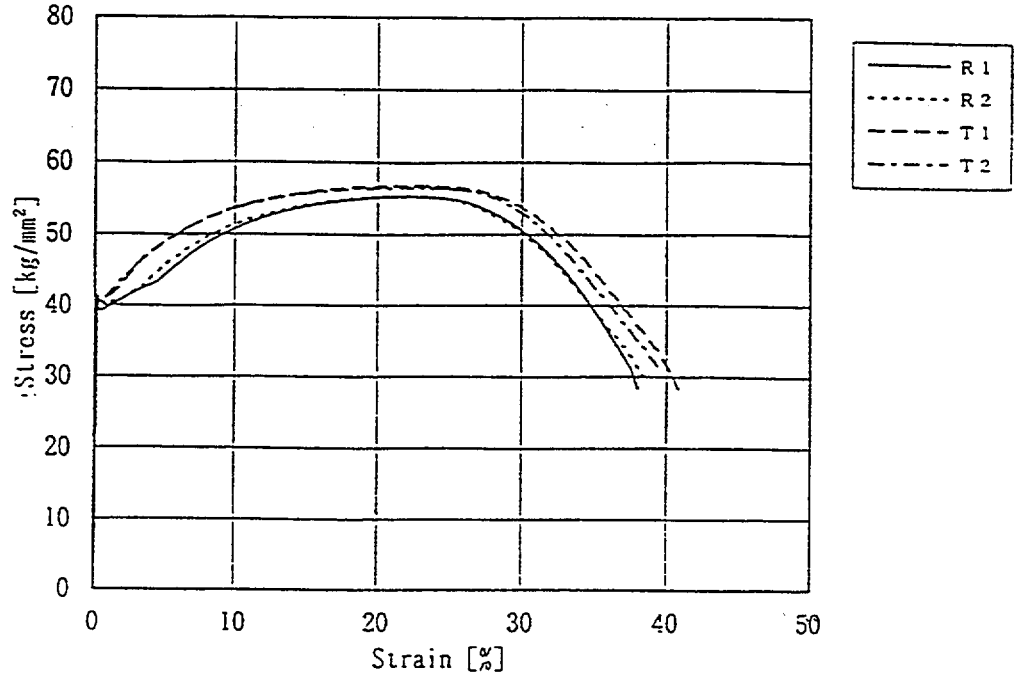

Figure C.1. Stress-strain curves for SGV480: thickness 6.0 mm plate, location 1.

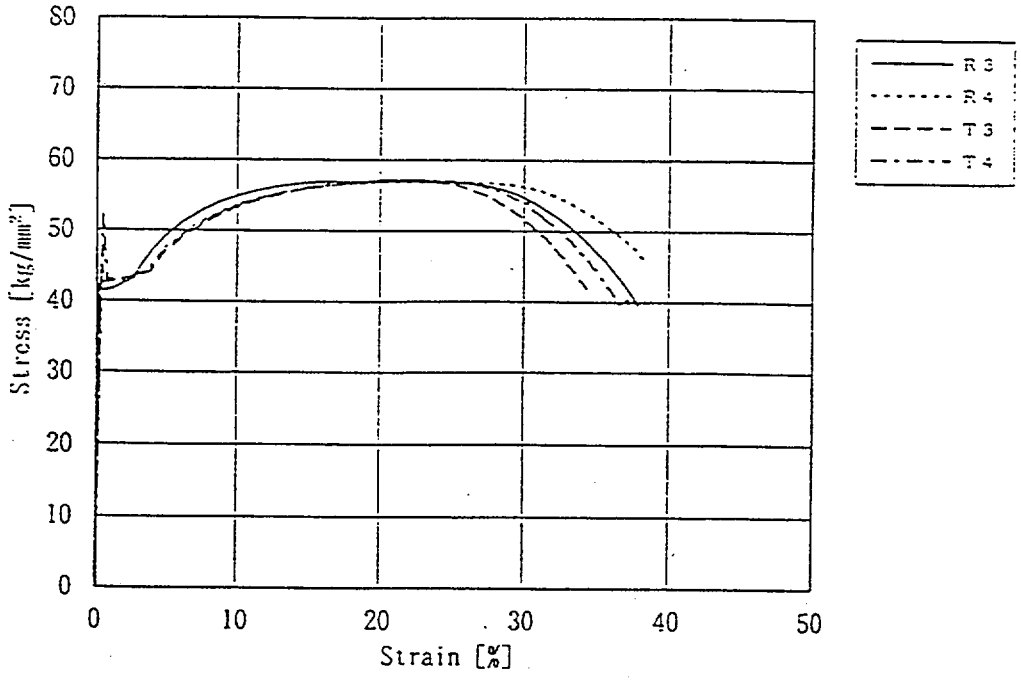

Figure C.2. Stress-strain curves for SGV480: thickness 6.0 mm plate, location 2.

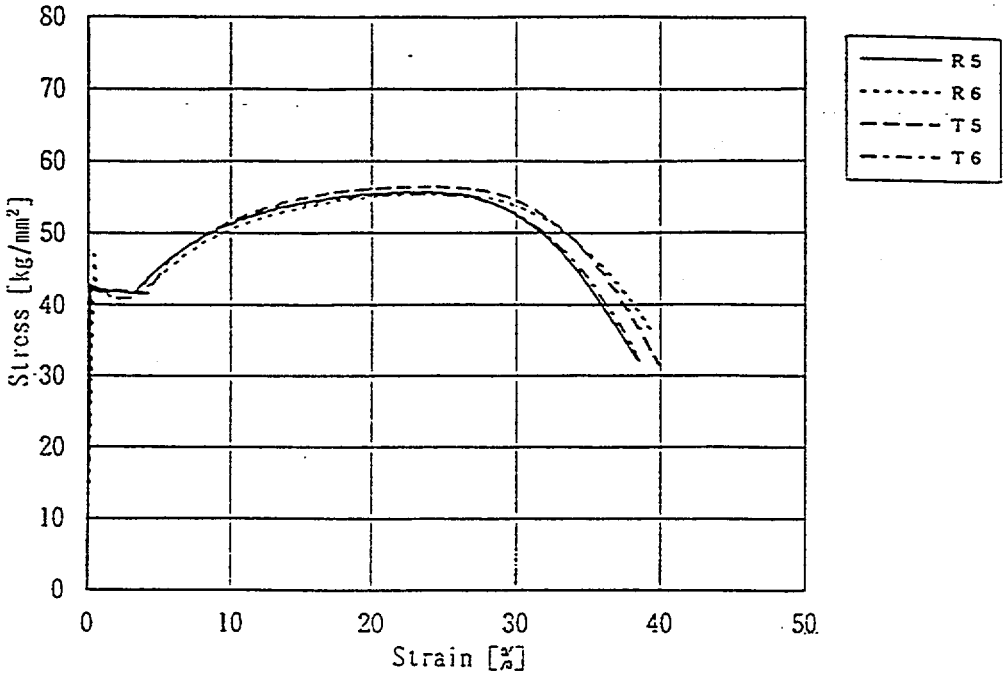

Figure C.3. Stress-strain curves for SGV480: thickness 7.5 mm plate, location 3.

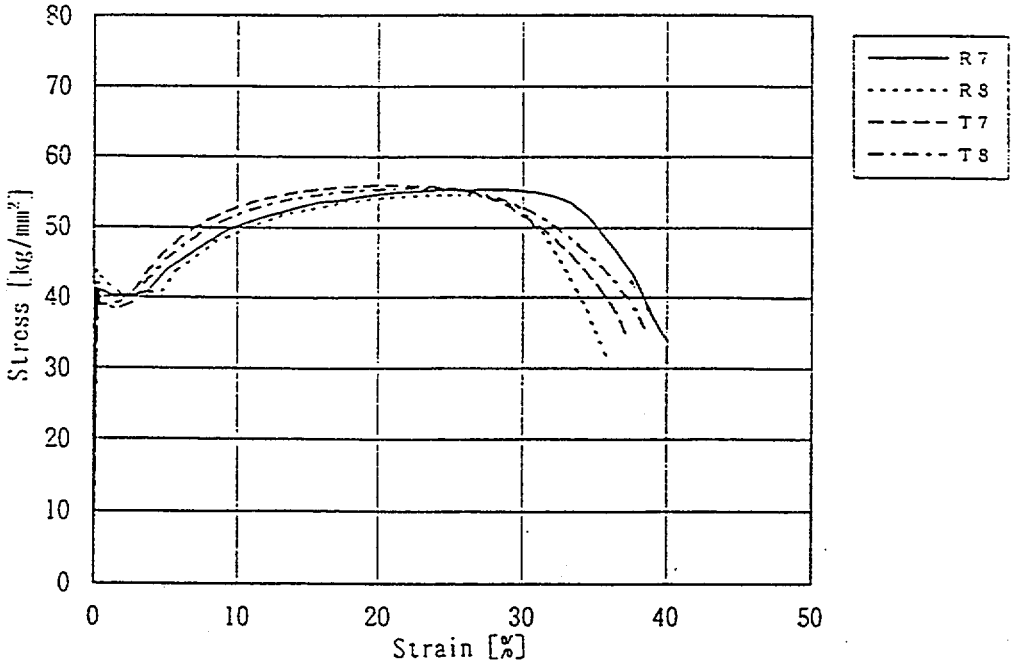

Figure C.4. Stress-strain curves for SGV480: thickness 8.0 mm plate, location 4.

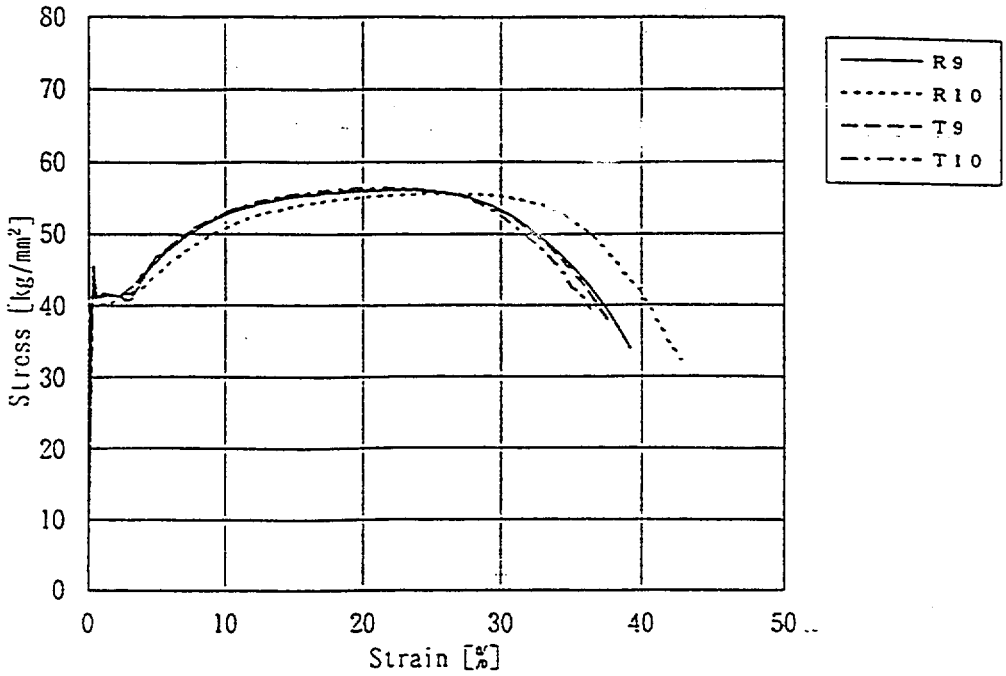

Figure C.5. Stress-strain curves for SGV480: thickness 8.5 mm plate, location 5.

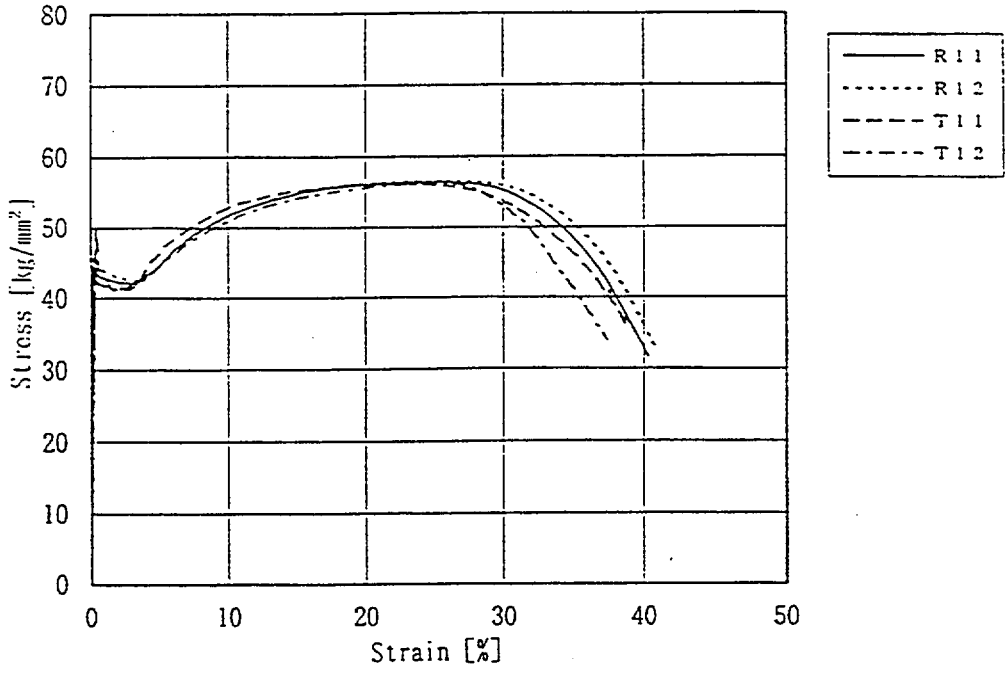

Figure C.6. Stress-strain curves for SGV480: thickness 9.5 mm plate, location 6.

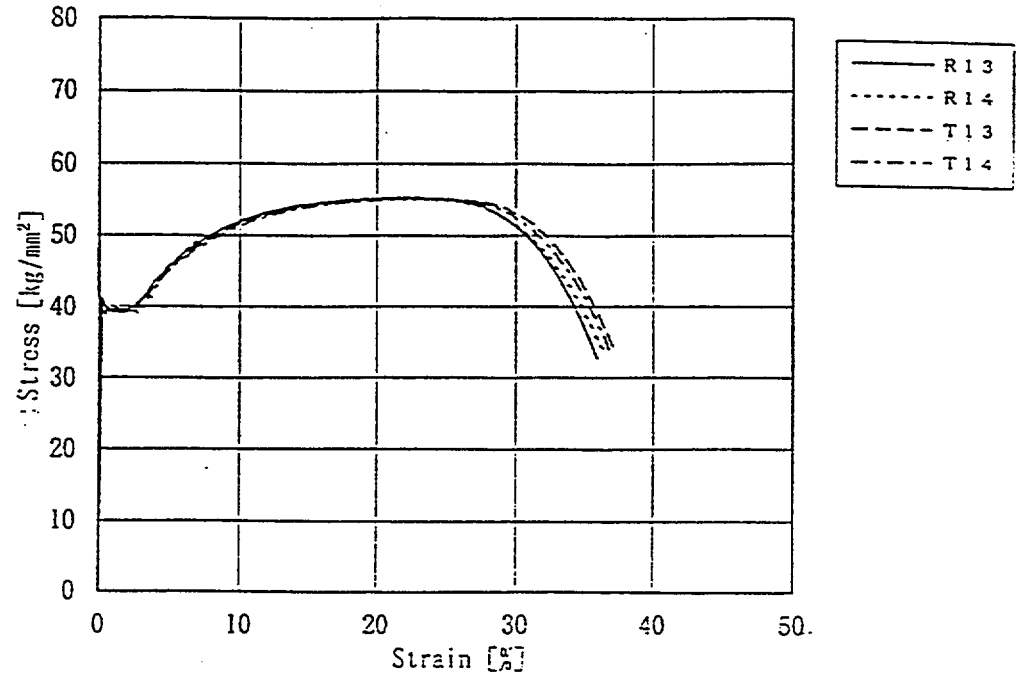

Figure C.7. Stress-strain curves for SGV480: thickness 12.5 mm plate, location 7.

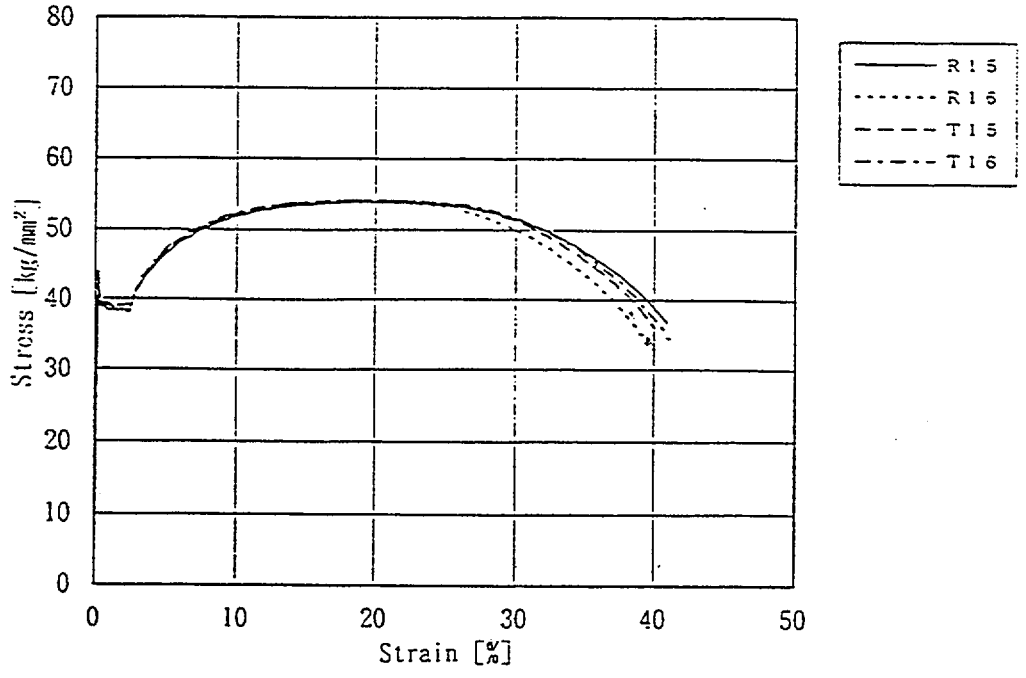

Figure C.8. Stress-strain curves for SGV480: thickness 19.0 mm plate, location 8.

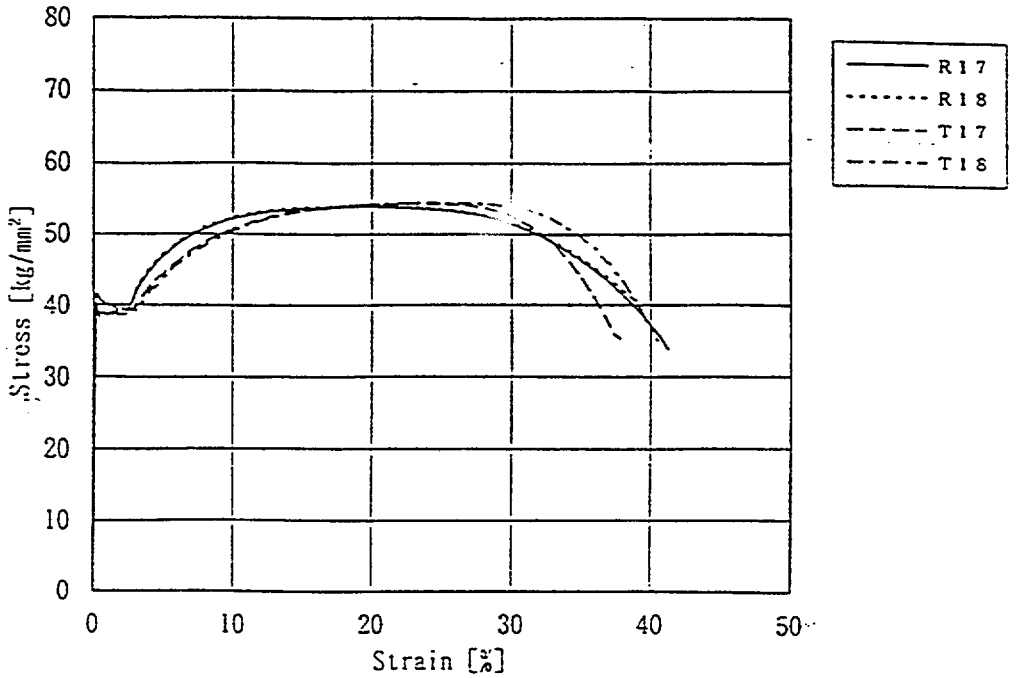

Figure C.9. Stress-strain curves for SGV480: thickness 20.0 mm plate, location 9.

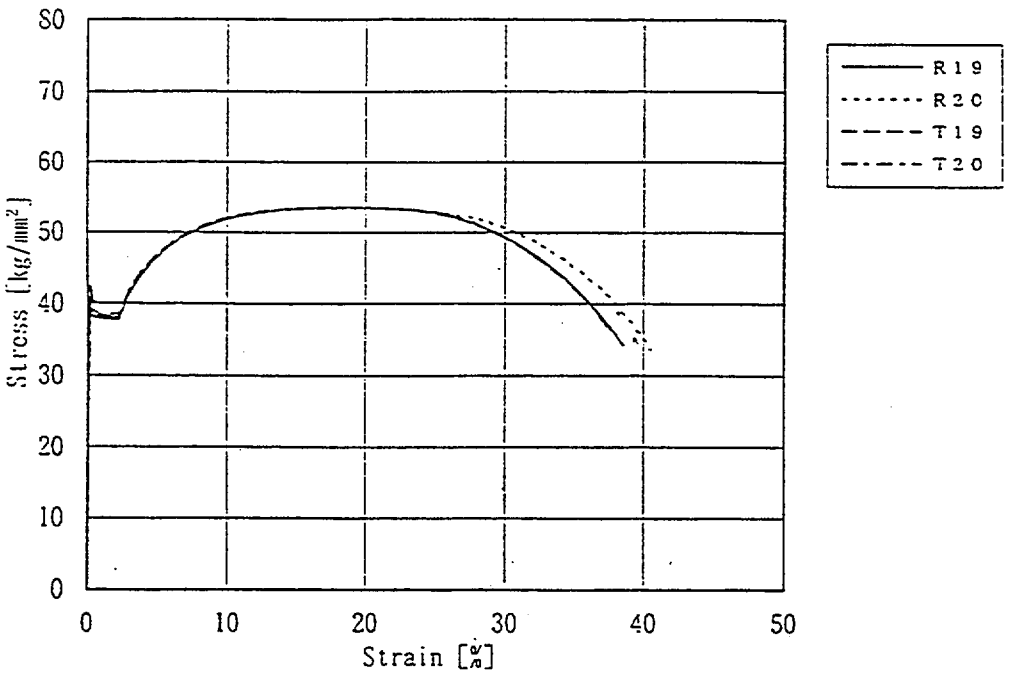

Figure C.10. Stress-strain curves for SGV480: thickness 28.0 mm plate, location 10.

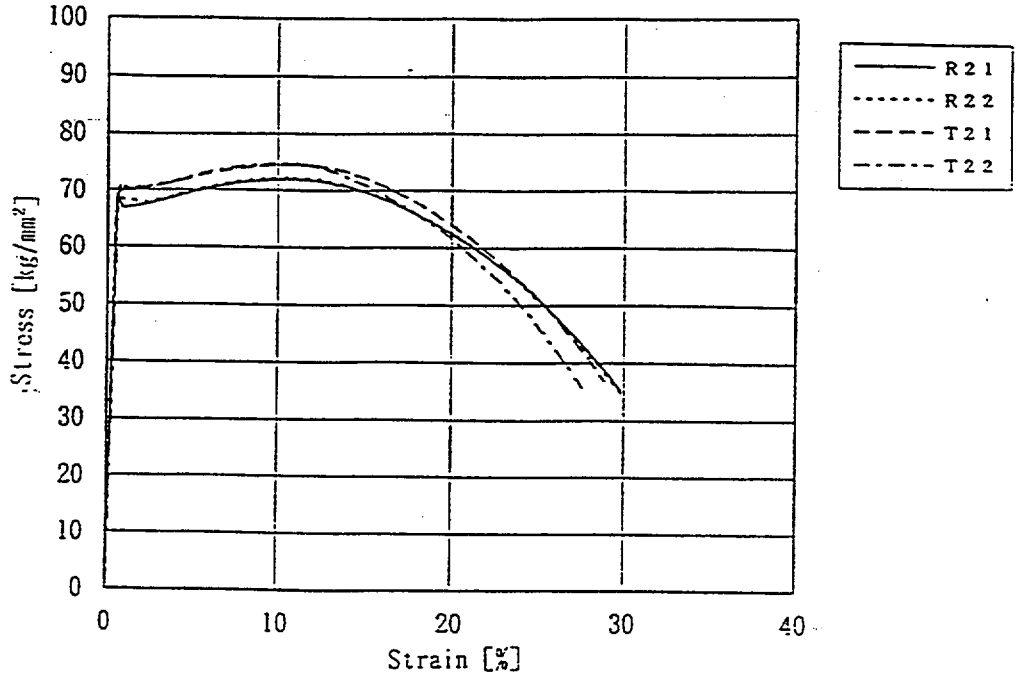

Figure C.11. Stress-strain curves for SPV490: thickness 9 mm plate, location 11.

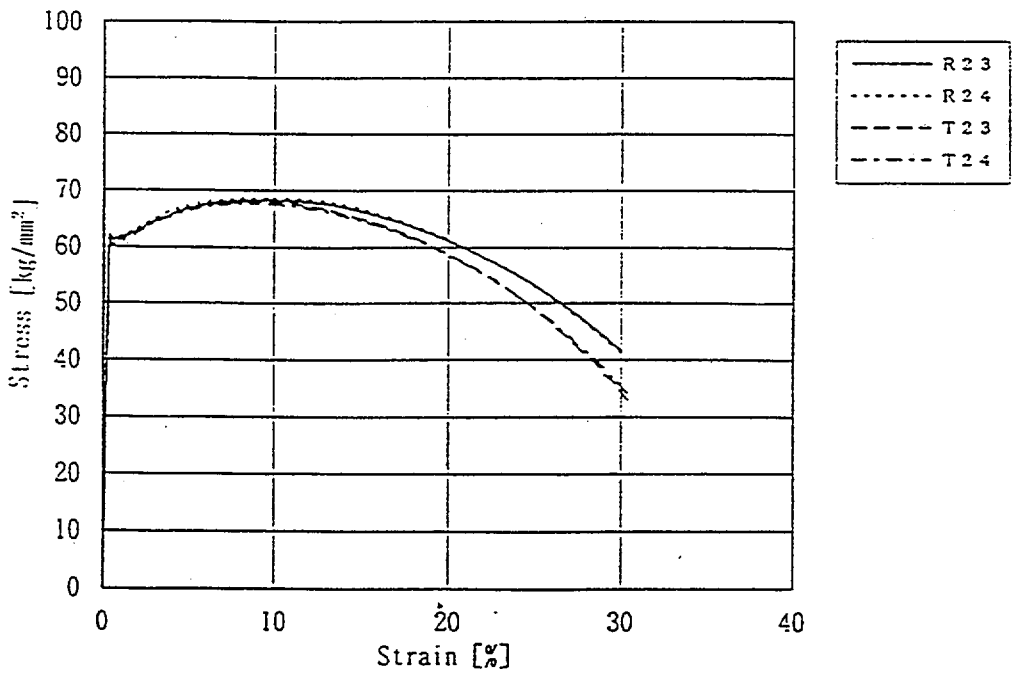

Figure C.12. Stress-strain curves for SPV490: thickness 17.5 mm plate, location 12.

Appendix D

SCV Instrument List and Drawings

Section i. SCV Instrument List

Guide to Table D.1

A complete table providing information on the location of all of the instrumentation is included in the Instrument List Table (Table D.1). The information in the table is intended to provide the relationship between the location of each instrument, its name and enough data acquisition identification information to uniquely specify each instrument to the data acquisition system (DAS).

The instrument ID (name) contains fields that identify the type of instrument, location (interior or exterior), location on the model, the number of the sensor, and, in the case of multi-element sensors, the number of that element. The instrument name format is as follows:

(type abbr.)-(surface designation)-(region designation)-(sequence number in region)

For example, the instrument names for the two strain rosettes located on the outside and inside surface, respectively, of the model at the apex are

RSG-O-THD-1 RSG-I-THD-2

The instrument types are abbreviated as follows:

Type Abbreviation	Description
SSGH	single strain gage, aligned in the hoop direction
SSGM	single strain gage, aligned in the meridional direction
STG	strip strain gage (will include several channels)
RSG	rosette strain gage (will include 3 channels)
VCP	vertically-aligned, cable potentiometer displacement transducer
HCP	horizontally-aligned, cable potentiometer displacement transducer
IDT	inclinometer displacement transducer
TC	thermocouple
RTD	resistance temperature detector
PG	pressure gauge
CD	contact detector
LVDT	linear variable differential transformer (displacement transducer)

The region designation part of the instrument name is based on the area of the vessel that the instruments are installed. This designation is used only to simplify the sequential numbering scheme. The designation list is as follows (see Figure D.1 for the layout of the regions):

Location Designation	Description	Region Number in Figure D.1
THD	top head	1
UCYS	upper cylindrical shell	2
KNU	knuckle	3
SPH	spherical shell	4
UST	upper stiffener	5
UCS	upper conical shell	6
MST	middle stiffener	7
MCS	middle conical shell	8
MCI	material change interface	9
LCS	lower conical shell	10
LST	lower stiffeners	11
LCYS	lower cylindrical shell	12
EQH	equipment hatch	13*
CS	contact structure	(not shown)

* Note: This region encompasses all of the instrumentation that is installed around the equipment hatch.

The Sensor Designation in Table D.1 is the manufacturer's part number.

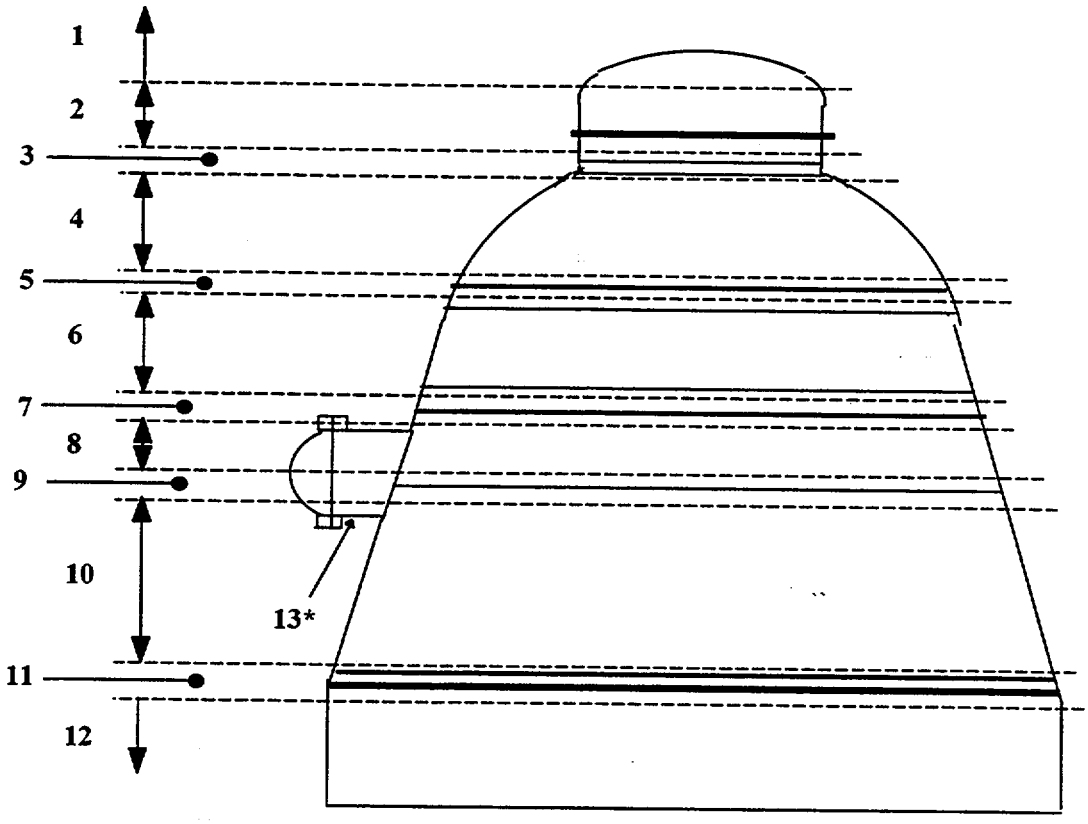

Figure D.1 Side view of the SCV model.

All location data (i.e., azimuth angle and vertical elevation), with the exception of those instruments located around the equipment hatch, are measured from the following references:

Azimuth Angle Zero Reference - 90° counterclockwise from equipment hatch centerline looking from above the vessel, clockwise positive (see Figure D.2)

Vertical Elevation Zero Reference - top of the ring support girder

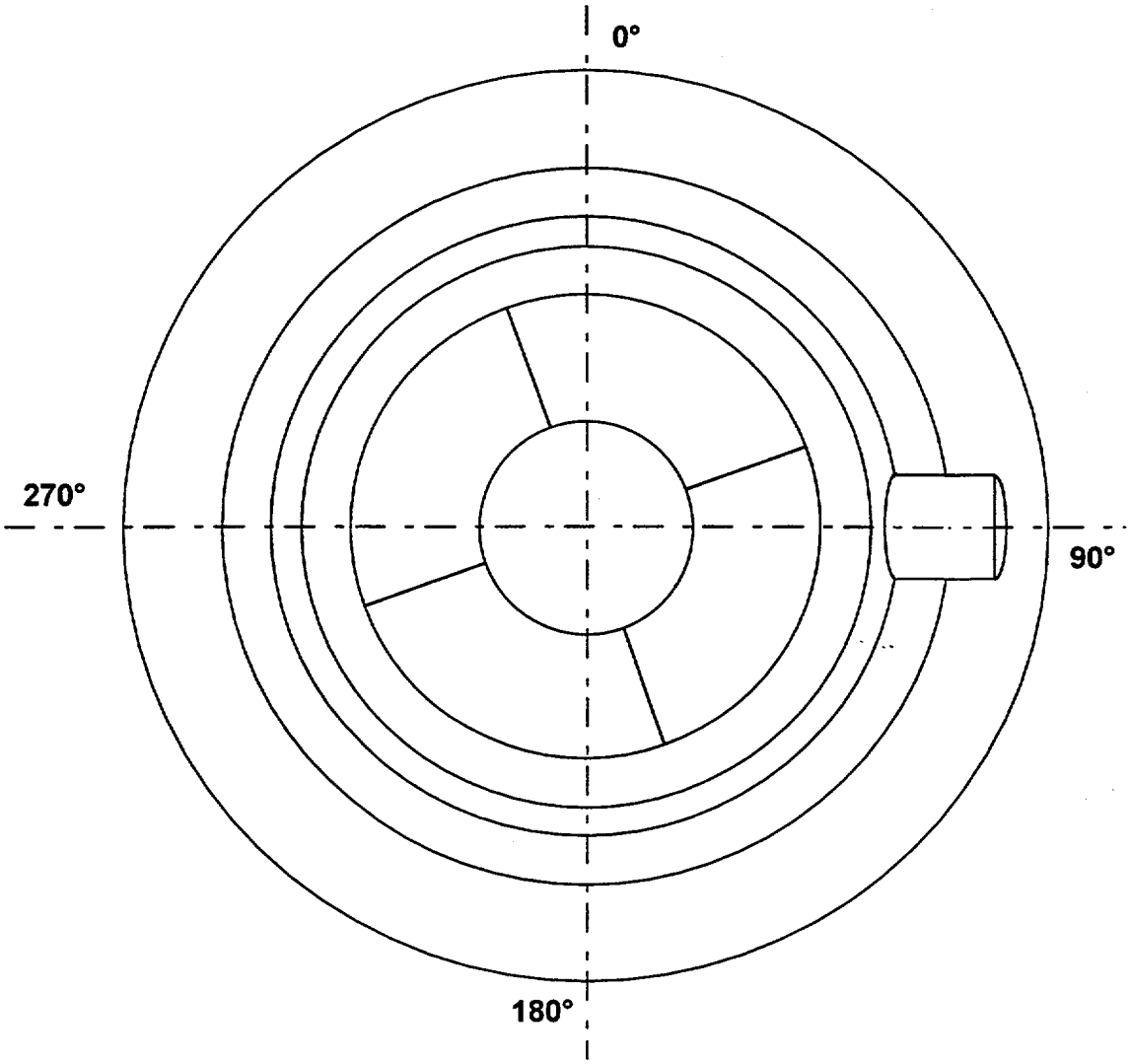

Figure D.2 Overhead view of the SCV model.

Equipment hatch location data are shown in the table with asterisks after each measurement. This is to remind the reader that these data are taken with respect to a radial-angular coordinate system with the origin located at the center of the hatch and the zero degree reference at the "top" as viewed from a drawing, clockwise positive. To emphasize this fact, new headers are placed in the table above the equipment hatch entries.

Table D.1 SCV Instrument List

Instrument ID (Name)	Azimuth Angle (degree)	Vertical Elevation (m)	Sensor Designation
RSG-O-THD-1a	Apex	4.000	EP-08-250RD-350
RSG-O-THD-1b	Apex	4.000	EP-08-250RD-350
RSG-O-THD-1c	Apex	4.000	EP-08-250RD-350
RSG-I-THD-2a	Apex	4.000	EP-08-250RD-350
RSG-I-THD-2b	Apex	4.000	EP-08-250RD-350
RSG-I-THD-2c	Apex	4.000	EP-08-250RD-350
RSG-O-THD-3a	90	4.000	EP-08-250RD-350
RSG-O-THD-3b	90	4.000	EP-08-250RD-350
RSG-O-THD-3c	90	4.000	EP-08-250RD-350
RSG-I-THD-4a	90	4.000	EP-08-250RD-350
RSG-I-THD-4b	90	4.000	EP-08-250RD-350
RSG-I-THD-4c	90	4.000	EP-08-250RD-350
RSG-O-THD-5a	0	4.000	EP-08-250RD-350
RSG-O-THD-5b	0	4.000	EP-08-250RD-350
RSG-O-THD-5c	0	4.000	EP-08-250RD-350
RSG-I-THD-6a	0	4.000	EP-08-250RD-350
RSG-I-THD-6b	0	4.000	EP-08-250RD-350
RSG-I-THD-6c	0	4.000	EP-08-250RD-350
RSG-O-THD-7a	270	4.000	EP-08-250RD-350
RSG-O-THD-7b	270	4.000	EP-08-250RD-350
RSG-O-THD-7c	270	4.000	EP-08-250RD-350
RSG-I-THD-8a	270	4.000	EP-08-250RD-350
RSG-I-THD-8b	270	4.000	EP-08-250RD-350
RSG-I-THD-8c	270	4.000	EP-08-250RD-350
RSG-O-THD-9a	180	4.000	EP-08-250RD-350
RSG-O-THD-9b	180	4.000	EP-08-250RD-350
RSG-O-THD-9c	180	4.000	EP-08-250RD-350
RSG-I-THD-10a	180	4.000	EP-08-250RD-350
RSG-I-THD-10b	180	4.000	EP-08-250RD-350
RSG-I-THD-10c	180	4.000	EP-08-250RD-350
VCP-I-THD-11	Apex	4.000	PT-101-5
TCT-I-THD-12	Apex	4.002	CO3-T

Instrument ID (Name)	Azimuth Angle (degree)	Vertical Elevation (m)	Sensor Designation
STG-O-UCYS-1a	0	3.623	EP-08-125MW-120
STG-O-UCYS-1b	0	3.623	EP-08-125MW-120
STG-O-UCYS-1c	0	3.623	EP-08-125MW-120
STG-O-UCYS-1d	0	3.623	EP-08-125MW-120
STG-O-UCYS-1e	0	3.623	EP-08-125MW-120
SSGH-O-UCYS-2	CAG[1] to UCYS-1	3.623	EP-08-125AC-350
STG-O-UCYS-3a	90	3.623	EP-08-125MW-120
STG-O-UCYS-3b	90	3.623	EP-08-125MW-120
STG-O-UCYS-3c	90	3.623	EP-08-125MW-120
STG-O-UCYS-3d	90	3.623	EP-08-125MW-120
STG-O-UCYS-3e	90	3.623	EP-08-125MW-120
SSGH-O-UCYS-4	CAG to UCYS-3	3.623	EP-08-125AC-350
STG-O-UCYS-5a	180	3.623	EP-08-125MW-120
STG-O-UCYS-5b	180	3.623	EP-08-125MW-120
STG-O-UCYS-5c	180	3.623	EP-08-125MW-120
STG-O-UCYS-5d	180	3.623	EP-08-125MW-120
STG-O-UCYS-5e	180	3.623	EP-08-125MW-120
SSGH-O-UCYS-6	CAG to UCYS-5	3.623	EP-08-125AC-350
STG-O-UCYS-7a	270	3.623	EP-08-125MW-120
STG-O-UCYS-7b	270	3.623	EP-08-125MW-120
STG-O-UCYS-7c	270	3.623	EP-08-125MW-120
STG-O-UCYS-7d	270	3.623	EP-08-125MW-120
STG-O-UCYS-7e	270	3.623	EP-08-125MW-120
SSGH-O-UCYS-8	CAG to UCYS-7	3.623	EP-08-125AC-350
STG-O-UCYS-9a	0	3.573	EP-08-125MW-120
STG-O-UCYS-9b	0	3.573	EP-08-125MW-120
STG-O-UCYS-9c	0	3.573	EP-08-125MW-120
STG-O-UCYS-9d	0	3.573	EP-08-125MW-120
STG-O-UCYS-9e	0	3.573	EP-08-125MW-120
SSGH-O-UCYS-10	CAG to UCYS-9	3.573	EP-08-125AC-350
STG-O-UCYS-11a	90	3.573	EP-08-125MW-120
STG-O-UCYS-11b	90	3.573	EP-08-125MW-120
STG-O-UCYS-11c	90	3.573	EP-08-125MW-120
STG-O-UCYS-11d	90	3.573	EP-08-125MW-120

[1] CAG = Cross axis gage

Instrument ID (Name)	Azimuth Angle (degree)	Vertical Elevation (m)	Sensor Designation
STG-O-UCYS-11e	90	3.573	EP-08-125MW-120
SSGH-O-UCYS-12	CAG to UCYS-11	3.573	EP-08-125AC-350
STG-O-UCYS-13a	180	3.573	EP-08-125MW-120
STG-O-UCYS-13b	180	3.573	EP-08-125MW-120
STG-O-UCYS-13c	180	3.573	EP-08-125MW-120
STG-O-UCYS-13d	180	3.573	EP-08-125MW-120
STG-O-UCYS-13e	180	3.573	EP-08-125MW-120
SSGH-O-UCYS-14	CAG to UCYS-13	3.573	EP-08-125AC-350
STG-O-UCYS-15a	270	3.573	EP-08-125MW-120
STG-O-UCYS-15b	270	3.573	EP-08-125MW-120
STG-O-UCYS-15c	270	3.573	EP-08-125MW-120
STG-O-UCYS-15d	270	3.573	EP-08-125MW-120
STG-O-UCYS-15e	270	3.573	EP-08-125MW-120
SSGH-O-UCYS-16	CAG to UCYS-15	3.573	EP-08-125AC-350
STG-I-UCYS-17a	0	3.573	EP-08-125MW-120
STG-I-UCYS-17b	0	3.573	EP-08-125MW-120
STG-I-UCYS-17c	0	3.573	EP-08-125MW-120
STG-I-UCYS-17d	0	3.573	EP-08-125MW-120
STG-I-UCYS-17e	0	3.573	EP-08-125MW-120
SSGH-I-UCYS-18	CAG to UCYS-17	3.573	EP-08-125AC-350
STG-I-UCYS-19a	90	3.573	EP-08-125MW-120
STG-I-UCYS-19b	90	3.573	EP-08-125MW-120
STG-I-UCYS-19c	90	3.573	EP-08-125MW-120
STG-I-UCYS-19d	90	3.573	EP-08-125MW-120
STG-I-UCYS-19e	90	3.573	EP-08-125MW-120
SSGH-I-UCYS-20	CAG to UCYS-19	3.573	EP-08-125AC-350
STG-I-UCYS-21a	180	3.573	EP-08-125MW-120
STG-I-UCYS-21b	180	3.573	EP-08-125MW-120
STG-I-UCYS-21c	180	3.573	EP-08-125MW-120
STG-I-UCYS-21d	180	3.573	EP-08-125MW-120
STG-I-UCYS-21e	180	3.573	EP-08-125MW-120
SSGH-I-UCYS-22	CAG to UCYS-21	3.573	EP-08-125AC-350
STG-I-UCYS-23a	270	3.573	EP-08-125MW-120
STG-I-UCYS-23b	270	3.573	EP-08-125MW-120
STG-I-UCYS-23c	270	3.573	EP-08-125MW-120
STG-I-UCYS-23d	270	3.573	EP-08-125MW-120

Instrument ID (Name)	Azimuth Angle (degree)	Vertical Elevation (m)	Sensor Designation
STG-I-UCYS-23e	270	3.573	EP-08-125MW-120
SSGH-I-UCYS-24	CAG to UCYS-23	3.573	EP-08-125AC-350
STG-O-UCYS-25a	0	3.472	EP-08-125MW-120
STG-O-UCYS-25b	0	3.472	EP-08-125MW-120
STG-O-UCYS-25c	0	3.472	EP-08-125MW-120
STG-O-UCYS-25d	0	3.472	EP-08-125MW-120
STG-O-UCYS-25e	0	3.472	EP-08-125MW-120
SSGH-O-UCYS-26	CAG to UCYS-25	3.472	EP-08-125AC-350
SSGM-I-UCYS-27	0	3.472	EP-08-250AE-350
STG-O-UCYS-28a	90	3.472	EP-08-125MW-120
STG-O-UCYS-28b	90	3.472	EP-08-125MW-120
STG-O-UCYS-28c	90	3.472	EP-08-125MW-120
STG-O-UCYS-28d	90	3.472	EP-08-125MW-120
STG-O-UCYS-28e	90	3.472	EP-08-125MW-120
SSGH-O-UCYS-29	CAG to UCYS-28	3.472	EP-08-125AC-350
SSGM-I-UCYS-30	90	3.472	EP-08-250AE-350
STG-O-UCYS-31a	180	3.472	EP-08-125MW-120
STG-O-UCYS-31b	180	3.472	EP-08-125MW-120
STG-O-UCYS-31c	180	3.472	EP-08-125MW-120
STG-O-UCYS-31d	180	3.472	EP-08-125MW-120
STG-O-UCYS-31e	180	3.472	EP-08-125MW-120
SSGH-O-UCYS-32	CAG to UCYS-31	3.472	EP-08-125AC-350
SSGM-I-UCYS-33	180	3.472	EP-08-250AE-350
STG-O-UCYS-34a	270	3.472	EP-08-125MW-120
STG-O-UCYS-34b	270	3.472	EP-08-125MW-120
STG-O-UCYS-34c	270	3.472	EP-08-125MW-120
STG-O-UCYS-34d	270	3.472	EP-08-125MW-120
STG-O-UCYS-34e	270	3.472	EP-08-125MW-120
SSGH-O-UCYS-35	CAG to UCYS-34	3.472	EP-08-125AC-350
SSGM-I-UCYS-36	270	3.472	EP-08-250AE-350
HCP-I-UCYS-39	45	3.570	PT-101-5
HCP-I-UCYS-40	135	3.570	PT-101-5
HCP-I-UCYS-41	225	3.570	PT-101-5
HCP-I-UCYS-42	315	3.570	PT-101-5
TCT-I-UCYS-43	180	3.120	CO3-T
HCP-O-UCYS-43	45	3.570	PT-101-5

Instrument ID (Name)	Azimuth Angle (degree)	Vertical Elevation (m)	Sensor Designation
HCP-O-UCYS-44	135	3.570	PT-101-5
HCP-O-UCYS-45	225	3.570	PT-101-5
HCP-O-UCYS-46	315	3.570	PT-101-5
TCT-I-UCYS-47	0	0.250	CO3-T
STG-O-KNU-1a	0	3.319	EP-08-125MW-120
STG-O-KNU-1b	0	3.319	EP-08-125MW-120
STG-O-KNU-1c	0	3.319	EP-08-125MW-120
STG-O-KNU-1d	0	3.319	EP-08-125MW-120
STG-O-KNU-1e	0	3.319	EP-08-125MW-120
SSGH-O-KNU-2	CAG to KNU-1	3.319	EP-08-125AC-350
STG-O-KNU-3a	90	3.319	EP-08-125MW-120
STG-O-KNU-3b	90	3.319	EP-08-125MW-120
STG-O-KNU-3c	90	3.319	EP-08-125MW-120
STG-O-KNU-3d	90	3.319	EP-08-125MW-120
STG-O-KNU-3e	90	3.319	EP-08-125MW-120
SSGH-O-KNU-4	CAG to KNU-3	3.319	EP-08-125AC-350
STG-O-KNU-5a	180	3.319	EP-08-125MW-120
STG-O-KNU-5b	180	3.319	EP-08-125MW-120
STG-O-KNU-5c	180	3.319	EP-08-125MW-120
STG-O-KNU-5d	180	3.319	EP-08-125MW-120
STG-O-KNU-5e	180	3.319	EP-08-125MW-120
SSGH-O-KNU-6	CAG to KNU-5	3.319	EP-08-125AC-350
STG-O-KNU-7a	270	3.319	EP-08-125MW-120
STG-O-KNU-7b	270	3.319	EP-08-125MW-120
STG-O-KNU-7c	270	3.319	EP-08-125MW-120
STG-O-KNU-7d	270	3.319	EP-08-125MW-120
STG-O-KNU-7e	270	3.319	EP-08-125MW-120
SSGH-O-KNU-8	CAG to KNU-7	3.319	EP-08-125AC-350
STG-I-KNU-9a	0	3.319	EP-08-125MW-120
STG-I-KNU-9b	0	3.319	EP-08-125MW-120
STG-I-KNU-9c	0	3.319	EP-08-125MW-120
STG-I-KNU-9d	0	3.319	EP-08-125MW-120
STG-I-KNU-9e	0	3.319	EP-08-125MW-120
SSGH-I-KNU-10	CAG to KNU-9	3.319	EP-08-125AC-350
STG-I-KNU-11a	90	3.319	EP-08-125MW-120

Instrument ID (Name)	Azimuth Angle (degree)	Vertical Elevation (m)	Sensor Designation
STG-I-KNU-11b	90	3.319	EP-08-125MW-120
STG-I-KNU-11c	90	3.319	EP-08-125MW-120
STG-I-KNU-11d	90	3.319	EP-08-125MW-120
STG-I-KNU-11e	90	3.319	EP-08-125MW-120
SSGH-I-KNU-12	CAG to KNU-11	3.319	EP-08-125AC-350
STG-I-KNU-13a	180	3.319	EP-08-125MW-120
STG-I-KNU-13b	180	3.319	EP-08-125MW-120
STG-I-KNU-13c	180	3.319	EP-08-125MW-120
STG-I-KNU-13d	180	3.319	EP-08-125MW-120
STG-I-KNU-13e	180	3.319	EP-08-125MW-120
SSGH-I-KNU-14	CAG to KNU-13	3.319	EP-08-125AC-350
STG-I-KNU-15a	270	3.319	EP-08-125MW-120
STG-I-KNU-15b	270	3.319	EP-08-125MW-120
STG-I-KNU-15c	270	3.319	EP-08-125MW-120
STG-I-KNU-15d	270	3.319	EP-08-125MW-120
STG-I-KNU-15e	270	3.319	EP-08-125MW-120
SSGH-I-KNU-16	CAG to KNU-15	3.319	EP-08-125AC-350
TCK-O-KNU-17	0	3.530	KQSS-116-U-240
HCP-I-KNU-17	0	3.319	PT-101-2
VCP-I-KNU-18	0	3.319	PT-101-2
HCP-I-KNU-19	90	3.319	PT-101-2
VCP-I-KNU-20	90	3.319	PT-101-2
IDT-I-KNU-21	180	4.002	SSY0140-390X
IDT-I-KNU-22	270	4.002	SSY0140-390Y
RSG-O-SPH-1a	45	3.132	EP-08-250RD-350
RSG-O-SPH-1b	45	3.132	EP-08-250RD-350
RSG-O-SPH-1c	45	3.132	EP-08-250RD-350
RSG-I-SPH-2a	45	3.132	EP-08-250RD-350
RSG-I-SPH-2b	45	3.132	EP-08-250RD-350
RSG-I-SPH-2c	45	3.132	EP-08-250RD-350
RSG-O-SPH-3a	135	3.132	EP-08-250RD-350
RSG-O-SPH-3b	135	3.132	EP-08-250RD-350
RSG-O-SPH-3c	135	3.132	EP-08-250RD-350
RSG-I-SPH-4a	135	3.132	EP-08-250RD-350
RSG-I-SPH-4b	135	3.132	EP-08-250RD-350

Instrument ID (Name)	Azimuth Angle (degree)	Vertical Elevation (m)	Sensor Designation
RSG-I-SPH-4c	135	3.132	EP-08-250RD-350
RSG-O-SPH-5a	225	3.132	EP-08-250RD-350
RSG-O-SPH-5b	225	3.132	EP-08-250RD-350
RSG-O-SPH-5c	225	3.132	EP-08-250RD-350
RSG-I-SPH-6a	225	3.132	EP-08-250RD-350
RSG-I-SPH-6b	225	3.132	EP-08-250RD-350
RSG-I-SPH-6c	225	3.132	EP-08-250RD-350
RSG-O-SPH-7a	315	3.132	EP-08-250RD-350
RSG-O-SPH-7b	315	3.132	EP-08-250RD-350
RSG-O-SPH-7c	315	3.132	EP-08-250RD-350
RSG-I-SPH-8a	315	3.132	EP-08-250RD-350
RSG-I-SPH-8b	315	3.132	EP-08-250RD-350
RSG-I-SPH-8c	315	3.132	EP-08-250RD-350
HCP-I-SPH-9	0	3.220	PT-101-2
VCP-I-SPH-10	0	3.220	PT-101-2
HCP-I-SPH-11	90	3.220	PT-101-2
VCP-I-SPH-12	90	3.220	PT-101-2
HCP-I-SPH-13	0	3.100	PT-101-2
VCP-I-SPH-14	0	3.100	PT-101-2
HCP-I-SPH-15	90	3.100	PT-101-2
VCP-I-SPH-16	90	3.100	PT-101-2
HCP-I-SPH-17	0	2.980	PT-101-2
VCP-I-SPH-18	0	2.980	PT-101-2
HCP-I-SPH-19	90	2.980	PT-101-2
VCP-I-SPH-20	90	2.980	PT-101-2
SSGM-O-UST-1	0	2.924	EP-08-250AE-350
SSGM-O-UST-2	90	2.924	EP-08-250AE-350
SSGM-O-UST-3	180	2.924	EP-08-250AE-350
SSGM-O-UST-4	270	2.924	EP-08-250AE-350
SSGM-I-UST-5	0	2.924	EP-08-250AE-350
SSGM-I-UST-6	90	2.924	EP-08-250AE-350
SSGM-I-UST-7	180	2.924	EP-08-250AE-350
SSGM-I-UST-8	270	2.924	EP-08-250AE-350
SSGM-O-UST-9	0	2.865	EP-08-250AE-350
SSGM-O-UST-10	90	2.865	EP-08-250AE-350

Instrument ID (Name)	Azimuth Angle (degree)	Vertical Elevation (m)	Sensor Designation
SSGM-O-UST-11	180	2.865	EP-08-250AE-350
SSGM-O-UST-12	270	2.865	EP-08-250AE-350
SSGM-I-UST-13	0	2.865	EP-08-250AE-350
SSGM-I-UST-14	90	2.865	EP-08-250AE-350
SSGM-I-UST-15	180	2.865	EP-08-250AE-350
SSGM-I-UST-16	270	2.865	EP-08-250AE-350
HCP-I-UST-17	0	2.915	PT-101-2
HCP-I-UST-18	90	2.915	PT-101-2
HCP-I-UST-19	180	2.915	PT-101-2
HCP-I-UST-20	270	2.915	PT-101-2
SSGM-O-UCS-1	0	2.675	EP-08-250AE-350
SSGM-O-UCS-2	90	2.675	EP-08-250AE-350
SSGM-O-UCS-3	180	2.675	EP-08-250AE-350
SSGM-O-UCS-4	270	2.675	EP-08-250AE-350
SSGM-I-UCS-5	0	2.675	EP-08-250AE-350
SSGM-I-UCS-6	90	2.675	EP-08-250AE-350
SSGM-I-UCS-7	180	2.675	EP-08-250AE-350
SSGM-I-UCS-8	270	2.675	EP-08-250AE-350
RSG-O-UCS-9a	0	2.485	EP-08-250RD-350
RSG-O-UCS-9b	0	2.485	EP-08-250RD-350
RSG-O-UCS-9c	0	2.485	EP-08-250RD-350
RSG-I-UCS-10a	0	2.485	EP-08-250RD-350
RSG-I-UCS-10b	0	2.485	EP-08-250RD-350
RSG-I-UCS-10c	0	2.485	EP-08-250RD-350
RSG-O-UCS-11a	90	2.485	EP-08-250RD-350
RSG-O-UCS-11b	90	2.485	EP-08-250RD-350
RSG-O-UCS-11c	90	2.485	EP-08-250RD-350
RSG-I-UCS-12a	90	2.485	EP-08-250RD-350
RSG-I-UCS-12b	90	2.485	EP-08-250RD-350
RSG-I-UCS-12c	90	2.485	EP-08-250RD-350
RSG-O-UCS-13a	180	2.485	EP-08-250RD-350
RSG-O-UCS-13b	180	2.485	EP-08-250RD-350
RSG-O-UCS-13c	180	2.485	EP-08-250RD-350
RSG-I-UCS-14a	180	2.485	EP-08-250RD-350
RSG-I-UCS-14b	180	2.485	EP-08-250RD-350

Instrument ID (Name)	Azimuth Angle (degree)	Vertical Elevation (m)	Sensor Designation
RSG-I-UCS-14c	180	2.485	EP-08-250RD-350
RSG-O-UCS-15a	270	2.485	EP-08-250RD-350
RSG-O-UCS-15b	270	2.485	EP-08-250RD-350
RSG-O-UCS-15c	270	2.485	EP-08-250RD-350
RSG-I-UCS-16a	270	2.485	EP-08-250RD-350
RSG-I-UCS-16b	270	2.485	EP-08-250RD-350
RSG-I-UCS-16c	270	2.485	EP-08-250RD-350
RSG-O-UCS-17a	45	2.485	EP-08-250RD-350
RSG-O-UCS-17b	45	2.485	EP-08-250RD-350
RSG-O-UCS-17c	45	2.485	EP-08-250RD-350
RSG-I-UCS-18a	45	2.485	EP-08-250RD-350
RSG-I-UCS-18b	45	2.485	EP-08-250RD-350
RSG-I-UCS-18c	45	2.485	EP-08-250RD-350
RSG-O-UCS-19a	135	2.485	EP-08-250RD-350
RSG-O-UCS-19b	135	2.485	EP-08-250RD-350
RSG-O-UCS-19c	135	2.485	EP-08-250RD-350
RSG-I-UCS-20a	135	2.485	EP-08-250RD-350
RSG-I-UCS-20b	135	2.485	EP-08-250RD-350
RSG-I-UCS-20c	135	2.485	EP-08-250RD-350
SSGM-O-UCS-21	0	2.295	EP-08-250AE-350
SSGM-O-UCS-22	45	2.295	EP-08-250AE-350
SSGM-O-UCS-23	90	2.295	EP-08-250AE-350
SSGM-O-UCS-24	135	2.295	EP-08-250AE-350
SSGM-O-UCS-25	180	2.295	EP-08-250AE-350
SSGM-O-UCS-26	270	2.295	EP-08-250AE-350
SSGM-I-UCS-27	0	2.295	EP-08-250AE-350
SSGM-I-UCS-28	45	2.295	EP-08-250AE-350
SSGM-I-UCS-29	90	2.295	EP-08-250AE-350
SSGM-I-UCS-30	135	2.295	EP-08-250AE-350
SSGM-I-UCS-31	180	2.295	EP-08-250AE-350
SSGM-I-UCS-32	270	2.295	EP-08-250AE-350
HCP-I-UCS-33	0	2.694	PT-101-2
HCP-I-UCS-34	90	2.694	PT-101-2
HCP-I-UCS-35	180	2.694	PT-101-2
HCP-I-UCS-36	270	2.694	PT-101-2
RSG-O-UCS-37a	225	2.485	EP-08-250RD-350

Instrument ID (Name)	Azimuth Angle (degree)	Vertical Elevation (m)	Sensor Designation
RSG-O-UCS-37b	225	2.485	EP-08-250RD-350
RSG-O-UCS-37c	225	2.485	EP-08-250RD-350
RSG-O-UCS-38a	315	2.485	EP-08-250RD-350
RSG-O-UCS-38b	315	2.485	EP-08-250RD-350
RSG-O-UCS-38c	315	2.485	EP-08-250RD-350
RSG-O-UCS-39a	45	2.430	EP-08-250RD-350
RSG-O-UCS-39b	45	2.430	EP-08-250RD-350
RSG-O-UCS-39c	45	2.430	EP-08-250RD-350
RSG-O-UCS-40a	135	2.430	EP-08-250RD-350
RSG-O-UCS-40b	135	2.430	EP-08-250RD-350
RSG-O-UCS-40c	135	2.430	EP-08-250RD-350
SSGM-O-UCS-41	202	2.245	EP-08-250AE-350
SSGM-O-UCS-42	202	2.150	EP-08-250AE-350
SSGM-I-UCS-43	202	2.150	EP-08-250AE-350
TCT-I-UCS-44	180	2.883	CO3-T
SSGM-O-MST-1	0	2.100	EP-08-250AE-350
SSGM-O-MST-2	45	2.100	EP-08-250AE-350
SSGM-O-MST-3	90	2.100	EP-08-250AE-350
SSGM-O-MST-4	135	2.100	EP-08-250AE-350
SSGM-O-MST-5	180	2.100	EP-08-250AE-350
SSGM-O-MST-6	270	2.100	EP-08-250AE-350
SSGM-I-MST-7	0	2.100	EP-08-250AE-350
SSGM-I-MST-8	45	2.100	EP-08-250AE-350
STG-I-MST-9a	90	2.100	EP-08-125MW-120
STG-I-MST-9b	90	2.100	EP-08-125MW-120
STG-I-MST-9c	90	2.100	EP-08-125MW-120
STG-I-MST-9d	90	2.100	EP-08-125MW-120
STG-I-MST-9e	90	2.100	EP-08-125MW-120
SSGM-I-MST-10	135	2.100	EP-08-250AE-350
SSGM-I-MST-11	180	2.100	EP-08-250AE-350
SSGM-I-MST-12	270	2.100	EP-08-250AE-350
SSGM-O-MST-13	0	2.042	EP-08-250AE-350
SSGM-O-MST-14	45	2.042	EP-08-250AE-350
SSGM-O-MST-16	135	2.042	EP-08-250AE-350
SSGM-O-MST-17	180	2.042	EP-08-250AE-350

Instrument ID (Name)	Azimuth Angle (degree)	Vertical Elevation (m)	Sensor Designation
SSGM-O-MST-18	270	2.042	EP-08-250AE-350
SSGM-I-MST-19	0	2.042	EP-08-250AE-350
SSGM-I-MST-20	45	2.042	EP-08-250AE-350
SSGH-I-MST-21	90	2.042	EP-08-250AE-350
SSGM-I-MST-22	135	2.042	EP-08-250AE-350
SSGM-I-MST-23	180	2.042	EP-08-250AE-350
SSGM-I-MST-24	270	2.042	EP-08-250AE-350
TCK-O-MST-25	180	2.080	KQSS-116-U-240
HCP-I-MST-25	0	2.071	PT-101-2
HCP-I-MST-26	90	2.071	PT-101-2
HCP-I-MST-27	180	2.071	PT-101-2
HCP-I-MST-28	270	2.071	PT-101-2
RSG-I-MCS-1a	0	1.821	EP-08-250RD-350
RSG-I-MCS-1b	0	1.821	EP-08-250RD-350
RSG-I-MCS-1c	0	1.821	EP-08-250RD-350
RSG-I-MCS-2a	180	1.821	EP-08-250RD-350
RSG-I-MCS-2b	180	1.821	EP-08-250RD-350
RSG-I-MCS-2c	180	1.821	EP-08-250RD-350
RSG-I-MCS-3a	270	1.821	EP-08-250RD-350
RSG-I-MCS-3b	270	1.821	EP-08-250RD-350
RSG-I-MCS-3c	270	1.821	EP-08-250RD-350
HCP-I-MCS-4	0	1.813	PT-101-2
HCP-I-MCS-5	90	1.813	PT-101-2
HCP-I-MCS-6	180	1.813	PT-101-2
HCP-I-MCS-7	270	1.813	PT-101-2
RSG-I-MCI-1a	0	1.600	EP-08-250RD-350
RSG-I-MCI-1b	0	1.600	EP-08-250RD-350
RSG-I-MCI-1c	0	1.600	EP-08-250RD-350
SSGM-O-MCI-2	0	1.600	EP-08-250AE-350
RSG-I-MCI-3a	45	1.600	EP-08-250RD-350
RSG-I-MCI-3b	45	1.600	EP-08-250RD-350
RSG-I-MCI-3c	45	1.600	EP-08-250RD-350
SSGM-O-MCI-4	45	1.600	EP-08-250AE-350
RSG-I-MCI-5a	135	1.600	EP-08-250RD-350

Instrument ID (Name)	Azimuth Angle (degree)	Vertical Elevation (m)	Sensor Designation
RSG-I-MCI-5b	135	1.600	EP-08-250RD-350
RSG-I-MCI-5c	135	1.600	EP-08-250RD-350
SSGM-O-MCI-6	135	1.600	EP-08-250AE-350
RSG-I-MCI-7a	180	1.600	EP-08-250RD-350
RSG-I-MCI-7b	180	1.600	EP-08-250RD-350
RSG-I-MCI-7c	180	1.600	EP-08-250RD-350
SSGM-O-MCI-8	180	1.600	EP-08-250AE-350
RSG-I-MCI-9a	225	1.600	EP-08-250RD-350
RSG-I-MCI-9b	225	1.600	EP-08-250RD-350
RSG-I-MCI-9c	225	1.600	EP-08-250RD-350
SSGM-O-MCI-10	225	1.600	EP-08-250AE-350
RSG-I-MCI-11a	270	1.600	EP-08-250RD-350
RSG-I-MCI-11b	270	1.600	EP-08-250RD-350
RSG-I-MCI-11c	270	1.600	EP-08-250RD-350
SSGM-O-MCI-12	270	1.600	EP-08-250AE-350
RSG-I-MCI-13a	315	1.600	EP-08-250RD-350
RSG-I-MCI-13b	315	1.600	EP-08-250RD-350
RSG-I-MCI-13c	315	1.600	EP-08-250RD-350
SSGM-O-MCI-14	315	1.600	EP-08-250AE-350
HCP-I-MCI-15	0	1.633	PT-101-2
HCP-I-MCI-16	90	1.633	PT-101-2
HCP-I-MCI-17	180	1.633	PT-101-2
HCP-I-MCI-18	270	1.633	PT-101-2
VCP-O-MCI-19	90	1.633	PT-101-2
HCP-O-MCI-21	90	1.633	PT-101-2
TCT-I-MCI-22	180	2.485	CO3-T
TCT-I-MCI-23	270	2.070	CO3-T
TCT-I-MCI-24	0	1.579	CO3-T
HCP-I-LCS-1	0	1.453	PT-101-2
HCP-I-LCS-2	90	1.453	PT-101-2
HCP-I-LCS-3	180	1.453	PT-101-2
HCP-I-LCS-4	270	1.453	PT-101-2
RSG-O-LCS-5a	45	1.453	EP-08-250RD-350
RSG-O-LCS-5b	45	1.453	EP-08-250RD-350
RSG-O-LCS-5c	45	1.453	EP-08-250RD-350

Instrument ID (Name)	Azimuth Angle (degree)	Vertical Elevation (m)	Sensor Designation
RSG-I-LCS-6a	45	1.453	EP-08-250RD-350
RSG-I-LCS-6b	45	1.453	EP-08-250RD-350
RSG-I-LCS-6c	45	1.453	EP-08-250RD-350
RSG-O-LCS-7a	135	1.453	EP-08-250RD-350
RSG-O-LCS-7b	135	1.453	EP-08-250RD-350
RSG-O-LCS-7c	135	1.453	EP-08-250RD-350
RSG-I-LCS-8a	135	1.453	EP-08-250RD-350
RSG-I-LCS-8b	135	1.453	EP-08-250RD-350
RSG-I-LCS-8c	135	1.453	EP-08-250RD-350
RSG-I-LCS-9a	0	1.254	EP-08-250RD-350
RSG-I-LCS-9b	0	1.254	EP-08-250RD-350
RSG-I-LCS-9c	0	1.254	EP-08-250RD-350
RSG-I-LCS-10a	180	1.254	EP-08-250RD-350
RSG-I-LCS-10b	180	1.254	EP-08-250RD-350
RSG-I-LCS-10c	180	1.254	EP-08-250RD-350
RSG-I-LCS-11a	270	1.254	EP-08-250RD-350
RSG-I-LCS-11b	270	1.254	EP-08-250RD-350
RSG-I-LCS-11c	270	1.254	EP-08-250RD-350
RSG-O-LCS-12a	45	1.400	EP-08-250RD-350
RSG-O-LCS-12b	45	1.400	EP-08-250RD-350
RSG-O-LCS-12c	45	1.400	EP-08-250RD-350
RSG-O-LCS-13a	135	1.400	EP-08-250RD-350
RSG-O-LCS-13b	135	1.400	EP-08-250RD-350
RSG-O-LCS-13c	135	1.400	EP-08-250RD-350
RSG-I-LST-1a	0	0.947	EP-08-250RD-350
RSG-I-LST-1b	0	0.947	EP-08-250RD-350
RSG-I-LST-1c	0	0.947	EP-08-250RD-350
SSGM-O-LST-2	0	0.947	EP-08-250AE-350
SSGM-I-LST-3	45	0.947	EP-08-250AE-350
SSGM-O-LST-4	45	0.947	EP-08-250AE-350
RSG-I-LST-5a	90	0.947	EP-08-250RD-350
RSG-I-LST-5b	90	0.947	EP-08-250RD-350
RSG-I-LST-5c	90	0.947	EP-08-250RD-350
SSGM-O-LST-6	90	0.947	EP-08-250AE-350
SSGM-I-LST-7	135	0.947	EP-08-250AE-350

Instrument ID (Name)	Azimuth Angle (degree)	Vertical Elevation (m)	Sensor Designation
SSGM-O-LST-8	135	0.947	EP-08-250AE-350
RSG-I-LST-9a	180	0.947	EP-08-250RD-350
RSG-I-LST-9b	180	0.947	EP-08-250RD-350
RSG-I-LST-9c	180	0.947	EP-08-250RD-350
SSGM-O-LST-10	180	0.947	EP-08-250AE-350
SSGM-I-LST-11	225	0.947	EP-08-250AE-350
SSGM-O-LST-12	225	0.947	EP-08-250AE-350
RSG-I-LST-13a	270	0.947	EP-08-250RD-350
RSG-I-LST-13b	270	0.947	EP-08-250RD-350
RSG-I-LST-13c	270	0.947	EP-08-250RD-350
SSGM-O-LST-14	270	0.947	EP-08-250AE-350
SSGM-I-LST-15	315	0.947	EP-08-250AE-350
SSGM-O-LST-16	315	0.947	EP-08-250AE-350
SSGM-O-LST-17	0	0.797	EP-08-250AE-350
SSGM-O-LST-18	45	0.797	EP-08-250AE-350
SSGM-O-LST-19	90	0.797	EP-08-250AE-350
SSGM-O-LST-20	135	0.797	EP-08-250AE-350
SSGM-O-LST-21	180	0.797	EP-08-250AE-350
SSGM-O-LST-22	225	0.797	EP-08-250AE-350
SSGM-O-LST-23	270	0.797	EP-08-250AE-350
SSGM-O-LST-24	315	0.797	EP-08-250AE-350
SSGM-I-LST-25	0	0.797	EP-08-250AE-350
SSGM-I-LST-26	45	0.797	EP-08-250AE-350
SSGM-I-LST-27	90	0.797	EP-08-250AE-350
SSGM-I-LST-28	135	0.797	EP-08-250AE-350
SSGM-I-LST-29	180	0.797	EP-08-250AE-350
SSGM-I-LST-30	225	0.797	EP-08-250AE-350
SSGM-I-LST-31	270	0.797	EP-08-250AE-350
SSGM-I-LST-32	315	0.797	EP-08-250AE-350
TCK-O-LST-33	0	0.770	KQSS-116-U-240
HCP-I-LST-33	0	0.852	PT-101-2
TCK-O-LST-34	90	0.770	KQSS-116-U-240
HCP-I-LST-34	90	0.852	PT-101-2
TCK-O-LST-35	180	0.770	KQSS-116-U-240
HCP-I-LST-35	180	0.852	PT-101-15
HCP-I-LST-36	270	0.852	PT-101-2

Instrument ID (Name)	Azimuth Angle (degree)	Vertical Elevation (m)	Sensor Designation
TCK-O-LST-36	270	0.770	KQSS-116-U-240
HCP-I-LCYS-1	0	0.750	PT-101-2
HCP-I-LCYS-2	90	0.750	PT-101-5
HCP-I-LCYS-3	180	0.750	PT-101-5
HCP-I-LCYS-4	270	0.750	PT-101-2
RSG-I-LCYS-9a	0	0.500	EP-08-250RD-350
RSG-I-LCYS-9b	0	0.500	EP-08-250RD-350
RSG-I-LCYS-9c	0	0.500	EP-08-250RD-350
RSG-I-LCYS-10a	90	0.500	EP-08-250RD-350
RSG-I-LCYS-10b	90	0.500	EP-08-250RD-350
RSG-I-LCYS-10c	90	0.500	EP-08-250RD-350
RSG-I-LCYS-11a	180	0.500	EP-08-250RD-350
RSG-I-LCYS-11b	180	0.500	EP-08-250RD-350
RSG-I-LCYS-11c	180	0.500	EP-08-250RD-350
RSG-I-LCYS-12a	270	0.500	EP-08-250RD-350
RSG-I-LCYS-12b	270	0.500	EP-08-250RD-350
RSG-I-LCYS-12c	270	0.500	EP-08-250RD-350
SSGM-O-LCYS-13	0	0.270	SG-159-11-50-6S
SSGM-O-LCYS-14	45	0.270	SG-159-11-50-6S
SSGM-O-LCYS-15	90	0.270	SG-159-11-50-6S
SSGM-O-LCYS-16	135	0.270	SG-159-11-50-6S
SSGM-O-LCYS-17	180	0.270	SG-159-11-50-6S
SSGM-O-LCYS-18	225	0.270	SG-159-11-50-6S
SSGM-O-LCYS-19	270	0.270	SG-159-11-50-6S
SSGM-O-LCYS-20	315	0.270	SG-159-11-50-6S
SSGM-I-LCYS-21	0	0.270	EP-08-250AE-350
SSGM-I-LCYS-22	45	0.270	EP-08-250AE-350
SSGM-I-LCYS-23	90	0.270	EP-08-250AE-350
SSGM-I-LCYS-24	135	0.270	EP-08-250AE-350
SSGM-I-LCYS-25	180	0.270	EP-08-250AE-350
SSGM-I-LCYS-26	225	0.270	EP-08-250AE-350
SSGM-I-LCYS-27	270	0.270	EP-08-250AE-350
SSGM-I-LCYS-28	315	0.270	EP-08-250AE-350
TCK-O-LCYS-29	0	0.270	KQSS-116-U-240
HCP-I-LCYS-29	0	0.270	PT-101-15

Instrument ID (Name)	Azimuth Angle (degree)	Vertical Elevation (m)	Sensor Designation
TCK-O-LCYS-30	90	0.270	KQSS-116-U-240
HCP-I-LCYS-30	90	0.270	PT-101-15
TCK-O-LCYS-31	180	0.270	KQSS-116-U-240
HCP-I-LCYS-31	180	0.270	PT-101-15
TCK-O-LCYS-32	270	0.270	KQSS-116-U-240
HCP-I-LCYS-32	270	0.270	PT-101-15
HCP-I-BHD-1	0	-0.064	PT-101-2
PG-I-BHD-1	NA	NA	4040
LC-O-BHD-1	0	-1.600	LW-190
HCP-I-BHD-2	90	-0.064	PT-101-2
PG-I-BHD-2	NA	NA	4040
LC-O-BHD-2	270	-1.600	LW-190
VCP-I-BHD-3	90	-1.143	PT-101-2
LC-O-BHD-3	90	-1.600	LW-190
LC-O-BHD-4	180	-1.600	LW-190
RSG-O-CS-1a	0	3.131	EP-08-250RD-350
RSG-O-CS-1b	0	3.131	EP-08-250RD-350
RSG-O-CS-1c	0	3.131	EP-08-250RD-350
RSG-O-CS-2a	0	2.508	EP-08-250RD-350
RSG-O-CS-2b	0	2.508	EP-08-250RD-350
RSG-O-CS-2c	0	2.508	EP-08-250RD-350
RSG-O-CS-3a	0	1.524	EP-08-250RD-350
RSG-O-CS-3b	0	1.524	EP-08-250RD-350
RSG-O-CS-3c	0	1.524	EP-08-250RD-350
RSG-O-CS-4a	0	0.500	EP-08-250RD-350
RSG-O-CS-4b	0	0.500	EP-08-250RD-350
RSG-O-CS-4c	0	0.500	EP-08-250RD-350
RSG-O-CS-5a	270	3.131	EP-08-250RD-350
RSG-O-CS-5b	270	3.131	EP-08-250RD-350
RSG-O-CS-5c	270	3.131	EP-08-250RD-350
RSG-O-CS-6a	270	2.508	EP-08-250RD-350
RSG-O-CS-6b	270	2.508	EP-08-250RD-350
RSG-O-CS-6c	270	2.508	EP-08-250RD-350
RSG-O-CS-7a	270	1.524	EP-08-250RD-350

Instrument ID (Name)	Azimuth Angle (degree)	Vertical Elevation (m)	Sensor Designation
RSG-O-CS-7b	270	1.524	EP-08-250RD-350
RSG-O-CS-7c	270	1.524	EP-08-250RD-350
RSG-O-CS-8a	270	0.500	EP-08-250RD-350
RSG-O-CS-8b	270	0.500	EP-08-250RD-350
RSG-O-CS-8c	270	0.500	EP-08-250RD-350
RSG-O-CS-9a	180	3.131	EP-08-250RD-350
RSG-O-CS-9b	180	3.131	EP-08-250RD-350
RSG-O-CS-9c	180	3.131	EP-08-250RD-350
RSG-O-CS-10a	180	2.508	EP-08-250RD-350
RSG-O-CS-10b	180	2.508	EP-08-250RD-350
RSG-O-CS-10c	180	2.508	EP-08-250RD-350
RSG-O-CS-11a	180	1.524	EP-08-250RD-350
RSG-O-CS-11b	180	1.524	EP-08-250RD-350
RSG-O-CS-11c	180	1.524	EP-08-250RD-350
RSG-O-CS-12a	180	0.500	EP-08-250RD-350
RSG-O-CS-12b	180	0.500	EP-08-250RD-350
RSG-O-CS-12c	180	0.500	EP-08-250RD-350
RSG-O-CS-13a	90	3.131	EP-08-250RD-350
RSG-O-CS-13b	90	3.131	EP-08-250RD-350
RSG-O-CS-13c	90	3.131	EP-08-250RD-350
RSG-O-CS-14a	90	2.508	EP-08-250RD-350
RSG-O-CS-14b	90	2.508	EP-08-250RD-350
RSG-O-CS-14c	90	2.508	EP-08-250RD-350
RSG-O-CS-15a	90	0.500	EP-08-250RD-350
RSG-O-CS-15b	90	0.500	EP-08-250RD-350
RSG-O-CS-15c	90	0.500	EP-08-250RD-350
LVDT-O-CS-16	0	3.383	GCD-121-2000
LVDT-O-CS-17	0	3.131	GCD-121-2000
LVDT-O-CS-18	0	2.508	GCD-121-2000
LVDT-O-CS-19	0	1.524	GCD-121-2000
LVDT-O-CS-20	0	0.500	GCD-121-2000
LVDT-O-CS-21	270	3.383	GCD-121-2000
LVDT-O-CS-22	270	3.131	GCD-121-2000
LVDT-O-CS-23	270	2.508	GCD-121-2000
LVDT-O-CS-24	270	1.524	GCD-121-2000
LVDT-O-CS-25	270	0.500	GCD-121-2000

Instrument ID (Name)	Azimuth Angle (degree)	Vertical Elevation (m)	Sensor Designation
CD-O-CS-27	0	3.245	BZ-2R72-A2
CD-O-CS-28	0	3.017	BZ-2R72-A2
CD-O-CS-29	0	2.772	BZ-2R72-A2
CD-O-CS-30	0	2.640	BZ-2R72-A2
CD-O-CS-31	0	2.376	BZ-2R72-A2
CD-O-CS-32	0	2.244	BZ-2R72-A2
CD-O-CS-33	0	1.914	BZ-2R72-A2
CD-O-CS-34	0	1.719	BZ-2R72-A2
CD-O-CS-35	0	1.329	BZ-2R72-A2
CD-O-CS-36	0	1.134	BZ-2R72-A2
CD-O-CS-37	0	0.625	BZ-2R72-A2
CD-O-CS-38	0	0.375	BZ-2R72-A2
CD-O-CS-39	90	3.383	BZ-2R72-A2
CD-O-CS-40	90	3.245	BZ-2R72-A2
CD-O-CS-41	90	3.131	BZ-2R72-A2
CD-O-CS-42	90	3.017	BZ-2R72-A2
CD-O-CS-43	90	2.772	BZ-2R72-A2
CD-O-CS-44	90	2.640	BZ-2R72-A2
CD-O-CS-45	90	2.508	BZ-2R72-A2
CD-O-CS-46	90	2.376	BZ-2R72-A2
CD-O-CS-47	90	2.244	BZ-2R72-A2
CD-O-CS-48	90	1.914	BZ-2R72-A2
CD-O-CS-49	90	1.329	BZ-2R72-A2
CD-O-CS-50	90	1.134	BZ-2R72-A2
CD-O-CS-51	90	0.625	BZ-2R72-A2
CD-O-CS-52	90	0.500	BZ-2R72-A2
CD-O-CS-53	90	0.375	BZ-2R72-A2
CD-O-CS-55	180	3.383	BZ-2R72-A2
CD-O-CS-56	180	3.245	BZ-2R72-A2
CD-O-CS-57	180	3.131	BZ-2R72-A2
CD-O-CS-58	180	3.017	BZ-2R72-A2
CD-O-CS-59	180	2.772	BZ-2R72-A2
CD-O-CS-60	180	2.640	BZ-2R72-A2
CD-O-CS-61	180	2.508	BZ-2R72-A2
CD-O-CS-62	180	2.376	BZ-2R72-A2
CD-O-CS-63	180	2.244	BZ-2R72-A2

Instrument ID (Name)	Azimuth Angle (degree)	Vertical Elevation (m)	Sensor Designation
CD-O-CS-64	180	1.914	BZ-2R72-A2
CD-O-CS-65	180	1.719	BZ-2R72-A2
CD-O-CS-66	180	1.524	BZ-2R72-A2
CD-O-CS-67	180	1.329	BZ-2R72-A2
CD-O-CS-68	180	1.134	BZ-2R72-A2
CD-O-CS-69	180	0.625	BZ-2R72-A2
CD-O-CS-70	180	0.500	BZ-2R72-A2
CD-O-CS-71	180	0.375	BZ-2R72-A2
CD-O-CS-73	270	3.245	BZ-2R72-A2
CD-O-CS-74	270	3.017	BZ-2R72-A2
CD-O-CS-75	270	2.772	BZ-2R72-A2
CD-O-CS-76	270	2.640	BZ-2R72-A2
CD-O-CS-77	270	2.376	BZ-2R72-A2
CD-O-CS-78	270	2.244	BZ-2R72-A2
CD-O-CS-79	270	1.914	BZ-2R72-A2
CD-O-CS-80	270	1.719	BZ-2R72-A2
CD-O-CS-81	270	1.329	BZ-2R72-A2
CD-O-CS-82	270	1.134	BZ-2R72-A2
CD-O-CS-83	270	0.625	BZ-2R72-A2
CD-O-CS-84	270	0.375	BZ-2R72-A2

The location of the following gages positioned around the equipment hatch is measured relative to a local coordinate system with radial distances R and angular locations θ specified. Measurement origins are R=0 at the center of the equipment hatch and θ=0 at the top center of the equipment hatch increasing positively clockwise viewed from outside the SCV model.

Instrument ID (Name)	Azimuth Angle θ (degree)	Radial Dist. R (m)	Sensor Designation
RSG-I-EQH-1a	0	0.2600	EP-08-250RD-350
RSG-I-EQH-1b	0	0.2600	EP-08-250RD-350
RSG-I-EQH-1c	0	0.2600	EP-08-250RD-350
STG-I-EQH-2a	0	0.3600	EP-08-125MW-120
STG-I-EQH-2b	0	0.3600	EP-08-125MW-120
STG-I-EQH-2c	0	0.3600	EP-08-125MW-120
STG-I-EQH-2d	0	0.3600	EP-08-125MW-120
STG-I-EQH-2e	0	0.3600	EP-08-125MW-120
SSGH-I-EQH-3	CAG to EQH-2	0.3600	EP-08-125AC-350

Instrument ID (Name)	Azimuth Angle θ (degree)	Radial Dist. R (m)	Sensor Designation
STG-O-EQH-4a	0	0.3600	EP-08-125MW-120
STG-O-EQH-4b	0	0.3600	EP-08-125MW-120
STG-O-EQH-4c	0	0.3600	EP-08-125MW-120
STG-O-EQH-4d	0	0.3600	EP-08-125MW-120
STG-O-EQH-4e	0	0.3600	EP-08-125MW-120
RSG-I-EQH-8a	45	0.3600	EP-08-250RD-350
RSG-I-EQH-8b	45	0.3600	EP-08-250RD-350
RSG-I-EQH-8c	45	0.3600	EP-08-250RD-350
RSG-I-EQH-9a	45	0.4100	EP-08-250RD-350
RSG-I-EQH-9b	45	0.4100	EP-08-250RD-350
RSG-I-EQH-9c	45	0.4100	EP-08-250RD-350
RSG-I-EQH-10a	45	0.4600	EP-08-250RD-350
RSG-I-EQH-10b	45	0.4600	EP-08-250RD-350
RSG-I-EQH-10c	45	0.4600	EP-08-250RD-350
RSG-I-EQH-11a	45	0.5600	EP-08-250RD-350
RSG-I-EQH-11b	45	0.5600	EP-08-250RD-350
RSG-I-EQH-11c	45	0.5600	EP-08-250RD-350
RSG-I-EQH-12a	67.5	0.3600	EP-08-250RD-350
RSG-I-EQH-12b	67.5	0.3600	EP-08-250RD-350
RSG-I-EQH-12c	67.5	0.3600	EP-08-250RD-350
RSG-I-EQH-13a	67.5	0.4100	EP-08-250RD-350
RSG-I-EQH-13b	67.5	0.4100	EP-08-250RD-350
RSG-I-EQH-13c	67.5	0.4100	EP-08-250RD-350
RSG-I-EQH-14a	67.5	0.4600	EP-08-250RD-350
RSG-I-EQH-14b	67.5	0.4600	EP-08-250RD-350
RSG-I-EQH-14c	67.5	0.4600	EP-08-250RD-350
RSG-I-EQH-15a	90	0.2600	EP-08-250RD-350
RSG-I-EQH-15b	90	0.2600	EP-08-250RD-350
RSG-I-EQH-15c	90	0.2600	EP-08-250RD-350
STG-I-EQH-16a	90	0.3600	EP-08-125MW-120
STG-I-EQH-16b	90	0.3600	EP-08-125MW-120
STG-I-EQH-16c	90	0.3600	EP-08-125MW-120
STG-I-EQH-16d	90	0.3600	EP-08-125MW-120
STG-I-EQH-16e	90	0.3600	EP-08-125MW-120
SSGM-I-EQH-17	CAG to EQH-16	0.3600	EP-08-125AC-350
SSGH-O-EQH-18	90	0.3600	EP-08-250AE-350

Instrument ID (Name)	Azimuth Angle θ (degree)	Radial Dist. R (m)	Sensor Designation
RSG-I-EQH-19a	90	0.4100	EP-08-250RD-350
RSG-I-EQH-19b	90	0.4100	EP-08-250RD-350
RSG-I-EQH-19c	90	0.4100	EP-08-250RD-350
RSG-I-EQH-20a	90	0.4600	EP-08-250RD-350
RSG-I-EQH-20b	90	0.4600	EP-08-250RD-350
RSG-I-EQH-20c	90	0.4600	EP-08-250RD-350
RSG-I-EQH-21a	90	0.5600	EP-08-250RD-350
RSG-I-EQH-21b	90	0.5600	EP-08-250RD-350
RSG-I-EQH-21c	90	0.5600	EP-08-250RD-350
RSG-I-EQH-22a	135	0.3600	EP-08-250RD-350
RSG-I-EQH-22b	135	0.3600	EP-08-250RD-350
RSG-I-EQH-22c	135	0.3600	EP-08-250RD-350
RSG-I-EQH-23a	135	0.4100	EP-08-250RD-350
RSG-I-EQH-23b	135	0.4100	EP-08-250RD-350
RSG-I-EQH-23c	135	0.4100	EP-08-250RD-350
RSG-I-EQH-24a	135	0.4600	EP-08-250RD-350
RSG-I-EQH-24b	135	0.4600	EP-08-250RD-350
RSG-I-EQH-24c	135	0.4600	EP-08-250RD-350
RSG-I-EQH-25a	135	0.5600	EP-08-250RD-350
RSG-I-EQH-25b	135	0.5600	EP-08-250RD-350
RSG-I-EQH-25c	135	0.5600	EP-08-250RD-350
RSG-I-EQH-26a	180	0.2600	EP-08-250RD-350
RSG-I-EQH-26b	180	0.2600	EP-08-250RD-350
RSG-I-EQH-26c	180	0.2600	EP-08-250RD-350
SSGH-I-EQH-27	CAG to EQH-28	0.3600	EP-08-125AC-350
STG-I-EQH-28a	180	0.3600	EP-08-125MW-120
STG-I-EQH-28b	180	0.3600	EP-08-125MW-120
STG-I-EQH-28c	180	0.3600	EP-08-125MW-120
STG-I-EQH-28d	180	0.3600	EP-08-125MW-120
STG-I-EQH-28e	180	0.3600	EP-08-125MW-120
SSGM-O-EQH-29	180	0.3600	EP-08-250AE-350
RSG-I-EQH-30a	180	0.4100	EP-08-250RD-350
RSG-I-EQH-30b	180	0.4100	EP-08-250RD-350
RSG-I-EQH-30c	180	0.4100	EP-08-250RD-350
RSG-I-EQH-31a	180	0.4600	EP-08-250RD-350
RSG-I-EQH-31b	180	0.4600	EP-08-250RD-350

Instrument ID (Name)	Azimuth Angle θ (degree)	Radial Dist. R (m)	Sensor Designation
RSG-I-EQH-31c	180	0.4600	EP-08-250RD-350
SSGM-I-EQH-33	210	0.3600	EP-08-250AE-350
SSGH-I-EQH-34	210	0.3600	EP-08-250AE-350
SSGM-I-EQH-35	240	0.3600	EP-08-250AE-350
SSGH-I-EQH-36	240	0.3600	EP-08-250AE-350
STG-I-EQH-37a	270	0.3600	EP-08-125MW-120
STG-I-EQH-37b	270	0.3600	EP-08-125MW-120
STG-I-EQH-37c	270	0.3600	EP-08-125MW-120
STG-I-EQH-37d	270	0.3600	EP-08-125MW-120
STG-I-EQH-37e	270	0.3600	EP-08-125MW-120
SSGM-I-EQH-38	270	0.3600	EP-08-250AE-350
SSGM-I-EQH-39	300	0.3600	EP-08-250AE-350
SSGH-I-EQH-40	300	0.3600	EP-08-250AE-350
SSGM-I-EQH-41	330	0.3600	EP-08-250AE-350
SSGH-I-EQH-42	330	0.3600	EP-08-250AE-350
SSGH-O-EQH-43	270	0.3600	EP-08-250AE-350
RSG-I-EQH-44a	95	0.3600	EP-08-250RD-350
RSG-I-EQH-44b	95	0.3600	EP-08-250RD-350
RSG-I-EQH-44c	95	0.3600	EP-08-250RD-350
RSG-I-EQH-45a	265	0.3600	EP-08-250RD-350
RSG-I-EQH-45b	265	0.3600	EP-08-250RD-350
RSG-I-EQH-45c	265	0.3600	EP-08-250RD-350
TCK-O-EQH-46	180	0.220	KQSS-116-U-240
RSG-I-EQH-47a	270	0.520	EP-08-250RD-350
RSG-I-EQH-47b	270	0.520	EP-08-250RD-350
RSG-I-EQH-47c	270	0.520	EP-08-250RD-350
TCT-I-EQH-47	85	0.280	CO3-T
TCT-I-EQH-48	275	0.280	CO3-T

Section ii. SCV Instrument Drawings

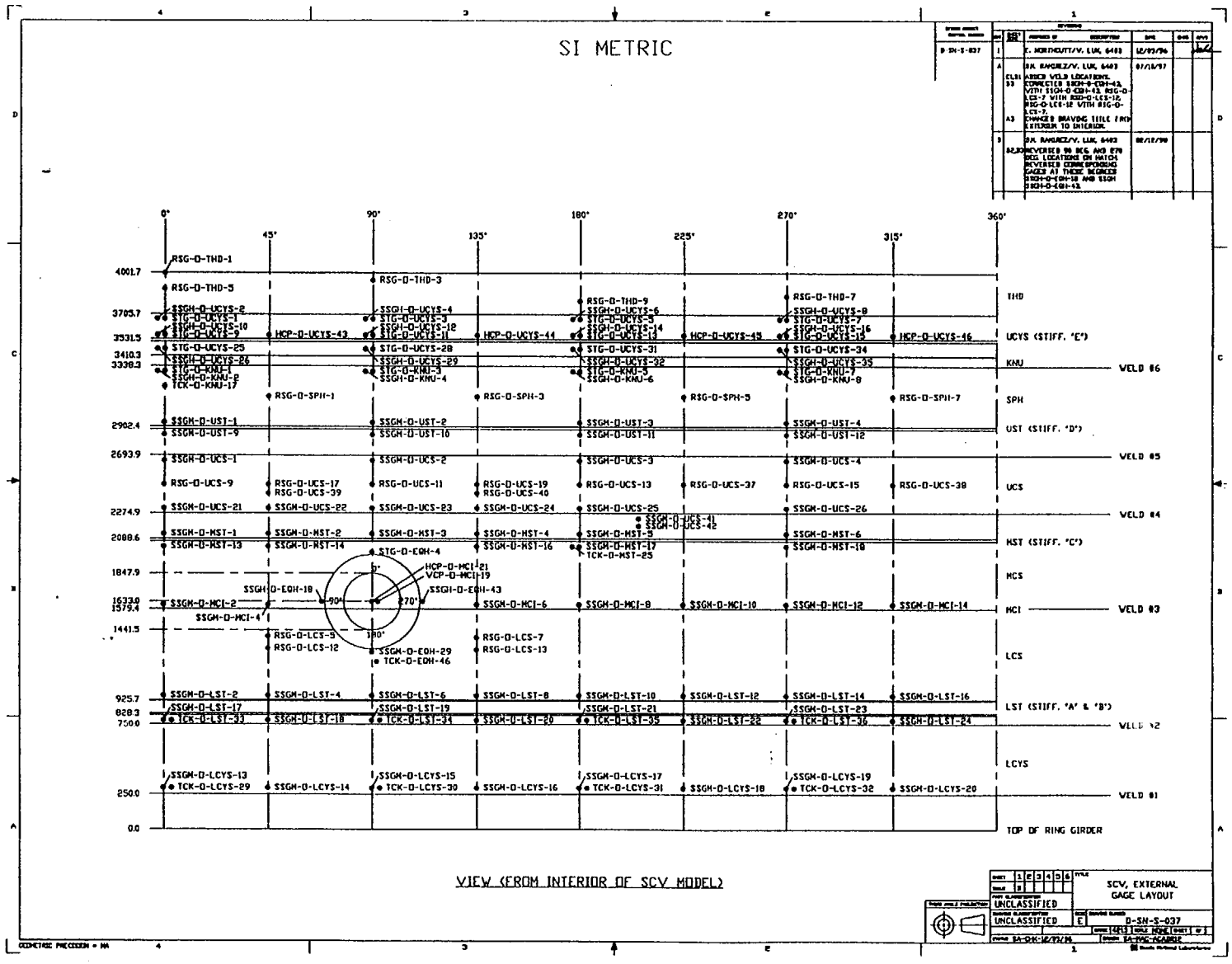

Figure D.3 Steel containment vessel (SCV) external gage layout.

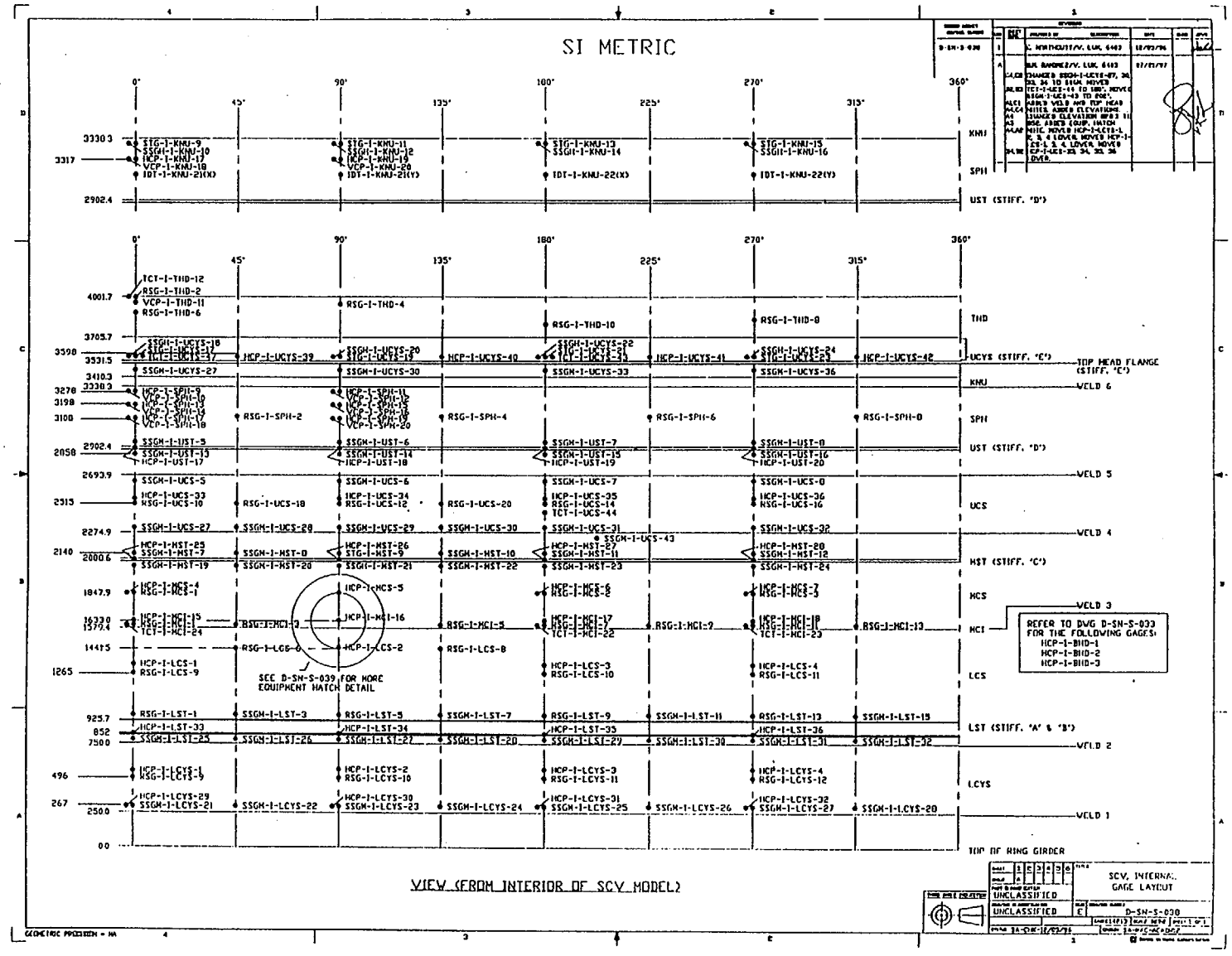

Figure D.4 Steel containment vessel (SCV) internal gage layout.

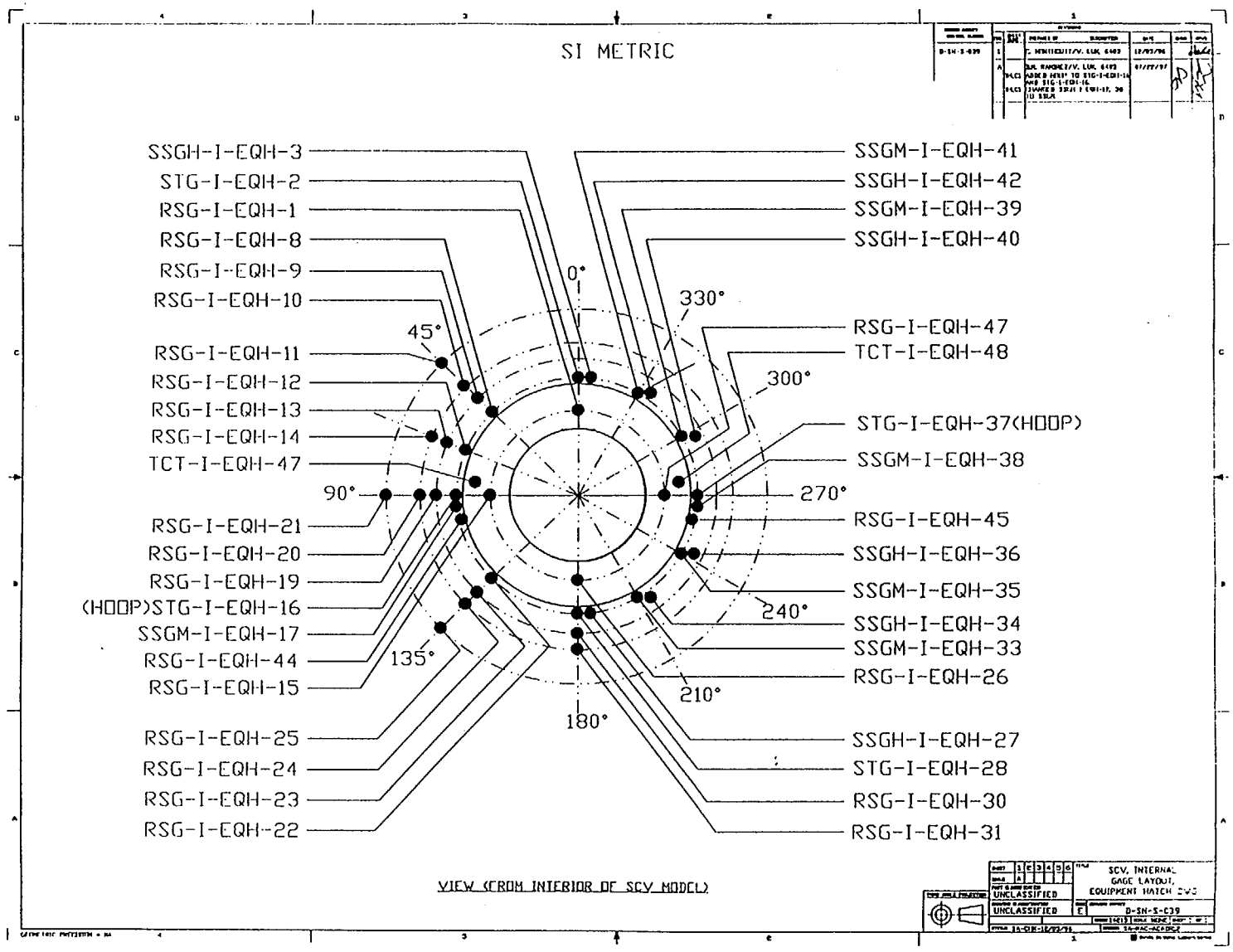

Figure D.5 Steel containment vessel (SCV) internal gage layout around equipment hatch.

Appendix E

Input/Output Structure for the SCV/DAS Software Package

Section i. File Structure Description

There were two basic sets of input/output files in the DAS software package:

1. a configuration file that provided the necessary input data to the DAS software, and
2. data files into which the recorded data were placed.

Section ii. Data File Structure

The output data file structure was designed to allow plotting of selected segments of data with a standard plotting software. This file structure has the following features:

1. providing the users with a clear link between the columns of numbers in a data file and the location and type of instrument originating the data,
2. using nomenclature for naming the files with the following information:

   (a) nature of the data contained and (b) specific type of instruments represented in the files.
3. generating an easily accessible set of files for archival purposes anticipating future inquiries for analysis and presentation.
4. facilitating rapid data correction and post-processing.

Two separate folders below a "main" data folder organize the data files. The folder structure is shown in Figure E.1.

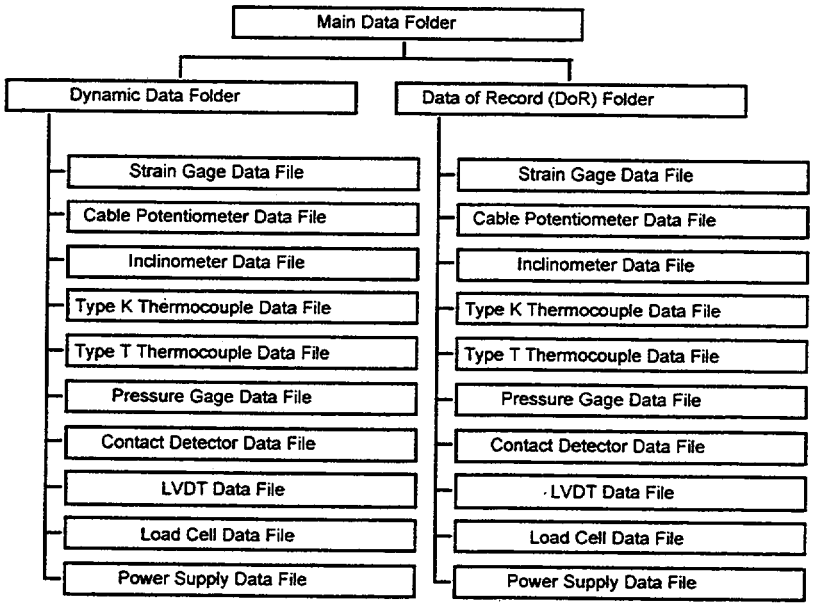

Figure E.1 Data file folder structure.

All data from the high pressure test were stored as *raw* data signals (i.e., defined as the output of the analog-to-digital conversion steps in the DAS process). Posttest data reduction was performed to convert the raw data into

the reduced data with selected engineering units. Table E.1 lists the raw and reduced data units for the instruments used in the SCV model test.

Table E.1 Description of Raw and Reduced Data for the SCV Model Test

Instrument Type	Raw Data Units	Reduced Data Units
strain gage	strain or micro-strain (depending on gage factor format)	percent strain
cable-type displacement transducer	DC volts	displacement (mm)
LVDT	DC volts	displacement (mm)
inclinometer-type displacement transducer	DC volts	tilt angle (°)
thermocouple	temperature (°C)	same as raw
contact detectors	DC volts	same as raw
pressure gage	DC volts	pressure (MPa)
load cells	DC volts	load (Newton's)
power supplies	DC volts	same as raw (data used to reduce instrument voltages to CPOT distances)

It should be noted that the raw data in this table indicate the nature of the data signal collected from the mainframe without any processing. The data from some of the instruments were used to "compensate" or "correct" the raw data from other instruments for the purposes of optimizing data accuracy. Figure E.2 illustrates the basic data flow diagram for the SCV model test.

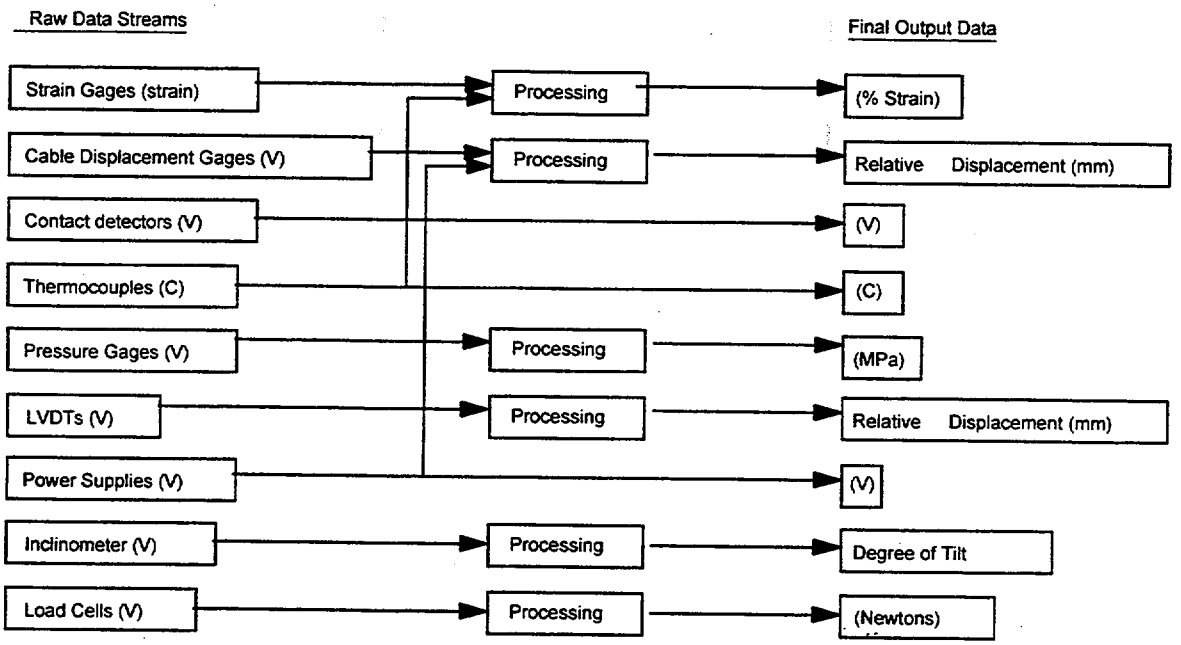

Figure E.2 Basic SCV data flow diagram.

Appendix F

High Pressure Test Data Correction

F.1 Introduction

This chapter describes the procedures used to correct the raw test data. Appendix D details the location and orientation of every instrument.

F.2 High Pressure Test Data

Two sets of data, a dynamic pressure set and a Data of Record (DoR) set, were collected during the steel containment vessel (SCV) high pressure test. For the former set, data scans for all instruments were taken continuously throughout the duration of the test. For the latter set, the system was allowed to reach steady-state conditions before the "data of record" were scanned and stored. Appendix G contains the test data files for the corrected DoR package from the SCV high pressure test. Data from 13 categories of gages are included:

- contact detectors
- horizontal displacement transducers
- tilt sensors
- load cells
- LVDTs
- pressure gages
- rosette strain gages
- single element strain gages - hoop direction
- single element strain gages - meridional direction
- strip gages
- type K thermocouples
- type T thermocouples
- vertical displacement transducers

Data from each gage are plotted against the high pressure test's pressure history data. There is one plot per gage and, in general, one gage per plot. The exceptions to this format are the 3-element rosette gages and the 5-element strip gages. For these two categories, all of the elements of one complete gage are plotted on the same plot. The plots are organized according to the gage types listed above. They are also sequentially numbered in each gage-type section.

It is important to note that the pressure values shown in all of the data plots represent gage pressure not absolute pressure.

After correcting the data for various effects, the data were converted into engineering units. Details on the corrections are contained in Section F.3. Appendix G provides a detailed description of the data files.

It is important to note that there are three misnamed gages: SSGH-I-EQH-17, SSGH-I-EQH-38, and SSGM-O-EQH-43. The first two gages actually measure meridional strain and are associated (cross-axis) with strip gages STG-I-EQH-16 and STG-I-EQH-37, respectively. The SSGM-O-EQH-43 gage is actually a hoop gage not a meridional gage.

Appendix G also contains the calculated equivalent plastic strains for the rosette gage data. Section F.4 presents the equations used to obtain these.

For the rosette gages, there are three elements per gage. These elements are labeled a, b, and c, and indicate hoop strain, meridional strain, and the strain at 45°, however not in that order. For the rosette gages contained in the **exterior** of the SCV model (gage names of the type: RSG-O-XXX-XXX), the element labeled "a" indicates the hoop strain and the element labeled "c" indicates the meridional strain. With the exception of the 24 gages listed below, for the rosette gages contained in the **interior** of the SCV model (gage names of the type: RSG-I-XXX-XXX), the element labeled "a" indicates the meridional strain and the element labeled "c" indicates the hoop strain. For all but one rosette gage, element "b" indicates the strain at 45°.

The first exception is gage RSG-I-EQH-45. For this gage, element "a" indicates the 45° strain, element "b" indicates the hoop strain, and element "c" indicates the meridional strain.

As noted, there are 23 more interior rosette gages that do not follow the standard direction convention given above. For this group of gages, element "a" indicates hoop strain, and element "c" indicates meridional strain. The affected gages are listed below.

RSG-I-EQH-1
RSG-I-EQH-8
RSG-I-EQH-9
RSG-I-EQH-10
RSG-I-EQH-11
RSG-I-EQH-12
RSG-I-EQH-13
RSG-I-EQH-14
RSG-I-EQH-15
RSG-I-EQH-19
RSG-I-EQH-20
RSG-I-EQH-21
RSG-I-EQH-22
RSG-I-EQH-23
RSG-I-EQH-24
RSG-I-EQH-25
RSG-I-EQH-26
RSG-I-EQH-30
RSG-I-EQH-31
RSG-I-EQH-44
RSG-I-LST-1
RSG-I-LST-9
RSG-I-LST-13

F.3 Data Corrections

This section presents the corrections made to the SCV high pressure test DoR data, including corrections to compensate for temperature effects, reference point movement, and such. Standard data reduction from raw data (usually volts) to engineering units is not discussed.

F.3.1 Corrections Made to Strain Gage Raw Data

Basic strain data reduction is accomplished through two major steps: (1) firmware reduction from measurements of the bridge-balancing voltages to values of strain and (2) post-test data corrections to compensate for various effects (i.e., temperature effects).

The former of these major steps will not be discussed here except to note that the data acquisition firmware automatically converts the voltages received from the strain gages to strain data. Therefore, for the SCV test, the raw data from strain gages are in microstrain.

The latter of the two major reduction steps (referred to here as the data corrections) will be discussed in the following sections.

The least count requirement for the strain gages used in this test was ± 0.01 % strain. The data acquisition system used in the SCV high pressure test recorded seven significant digits for each data point. This is not meant to imply that the data are believed to be accurate to that extent. A study on the uncertainty of the data from the various instruments yielded uncertainty ranges for each type of gage used. The results of this study can be seen in Appendix B of the report on SCV Model High Pressure Test Data[1].

The strain gage raw data obtained during the SCV high pressure test are in the units of microstrain. Three types of data correction were performed on the raw strain gage data. These are corrections for gage-specific factors, corrections for temperature effects, and corrections for transverse sensitivity.

F.3.1.1 Instrument-Specific Gage Factor Correction

The data acquisition system (DAS) used in the SCV high pressure test assumed a gage factor (GFAC) of 2.0 for all strain gages. This value was used in the internal firmware of the DAS hardware to determine the strain values output by the system. However, each strain gage has associated with it a specific gage factor, which is identified and provided by the manufacturer. The data from each gage were corrected after the test to reflect the correct (GFAC) for that gage.

F.3.1.2 Corrections for Temperature Effects

There are two corrections that may be made for temperature effects on strain gages. The first is an adjustment of the strain gage data for apparent strain. Apparent strain is a value of strain that appears in the raw data as an artifact of the temperature at which the data were taken. This strain amount must be removed from the raw data to compensate for this effect. If the strain readings were taken at the temperature at which the strain gages were calibrated, there would be no apparent strain.

Although the strain of interest in the SCV high pressure test was that strain caused by pressure-induced expansion of the model, no attempt was made to eliminate from the strain data the amount of strain caused by thermal expansion of the model.

The second correction for temperature effects, a correction to adjust the gage specific gage factor (GFAC) for temperature, was not done. For each gage, the manufacturer provides a GFAC, a factor determined at a temperature of 24°C. The GFAC value will change with temperature. The maximum temperature read by the suite of thermocouples used in the SCV high pressure test was 34.3°C. Using the curves provided by the gage manufacturer and this maximum temperature value, the maximum change due to temperature effects in the GFAC for any gage would be 0.0794% of the strain reading. Given the specified gage accuracy (uncertainty), this set of corrections to the GFACs was not done.

F.3.1.3 Corrections for Transverse Strain Sensitivity

The final set of corrections performed on the strain gage data involved correcting for transverse strain sensitivity. These corrections were performed only for the rosette gage data and the strip gage data. For the latter we had previ-

---

[1] Rightley, G. S., "Steel Containment Vessel Model High Pressure Test Data," Project Report No. R-SN-S-006, Rev. C, Sandia National Laboratories, NM, January 1998.

ously identified cross-axis gages (of the type SSGH) for use in these corrections. Transverse sensitivity refers to the response of the gages due to cross axis strain.

F.3.1.4 Failure of Cross-Axis Gages

In some cases, the cross-axis gage that was used for a rosette or strip gage transverse sensitivity correction failed while the primary gage itself continued to record valid data. In these cases, the rosette or strip gage data was not corrected for transverse sensitivity for times after failure of the cross-axis gage.

F.3.2 Corrections Made to Cable Potentiometers

F.3.2.1 General Corrections

Each cable potentiometer (CPOT) has a specific sensitivity factor. This sensitivity is of the form $mV/(V*in)$. The signal in mV is normalized by the excitation voltage and divided by the sensitivity factor to obtain the CPOT length in inches. It is necessary to monitor the excitation voltage used for each measurement.

For each cable potentiometer location, the *initial length reading* must be algebraically combined with each subsequent reading to provide the differential displacement throughout the experiment. For all vertically oriented CPOTs and for all external, horizontal CPOTs this was done immediately after reduction to engineering units. For the internal, horizontal CPOTs this was done later, as will be explained.

The geometry showing the general reduction of the CPOT data is shown in Figure F.1. It should be noted that this assumes that the angle between the cable's original horizontal line and its displaced line is small so that the true horizontal and vertical components of the displacement are equal to the indicated displacement.

The axes and nomenclature are shown in Figure F.2.

F.3.2.2 Corrections for Movement of Central Support Column

Each interior cable displacement measurement was corrected for the rigid body motion of the central support column. This was accomplished by monitoring the motion of the central column.

The central column motions monitored were:

1. rotation of the column about horizontal orthogonal axes at its base,
2. translation of the column along these same two axes and
3. translation of the column vertically due to ring support deformation.

The following data were collected for this purpose:

1. *tilt* of the column in two axes
2. *X-axis displacement* of the column,
3. *Y-axis displacement* of the column and
4. *Z-axis displacement* of the column

The following items were also used for correction of the internal, horizontal displacement measurements (after conversion from their raw, DC volts, form).

1. height of gage from base of column, H_{gage}

2. angular location of gage, θ_{gage}, measured from the 0° cardinal line, clockwise positive.

In Figure F.2, positive x, y, and z are shown and θy is positive clockwise with respect to the positive y-axis, and θx is positive clockwise with respect to the positive x-axis.

The correction to any internal displacement measurement can be presented in distinct segments based on the horizontal plane translational motion, the vertical translation, and the rotation about the column base.

(Note that the correction must be applied to each measurement of displacement, and it must be applied based on the column motion data taken during the same scan, i.e., at the same moment in time, as the original displacement data.)

F.3.2.3 Correction for Horizontal Plane Translations

This correction was performed only on the internal, horizontal CPOT data. This correction involved an algebraic combination of the readings of the x- and y-axis displacements of the central column with the x- and y-axis components of the initial reading of each displacement gage.

F.3.2.4 Correction in Vertical Displacement Measurements for Vertical Translations

The correction for this gage measurement is a straightforward combination of the vertical displacement recorded and the vertical translation experienced by the central column base. See Figure F.3.

F.3.2.5 Correction in Horizontal Displacement Measurements for Vertical Translations

A sketch of the geometry for this case is shown in F.4. Note that the motion imparts an elongation of the cable-type displacement transducer. Vertical displacement measurements of the attachment point would be required to resolve this issue.

A study was done which showed that the maximum effect of this motion on the displacement values was ±0.8%. Thus, corrections of this type were not performed on the SCV data.

F.3.2.6 Correction in Vertical Displacement Measurements for Horizontal Plane Translations

In a similar manner, the correction for vertical displacement given horizontal plane motion of the column was not performed.

F.3.2.7 Correction for Rigid-Body Rotations

The corrections for the rigid body rotations of the central column were not done. The data from the SCV high pressure test showed that there was negligible rotation of the column.

F.4 Calculated Data

Once the data from the rosette gages were checked and verified, an additional set of calculations was done. First, the principal strains experienced throughout the test by each rosette gage were calculated. Then these principal strains were used to determine the equivalent plastic strains seen.

F.4.1.1 Principal Strains

The equation for principal strains for a 3-element rectangular rosette gages is shown in Equation 1.

$$\varepsilon_{p,q} = \frac{1}{2}\left[\varepsilon_1 + \varepsilon_3 \pm \sqrt{(\varepsilon_1 - \varepsilon_3)^2 + (2\varepsilon_2 - \varepsilon_1 - \varepsilon_3)^2}\right] \quad (1)$$

Where ε_1 and ε_3 are the gage elements located 90° apart and ε_2 is the element located at 45°.

F.4.1.2 Equivalent Plastic Strains

The principal strains, ε_p and ε_q, can be used to compute the equivalent plastic strain from rosette gage data. Assume that the elastic part of the strain is negligible. (This assumption is valid for values of equivalent plastic strain, ε^P, considerably greater than the yield strain.) Equation 2 may be used to perform the calculation.

$$\varepsilon^P = 2\sqrt{\frac{\left(\varepsilon_p{}^2 + \varepsilon_q{}^2 + \varepsilon_p \varepsilon_q\right)}{3}} \quad (2)$$

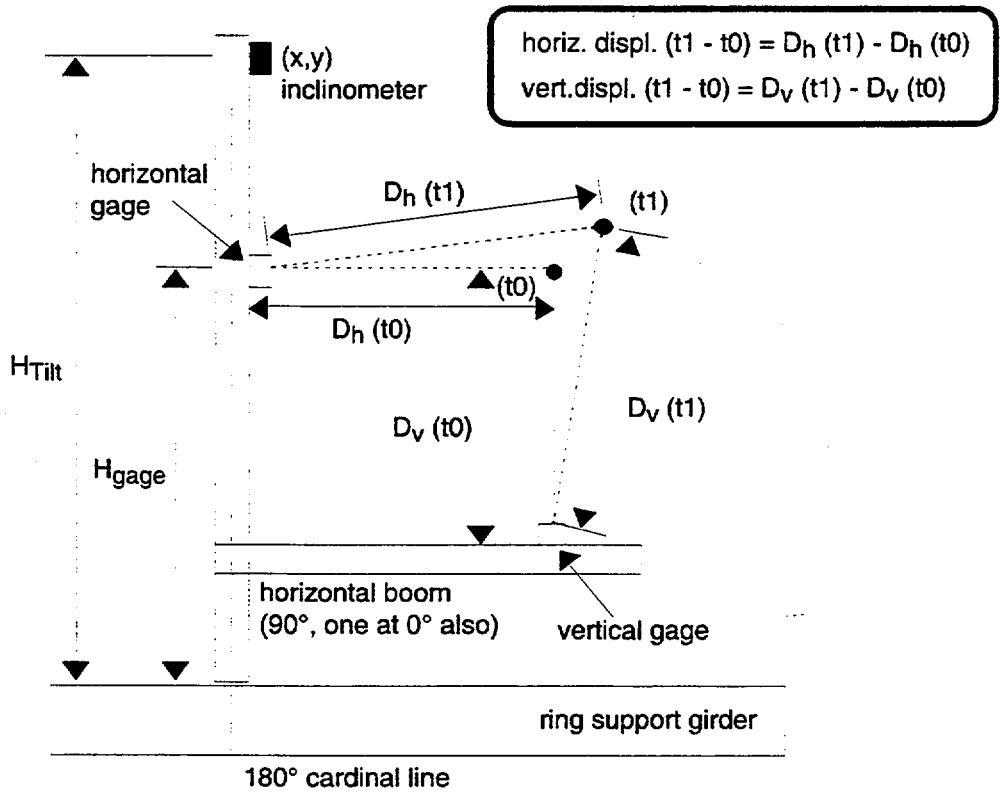

Figure F.1 Displacement measurements (showing offset subtraction).

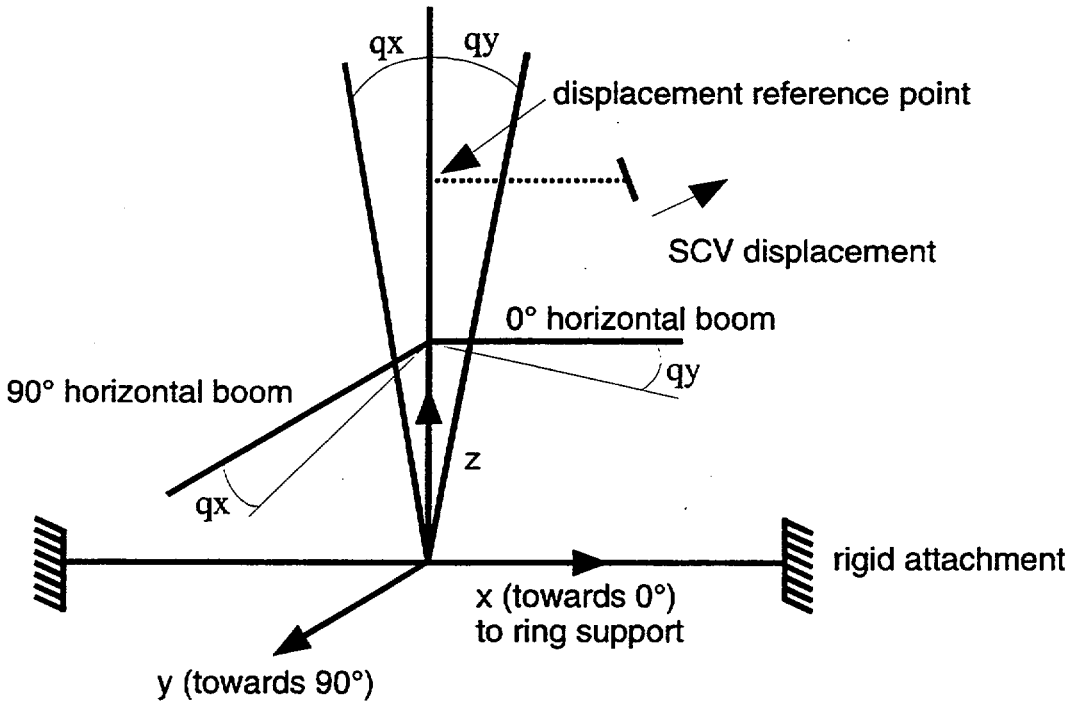

Figure F.2 Central column motion measurements.

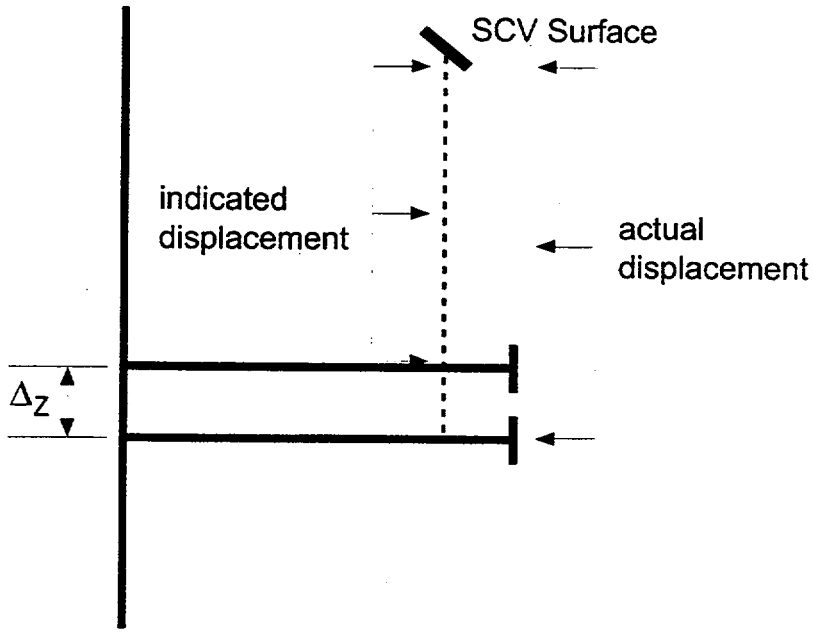

Figure F.3 Geometry for vertical translation of central column - vertical gages.

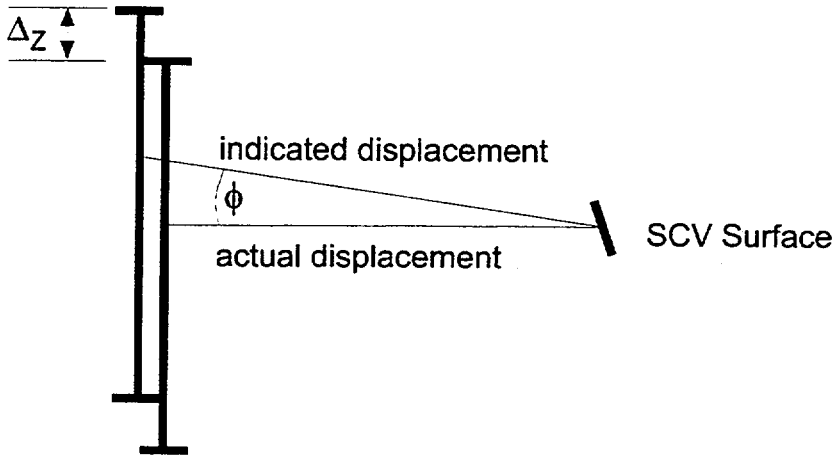

Figure F.4 Geometry for vertical translation of central column - horizontal gages.

Appendix G

Test Data Files for the High Pressure Test

SCV High Pressure Test Data

On the enclosed CD, there are the data files containing the corrected DoR data from the SCV high pressure test. Additionally, the dynamic data pressure file is included to provide a full history of the SCV model pressure during the high pressure test.

The data in these files have been corrected and checked.

These files are Microsoft Excel files. Each file contains several worksheets. In each file one worksheet contains the data in column format. The other worksheets in each file are plots of the data. On the worksheet containing the listed data, there are a time column (minutes), a pressure column (MPa), and columns of data for the gages of the type specified in the file name. Each file name is comprised of the gage type and the units for the gage data in the file. See below for more detail.

SCV High Pressure Test Data Files

CD_VOLTS.XLS	contains the contact detector data in volts
hcp_mm.XLS	contains the horizontal displacement gage data in mm, all data is with respect to a global coordinate system, this means that a positive displacement indicates the SCV vessel growing outward, a negative displacement indicates the SCV pulling inward
IDT_DEGR.XLS	contains the central column tilt sensor data in degrees of offset
LC_Newtons.XLS	contains the load cell data in Newtons
LVDT_mm.XLS	contains the LVDT data in mm (gap closure)
PG_DOR_MPa.XLS	contains the DoR pressure gage data in MPa
PG_dynamic_MPa.XLS	contains the dynamic pressure gage data in MPa
TCK_DEGREES.XLS	contains the type K thermocouple data in degrees C
TCT_DEGREES.XLS	contains the type T thermocouple data in degrees C
VCP_mm.XLS	contains the vertical displacement gage data in mm

Strain Gage Data are in Percent Strain

RSG_1 _%.XLS	contains some of the rosette strain gage data
RSG_2 _%.XLS	contains the rest of the rosette strain gage data
SSGH _%.XLS	contains the single strain gage data in the hoop direction
SSGM _%.XLS	contains the single strain gage data in the meridional direction
STG _%.XLS	contains the strip gage data

IMPORTANT: Please note that the two misnamed MERIDIONAL gages, SSGH-I-EQH-17 and SSGH-I-EQH-38, are located in the SSGH _%.dat file NOT in the SSGM _%.dat file. The strip gages that are associated with these meridional gages are STG-I-EQH-16 and STG-I-EQH-37. Remember that these strip gages are recording HOOP

strains not meridional strains like the rest of the strip gages. Also, note that the misnamed HOOP gage, SSGM-O-EQH-43, is located in the SSGM_%.dat file NOT in the SSGH_%.dat file.

An additional file was added to this CD.

EPS_corrected.dat. contains the time and pressure for the DoR readings plus the calculated equivalent plastic strain values from the corrected rosette gage data taken during the high pressure test.

Appendix H

Acoustic Emission Results

H.1 Introduction

An acoustic emission source location system, which operated independently of the other instrumentation data channels, was used to monitor the entire surface of the steel containment vessel (SCV) model above the ring support girder. The purpose of the acoustic monitoring was to detect and approximately locate emission sources that occurred in the shell of the SCV model during the high pressure test in real time and then to try to gain additional information on the model response through the posttest analysis.

In the SCV model, the sources of acoustic emission were primarily crack initiation and flaw growth, and secondarily spallation or fracture of corrosion particles and rubbing of adjacent surfaces when the SCV model made contact with the contact structure. When an emission occurred, one or a group of sensors would detect it, and the associated computer program would calculate the approximate location of its source.

Several terms that are unique to the acoustic emission testing are introduced here. A hit is registered when the acoustic system is triggered by an acoustic wave with an amplitude that exceeds a preset threshold passes underneath a sensor. When several sensors are triggered by the same acoustic wave at times consistent with travel from a single point on the SCV model, the data set is called an event. If the time data from an event are used to calculate a location on the SCV model and the calculated location is consistent with acoustic travel times to at least the first six sensors hit, the event is called a located event.

H.2 Acoustic Emission Sensors

The acoustic emission system had 24 sensors that were applied to the SCV model with magnetic hold-downs and acoustically coupled with silicone vacuum grease. Locations of the sensors are given in Table H.1. The meridional distances were measured along the interior or exterior surface of the model, starting from the ring support girder. Sensors 1–16 and sensors 22 and 23 were mounted inside the model because the contact structure prevented their placement on the outside. Figure H.1 provides a schematic of the sensor locations. Sensors 17–21 were mounted on the outside of the model above the contact structure. Sensor 24 was mounted in the middle of the equipment hatch on the outside.

H.3 Real-Time Test

The acoustic emission system was a part of the high pressure test of the SCV model. The pressurization curve for the high pressure test recorded by the acoustic emission system is shown in Figure H.2. During the initial gas flow, there was excessive acoustic emission. The gas flow noise stopped at about 0.35 Mpa, and the first located emission was detected at 0.44 MPa (64 psi). Figure H.3 shows the events located by the top and the bottom sensor arrays during the test. Figure H.4 shows curves of the total signal strength from the located events versus the pressure for the two arrays. There is an apparent change in the slope of the curves around 3.5 MPa (508 psi) and an increase in the acoustic emission rate above this pressure level, but there were no serious changes until the appearance of a major leak at 4.62 MPa (672 psi). After the leak started, no more located events were detected. However, the leak produced large amounts of acoustic emission. Figure H.5 is a graph of the total signal strength, as a function of pressure, from all the hits during the test. The noise of flowing gas during the start of pressurization and the leak noise at the end of the test are quite obvious. These two events generated most of the acoustic emission during the test.

The posttest examination of the interior of the SCV model showed a tear in the wall near the equipment hatch. The acoustic emission system did detect activity from the area near this tear. It can be seen in Figure H.3 as the group of events in the center of the triangle formed by sensors 2, 5, and 6. However, this activity did not appear any worse than several other areas shown in Figure H.5. The posttest metallographic examination of the tear showed that it was primarily ductile in nature. Ductile tears produce fewer and lower amplitude emissions than do brittle tears. The metallographic results explain why the acoustic emissions associated with the tear were not distinguishably recognized during the high pressure test.

Table H.1. Acoustic System Sensor Locations for the SCV Model High Pressure Test

Sensor	Meridional Distance (mm)	Azimuth Angle (Degrees)	Sensor	Meridional Distance (mm)	Azimuth Angle (Degrees)
1	510	[illegible]	13	3400	45
2	515	94	14	3400	135
3	515	177	15	3400	225
4	510	274	16	3400	315
5	1650	41	17*	3805	351
6	1670	131	18*	3805	90
7	1670	221	19*	3805	171
8	1670	311	20*	3805	270
9	2690	356	21*	37 mm from top head center	225
10	2690	96	22	1210	67
11	2675	176	23	1215	113
12	2665	276	24*	center of equipment hatch	

* indicates that sensor was located on the exterior of the model.

H.4 Posttest Analysis

Posttest analysis of the acoustic emission data from the high pressure test was done for several reasons. Accurate calculation of the locations of the acoustic emission sources allowed use of a clustering algorithm to determine locations where critical structural damage might occur during the test. It also allowed determination of the pressure dependence of the acoustic emission from each of the clusters.

The first problem in the posttest analysis was to determine which collections of hits constituted an event. The most important point in determining an event is to find the first sensor hit, which signals the starting time for the event. For the SCV model, an event definition time, which is the time interval between the detection of the first and the last hit in an event, of 2.0 milliseconds was chosen. A manual search of the data and the selected hits for each event showed this interval to be a reasonable selection.

At a minimum three sensors are required to be hits in order to locate an emission source on a plane. The initial time of an event and the x and y coordinates of the source are needed for accurate data. Because the acoustic emission data are not very accurate in the high pressure test, a fixed trigger level was used to produce uncertainties in the calculated time of arrival at the sensor. Two methods of alleviating some of these uncertainties were used in this analysis. First, an over-determined data set was used when possible. The values from the first six sensors on the cone that were hit comprised the event data set. If six sensors were not hit, data from as few as three were used. A nonlinear least squares fitting program was used to calculate the most probable location of the source. This program also calculated a goodness of fit parameter for the calculated answer. Data sets that had a goodness of fit parameter of less than 0.85 and those whose calculated location was more than 1400 mm away from the center of the triangle formed by the first three sensors hit were not included in the set of located events.

The second method of reducing the uncertainty in the locations was to use a simple procedure developed by Ge and Kaiser[1] to determine what acoustic velocity should be used for the travel time from the source to each sensor that was hit. In the high pressure test, an extensional velocity was assumed for the waves to all sensors. The sensors that could not have had an extensional velocity were assigned the flexural velocity. Those whose arrival times were later than 10% greater than the flexural velocity would have allowed were dropped from the data set. If the calculation with these velocities did not have a goodness-of-fit parameter that exceeded 0.85, a flexural velocity was assumed for all sensors. If the parameter still did not exceed 0.85 with all flexural velocities, that event was not included in the set of located events.

To simplify the problem of locating an emission source on a plane, the conical section of the SCV model that is made of a thin steel shell was theoretically cut along the zero degree longitude and the surface unrolled onto a plane, without distorting the conical surface. The cylindrical surface below the cone was also treated on the same plane as the cone. The distortion produced by this procedure was not thought to have a significant effect on the location of the events on the cylindrical surface. The spherical surface above the conical section was treated as either a cone or a slice of a sphere. The head of the model was treated as a cylinder with a hemisphere on its top. These two latter approximations proved unnecessary because of the small number of widely scattered events originating on these surfaces. The events on these surfaces were calculated using a planar approximation of a surface within the triangle formed by the three first-hit sensors.

A total of 446 events out of 650 data sets on the conical section met the criteria and were kept in the set of located events. Many of the discarded events were either of very low amplitude or appeared to be mixed with another event. The accuracy of the location calculations was approximately ±50 mm. This uncertainty is produced primarily by the uncertainties in the triggering points on the individual waveforms. The uncertainty due to a finite shell thickness is 10 mm or less.

A cluster-seeking program was used to determine the nature of acoustic emissions. A cluster is defined as a collection of located events placed within a confined area. A crude estimate of the area of the conical plus cylindrical sections divided by the number of located events gave a rough density of one event per 7000 mm^2. It was decided that a cluster should have at least ten times that density. A circle with a radius of 100 mm was chosen as the smallest area in light of the uncertainty in the location accuracy. The criterion for the existence of a cluster was then set as four or more events within this area. As each location was calculated, the program checked whether it was within 100 mm of any other location. Two locations within this distance form the nucleus of a cluster. The center of the cluster is then calculated. Each succeeding center was investigated to check whether it was within 100 mm of another cluster center. If it was within the 100 mm separation, it was added to the cluster and a new center was then calculated. A growing flaw will show a steady or increasing emission rate as the stress field is increased. A source that does not emit with increasing stress field is either an arrested flaw or an event which does not affect the structural integrity of the model, such as a corrosion particle flaking off. Therefore, if the cluster did not contain at least one event at a pressure greater than 90% of the failure pressure, it was not defined a significant cluster.

Figure H.6 is a map of the flattened conical section with the cylindrical attached skirt, and it identifies all located events and the significant clusters superimposed over the events. Included are the positions of the sensors, the two detected tears in the SCV model, and the stiffener ring. A group of overlapping clusters is counted as one cluster, and all clusters are identified with a letter. In cluster D, the two clusters do not touch but both appear associated with the structural damage lying between them.

The total signal strength is shown in Figure H.4 as a function of pressure for the entire test. Figure H.7 shows the total signal strength as a function of pressure for clusters A, B, C, and D, which are the largest clusters, graphed on the same scale. The curves for clusters E, F, and G were very similar to the Cluster D curve. The curve for Cluster H had about half the envelope strength of Cluster D, and the curves for clusters I and J were each composed of four very small events around 4.5 MPa. These curves show the severity of the clusters, and each curve provides the information on the pressure level for the onset of flaw growth. In addition, the number of located events in each 50-

[1] M. Ge and P. K. Kaiser, "Interpretation of Physical Status of Arrival Picks for Microseismic Source Location," Bulletin of the Seismological Society of America 80, 6, pp. 1643–1660, 1990.

mm-high slice of the conical section and skirt is shown Figure H.8. The peak of this curve corresponds to the position of the stiffening ring.

The nine events located on the spherical slice were well scattered. No two events were close enough to form a cluster according to the chosen definition. Only one occurred above 4.4 MPa. The 21 events detected from the top head were scattered over seven of the triangles formed by sensors in the region. Three triangles had four or more events in them. In two of these triangles, the events were well scattered, both in space and pressure. In the third triangle, formed by sensors 13-17-18, there were four events located within a cluster radius of 20 mm. However, the highest pressure event in this cluster occurred at 3.65 MPa, so the cluster was not attributed to any structural problems.

H.5 Discussion

The only significant acoustic emissions occurred in the conical section and, to a lesser extent, the cylindrical skirt. The top head, the spherical slice, the knuckle region and their attendant welds gave no sign of any serious problem. Examination of Figure H.6 shows that most of the clustering of the emission sources bordered the location of the middle stiffening ring. Figure H.8 shows that the highest density for all located events was also found in this section. The only serious cluster not located near this stiffening ring was Cluster A that was located by the tear that terminated the test. Clusters I and J, each comprised of four events with a very low signal strength, are considered insignificant.

The large tear, roughly 190-mm long, at the equipment hatch area of the SCV model occurred just above the Cluster A, as shown in Figure H.6. Most of the events in this cluster were located below the tear. It was thought that these events were produced by the precursor to the tear and that the offset of the cluster location was caused by the acoustic path distortions caused both by the equipment hatch opening and by the tear itself. The plot of the signal strength as a function of pressure shown in Figure H.7 for Cluster A shows several well-spaced events below 4.0 Mpa, but most of the events appear above 4.2 MPa. Emission continued until the test was stopped. The events that appeared at lower pressures may have been produced by the discontinuities in the weld along the equipment hatch reinforcement plate. It should be noted in the graph for Cluster A (Figure H.7) that there is no emission immediately prior to the leak. The last located event in Cluster A occurred 3 minutes and 36 seconds before the acoustic leak signal was detected. This observation indicates that the opening that stopped the test was a ductile tear and not a propagating crack.

Cluster B, whose activity plot is also shown in Figure H.7, extends downward from the stiffening ring. Posttest inspection of the model revealed that there is no visible flaw in this region. However, after the contact structure was removed, many vertical parallel stretch marks were found on the painted exterior surface of the model)Figure H.9). Unfortunately, visual examination of the painted surface cannot determine whether the acoustic emissions were caused by paint fracture or slow tearing. There were at least two other areas on the model that had similar paint cracks but did not produce a strong cluster of emission at high pressures. The most probable interpretation is to associate the upper emission locations with the stiffener ring and at least some of the lower emission locations with the paint cracks.

Clusters B, C, D, E, F, G, and H appear to be associated with the stiffening ring which was welded to the inside of the conical shell section. There are two small weld relief openings at the stiffening ring, located at 21° and 201° near clusters C and D, respectively. Posttest inspection of the model revealed that there was a small tear at 21°, and the shell within the opening at 201° experienced local necking. It is interesting to note that Cluster D consists of two clusters with a gap in the middle, exactly at the position of the ductile tear. This is consistent with the tear being ductile and not a propagating crack.

The question remains as to the cause of the acoustic emission in the vicinity of the stiffening ring. The ring was attached to the shell by partial penetration welds, leaving a small void between the shell and the ring between the welds. It is probable that this type of weld geometry may become starter sites for micro-cracking. In addition, any weld flux trapped in this void can crack with small changes in the void geometry. Both microcracks and flux cracking produce acoustic emissions.

It had been expected that when the contact structure and the model came in contact, acoustic emission would be generated by the two surfaces sliding against each other. This emission would be characterized by very long events. No such events or hits were detected. However, posttest examination of the contact regions showed that some wires between the two structures were flattened. These wires, and to a lesser extent, the thick paint on the exterior of the model would tend to prevent direct contact of the metal structures. The only evidence of the effect of the contact structure is seen in Figure H.7, the curve for Cluster C: while there was emission continuously to the failure pressure, the rate dropped off suddenly at 4.0 MPa. This phenomenon could have been caused by a local contact, thus reducing the local deformation in the conical shell section above 4.0 MPa.

H.6 Conclusions

The real time acoustic emission monitoring of the high pressure test of the SCV model provided information on the general condition of the model throughout the test. It did not generate data to signal the onset of model failure in terms of failure pressure and failure locations on the model. The posttest metallurgical evaluation results indicate that the tear at the equipment hatch reinforcement plate was caused by a ductile shear. This failure mode might prevent the acoustic emission device from providing data on model failure. The ductile tearing did not generate detectable acoustic emission at the selected threshold of detection (the trigger threshold was 45 dB - 180 microvolts out of the sensor).

The posttest acoustic emission analysis identified two regions on the SCV model that suffered damage during the high pressure test. Cluster A is located approximately at the site of the ductile tear that ended the test. The acoustic emission data in Figure H.7 indicate that the major damage occurred between 4.20 and 4.30 MPa. However, Figure H.5 shows that the large gas leak did not start until 4.62 MPa. This leads to the conclusion that some tearing in the model shell occurred from 4.2 to 4.3 MPa at this site but that ductile tearing did not open the large leak path until 4.62 MPa. The second damaged region, including the clusters B through H, was located along the middle stiffening ring. The partial penetration weld at the stiffening ring created a void between the ring and the shell, resulting in many possible crack initiation sites. Acoustic emission activity curves for the clusters along the ring indicate that some microcracking started at the base of the ring around 3.5 MPa.

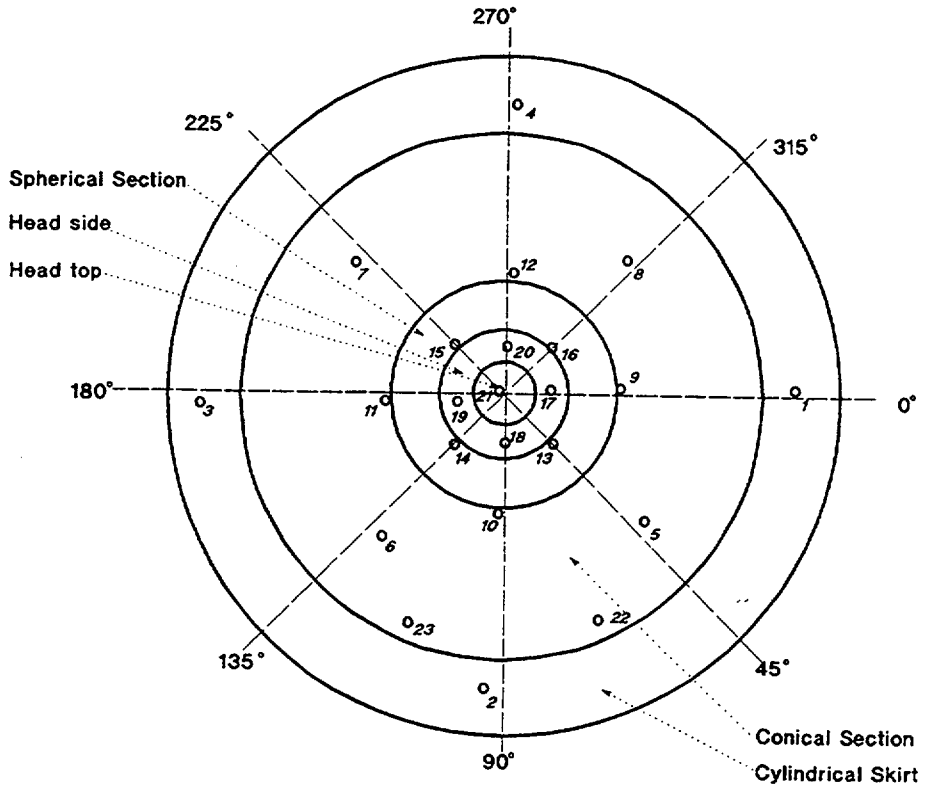

Figure H.1 Schematic representation of the sensor layout on the SCV model.

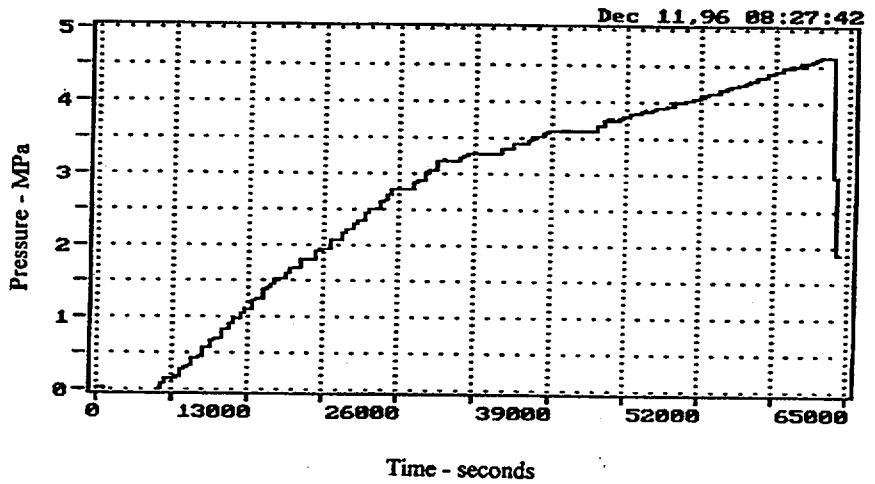

Figure H.2 Pressure as a function of time in the SCV high pressure test.

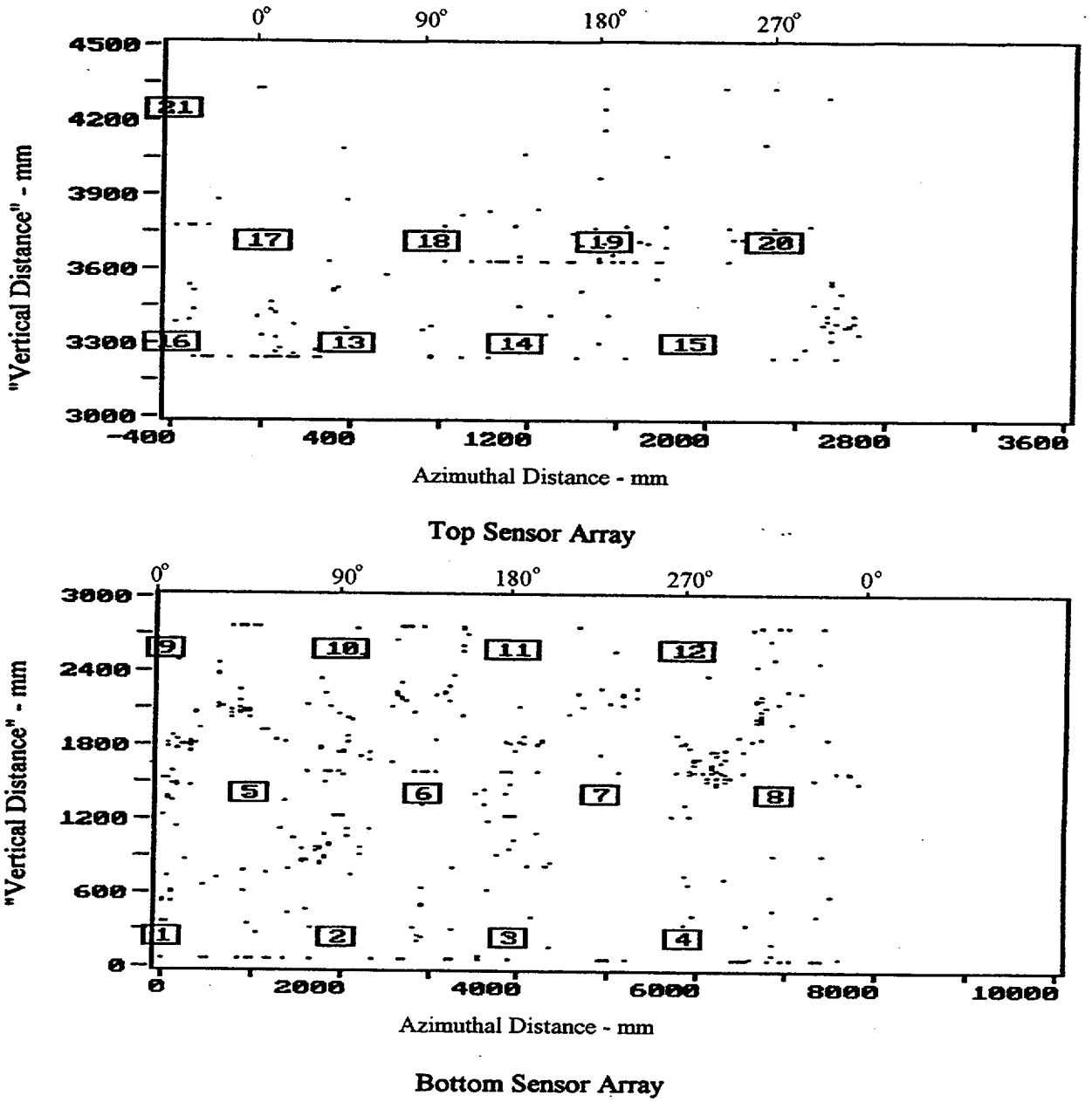

Figure H.3 Total event locations recorded in the high pressure test.

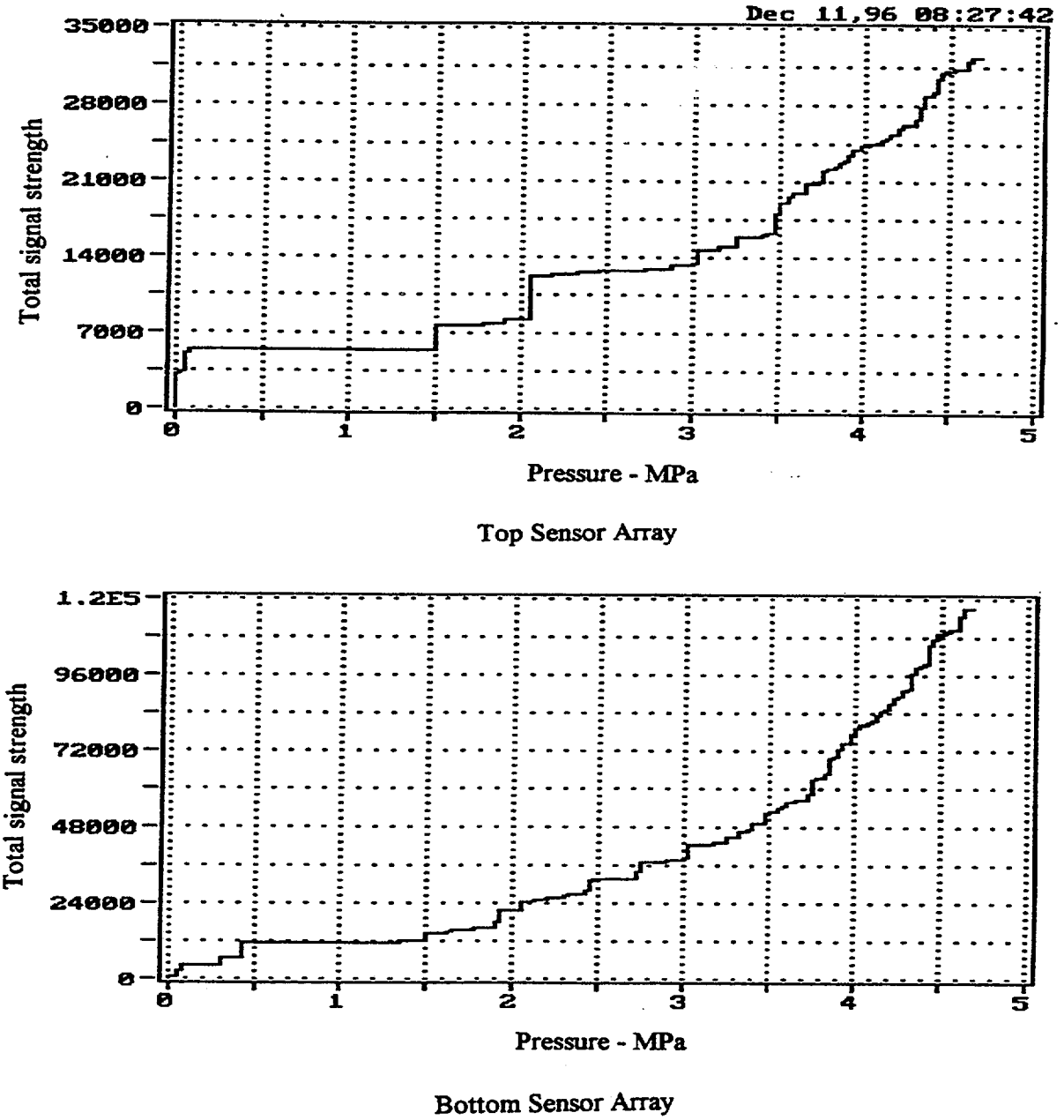

Figure H.4 Total signal strength of located events vs pressure for top and bottom arrays.

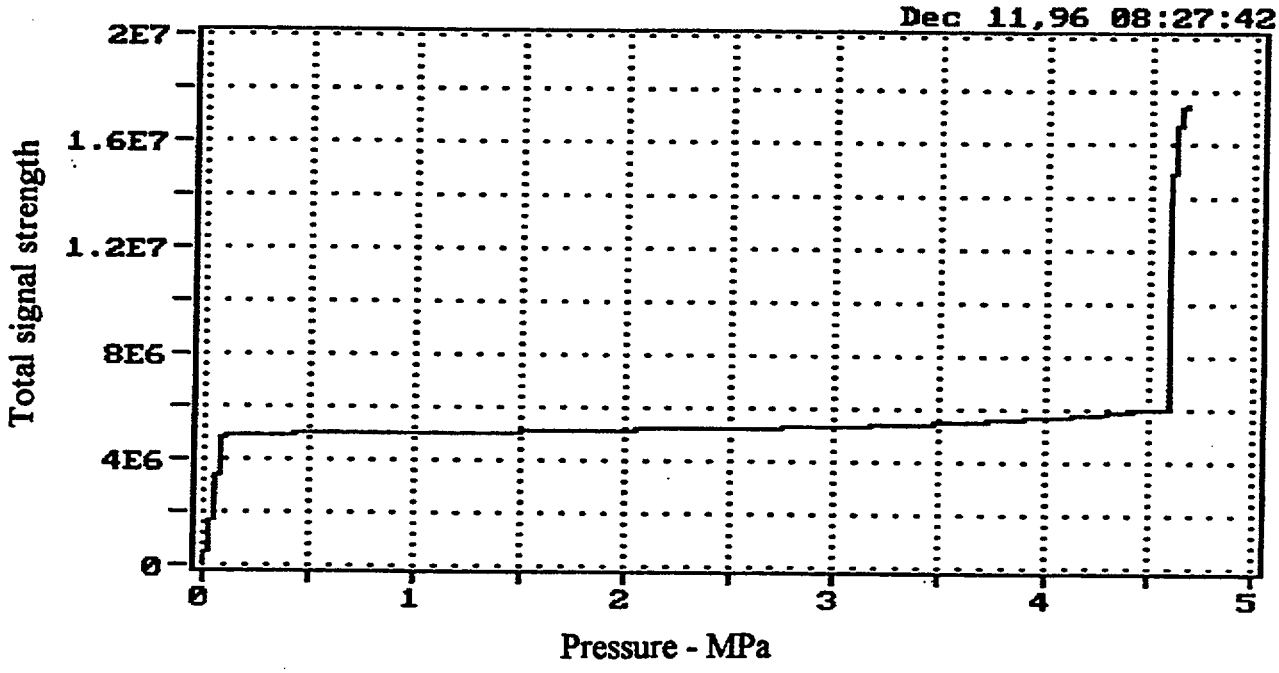

Figure H.5 Total hit signal strength for entire test showing gas inflow noise and leak noise.

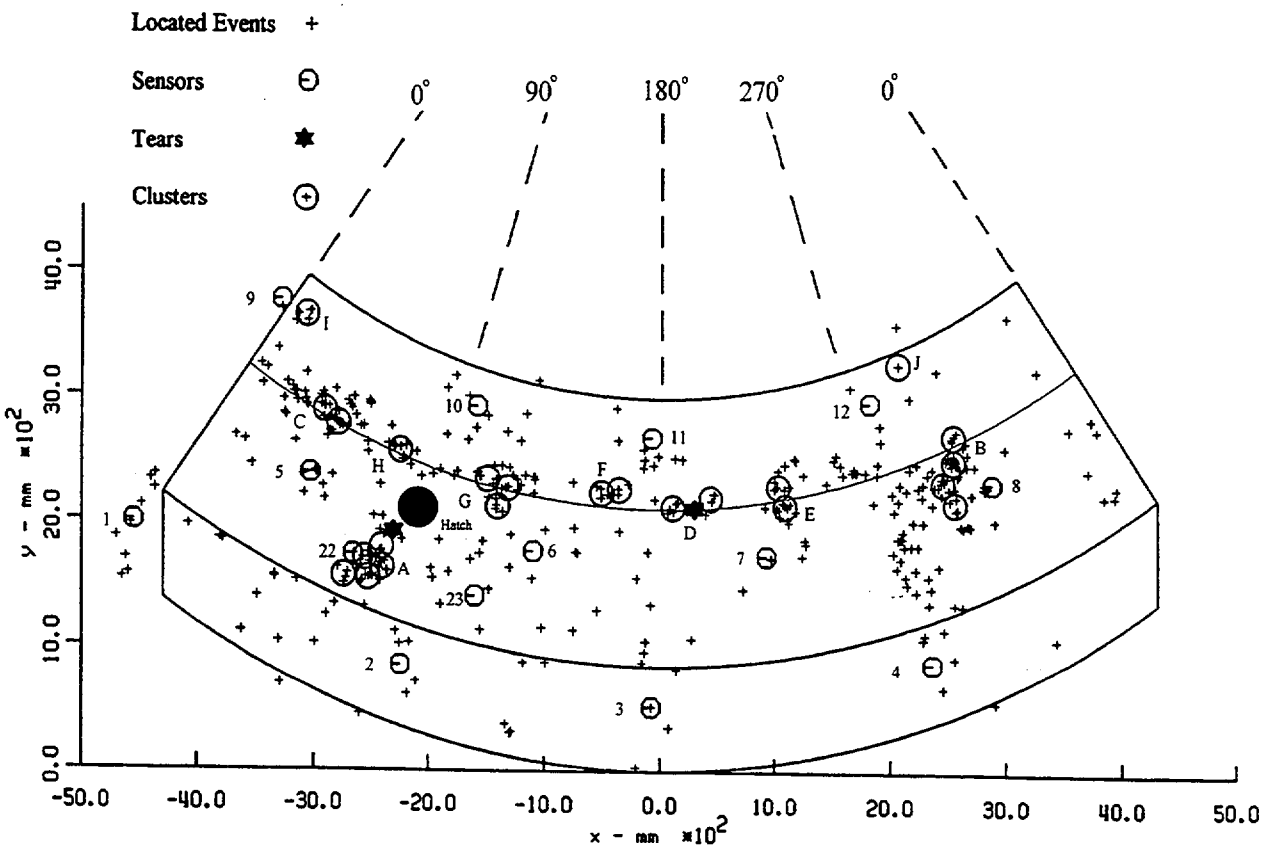

Figure H.6 Map of the flattened conical section and cylindrical skirt.

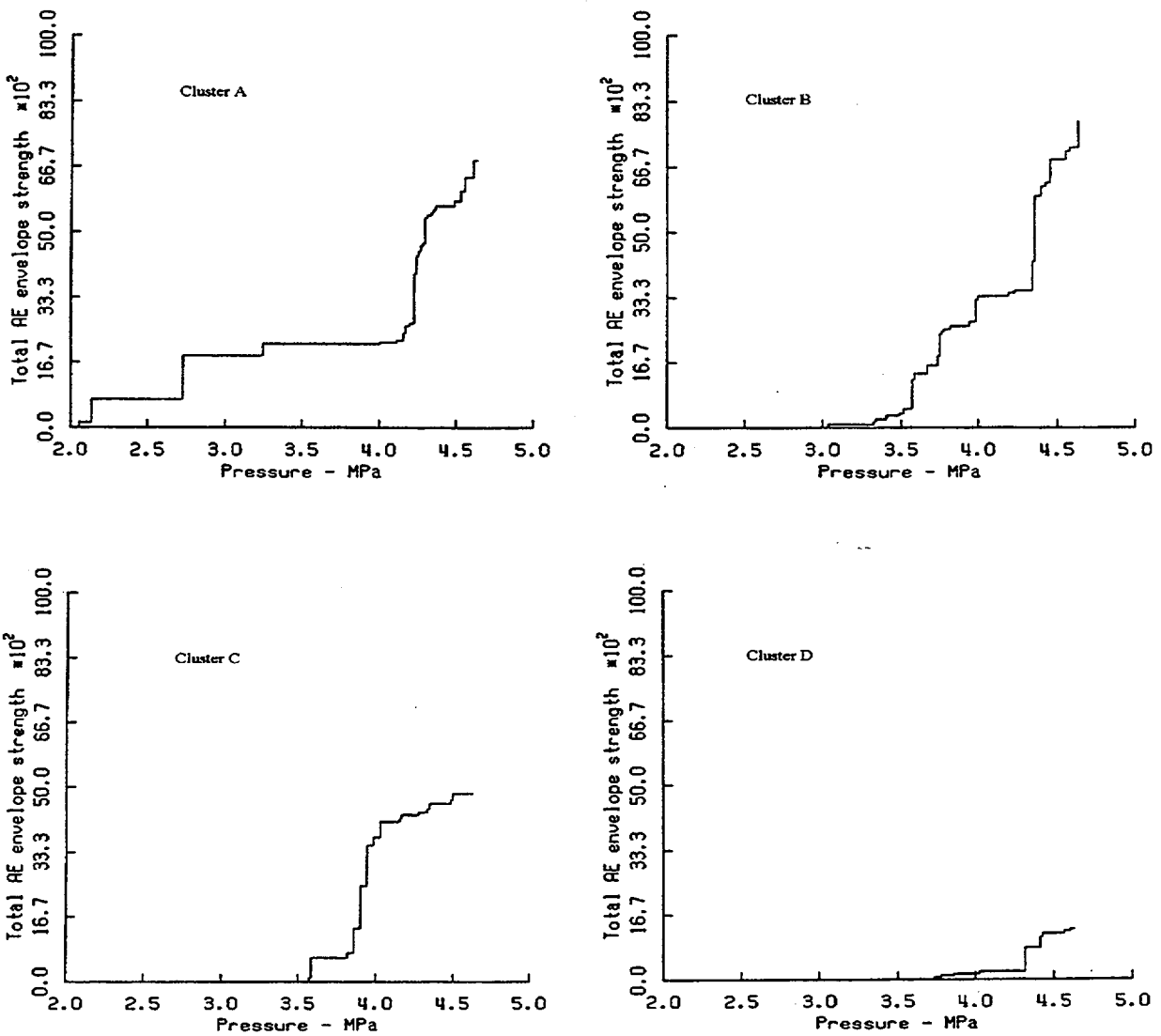

Figure H.7 Total signal strength as a function of pressure.

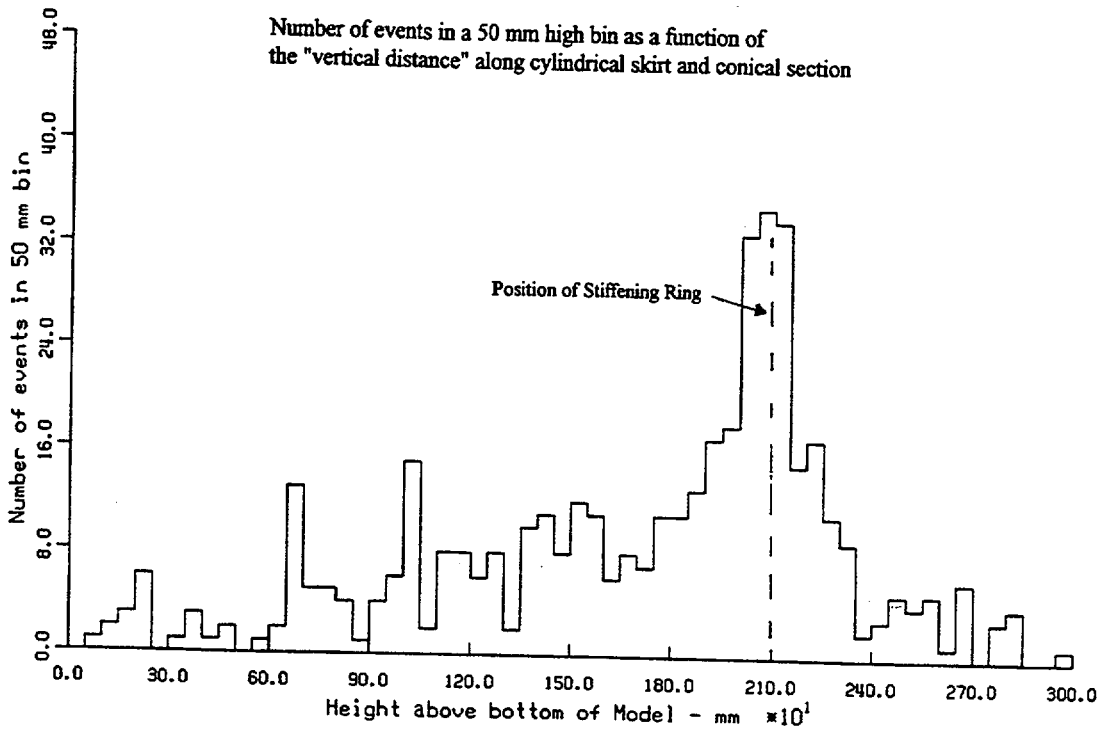

Figure H.8 Distribution of located events as a function of meridional distance above the ring support girder.

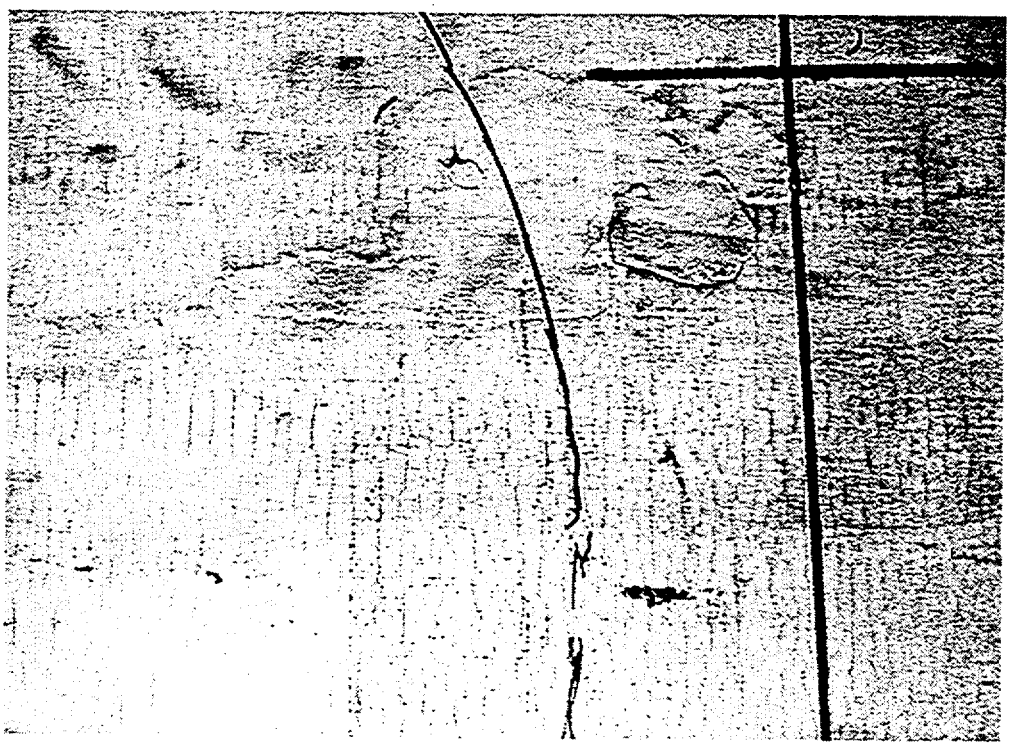

Figure H.9 Paint cracks on outside of SCV model at Cluster B and the curved line encloses Cluster B.

Appendix I

Listing of All Sample Hardness Measurements (Rockwell B Scale)

Appendix I: Listing of All Sample Hardness Measurements (Rockwell B Scale)

Sample	Material	Zone Description	Average (x)	Standard Deviation (s)	Raw Data				
Plate	SPV490	Base Metal	98.8	0.7	99.2	98.1	97.6	98.4	98.6
SCV-74-1	SPV490	Base Metal	98.1	1.0	98.8	99.6	98.4	98.7	98.0
		HAZ	91.5	1.1	92.8	92.1	90.1	90.4	92.1
		Fusion Zone	95.1	1.1	95.5	94.7	96.4	95.6	93.3
SCV-74-3	SGV480 (Side)	Base Metal	89.18	0.15	89.0	89.1	89.3	89.1	89.4
		HAZ	92.20	1.49	89.9	94.3	91.4	92.3	93.1
	SPV490 (Side)	Base Metal	94.24	0.39	94.8	94.4	93.9	93.7	94.4
		HAZ	90.82	1.80	90.1	89.3	89.2	92.2	93.8
		Fusion Zone	92.10	0.96	92.7	90.2	92.6	92.7	92.3
SCV-106-1	SPV490	Base Metal	97.36	1.22	97.4	98.6	97.2	99.0	97.2
					97.1	96.2	95.5	97.2	100.0
		HAZ	92.06	1.69	95.1	92.7	91.0	91.0	90.5
		Fusion Zone	97.21	1.11	98.6	98.6	97.8	97.3	98.4
					97.6	98.4	96.2	98.6	96.4
SCV-106-2	SPV490	Base Metal	96.96	1.34	94.8	95.4	95.3	96.4	99.8
					96.6	96.2	97.5	96.6	96.4
		HAZ	88.64	1.04	90.1	89.5	87.3	87.8	88.5
		Fusion Zone	94.93	2.58	94.1	94.7	96.5	98.3	98.9
SCV-340	SPV490	Base Metal	97.93	0.84	96.8	99.1	99.0	96.5	96.8
					98.3	98.3	97.9	98.1	98.5
		HAZ (areas of minimum deformation)	96.65	1.83	93.8	97.0	97.5	98.3	92.9
		Fusion Zone	97.63	0.55	97.1	97.7	98.1	97.2	96.4
					98.6	97.4	97.8	97.7	97.2
SCV-21	SGV480	Base Metal	88.82	1.26	89.7	90.3	90.0	88.4	87.3
		HAZ (undeformed area)	92.75	0.56	92.6	92.4	92.3	93.7	
		HAZ (deformed area)	95.08	2.27	91.0	94.7	95.3	97.1	97.3
		Fusion Zone	95.53	0.82	95.9	94.6	95.7	97.3	94.7

NRC FORM 335 (2-89) NRCM 1102, 3201, 3202

U.S. NUCLEAR REGULATORY COMMISSION

BIBLIOGRAPHIC DATA SHEET

(See instructions on the reverse)

1. REPORT NUMBER (Assigned by NRC, Add Vol., Supp., Rev., and Addendum Numbers, if any)
NUREG/CR-5679
SAND 98-2701

2. TITLE AND SUBTITLE

Design, Instrumentation, and Testing of a Steel Containment Vessel Model

3. DATE REPORT PUBLISHED

MONTH	YEAR
February	2000

4. FIN OR GRANT NUMBER
A1401

5. AUTHOR(S)
Vincent K. Luk/Sandia National Laboratories
Michael F. Hessheimer/Sandia National Laboratories
Gina S. Rightley/Sandia National Laboratories
L. Dwight Lambert/Sandia National Laboratories
Eric W. Klamerus/Sandia National Laboratories

6. TYPE OF REPORT
Technical

7. PERIOD COVERED *(Inclusive Dates)*
6/92 to 5/98

8. PERFORMING ORGANIZATION – NAME AND ADDRESS *(If NRC, provide Division, Office or Region, U.S. Nuclear Regulatory Commission, and mailing address; if contractor, provide name and mailing address.)*

Sandia National Laboratories
P. O. Box 5800, MS 0744
Albuquerque, NM 87185-0744

9. SPONSORING ORGANIZATION – NAME AND ADDRESS *(If NRC, type "Same as above", if contractor, provide NRC Division, Office or Region, U.S. Nuclear Regulatory Commission, and mailing address.)*

Systems Safety Department
Nuclear Power Engineering Corporation
Fujita-Kanko Building
17-1, 3-Chome, Toranomon, Minato-Ku
Tokyo 105, Japan

Division of Engineering Technology
Office of Nuclear Regulatory Research
U.S. Nuclear Regulatory Commission
Washington, D.C. 20555

10. SUPPLEMENTARY NOTES
T. Hashimoto, NUPEC Project Manager

J. F. Costello, NRC Project Manager

11. ABSTRACT *(200 words or less)*

The Nuclear Power Engineering Corporation (NUPEC) of Japan and the U.S. Nuclear Regulatory Commission (NRC) are co-sponsoring and jointly funding a cooperative containment integrity research project at Sandia National Laboratories (SNL) to conduct a failure test of a steel containment vessel (SCV) model and contact structure assembly. The SCV model, representative of an improved Mark-II Boiling Water Reactor (BWR) containment vessel, is scaled 1:10 in geometry and 1:4 in shell thickness. The contact structure, a thick bell-shaped steel shell, provides a simplified representation of a concrete reactor shield building in the actual plant. The high pressure test of the SCV model was conducted at SNL on December 11-12, 1996 to provide data on the structural response of the SCV model up to its failure in order to validate analytical modeling, to find its pressure capacity, and to observe the failure mode and mechanisms.

The SCV model and the contact structure were instrumented with strain gages, displacement transducers, contact detection devices, pressure transducers, and thermocouples. The maximum pressure achieved during the high pressure test was 4.66 MPa or approximately 6 times the scaled design pressure. Posttest model inspection revealed that the leakage was caused by a large tear, about 190-mm-long, along a weld seam at the outside edge of the equipment hatch reinforcement plate. This report describes the design, instrumentation, test operation and results of the SCV model.

12. KEY WORDS/DESCRIPTORS *(List words or phrases that will assist researchers in locating the report.)*

Steel Containment Vessel, Design, Instrumentation, Failure Test, Pressurization System, Data Acquisition and Correction, Failure Pressure and Mechanisms

13. AVAILABILITY STATEMENT
Unlimited

14. SECURITY CLASSIFICATION
(This Page)
Unclassified

(This Report)
Unclassified

15. NUMBER OF PAGES

16. PRICE